

Alma Mater Studiorum – Università di Bologna

DOTTORATO DI RICERCA IN
Scienze Chimiche
Ciclo XXV

Settore Concorsuale di afferenza: 03/B1

Settore Scientifico disciplinare: CHIM/03

**DEVELOPMENT OF NEWLY CONCEIVED BIOMIMETIC
NANO-STRUCTURED BIOMATERIALS AS SCAFFOLDS
FOR BONE AND OSTEOCHONDRAL REGENERATION**

Presentata da: *Dott.ssa D'Alessandro Teresa*

Coordinatore Dottorato
Prof.ssa Adriana Bigi

Relatore
Prof. Norberto Roveri

Correlatore
Dott.ssa Anna Tampieri

Esame finale anno 2013

Contents

Aim of research	I
PART I: GENERAL TOPICS	
1 Introduction	1
1.1 Biomaterials.....	1
1.2 Biomaterials for bone substitution.....	1
1.2.1 Biomimetic materials.....	3
1.3 Bone tissue.....	4
1.3.1 Biology of bone tissue	4
1.3.2 Morphology and structure of bone tissue	5
1.3.3 Articular bone region.....	7
1.3.4 Vertebral bone region.....	9
1.3.5 Degeneration of bone tissue.....	11
1.3.6 Biomineralization process.....	13
1.3.7 Biological bone mineral phase.....	15
References	16
2 Biomaterials for regenerative medicine: treatment of musculoskeletal diseases	19
2.1 Rigenation of bone and osteo-cartilaginous tissue: problems and solutions.....	20
2.2 The most important musculoskeletal diseases: Osteoporosis (OP) and Osteoarthritis (OA).....	23
2.3 Current clinical treatments for OA and OP.....	24
2.3.1 Main problems in the treatment of OA.....	25
2.3.2 Main problems in the tratment of OP.....	26
2.3.3 Newly conceived biomaterials as scaffolds for the treatment of OA and OP.....	27
References	31

3 Magnetism in biomedical applications: a new concept for tissue regeneration	35
3.1 Biomedical applications.....	35
3.1.1 Magnetic bioseparation.....	35
3.1.2 Drug delivery.....	36
3.1.3 MRI contrast agents.....	37
3.1.4 Hyperthermia for the treatment of cancer.....	38
3.1.5 Magnetic therapy for the treatment of bone disease.....	39
3.2 Magnetic materials.....	41
3.2.1 The influence of temperature.....	43
3.2.2 Factors affecting magnetic properties.....	44
3.2.3 Intelligent magnetic nanobiomaterials for Tissue Engineering	45
References	47
4 Biomimetic materials	51
4.1 Calcium phosphate in biological systems.....	51
4.2 Tricalcium phosphate (TCP).....	52
4.3 Bioactivity of calcium phosphate.....	53
4.4 Apatites.....	54
4.4.1 Hydroxyapatite: structure and chemistry.....	54
4.4.2 Biological Apatites.....	56
4.4.3 Effect of Carbonate.....	57
4.4.4 Effect of Magnesium.....	58
4.4.5 Effect of Strontium.....	58
4.5 Non-stoichiometric and substituted HA.....	60
4.6 Natural polymer.....	63
4.6.1 Collagen.....	64
4.6.2 Alginate.....	66
4.6.3 Gelatin.....	68
References	70

PART II: EXPERIMENTAL

5 Analytical Tecnique	75
5.1 X-Ray Diffraction (XRD).....	75
5.1.1 Quantitative phase analysis: Reference Intensity Ratio (RIR) method.....	80
5.1.2 Rietveld Method.....	81
5.2 Fourier-Transform Infrared Spectroscopy (FTIR).....	81
5.3 Inductively Coupled Plasma Atomic Emission Spectroscopy (ICP-AES)...	83
5.4 Scanning Electron Microscopy (SEM).....	84
5.5 Thermogravimetric and Thermoanalytical analyses (TG-DTA).....	88
5.6 Powder analysis.....	89
5.6.1 Specific Surface Area.....	89
5.6.2 Granulometric Analysis.....	91
5.7 Mechanical properties.....	92
5.8 Magnetic measurements.....	94
5.6.1 Magnetic Susceptibility.....	94
6 Magnetic Fe²⁺/Fe³⁺ doped Hydroxyapatite (FeHA)	97
6.1 Synthesis of FeHA powder.....	98
6.2 Chemical, structural and magnetic characterization of FeHA powder.....	100
6.2.1 Phase analysis by XRD.....	102
6.2.2 Chemical analysis by ICP.....	105
6.2.3 Magnetic and microstructural investigation.....	107
6.2.4 Hyperthermia effect of FeHA powder.....	111
6.3 Development of FeHA granulate.....	112
6.4 Biocompatibility tests.....	113
6.4.1 <i>In vitro</i> evaluation of biocompatibility and cell morphology.....	113
6.4.2 Effects of the <i>in vitro</i> applications of a static magnetic field.....	115
6.4.3 <i>In vivo</i> pilot experimental and histological analysis.....	117
6.5 Conclusion.....	119
References	121
7 Development of magnetic biohybrid FeHA/Coll scaffolds	123
7.1 Synthesis process of HA/Coll composite.....	123
7.2 Synthesis process of FeHA/Coll composites.....	124

7.3	Chemico-physical and magnetic characterization of FeHA/Coll composites.....	125
7.3.1	X-ray diffraction analysis (XRD).....	125
7.3.2	Thermogravimetric analysis (TG-DTG).....	126
7.3.3	Infrared spectroscopy analysis (FTIR).....	128
7.3.4	Morphological analysis by scanning electron microscopy (SEM) and by transmission electron microscope (TEM).....	131
7.3.5	Chemical analysis by ICP.....	133
7.3.6	Magnetic properties of FeHA/Coll composites.....	134
7.4	<i>In vitro</i> evaluation of FeHA/Coll scaffolds.....	138
7.5	Development of a three-layer magnetic scaffold.....	140
7.6	Conclusion.....	142
	References	143
8	Bioactive calcium phosphate bone cement: basic concepts	145
8.1	Features of injectable bone cements.....	145
8.2	Hardening mechanism.....	147
8.3	Cement microstructure and porosity.....	147
8.4	Bioactivity and resorption of calcium phosphate cement.....	148
	References	150
9	Development of biomimetic calcium phosphate bone cement	153
9.1	Synthesis of metastable CaP phase.....	154
9.1.1	Synthesis of α -TCP.....	154
9.1.2	Synthesis of Sr α -TCP.....	154
9.2	Development of biomimetic hydroxyapatite based bone cement.....	159
9.2.1	Hydrolysis of α -TCP powder: synthesis of HA cement.....	159
9.2.2	Hydrolysis of Sr α -TCP powder: synthesis of SrHA cement.....	163
9.2.3	Intoduction of carbonate ions during Sr α -TCP hydrolysis: synthesis of SrCHA.....	169
9.3	Introduction of polymeric phase into calcium phosphate cement.....	171
9.3.1	Calcium phosphate/gelatine bone cement.....	173
9.3.2	Calcium phosphate/Sodium alginate bone cement.....	177
9.4	Porosity measurements.....	181
9.5	Mechanical properties.....	182

9.5.1	Compression strength.....	183
9.5.2	Young's Modulus.....	184
9.6	Route to enhance the mechanical properties of CaP bone cement.....	185
9.6.1	Incorporation of TiO ₂ as bio-active reinforcing phase.....	186
9.6.2	Sodium alginate cross-linking.....	187
9.7	Conclusion.....	192
	References	194
	Conclusion and Future Perspective	197

Aim of research

The present research activity is focused on the development of a new class of biomaterials and device for application in regenerative medicine, particularly in the repair/regeneration of hard tissue such as bone and osteochondral regions.

The new biomaterials were designed to provide new solutions towards the local treatment of hard tissues affected by degenerative diseases such as Osteoarthritis (OA) and Osteoporosis (OP) or serious traumas. These pathologies affect an ever increasing number of people worldwide with huge socio-economic impact. Although the incidence of such diseases has historically been linked to ageing, more recently the number of relatively young people affected by these diseases has increased, due to new life-styles (e.g. intense sport activity, obesity, alcohol consumption). In the most serious cases, lesions involving osteocartilaginous regions or vertebral bodies can lead to severe complications affecting the neuro-muscular system and can significantly impair the patient's quality of life and longevity. The current therapies mainly aim at blocking the progress of the diseases and/or to provide a physical sustains, in case of vertebral weakening. Such approach, however, has several limitations and drawbacks, and does not provide tissue regeneration and the recovery of the original functions.

During the last decade the scientific research has increasingly pushed towards the development of tissue-mimicking constructs addressed to tissue regeneration. In particular, it is widely accepted that the regeneration of hard connective tissues requires the implantation of porous bio-resorbable scaffolds exhibiting chemical-physical and morphological mimicry with the target tissues so to provide environmental cues for cell adhesion, proliferation and specific differentiation.

With regard to bone, biomimetic apatites, i.e. nanostructured calcium phosphates mimicking the composition and the nanostructure of the mineral bone, are considered the golden biomaterials for regenerative bone scaffolds. In this respect, the Research Group on Biomaterials at ISTE-CNR has 20 years of experience in the synthesis and characterization of nano-apatites with different crystal order and ionic substitutions, suitable to activate specific biologic functions relevant for bone tissue regeneration.

With regard to complex osteochondral regions, ISTE-CNR developed in 2001 a biologically-inspired mineralization processes mimicking the cascade of events yielding

new bone formation, that enabled the synthesis of biomimetic hybrid hydroxyapatite/collagen composites mimicking multifunctional osteochondral regions. By this process, biomimetic, ion-substituted nanoapatites can be heterogeneously nucleated on collagen fibrils, the assembling and organization of which is mediated by several physical, chemical, morphological and structural control mechanisms, activated by pH and temperature control. These scaffolds demonstrated very high regenerative potential and were subsequently patented, scaled up and brought to the market as bone and osteochondral scaffolds.

With respect to this previous knowledge, the present work intended to develop new improved scaffolds for bone and osteochondral tissue regeneration, aimed to achieve faster regeneration and improved texturing of the newly formed tissues. Indeed scientific research is increasingly being devoted to develop new approaches for stimulating cell activity, including the design of specific 3D morphologies and the development of smart, stimuli-responsive, drug delivery systems. A particularly intriguing approach is based on the use of magnetism: recent findings show that the local application of weak magnetic fields may stimulate cells to produce new bone tissue in a more ordered manner.

With this in mind the present research thesis was specifically focused on the synthesis and physico-chemical-morphological characterization of:

- i) a new iron-substituted apatite phase (FeHA) with intrinsic superparamagnetic properties;
- ii) new biomimetic hybrid scaffolds with superparamagnetic properties for bone and osteochondral regeneration, obtained by biologically-inspired mineralization processes;
- iii) new self-setting injectable pastes based on calcium phosphates functioning as apatitic bone cements for regenerative vertebroplasty.

More specifically, in the present work a new apatite phase with superparamagnetic properties was developed, by performing ionic substitutions in the apatite lattice, particularly of bi- and tri-valent iron ions replacing calcium, achieved by fine control of the synthesis conditions. The new apatite phase resulted of great potential, due to the possibility of using biocompatible, bioactive and bio-resorbable superparamagnetic phases for a number of applications, spanning from regenerative medicine to theranostics and imaging, thus overcoming the current use of magnetite nanoparticles, which raise several concerns for their long-term cytotoxicity.

The development of this new phase was exploited in the generation of biologically-inspired mineralization process enabling the heterogeneous nucleation of superparamagnetic nano-apatite on collagen fibrils. By reproducing the conditions of formation of new bone tissue, thus obtaining highly biomimetic bone, osteochondral scaffolds with intrinsic superparamagnetic properties were synthesized. This approach may open the way to the generation of new scaffolds with multiple functionality, i.e. the possibility to activate the scaffold by remote magnetic control and provide local signals to enhance the regenerative processes. Additionally, the remote magnetic activation can enable the recall and controlled delivery of osteogenic and angiogenic growth factors linked to magnetic nanoparticles so to achieve scaffolds functioning as a flexible “workstation” able to regulate and guide tissue regeneration on the basis of the personal needs of the patient.

In the view of specific treatments for patients affected by osteoporosis or traumas involving vertebrae weakening or fracture, the present work was also dedicated to the development of new self-setting injectable pastes based on strontium-substituted calcium phosphates, able to harden *in vivo* and transform into strontium-substituted hydroxyapatite. The addition of strontium may provide an anti-osteoporotic effect, aiding to restore the physiologic bone turnover. The ceramic-based paste was also added with bio-polymers, able to be progressively resorbed thus creating additional porosity in the cement body that favour cell colonization and osseointegration. This approach may enable innovative therapies against the weakening of vertebral bodies due to osteoporosis or serious traumas. In this respect, the current clinical approach is mainly the percutaneous injection of acrylic bone cements, which can harden in few minutes and allow the early dismissal of the patient after surgery. However, due to several drawbacks related to the exothermy of the polymerization reaction, the bioinertness of acrylic phases and the excessive stiffness of the cement in relationship with the surrounding bone, this solution is not suitable for relatively young patients (<60-65 years) and/or severe patients, and reliable regenerative solutions for vertebroplasty are still missing. The set up and development of regenerative bone cements were made difficult so far by the high complexity of the processes required to establish pastes characterized, at the same time, by high bioactivity, osteogenic and osteoconductive character, the absence of any adverse reactions, in association with good injectability, low setting times (in the order of minutes) and sufficient compression strength allowing stable fixation upon injection.

The new bio-devices developed in the present work may enable new tissue regeneration-based treatments and minimally-invasive surgical approach that have the potential to overcome the limitations and drawbacks associated with the current therapies. In these clinical situations, the development of biomimetic, bioresorbable scaffolds with regenerative ability is regarded by clinicians as breakthrough solutions in the cure of these debilitating pathologies. In fact, autologous bone grafts are not always readily available in sufficient amounts, and its use poses concerns on the patient health and pain, bone allografts are inferior to autologous bone, are expensive, and have known risks of bacterial contamination, viral transmission and immunogenicity. Moreover the use of the new superparamagnetic iron-substituted apatite nanoparticles and hybrid scaffolds may pave the way to the establishment of newly conceived therapies for tissue regeneration, as well as novel applications in theranostics and imaging characterized by virtual absence of any drawbacks related to the cytotoxicity of nanoparticles.

PART I:
GENERAL TOPICS

CHAPTER 1

INTRODUCTION

1.1 Biomaterials

In the last few years the biomedical research area is going towards materials science aiming applications of materials to health care, the so-called *biomaterials*. They can be defined as implantable materials that must be in contact with living tissues with the final aim of achieving a correct biological interaction between the material and the host¹. In the first Consensus Conference of the European Society for Biomaterials (ESB) in 1976, a biomaterial was defined as “a nonviable material used in a medical device, intended to interact with biological systems”; however the ESB’s current definition is a “material intended to interface with biological systems to evaluate, treat, augment or replace any tissue, organ or function of the body”. This subtle change in definition is indicative of how the field of biomaterials has evolved. Biomaterials have moved from merely interacting with the body to influencing biological processes toward the goal of tissue regeneration. However, a more recent definition has been published: *A biomaterial is a substance that has been engineered to take a form which, alone or as part of a complex system, is used to direct, by control of interactions with components of living systems, the course of any therapeutic or diagnostic procedure, in human or veterinary medicine*².

1.2 Biomaterials for bone substitution

Biomaterials for bone substitution are employed mainly as fillers, or as structural substitutes or as coating for screws or similar device. The ultimate aim of biomaterials for bone substitution is to restore the structural integrity of the damaged bone.

The substitution of bone intends mainly to restore the structural functionality of the missing part, but it is not able to completely restore all its properties; the very complex composition and morphology of the bone tissue are responsible of its unique ability to

continuously adapt to the ever changing mechanical solicitations, so to be simultaneously light, tough and elastic and able to locally regenerate after traumas of limited extension. Thus, with the increasing of the expectance of life and well-being, the development of bone substitutes able to restore the whole functionality of the original tissue was of increasing importance in the last decades; beyond the commercial aspects, the problem has a highly social relevance as the patients can regain a more active and satisfactory life and sooner than in the past.

An ideal bone substitute should be **biomimetic**, i.e. able to perfectly mimic *in vivo* the behaviour of the natural bone. For this reason, not only biocompatibility is required, but features of bioactivity, osteoinductivity, osteoconductivity and bio-resorbability are also strongly needed.

Biocompatibility is the ability of a material to perform with an appropriate host response in a specific application, without having any toxic or injurious effects on biological systems. The scope of this definition is very wide and many subgroups of applications can be found to make more narrow definitions of biocompatibility. Anyway, for a long-term implantable medical device, like a bone substitute, the biocompatibility refers to the ability of the device to perform its intended function, with the desired degree of incorporation in the host, without eliciting any undesirable local or systemic effects in that host.

Bioactivity is the ability of the implant to bond to bone tissue. The process of bone bonding is the result of multiple, parallel and sequential reactions at the material-tissue interface. These interactions are related to either physicochemical phenomena that occur in the presence or absence of cells, or are related to reactions affected by cellular activity.

Osteoinductivity is the ability of a material to induce cell differentiation oriented to the synthesis of a bone matrix, able to mineralize in bone tissue.

Osteoconductivity is a passive property of the implant consisting in the ability of making easy the formation and diffusion of the new bone both through its chemical (presence of ions and substances able to enhance the cell activity for **osteogenesis**, the process of new bone development) and morphological (hierarchically organized porous structure able to host the growing bone tissue and the vascular system) features.

Bioresorbability is the ability of the implant to be dissolved by the *in vivo* processes of bone remodelling and to be replaced by the new bone tissue.

1.2.1 Biomimetic materials

Biomimetics is a new, very important, field of science that studies how Nature designs, processes and assembles/disassembles molecular building blocks to fabricate high performance mineral-polymer composites (e.g. mollusc shells, bone, tooth) and/or soft materials (e.g. skin, cartilage, tendons) and then applies these designs and processes to engineer new molecules and materials.

In nature, living organisms synthesize mineralized tissues and this process of biomineralization is under strict biological control. It involves the interactions of several biological macromolecules among themselves and with the mineral components. Generally, nature's design principles are based on a "Bottom-Up" strategy. Such processes lead to the formation of hierarchically structured organic-inorganic composites with mechanical properties optimized for a given function. A common theme in mineralized tissues is the intimate interaction between the organic and inorganic phases and this leads to the unique properties seen in biological materials. Therefore, understanding nature's design principles and ultimately mimicking the process may provide new approaches to synthesize biomaterials with unique properties for various applications.

In fact, in the last decades the activity of material scientists was more and more directed to the development of biomimetic scaffolds, able to drive and address cell activity towards proper differentiation and the repair of diseased human tissues³. In case of bone, this requires the synthesis of three-dimensional constructs able to exchange chemical signals promoting osteogenesis and to progressively be resorbed during the formation and remodelling of new bone. Besides, particularly for the regeneration of extensive portions of bone, a morphological and mechanical biomimesis is also required, to allow cell colonization and formation of a proper vascularization tree. The healing of load-bearing bones also requires scaffolds with a hierarchically organized morphology, to provide improved biomechanical behaviour and allow a proper mechano-transduction of the mechanical stimuli down to the cell level⁴.

1.3 Bone tissue

Bone is a bioceramic composite that has long held the attention of the materials engineer who seeks to duplicate its enviable mechanical properties, in which both high strength and fracture toughness can be achieved due to the unique architecture of this organic-inorganic composite.

1.3.1 Biology of bone tissue

Bone is a specialised connective tissue which forms the basis of the skeleton and, as such, its functions are numerous and complex. One of these functions, although not necessarily the most important, is to protect the internal organs from damage which could result from the physical trauma of everyday life. In combination with the associated musculature, the bones of the skeleton also provide a means of physical support, locomotion and related movement. One further role is that of a reservoir for a multitude of inorganic ions.

Three distinctly different cell types can be found within bone (Fig.1): the matrix-producing osteoblast, the tissue-resorbing osteoclast, and the osteocyte, which accounts for 90% of all cells in the adult skeleton⁵.

Osteoblasts (from the Greek words for "bone" and "germ" or embryonic) are the cells within bone that lay down the extracellular matrix and regulate its mineralization. Morphologically, these cells are cuboidal in shape and located at the bone surface together with their precursors, where they form a tight layer of cells. Osteoblasts are located on the surface of osteoid seams and also manufacture hormones, such as prostaglandins, to act on the bone itself. They robustly produce alkaline phosphatase, an enzyme that has a role in the mineralisation of bone, as well as many matrix proteins. Osteoblasts are the immature bone cells. When osteoblasts are trapped in the bone matrix, which they themselves produced, they become star-shaped cells named osteocytes, the most abundant cell found in bone.

Osteocytes are osteoblasts that remain in bone matrix until they degrade according to natural cycle of life. They are set both in cortical and trabecular bone localizing in hollows or bone gaps, among one lamella and the other. They have a flat and long shape with cytoplasmatic prolongations. Their function is to guarantee the survival of the surrounding tissue taking nourishing substances from the medullar hollow through cytoplasmatic channels (canaliculi)⁶. Osteocytes are not active producers or destroyers of

bone matrix, but are able to feel mechanical solicitations and, if necessary, control the other bone-cells activity such as deposition and reabsorption processes of mineral phase.

Osteoclasts (from the Greek words for "bone" and "broken") are multinucleated cells, like macrophages, derived from the hematopoietic lineage. They degrade the mineralized bone tissue giving rise to isolated micro-ambients where they release acid products dissolving organic and inorganic bone matrixes⁷. Their activity can be controlled, both from chemical signals (hormones, vitamins, low levels of calcium) and mechanical stresses. Those signals stimulate the bone remodelling: the demolition of some lamellae and rebuilding of others differently oriented to better compensate the applied load⁸. In brief, osteoclasts digest while osteoblasts reconstruct again bone tissue⁹.

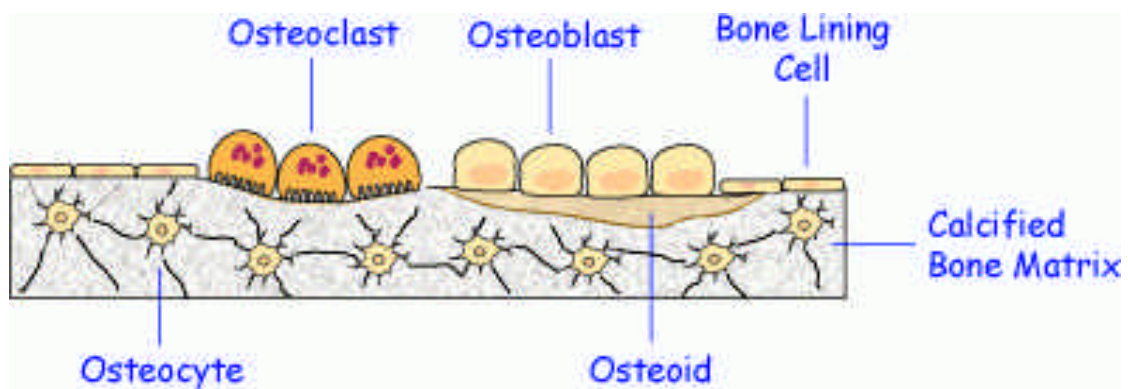


Fig. 1. Bone cells

Osteoid is comprised of type I collagen (~94%) and noncollagenous proteins. The hardness and rigidity of bone is due to the presence of mineral salt in the osteoid matrix, which is a crystalline complex of calcium and phosphate (hydroxyapatite). Calcified bone contains about 25% organic matrix (2-5% of which are cells), 5% water and 70% inorganic mineral (hydroxyapatite).

1.3.2 Morphology and structure of bone tissue

There are three different types of bone tissue, compact (*cortical bone*), trabecular (*cancellous bone*), and subchondral (Fig. 2). The compact one is the harder, outer tissue

of bones, the trabecular one is the sponge-like tissue inside bones, and the subchondral tissue is the smooth one at the apical and basal parts of bones, which is covered with cartilage (made up in turn of chondrocytes, collagen fibers and proteoglycans). Although macroscopically and microscopically different, *cortical bone* and *cancellous bone* are identical in their chemical composition.

Cortical bone, synonymous with **compact bone**, is one of the two types of osseous tissue that form bone. Cortical bone facilitates bone's main functions: to support the whole body, protect organs, provide levers for movement, and store and release chemical elements, mainly calcium. As its name implies, cortical bone forms the cortex or outer shell, of most bones. Cortical bone contributes about 80% of the weight of a human skeleton. The primary anatomical and functional unit of cortical bone is the osteon. Each osteon consists of concentric layers, or lamellae, of compact bone tissue that surround a central canal, the Haversian canal. The Haversian canal contains the bone's nerve and blood supplies. The boundary of an osteon is the cement line.

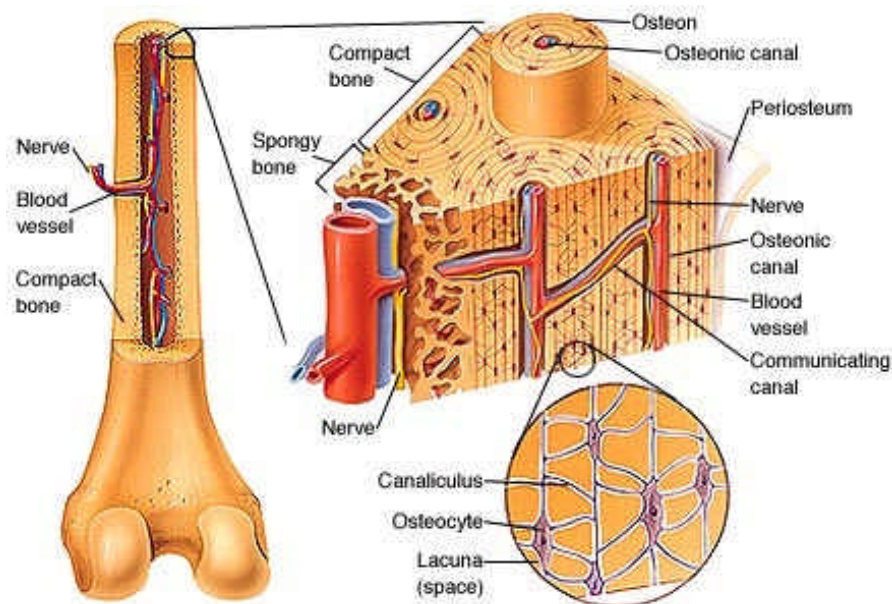


Fig. 2. Schematic drawing of the bone structure

Cancellous bone, synonymous with **trabecular bone** or **spongy bone**, is the other type of osseous tissue that forms bones. Compared to compact bone, it has a higher surface area but is less dense, softer, weaker, and less stiff. It typically occurs at the ends of long

bones, proximal to joints and within the interior of vertebrae. Cancellous bone is highly vascular and frequently contains red bone marrow where hematopoiesis, the production of blood cells, occurs. The primary anatomical and functional unit of cancellous bone is the trabecula, that is a small tissue element usually composed of dense collagenous tissue.

Subchondral bone region is the zone of epiphyseal bone just beneath the articular cartilage, and includes the subchondral plate and the underlying trabecular and subarticular bone. The subchondral plate comprises the deepest area of the articular cartilage, which is the calcified cartilage, and a thin cortical bone layer. The calcified cartilage is separated from the overlying hyaline cartilage by a line of demarcation called the tidemark.

Nevertheless, subchondral bone is recognised as a key factor in normal joint protection. In fact, subchondral bone has been shown to exert important shock-absorbing and supportive functions in normal joints. Subchondral bone can attenuate about 30% of the joint load, providing a mechanical base for joint cartilage¹⁰. Moreover, subchondral bone supplies nutrients to cartilage and facilitates the removal of metabolic waste products^{11,12}.

1.3.3 Articular bone region

Cartilage is a flexible connective tissue found in many areas in the bodies of humans and other animals, including the joints between bones, the rib cage, the ear, the nose, the bronchial tubes and the intervertebral discs.

The cartilaginous tissue, together with the bone tissue, belongs to the support skeletal tissues or connective tissues that have high mechanical properties. The cartilaginous tissue has high specific mechanical-elastic properties that allow to constantly reducing the friction induced by the loads on the articular surface during the normal movement activities of the human body. Moreover, the cartilaginous tissue is able to dissipate the peaks of mechanical stress on the sub-chondral bone. The connective tissue surrounding the cell cartilaginous component, namely the chondrocytes, (2% of the total volume of the cartilage) is dipped in an extracellular matrix/lattice consisting of collagen, proteoglycans and glycoproteins. For example, 2-40% of the connective tissue includes: 50-60% of collagen, 25-35% of proteoglycans and 10-15% of glycoproteins. The collagen molecules are uniformly distributed throughout the tissue and are responsible of its shape and mechanical strength. The proteoglycans and the glycoproteins bind to the collagen by

trapping the water within the matrix.

Cartilage is classified in three types that differ in the biochemical composition and structure of their extracellular matrix (ECM), the resulting mechanical properties and therefore their occurrence in the human body: *elastic cartilage*, *hyaline cartilage* and *fibrocartilage*.

Elastic cartilage is characterized by chondrons with only a few cells, a small concentration of proteoglycans (PGs), but much elastin. Elastin is interwoven into the collagen mesh and the more this protein is present, the more flexibility is provided to the tissue. Elastic cartilage is surrounded by perichondrium and appositional growth is guaranteed through cell differentiation of the connective tissue. This tissue type is less vulnerable to degenerative changes. Elastic cartilage is suitable to resist bending and so it can be found in the epiglottic cartilage, the smaller laryngeal cartilage, the external ear and auditory tube, or the small bronchi¹³.

A second type of cartilage is the *fibrocartilage*, providing other physical characteristics. Like the elastic type it contains a small concentration of PGs, but by contrast far less elastin. The meniscus is a fibrocartilaginous tissue composed primarily of an interlacing network of collagen fibers with a longitudinal, circumferential orientation which gives it unique functional properties. The ECM of fibrous cartilage consists of approximately 60-70% collagen, 8-13% non-collagenous proteins, and 1% PGs in dry weight. The water content in native meniscal tissue is around 70-75%¹⁴.

The third and most widespread cartilage in the human body is the *hyaline* type. As the name already implies, it appears as a white and slightly bluish tissue with a macroscopically smooth surface. Its resistance to compression or tensile forces is due to the net-like organized structure of the collagen type II fibers combined with a high concentration of PGs. Hyaline cartilage can be found in the nose, the trachea, bronchi, and most joints in synarthroidal as well as in diarthroidal joint¹⁵. In diarthroidal joints hyaline cartilage covers the contact zones of two interlocked bones and is called **articular cartilage** (Fig. 3).

Articular cartilage is a unique type of connective tissue. Although appearing homogeneous, articular cartilage has a highly ordered structure. It is organized on two levels: the structure and composition of articular cartilage varies according to its distance from the surface and also in relation to the distance from the cells. Typically, articular

cartilage is divided into four zones: superficial, middle (or transitional), deep (or radial), and the zone of calcified cartilage. Chondrocytes from the different zones differ in size, shape, and metabolic activity. The superficial zone is the thinnest, and forms the gliding surface of the joint. It is composed of thin collagen fibrils aligned parallel to the joint surface, with elongated, inactive chondrocytes directly subjacent. The middle zone is thicker than the superficial zone, with more spherical cells and with larger collagen fibrils that are not oriented in a parallel fashion. In the deep zone, the cells are spheroidal, arranged in a columnar orientation. The collagen fibers here are oriented in a parallel fashion, similar to the cells, vertical to the joint surface. In the zone of calcified cartilage, collagen fibrils insert into the calcified cartilage, providing both a mechanical transition from the cartilage to bone, as well as fixation between the two tissues¹⁶.

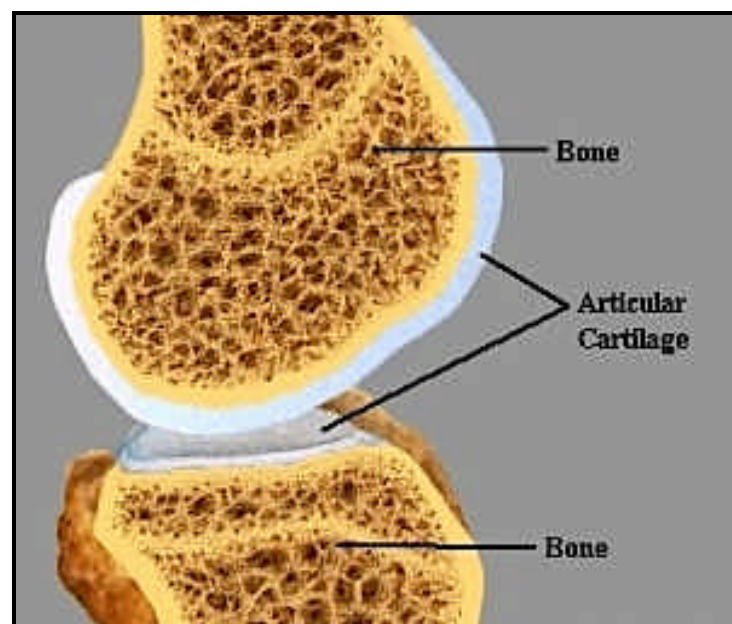


Fig. 3. Articular cartilage

1.3.4 Vertebral bone region

The intervertebral discs lie between the vertebral bodies, linking them together (Fig. 4). They are the main joints of the spinal column and occupy one-third of its height. Their major role is mechanical, as they constantly transmit loads arising from body weight and muscle activity through the spinal column. They provide flexibility to this, allowing bending, flexion and torsion.

They are approximately 7-10 mm thick and 4 cm in diameter (anterior - posterior plane) in the lumbar region of the spine¹⁷. The intervertebral discs are complex structures that consist of a thick outer ring of fibrous cartilage termed the annulus fibrosus, which surrounds a more gelatinous core known as the nucleus pulposus; the nucleus pulposus is sandwiched inferiorly and superiorly by cartilage end-plates. The central nucleus pulposus contains collagen fibres, which are organised randomly, and elastin fibres (sometimes up to 150µm in length), which are arranged radially¹⁸; these fibres are embedded in a highly hydrated aggrecan-containing gel.

The annulus is made up of a series of 15-25 concentric rings, or lamellae, with the collagen fibres lying parallel within each lamella. The fibres are orientated at approximately 60° to the vertical axis, alternating to the left and right of it in adjacent lamellae. Elastin fibres lie between the lamellae, possibly helping the disc to return to its original arrangement following bending, whether it be flexion or extension. They may also bind the lamellae together as elastin fibres pass radially from one lamella to the next. The cells of the annulus, particularly in the outer region, tend to be fibroblast-like, elongated, thin and aligned parallel to the collagen fibres. Toward the inner annulus the cells can be more oval. Cells of the disc, both in the annulus and nucleus, can have several long, thin cytoplasmic projections, which may be more than 30µm long. Such features are not seen in cells of articular cartilage¹⁹. Their function in disc is unknown but it has been suggested that they may act as sensors and communicators of mechanical strain within the tissue.

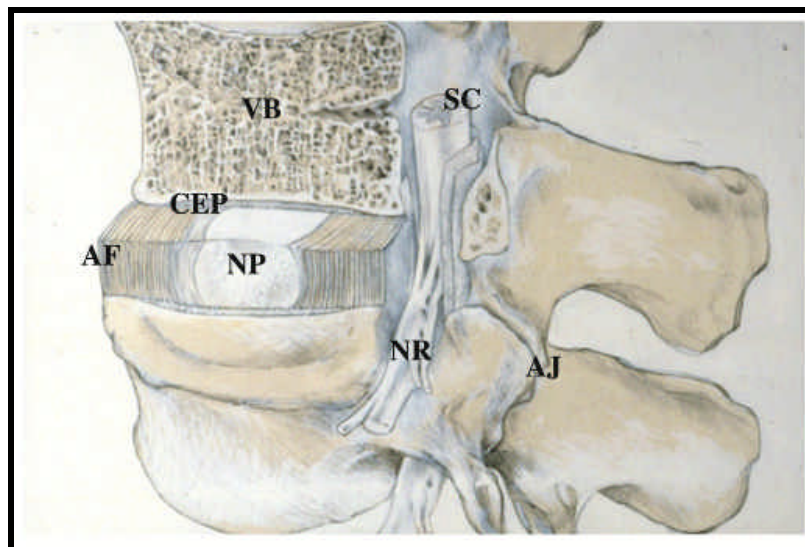


Fig. 4. A schematic view of a spinal segment and the intervertebral disc. The figure shows the organization of the disc with the nucleus pulposus (NP) surrounded by the lamellae of the annulus fibrosus (AF) and separated from the vertebral bodies (VB) by the cartilaginous end-plate (CEP). The figure also shows the relationship between the intervertebral disc and the spinal cord (SC), the nerve root (NR), and the apophyseal joints (AJ).

The third morphologically distinct region is the cartilage end-plate, a thin horizontal layer, usually less than 1mm thick, of hyaline cartilage. This interfaces the disc and the vertebral body. The collagen fibres within it run horizontal and parallel to the vertebral bodies, with the fibres continuing into the disc. The healthy adult disc has few (if any) blood vessels, but it has some nerves, mainly restricted to the outer lamellae, some of which terminate in proprioceptors. The cartilaginous end-plate, like other hyaline cartilages, is normally totally avascular and aneural in the healthy adult. Blood vessels present in the longitudinal ligaments adjacent to the disc and in young cartilage end-plates (less than about 12 months old) are branches of the spinal artery. Nerves in the disc have been demonstrated, often accompanying these vessels, but they can also occur independently, being branches of the sinuvertebral nerve or derived from the ventral rami or grey rami communicantes. Some of the nerves in discs also have glial support cells, or Schwann cells, alongside them²⁰.

1.3.5 Degeneration of bone tissue

Diseases of articular bone region

Traumas, inflammatory and degenerative diseases can induce significant damages to the

articular cartilage which, in a non negligible percentage, can evolve in chronic arthrosis disease. The cartilaginous tissue subjected to a damage, in particular to a deep damage, has a poor self-reparative ability considering the poorly vascularized anatomic region and the limited replication ability of the chondrocyte cells. The result of the self-reparative process of the cartilage is often a formation of fibrous tissue which certainly can not be compared, in terms of mechanical performances and physiological features, to a normal hyaline cartilage. Accordingly, the alteration of the viscoelastic and mechanical balance can lead to considerable pathological consequences with a following compromission of the articular function and with a pain occurrence, although the cartilaginous degeneration process in most of cases is an asymptomatic phenomenon.

The situation evolves in a more complex way in case of lesions involving the subchondral bone structure, when the complete demolition of the cartilaginous layer directly exposes the bone to the mechanical stress of the joint.

In conclusion, between the pathological conditions which can induce nearly always irreversible degenerative processes there may be listed, by mere way of example: the bad alignments (varus and valgoid conditions), the avascular necrosis, the osteoarthritis and the rheumatoid arthritis. The known surgical techniques currently utilized for the repair of the cartilaginous tissue are of course applied as a function of the dimensions and the depth of the defect.

Deseases of vertebral bone region

One of the major problems facing the elderly spine is the occurrence of vertebral fractures, which are associated with height loss, back pain, disability and even increased mortality rates. As these vertebral fractures are strongly correlated to low bone density, they are commonly attributed to osteoporosis.

Disc degeneration begins with the nucleus becoming dehydrated and more fibrous, followed by a loss of distinction between the nucleus and annulus, disorganized fibers in the annulus and, finally, a decreased disc height. With disc pressure measurements it was found that healthy discs show an area of constant pressure under the nucleus and the inner annulus. For degenerated discs the area of constant pressure was much smaller and the pressure within it was lower. Such a change in pressure in the disc and on the endplates would lead to bone adaptation in the adjacent vertebrae. Indeed, disc degeneration has

been found to be correlated to a changed bone density distribution within the vertebra²¹.

1.3.6 Bio-mineralization processes: the basis of bone formation

The formation of bone tissue takes place through different events²² that comprise the synthesis and modification of specific polypeptide chains inside osteoblast cells, which are then extruded into the extracellular space. Here, the collagen microfibrils, with a mean diameter of 1.5 nm, start to assemble into fibres. During the self-assembly of collagen fibres, a quarter-staggered arrangement of parallel molecules of tropocollagen (a triple helical-shaped molecule, precursor of collagen) is established, leaving a regular array of 40 nm gaps within each periodic unit. These areas are known as hole zones (40 nm in length and 5 nm in width) and as reported²³ are the preferential sites for the nucleation of the mineral phase (Fig. 5).

The nucleation of mineral nanocrystals takes place in specific loci corresponding to non-collagenous acidic macromolecules; many of which are highly charged from carboxylate groups that can bind Ca^{2+} ions. Following the chemical binding of Ca^{2+} , the supersaturation of physiological fluids in phosphate ions and other minor species (e.g. Na^+ and K^+) provokes the precipitation and nucleation of the mineral phase as nano-sized, plate-shaped particles, which are initially confined to the hole zones, and progressively extend along the collagen fibrils. The organic template transfers information to the mineral phase at the molecular level: (i) the chemical interaction of hydroxyapatite (HA, $\text{Ca}_5(\text{PO}_4)_3\text{OH}$) with collagen prevents the crystallization of the mineral phase, which is almost amorphous but is characterized by an apatite-like lattice; (ii) the size and shape of the nuclei are constrained by the activation of structural and morphological control mechanisms during the bio-mineralization process; (iii) the growth of nuclei is limited to very thin lamellae, which are spatially confined and have a specific crystal orientation; and (iv) lamellae organize through different hierarchical levels up to the macroscopic bone.

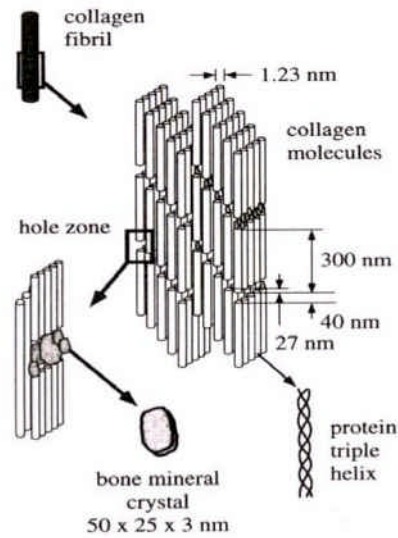


Fig. 5. Schematic illustration of nucleation of bone mineral crystals during the self-assembling of collagen fibres.

The crystal state of the substrate induces the nucleation and growth of the apatite nanocrystals along a specific crystallographic direction (Fig. 6). Crystal growth is limited to very few unit cells of the apatite lattice, with values ranging from 30-50 nm long, 15-30 nm wide, and 2-10 nm thick²⁴. The apatite platelets develop along the long axis of collagen, so that the apatite crystals grow preferentially along the *c* axis of the hexagonal apatite lattice.

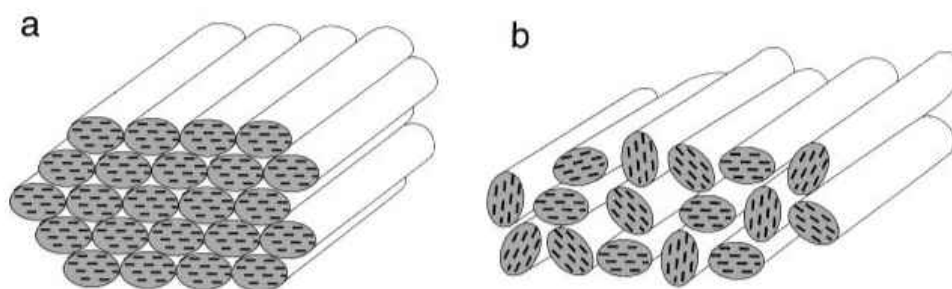


Fig. 6. Schematic illustration: (a) an arrangement of mineralized collagen fibrils aligned both with respect to crystal layers and fibril axes; (b) arrangement of mineralized collagen fibrils with only the fibril axes aligned.

1.3.7 Biological bone mineral phase

Bone mineral has the structure of a calcium-deficient apatite, with a Ca:P ratio <1.67 , which is the theoretical value for pure HA²⁵. Bone is a living tissue that is continuously undergoing remodelling and repair, therefore, the small size and/or non-stoichiometry of the crystals presumably endows the mineral phase with the solubility needed for resorption of the bone by osteoclasts (bone-resorbing cells). In fact, synthetic stoichiometric HA, although bioactive (stimulatory for bone formation), is rather slow to resorb because of the low solubility of HA under physiological conditions²⁶. Besides the very small crystallite size, the low crystallinity of bone mineral (in relation to synthetic HA) is also caused by incorporation of ions into its lattice, such as CO_3^{2-} , Na^+ , Mg^{2+} , SiO_4^{4-} or HPO_4^{2-} , which are present in the physiological environment and extremely important for the biochemistry of bone remodelling (see Chapter 4)²⁷.

References

1. Vallet-Regi M. *Chem. Eng. J.* **2008**, *137*, 1
2. Williams DF. *Biomaterials* 2009, *30*, 5897.
3. Yannas, I.V., 2001. *Tissue and Organ Regeneration in Adults*. Springer, New York.
4. Sprio S, Ruffini A, Valentini F, D'Alessandro T, Sandri M, Panseri S, Tampieri A. *J. Biotech.* **2010**, *156*, 347.
5. Sommerfeldt DW, Rubin CT. *Eur. Spine. J.* **2001**, *10*, S86.
6. Burger EH, Klein-Nulend J. *FASEB J.* **1999**, *13*, S101.
7. Vaananen HK, Zhao H, Mulari M, Halleen JM. *J.Cell.Sci.* **2000**, *113*, 377.
8. Frost M. *Anat. Rec.* **1990**, *226*, 403.
9. RJ Moore "BONE" © Woods and Ellis 2000.
10. Imhof H, Sulzbacher I, Grampp S, Czerny C, Youssefzadeh S, Kainberger F. *Invest. Radiol.* **2000**, *35*, 581.
11. Santos Castaneda, Jorge A. Roman-Blas, Raquel Largo, Gabriel Herrero-Beaumont. *Biochemical Pharmacology* **2012**, *83*, 315.
12. The Role of Subchondral Bone in Joint Disease, Christopher E. Kawcak; C. Wayne McIlwraith, Richard D. Park and S. P. James, AAEP PROCEEDINGS, Vol. 47, 2001
13. Montes GS. *Cell Biol. Int.* **2006**, *20*, 15.
14. Flugge LA, Miller-Deist LA, Petillo PA. *Chem. Biol.* **1999**, *6*, R157.
15. Buckwalter JA (1997) Cartilage. In: Dulbecco R (ed) *Encyclopedia of human biology*, vol 2. pp 431–445.
16. Newman AP. *Am. J. Sport. Med.* **1998**, *26*, 309.
17. Twomey LT, Taylor JR. *Clin. Orthop.* **1987**, *224*, 97.
18. Yu J, Winlove CP, Roberts S, Urban JP. *J. Anat.* **2002**, *201*, 465.
19. Errington RJ, Puustjarvi K, White IR, Roberts S, Urban JP. *J. Anat.* **1998**, *192*, 369.
20. Johnson WE, Evans H, Menage J, Eisenstein SM, El Haj A, Roberts S. *Spine* **2001**, *26*, 2550.
21. Homminga J, Aquarius R, Bultink VE, Jansen CTJ, Verdonschot N. *Medical Engineering & Physics.* **2012**, *34*, 453.

22. Olszta MJ et al. *Mater. Sci. Eng.* **2007**, *58*, 77.
23. Landis WJ et al. *J. Struct. Biol.* **1993**, *110*, 39.
24. Lowenstam HA and Weiner S. (1989) *On Bio-mineralization*, Oxford University Press.
25. LeGeros RZ (1991) *Calcium Phosphate in Oral Biology and Medicine*, Karger.
26. Dorozhkin SV and Epple M. *Angew. Chem. Int.* **2002**, *41*, 3130.
27. Bigi A. et al. *Calcif. Tissue Int.* **1992**, *50*, 439.

CHAPTER 2

BIOMATERIALS FOR REGENERATIVE MEDICINE: TREATMENT OF MUSCOLOSKELETAL DISEASES

Regenerative medicine is a critical frontier in biomedical and clinical research. It is the process of creating living, functional tissues to repair or replace tissue or organ function lost due to age, disease, damage, or congenital defects. This field holds the promise of regenerating damaged tissues and organs in the body by stimulating previously irreparable organs to heal themselves¹.

Regenerative medicine applies the principles of engineering and life sciences to enhance the comprehension of the fundamental biological mechanisms underlying the structure function relationships in physiologic and pathologic tissues and to accomplish alternative strategies for developing in vitro biological substitutes which are able to restore, maintain, or improve tissue, and organ function².

Musculoskeletal tissue damage is an increasing problem with a growing aging population. Regenerative medicine aims to repair and replace lost or damaged tissues by initiating the natural regeneration process. Most approaches currently pursued or contemplated within the framework of regenerative medicine, including cell-based therapies and living tissue engineering, rely greatly on the ability to synthesize or otherwise generate novel biomaterials, to fabricate or assemble biomaterials into appropriate two-dimensional (2D) and three-dimensional (3D) forms, and to tailor physical, chemical, structural and biological properties to achieve desired clinical efficacy.

In a regeneration strategy, biomaterials promote new tissue formation by providing adequate space (porosity) and appropriate surface to foster and direct cellular attachment, migration, proliferation, desired differentiation of specific cell phenotypes throughout the

scaffold where new tissue formation is needed^{3,4}.

Consequently, the 3D architecture plays a pivotal role. It refers to the way in which a bulk material is distributed in space from the macro, micro to nano scales (corresponding to tissue, cellular and molecular scales in a specific tissue, respectively)⁵. Such hierarchical porous architectures not only define the mechanical properties of the scaffold, but also the initial void space that is available for regenerating cells to form new tissues (including new blood vessels) as well as the pathways for mass transport via diffusion and/or convection. While interconnected macroporosity of a biomaterial is important to provide sufficient space for cellular activity⁶⁻⁹ interactions between cells and biomaterials occur at the interface, i.e. the entire internal pore walls of a 3D scaffold. The surface morphology or topography directly and significantly affects cell-scaffold interactions and ultimately tissue formation and function¹⁰.

2.1 Regeneration of bone and osteo-cartilaginous tissue: problems and solutions

Regeneration of bone tissue

The bone loss can occur in various situations such as trauma, tumors, atrophy and in different areas of bone tissue such as long, flat or short bones presenting a peculiar organization. The regeneration of bone tissue is a complex process that is known to be regulated by multiple factors and which occurs spontaneously under normal conditions. Nevertheless, the regeneration of bone does not occur in a complete way and this often leads to the formation of a fibrous tissue. In fact, the bone regeneration requires the formation of new bone tissue and blood vessels that mediate the transport of osteogenic precursors, of secretory molecules that act as activators for osteoblasts, transporters of nutrients and oxygen.

There are various therapeutic strategies for promoting the regeneration of bone tissue; some are based on the use of autologous bone tissue other on the use of biomaterials alone or associated with osteo-progenitor cells and/or growth factors.

Autografts have primarily been the material of choice to replace lost bone, although the use of autografts comes with some disadvantages such as the limited quantity available and its use also requires additional surgical procedures, and therefore, longer surgical time and possible complications of the wound of the donor site such as bleeding, pain and

infection among others. Allografts and xenografts have the potential of transferring pathogens. To avoid the biological risk, these materials are subjected to exhaustive procedures which have dramatic effects primarily on their osteogenic and osteoinductive properties and these procedures can also reduce their structural integrity leading to graft fracture¹¹.

An alternative is allogeneic bone grafting, obtained from human cadavers or living donors, which bypasses the problems associated with harvesting and quantity of graft material. Allogeneic bone is available in many preparations, including demineralised bone matrix (DBM), morcellised and cancellous chips, corticocancellous and cortical grafts, and osteochondral and whole-bone segments, depending on the recipient site requirements. Their biological properties vary, but overall, they possess reduced osteoinductive properties and no cellular component, because donor grafts are devitalised via irradiation or freeze-drying processing. There are issues of immunogenicity and rejection reactions, possibility of infection transmission, and cost.

Bone-graft substitutes have also been developed as alternatives to autologous or allogeneic bone grafts. They consist of scaffolds made of synthetic or natural biomaterials that promote the migration, proliferation and differentiation of bone cells for bone regeneration. A wide range of biomaterials and synthetic bone substitutes are currently used as scaffolds, including collagen, hydroxyapatite (HA), β -tricalcium phosphate (β -TCP) and calcium-phosphate cements, and glass ceramics, and the research into this field is ongoing¹².

The use of biomaterials as scaffolds for bone regeneration requires that scaffold is able to exchange chemical and biochemical signals with the surrounding physiological environment, in order to address the activity of progenitor cells towards selective differentiation. The proper cell behaviour also depends on physical signals imparted by the scaffold morphology and structure, which determine the cell conductivity and colonization of the inner part of the scaffold. Likewise, the establishment of an efficient vascular network is crucial for the process of tissue regeneration; in fact, biologic structures are organized on a basis of minimum energy expenditure, so the vascular system in living tissues is organized to exchange the fluids necessary for the organ activity with the highest efficiency.

Therefore, the design and development of three-dimensional (3D) mineralized scaffolds

reproducing the structure and the hierarchically organized morphology of long bones is still a challenge, due to limitations in the current manufacturing technologies. In this view, the new trends in materials science research are looking at the peerless characteristics and properties of natural structures as new sources of inspiration to obtain innovative and smart biomorphic devices¹³.

Regeneration of osteo-cartilagineouse tissue

Currently available treatments depend upon the size of the osteo-chondral defect and the condition of the overlying cartilage. Using reparative surgery, cartilage treatments include arthroscopic debridement, abrasion arthroplasty, and microfracture. These procedures stimulate the body to heal the injury, mainly resulting in the formation of fibrocartilage. Fibrocartilage is a scar tissue presenting diminished resilience, reduced stiffness, and poor wear characteristics when compared to hyaline cartilage. Thus, fibrocartilage is unlikely to withstand physiological loading and cannot guarantee to function successfully in long term. Nevertheless, other options are available with restorative surgery, namely, autografts recurring to mosai-coplasty procedures, allografts^{14,15} and biologic replaement using cultured autologous chondrocytes. The biggest challenge with autografts is to achieve a final round shape that mimics the surface of the articular joints. Allograft procedure is similar to autografts and mostly used after other surgeries have failed. It is not recommended for patients with OA, and the limited supply of donor tissue is a major problem of this practice. Autologous chondrocyte transplantation/implantation¹⁶ has also been described to help restoring the structural make-up of the articular cartilage. The intermediate and long-term functional and clinical results are promising, especially regarding the durability of the repair in human patients follow-up¹⁷.

Despite the availability of procedures, all current treatment options inflict further tissue destruction before any therapeutic effect can be achieved.

The implantation of cells in the afflicted area could be a direct approach in osteo-chondral strategies, but the request for a support material to promote regeneration, especially in large sized defects, is to be critically considered. This idea is inspired in nature itself as, in the body, the majority of cells subsist in a 3D world, anchored onto a network of extracellular matrix (ECM), which scaffolding design proposes to recreate.

Scaffold characteristics will greatly influence cells and should mimic the complex and

demanding environment to which cells are exposed to. Besides the tissue structural support and stimulation, either chemically or mechanically, the optimal scaffold should assist tissue functionality promoting the easy diffusion of nutrients, growth factors and cellular waste products. Additionally, the ideal scaffold should be biocompatible and its biodegradability adjustable to the time required for tissue regeneration¹⁸.

2.2 The most important musculoskeletal diseases: osteoporosis (OP) and osteoarthritis (OA)

Osteoarthritis (OA) and osteoporosis (OP) are among the most disabling degenerative diseases that affect millions of people each year, resulting in a strong negative socio-economic impact, particularly related to the progressive aging of the population's increased of life. In severe cases, these conditions may lead to severe complications affecting the neuromuscular system and may significantly impair quality of life of patients and their longevity.

Osteoporosis is the most prevalent skeletal disorder characterised by decreased bone mass and bone mineral density. Osteoporosis is characterized by a reduction of bone in the skeleton that results in skeletal fragility and an increased risk of fracture after minimal trauma. The three major osteoporotic fractures occur in the forearm, vertebral body, and hip, although fractures of the humerus, tibia, pelvis, and ribs are also common¹⁹.

Osteoporotic fractures are a major cause of morbidity, mortality, and health and social service expenditures in both sexes. More than half of all patients with hip fracture have pain at the fracture site 6 months after surgery, and only one third regain their former mobility. Osteoporotic patients with vertebral crush fractures complain not only of back pain, loss of height, and kyphosis, but also have substantially less energy, poorer sleep, more emotional problems, immobility, and social isolation²⁰.

Overall mortality is increased by about 17% after both femoral and vertebral fractures, but in the case of vertebral fracture, this may be due to coexisting conditions rather than to fracture itself²¹.

In OP the bone micro-architecture is disrupted, and the amount and variety of non-collagenous proteins in bone is altered. Furthermore, fractures are significantly exacerbated and healing is often impaired in osteoporotic patients. Post-menopausal OP is the most common and significant form of OP in which oestrogen deficiency gives rise to

a high turnover rate in bone metabolism. Accelerated bone resorption by osteoclasts has been established as a principal mechanism in OP, although the imbalance in bone remodelling as occurs in OP can be in part due also to inappropriate apoptosis of osteoblasts/osteocytes²²⁻²³.

Osteoarthritis is a chronic disease in which articular cartilage undergoes degeneration with age or after focal injury²⁴. OA is characterised by the progressive deterioration and sclerosis of articular cartilage and sub-chondral bone and changes in the synovial membrane as a result of mechanical and biological processes that modify cartilage homeostasis^{25,26}.

Two major retrogressive changes occur during the onset and progression of osteoarthritis. The first is calcification, which decreases the diffusion of nutrients and oxygen to the chondrocytes. Chondrocytes of the calcified matrix die, and the matrix is resorbed. The second change is termed cartilage fibrillation, and involves a splitting of the matrix of the articular surface along the direction of orientation of the collagen fibers to expose these fibers, giving the surface a fuzzy appearance. This occurs at first in patches, which then enlarge. As the condition progresses, there is variable loss of cartilage by apoptosis and autophagy and exposure of underlying bone, accompanied by increasing pain^{27,28}.

2.3 Current clinical treatments for OA and OP

Although OA and OP have completely different etiology and course, their degenerative effects lead to severe and almost similar symptoms. Currently (i) pharmacological treatments and ultimately (ii) tissue replacement and augmentation by implants are the main clinical interventions. However, both drug administration and implants suffer from significant limitations and they are not able to restore completely the patient's mobility and quality of life.

- (i) **The currently available pharmacological treatments** are mainly designed to reduce inflammation and pain, to increase calcium uptake and to modify the equilibrium among bone formation and resorption, favouring the bone apposition on the trabecular surfaces. However, the efficiency of such drugs is limited, in some cases controversial and often they are poorly tolerated and elicit side-effects following systemic administration. Alternative non-surgical

interventions including injectable visco-supplements are also used for the treatment of early osteoarthritis, but patients with severe OA tend not to respond to such treatments.

- (ii) **Tissue replacement and augmentation by implants** is adopted in cases where pharmacologic treatment proves ineffective and OA and OP conditions cause persistent pain and disability. In particular, implants such as artificial knee prostheses and vertebroplasty and/or kyphoplasty are adopted when the tissue structure and functionality is irreversibly compromised. However, the prosthetic solution is generally reserved for older patients, due to the fact that the life span of prosthetic materials is limited to 10-15 years. For that reason the treatment of early arthritis in relatively young and active patients is even more problematic as it leads to revision surgery. In recent years, innovative bioengineering approaches have been proposed for the early treatment of arthritis. However, despite the emergence of encouraging laboratory data, the clinical application of tissue engineering products have not produced the expected clinical benefits.

2.3.1 Main problems in the treatment of OA

The main challenge in the treatment of OA by regenerative medicine approaches is represented by the need to regenerate two different and adjacent tissues: the cartilage and the underlying trabecular bone. These two tissues are closely connected within the osteo-chondral unit despite their distinct physical, chemical and biological characteristics and different healing potential. Thus, aided regeneration of the osteo-chondral compartment by biomaterials or tissue engineering constructs requires tailored technological solutions able to fulfil the different histological and physiological features of both the tissue types.

Several therapeutic strategies used are employed to limit the pain associated with the disease including simple analgesics, non steroidal anti-inflammatory drugs (NSAIDS), intra-articular injection of glucocorticoids, hyaluronic acid preparations, and COX-2 specific inhibitors, rendered in combination with non-pharmacological therapy, such as patient education and physical/occupational therapy. However no medical intervention has been shown to halt disease progression or reverse joint damage in humans. Moreover,

many of these drugs are beset with serious side effects. Mesenchymal stem cells (MSCs) are now receiving enormous attention in numerous biomedical fields, including regenerative medicine, tissue protection, graft enhancement and immune-modulation. MSCs operate through a variety of effects or mechanisms on key cells of the innate and adaptive immune systems, mostly through manipulation of the cell cycle or inducing maturation arrest without apoptosis.

In recent decades a variety of biomaterials have been developed and launched on the market in order to face the increasing need for bone substitutes²⁹⁻³¹.

Solutions ranging from autografts and allografts, synthetic polymers (e.g. PLA, PGA) and coral-derived materials up to the more advanced bioceramics or bioceramic-polymers composites have been proposed. These biomaterials are mainly used as bone fillers and in cartilage mosaicplasty, but they are not suitable for supporting the regeneration of complex anatomical regions the biochemical requirements of which have been affected by pathologies. Despite the improvements of the clinical outcomes delivered by these biomaterials, ideal tissue regeneration has not yet been achieved. Furthermore, source limitations and production costs reduce the clinical potential of these biomaterials.

2.3.2 Main problems in the treatment of OP

To date, drug therapy is indicated both for the prevention and for the treatment of osteoporosis. There are several classes of drugs, whose main action is to inhibit bone resorption by stabilizing or increasing the amount of bone mass. The most effective drugs for the recovery of bone mineral density and especially to reduce the risk of pathologic fractures are bisphosphonates (alendronate, risendronate, pamidronate, clodronate), strontium ranelate, raloxifene and parathyroid hormone peptides. All these interventions have been shown to reduce the risk of vertebral fracture when given with calcium and vitamin D supplements³². Bisphosphonates for example are widely used to ameliorate the effects of osteoporosis by inhibiting osteoclast functions. These drugs also act to inhibit apoptosis of both osteocytes and osteoblasts and to increase the bone forming potential of osteoblasts. Despite their potential, bisphosphonates appear to lead to excessive reduction in bone turnover thus causing increase of micro-damages³³. Furthermore, experimental evidence supports the view that bone gained after anabolic treatment will be lost after the treatment is discontinued. Thus, it is vital to identify a treatment regimen that creates a

permanent reduction in fracture risk even after the therapy is discontinued. This might be achieved with a combination of biomaterials and drugs or with an entirely new approach. The surgical treatment of OP by vertebroplasty is performed to relieve pain related to pressure on the spinal nerves caused by the deformation and/or fracture of the vertebral bodies (VCF). Vertebroplasty and balloon kyphoplasty (injection of acrylic bone cement into a fractured vertebra) are widely used for this purpose, but they can only reduce the pain and do not provide tissue regeneration.

However, for OP and OA both the administration of the drug, both plants suffer from significant limitations and are not able to completely restore the patient's mobility and quality of life. In this clinical picture is strongly desired a tissue regeneration based on a minimally invasive surgical approach in order to allow early treatment and repeated tissue still bearing and with good biomechanical properties. The development of such treatments is considered by the clinical sector as a highly innovative solution in the treatment of these debilitating conditions, as it will overcome the limitations associated with current treatments.

2.3.3 Newly conceived biomaterials as scaffolds for the treatments of OA and OP

Although the systemic nature of OP and OA will always require a degree of pharmaceutical treatment, new biomimetic, minimally invasive biodegradable biomaterials and tissue engineering constructs, will provide a jump-start for bone regeneration and will enhance the chance of successful clinical outcome.

These new regenerative materials will eliminate the need for more radical surgical intervention and offer the accurate control of cell functions in the different histological compartments (i.e. bone and cartilage) through the simultaneous regulation of biochemical and chemical processes.

The repairing of the osteochondral defect, which often represents a pathological condition of a difficult solution for the surgeon, particularly when the subject is a young patient, results more complex. In these conditions, besides the restoration of the cartilaginous layer, it is important the reconstruction of the sub-chondral bone structure.

An emerging trend in the field of biomaterials research is the production of layered osteochondral scaffolds for the simultaneous treatment of compromised cartilage and subchondral bone in articular joint defects. These scaffolds seek to treat articular cartilage

lesions by augmenting marrow stimulation techniques, in which controlled damage is imparted to the subchondral bone plate to induce bleeding from the marrow cavity and allow marrow-derived stem cells to enter the lesion. By providing a scaffold to support and guide the reparative capacity of these cells, layered osteochondral scaffolds aim to induce the simultaneous regeneration of articular cartilage and the subchondral bone to which it is attached.

Therefore, nano-structured bio-hybrid composites as matrices for multifunctional anatomical regions, with chemical, topotactic and morphological features of the osteochondral tissue could be represent valid substitutes for the treatment of OA.

Many different types of biomaterials, both synthetic and natural, are being developed, modified, and evaluated. These biomaterials can be made bioactive by incorporation of growth factors or gene vectors to improve cell ingrowth, cell proliferation, or matrix production. Even anti-inflammatory factors can be incorporated to inhibit inflammatory processes, which are known to have negative effects on cartilage repair. Controlled release of these factors in time and may be even sequential release of a number of factors will be necessary for optimal control of the tissue repair process.

The major limitations of the scaffolds for bone and cartilage regeneration nowadays available on the market are related to the difficulties in controlling cell differentiation and angiogenesis processes and obtaining stable scaffold implantation in the pathological site. The *in vivo* provision of the scaffold with stem cells or/and growth factors in order to drive the tissue differentiation process and ensuing angiogenesis represents a most challenging request³⁴. During the regeneration, the restoration of the mechanical resistance to physiological stresses should be accompanied by a parallel advance of the angiogenic process, leading to a complete morphological and biological maturation of the tissue. This is only achieved if angiogenesis is permanently stimulated by the presence, close to the scaffold, of various angiogenic proteins (growth factors)^{35,36}. Mimicking endogenous growth factor production and delivery is still to be solved with conventional scaffolds³⁷⁻³⁹. Recently the idea of utilizing magnetic scaffolds for an additional control of the angiogenesis process *in vivo* was proposed⁴⁰. This approach is expected to enable the scaffolds with such an advantageous property as long term operation, via the continuous interaction and material exchange of the scaffold with the magnetic external supplier. In addition such scaffolds are expected to feature multiple use and possibly multipurpose

delivery capable of repairing large bone defects and sub-chondral lesions in the articular surface of the skeletal system.

For the treatment of OP injectable bone cements could be represent valid solution. Although several injectable bone cement have been developed⁴¹⁻⁴⁴ no ideal formulation has been already identified. The most important features of such formulations should be: easy injectability, high radio-opacity, appropriate setting time and resorption rates and mechanical properties similar to bone. PMMA cements are the most frequently used, due to their relatively high mechanical performance. Nevertheless, they have very important limitations including the exothermic polymerization reaction that leads to necrosis of all the contact tissues. In addition, the compact, bio-inert and non-degradable nature of the cement prevents the formation of new bone within the defect. It has also been reported that excessive cement rigidity reduces the endplate bulge of the augmented vertebra, thereby reducing the local spinal joint flexibility. As a consequence of the reduced joint flexibility there is an increase in the pressure on the intervertebral disc leading to an abnormal mechanical load transfer on the adjacent vertebral body with increased risk of fracture. It is also generally believed that the relatively hard bone cement leaks out from the vertebral body into the intervertebral disc resulting in new fractures as a consequence of the excessive stimulation of the adjacent endplate. Unlike PMMA-based materials, calcium/phosphate-based cements exhibit relatively lower mechanical properties, longer setting times, lack of radio-opacity, and can be tailored to improve most of their limitations and emphasise their intrinsic bioresorbability/ bioactivity. Recent studies have combined CaP-based cements with biodegradable polymers to create an open pore structure within the cement bulk over time. The gradual formation of pores upon degradation of the polymer phase opens a route for cell colonization thus favouring bone in-growth and, later, bone remodelling. However, research is still required to obtain tuneable rates of pore formation and cement resorption.

Various cell-based therapies have been developed over the past years and could find their implementation into a wide range of clinical application. It is now recognised that bone marrow mesenchymal stem cells (BMSCs)/osteoblast lineage cells may actively participate in the recovery of OP. In addition, various growth factors are known to influence the recruitment and differentiation of osteoblasts. Among these, transforming growth factors (TGF), fibroblast growth factors (FGF), insulin-like growth factors (IGF),

platelet derived growth factors (PDGF), and bone morphogenetic proteins (BMP) can be found in bone matrix and have been extensively studied regarding the influence on bone cells and their precursors both *in vitro* and *in vivo*. However, because of the lack of specificity and far-ranging side effects concerning cell proliferation and survival on various other cell types, systemic administration of growth factors is currently not feasible. On the other hand, transcriptional regulation of bone formation is a promising approach for future therapeutic strategies. In recent years, a number of transcription factors and cofactors that control osteogenesis and chondrogenesis have been identified, including runt-related transcription factor 2 (Runx2) for osteoblastic differentiation, the distal-less homeobox 5 (Dlx5), msh homeobox homologue 2 (Msx2), the Fos-family transcription factors, and the zinc finger-containing protein Osterix (Osx), which acts downstream of Runx2. New anabolic therapeutic concepts have been suggested that can exploit the role of such transcription factors on the osteogenic cascade. These include new targets which are responsible for a high bone mass in humans such as low-density lipoprotein (LDL)-receptor-related protein 5 (LRP5)^{45,46}.

Recently, a new OP mechanism has been discovered involving T cells able to induce bone cell apoptosis via the Fas/Fas ligand pathway. In this case, a stem cell-based intervention led to a higher bone density⁴⁷. This result suggests that new solutions in OP treatment can be obtained by harnessing the stem cells ability to balance the rate of bone remodelling through activation of osteoblasts and inhibition of osteoclasts.

References

1. www.nih.gov/about/researchresultsforthepublic/Regen.
2. Asnaghi MA, Candiani G, Farè S, Fiore GB, Petrini P, Raimondi MT, Soncini M, Mantero S. *J. Appl. Biomater. Biomech.* **2011**, *9*, 73.
3. Ma PX. *Mater. Today* **2004**, *7*, 30.
4. Ma, PX. Encyclopedia of Polymer Science and Technology. Kroschwitz, JI., editor. John Wiley & Sons; New Jersey: 2004.
5. Muschler GF, Nakamoto C, Griffith LG. *J. Bone Joint Surg. Am.* **2004**, *86A*,1541.
6. Roy TD, Simon JL, Ricci JL, Rekow ED, Thompson VP, Parsons JR. *J. Biomed. Mater. Res.* **2003**, *66A*, 283.
7. Lu JX, Flautre B, Anselme K, Hardouin P, Gallur A, Descamps M, Thierry B. *J. Mater. Sci. Mater. Med.* **1999**, *10*, 111.
8. Ishaug-Riley SL, Crane-Kruger GM, Yaszemski MJ, Mikos AG. *Biomaterials* **1998**, *19*, 1405.
9. Tsuruga E, Takita H, Itoh H, Wakisaka Y, Kuboki Y. *J. Biochem.* **1997**, *121*, 317.
10. Ma PX. *Adv. Drug Del. Rev.* **2008**, *60*, 184
11. Pérez-Sánchez MJ et al. *Med. Oral. Patol. Oral. Cir. Bucal.* **2010**, *15*, 517
12. Dimitriou et al. *BMC Medicine* **2011**, *9*, 66.
13. S. Sprio et al. *Journal of Biotechnology* **2010**, *156*, 347.
14. Lattermann C, Romine SE. *Clin Sports Med.* 2009, *28*, 285.
15. Gross AE, Shasha N, Aubin P. *Clin. Orthop. Relat. Res.* **2005**, 79.
16. Gikas PD, Bayliss L, Bentley G, Briggs TW. *J Bone Joint Surg. Br.* **2009**, *91*, 997.
17. Peterson L, Brittberg M, Kiviranta I, Akerlund EL, Lindahl A. *Am. J. Sports Med.* **2002**, *30*, 2.
18. Hutmacher DW, Schantz JT, Lam CX, Tan KC, Lim TC. *J. Tissue. Eng. Regen. Med.* **2007**, *1*, 245.
19. Francis RM, Sutcliffe A. Implications of osteoporotic fractures in the elderly. In: Drife JO, Study JWW, eds. *HRT and Osteoporosis. Proceedings of the 22nd Study Group of the Royal College of Obstetricians and Gynaecologists*. Berlin: Springer-Verlag; 1990:87-93.
20. Scane AC, Sutcliffe AM, Francis RM. *Osteoporosis Int.* **1994**, *4*, 89.
21. Cooper C. Epidemiology and definition of osteoporosis. In: Compston JE, ed.

- Osteoporosis. New Perspectives on Causes, Prevention and Treatment.* London: Royal College of Physicians of London; 1996:1-10.
22. Greenspan SL, Bone HG, et al. *Ann. Intern. Med.* **2007**, 146, 326.
 23. Ebeling PR. *N. Engl. J. Med.* **2008**, 358, 1474.
 24. Goldring SR, Goldring MB. *J. Musculoskelet Neuronal Interact* **2006**, 6, 376.
 25. Lorenz H. et al. *Prog. Histochem Cytochem.* **2006**, 40, 135.
 26. Goldring MB, Goldring SR. *Journal of cellular physiology.* **2007**, 213, 626.
 27. Almonte-Becerril M, Navarro-Garcia F, Gonzalez-Robles A. et al. *Apoptosis* **2010**, 15, 631.
 28. Kouri, JB, Aguilera JM, Reyes J, Lozoya KA, Gonzalez S. *J. Rheumatol.* **2000**, 27, 1005.
 29. Scheck RM, Taboas JM, et al. *Tissue Eng.* **2004**, 10, 1378.
 30. Gelinsky M, Welzel PB, et al. *Chem. Eng. J.* **2008**, 137, 84.
 31. Tampieri A, Celotti et al. *J. Biomed. Mater. Res.* **2003**, 67A, 618.
 32. A. Cooper, C. Cooper, R. Francis, JA. Kanis, D. Marsh, E.V. McCloskey, D.M. Reid, P. Selby, M. Wilkins. *Maturitas* **2009**, 62, 105.
 33. Khan AA, Sandor GK, Dore E. et al. *J Rheumatol.* 2009, 36, 478.
 34. JointEuropeanCommission/EuropeanTechnologyPlatformon Nanomedicine 2009 *Expert Report Roadmaps in Nanomedicine Towards 2020* available from <http://www.etpnanomedicine.eu/public/public/pressdocuments/publications/091022 ETPN Report 2009.pdf>
 35. Whitaker MJ, Quirk RA, Howdle S, Mand Shakesheff KM. *J. Pharm. Pharmacol.* **2001**, 53, 1427
 36. Glowacki. *J.Clin. Orthop.* **1998**, 355, S82
 37. Laschke MW et al. *Tissue Eng.* **2006**, 12, 2093
 38. Schieker M, Seitz H, Drosse I, Seitz S, Mutschler W. *Eur. J. Trauma* **2006**, 32, 114.
 39. Patel ZS, Young S, Tabata Y, Jansen JA, Wong MEK, Mikos AG. *Bone* **2008**, 43, 931.
 40. Bock N, Riminucci A, Dionigi C, Russo A, Tampieri A, Landi E, Goranov VA, Marcacci M, Dediu V. *Acta Biomater.* 2010, 6, 786.
 41. Gladius L. *J. Biomed. Mater. Res. Part B: Appl. Biomater.* **2006**, 76B, 456.

42. Lode A, Wolf-Brandstetter C et al. *J. Biomed. Mater. Res. A* **2007**, *81A*, 474.
43. Baroud G, Bohnner M. *Joint Bone Spine* **2006**, *73*, 144.
44. Bohnner M, Gbureckb U et al. *Biomaterials* **2005**, *26*, 6423.
45. Day TF, Yang Y. *The Journal of Bone and Joint Surgery (American)*. **2008**, *90*,19.
46. Schweizer L, Varmus H, *BMC Cell Biol.* **2003**, *4*, 4.
47. Yamaza T, Miura Y et al. DOI: 10.1371/journal.pone.0002615.

CHAPTER 3

MAGNETISM IN BIOMEDICAL APPLICATIONS: A NEW CONCEPT FOR TISSUE REGENERATION

Magnetism, which is an intrinsic property of every atom, has a profound influence on living organisms. The use of materials in biological environment for implantation or for replacement of a part or a function of the body in a reliable and physiologically acceptable manner was a challenge for the last several decades. Of late the combination of fine particles and magnetism in the field of biology and biomaterials has been found useful in sophisticated bio-medical applications such as cell separation¹⁻⁴, drug delivery⁵, and magnetic intracellular hyperthermia treatment of cancer⁶⁻⁸.

The development of nano technology along with involvement of magnetism, opened new windows of sophisticated biomedical applications such as diagnostic, cancer therapy etc⁹. Most recent areas, where magnetic materials particularly when of nano size are used in biological applications, are following reported:

- Magnetic bioseparation
- Drug delivery
- MRI contrast agent
- Therapy – Hyperthermia treatment of cancer

3.1 Biomedical applications

3.1.1 Magnetic bioseparation

Bioseparation is an important phenomenon for the success of several biological processes. Magnetic separation of cells and bio molecules is based on the contrast of magnetic susceptibility between separand (magnetic) and medium (containing other nonmagnetic)

materials. A few cells or biomolecules have intrinsic magnetic properties.

The magnetic separation of cells or bio molecules is more effectively done by the superparamagnetic materials, because it exhibits magnetic properties in presence of magnetic field only. In addition, ferromagnetic as well as superparamagnetic particles coated or encapsulated with polymers or liposome can be used for magnetic labelling. For this purpose, magnetite (Fe_3O_4) or haematite ($\gamma\text{-Fe}_2\text{O}_3$) have been extensively used as magnetic carriers.

3.1.2 Drug delivery

The activity of most pharmaceuticals or drugs against certain diseases or disease sites suffers from their inability to accumulate selectively in the pathological organ or cells. When the drug or pharmaceutical agent is introduced into the body intravenously, it gets distributed throughout the body. To reach the target site, the drug has to cross many biological barriers (organ, cells and its compartments), and hence there is a chance of its getting inactivated. Large quantities or doses have to be administered to get the required therapeutic concentration to a target site. As a result, many negative side effects may be caused by cytotoxic and/or antigenic drugs. The situation becomes particularly critical in case of drugs having very low therapeutic indices (e.g. most anti-cancer drug). However, the above problems may be solved by selectively and quantitatively accumulating the drug to the target site. Independent of the site and methods its administration, drug targeting at non-target sites should remain under certain minimum levels to avoid site reactions.

There are many different approaches to targeted drug delivery, e.g. direct application of drug into the affected zone, use of reactor molecules having high affinity to the affected site and physical targeting¹⁰. Targeted drug delivery by external physical force (magnetic field) is an innovative new approach, capable of effective drug targeting.

Mechanism:

Magnetic drug transport technique is based on the fact that the drug can be either encapsulated in to a magnetic micro-sphere (or nano-sphere) or conjugated on the surface of the micro/nano sphere. When the magnetic carrier is intravenously administered, the accumulation can take place within the area to which the magnetic field is applied and

often augmented by magnetic agglomeration¹¹. The accumulation of the carrier at the target site allows them to deliver the drug locally. Efficiency of accumulation of magnetic carrier depends on physiological parameters¹² e.g. particle size, surface characteristics, field strength and blood flow rate etc. The magnetic field assists to extravasate the magnetic carrier into the targeted site. Though little is known about the process of extrusion, magnetic targeted carriers (MTC) are pulled through some kind of pore/channel opened by the force of the magnet. It has been observed that immobilization of MTC occurs within the tumor area when magnetic field is removed¹³.

Site-directed drug targeting is one way of local or regional antitumor treatment. The efficiency of chemotherapy treatment may be enhanced to a great extent by magnetically assisted delivery of cytotoxic agent to the specific site. There are a large number of magnetic carrier systems which demonstrates increasing drug concentration efficiency at the tumor site^{14,15}. In case of brain tumours, the therapeutic ineffectiveness of chemotherapy is mainly due to the impervious nature of the blood-brain barrier (BBB), presence of drug resistance and lack of tumour selectivity.

The aim of the specific cell targeting is to enhance the efficiency of drug delivery and at the same time to reduce the toxicity. An immense improvement of existing approaches to diagnosis and treatment of various diseases could be conveyed by targeted delivery of pharmaceuticals. The therapeutic applications of drug targeting are under investigation and some clinical trials are also under way. The numerous results^{16,17} show that the magnetic drug targeting is a promising area in the development of new and cost-effective clinical protocols in the near future. Further “magnetic drug delivery” will undoubtedly rise from its investigative origins, along with nano-biotechnology, to play an important role in improving human health.

3.1.3 MRI contrast agents

Magnetic resonance imaging is considered to be one of the most powerful techniques in diagnostic, clinical medicine and biomedical research. The magnetic resonance images are obtained by placing the area of interest within a powerful, highly uniform static magnetic field. Since hydrogen nucleus (single proton) is abundant in the body due to the high water content of the biological living carriers, the static magnetic field will make most of the protons to align with the field. These protons (nuclear spins) then move out of

their alignment by the application of an alternating magnetic field, which in turn is produced by the radio frequency coil near the specimen (static magnetic field). The resonant frequency of the alternating magnetic field should be in the radio frequency range (15-60 MHz). The nuclei absorb energy from the oscillating magnetic field and undergo transition from the lower energy state to the higher energy state. When the alternating magnetic field is switched off, the nuclei that return to the equilibrium state thereby emitting energy at the same frequency as previously absorbed. Further, this induces a signal in the coil, which is the source of alternating magnetic field. This nuclear magnetization can be transformed to diagnostic images by a series of algorithms.

MRI can provide information that differs from other imaging modalities. Its major technological advantage is that it can characterize and discriminate among living carriers using their physical and biochemical properties. The ability of MRI techniques to get images in multiple planes offers special advantages for radiation or surgical treatment.

3.1.4 Hyperthermia for the treatment of cancer

Heat treatment of organs, such that the temperature is increased to 42-46°C and the viability of cancerous cells reduces, is known as hyperthermia. It is based on the fact that tumour cells are more sensitive to temperature than normal cells¹⁸⁻²⁰. In hyperthermia it is essential to establish a heat delivery system, such that the tumour cells are heated up or inactivated while the surrounding normal living tissue are unaffected. Though different hyperthermia techniques depend upon the heating methods used, each one has certain limitations. Boundary effects limit microwave, ultrasound, and magnetic hyperthermia.

Magnetic hyperthermia can be induced by two different methods. In the first method, known for several decades, finite size magnetic implants are surgically placed within the tumour site, which absorbs energy from externally applied magnetic field and dissipates it in the form of heat to the surrounding tumour sites. These tumour sites can be destroyed, if the temperature rises above 42°C. It is however difficult to get homogenous heat distribution through this method. In such a method it is expected that temperature rise will be observed close to the implanted material and there will be non-uniformity in the temperature distribution in the tumour region. A major drawback of this procedure (using bulk materials) is that it is an invasive method and required surgical removal after hyperthermia treatment. Therefore, repeated surgery may be required which could be

traumatic.

The alternative approach is to use fine particles as heat mediators instead of needles or rods such that hyperthermia becomes non-invasive. When fluids containing sub-micron sized magnetic particles (typically 1-100 nm)²¹ are injected, these particles are easily incorporated into the cells, since their diameters are in the nanometer range. These magnetic particles selectively heat up living tissue by coupling magnetic field to targeted magnetic nano particles. As a result, the whole tumour can be heated up uniformly. This is called intracellular hyperthermia. It has been shown that malignant cells take up nine times more magnetic nano particles than normal cells. Therefore the heat generated in malignant cells is more than in normal cells²². Also, as blood supply in the cancerous living tissue is not normal, the heat dissipation is much slower. Hence, the temperature rise in the region of tumour is higher than in the surrounding normal living tissue. It is therefore expected that this therapy is much more concentrated and localized.

To make the hyperthermia as a potential therapy, selective destruction of cancerous cells is important. Though the hyperthermia is based on the fact that the tumour cells are very much sensitive to heat in the range of 42-46 °C¹⁸⁻²⁰, it can assist the therapy to a high degree of selective destruction of cancerous cells. This is possible if targeted delivery of potential magnetic particles to the cancerous cells is made so that it will be much more effective to heat than the normal living tissue. For this, optimization of magnetic parameters of particles is essential, which includes synthesizing particles having high value of specific absorption rate^{23,24}.

3.1.5 Magnetic therapy for the treatment of bone disease

Magnetic therapy has been considered a promising alternative in disease treatments in health care, especially in the treatments of bone diseases. Research has indicated that magnetic fields may stimulate the proliferation and differentiation of osteoblasts, promote the expression of growth factors such as bone morphological protein, increase osteointegration, and accelerate new bone formation²⁵⁻²⁸. Magnetic fields were also found to be beneficial in promoting the integration of bone and implants, increasing bone density and calcium content, and accelerating the healing of bone fractures²⁹⁻³².

Singh P. et al.³³ reports the stimulating effect of static magnetic field (SMF) on microstructure and mineralization process of bone repair. A unilateral transverse fracture

of mid-shaft of metacarpal was surgically created in healthy goats under thiopental sedation and xylocaine analgesia. Two bar magnets (approximately 800 gauss/cm² field strength) were placed across the fracture line at opposite pole alignment immobilized in Plaster of Paris (POP) splint bandage for static magnetic field stimulation. Radiographs were taken at weekly intervals up to 45 days. Results show that formation of extracellular matrix and its microstructure can be influenced by non-invasive physical stimulus (magnetic field) for achieving an enhanced osteogenesis, leading to quicker regeneration of bone tissue in goats.

Kotani H. et al.³⁴ investigate the effects of a strong SMF (8 T) on bone formation in both in vivo and in vitro systems. After 60h of exposure to the SMF, cultured mouse osteoblastic MC3T3-E1 cells were transformed to rodlike shapes and were orientated in the direction parallel to the magnetic field. Although this strong SMF exposure does not affect cell proliferation, it up-regulate cell differentiation and matrix synthesis. The SMF also stimulate ectopic bone formation in and around subcutaneously implanted bone morphogenetic protein (BMP) 2-containing pellets in mice, in which the orientation of bone formation is parallel to the magnetic field. It is concluded that a strong SMF has the potency not only to stimulate bone formation, but also to regulate its orientation in both in vitro and in vivo models. In conclusion the combination of a strong SMF and a potent osteogenic agent such as BMP possibly may lead to an effective treatment of bone fractures and defects.

Yamamoto et al.³⁵ study the effects of SMF on osteoblastic differentiation, proliferation, and bone nodule formation using a rat calvaria cell culture. During a 20-day culture, the values of the total area and the number and average size of bone nodules showed high levels in the presence of SMF. In the matrix development and mineralization stages, the calcium content in the matrix and two markers of osteoblastic phenotype (alkaline phosphatase and osteocalcin) also showed a significant increase. Accordingly, these findings suggest that SMF stimulates bone formation by promoting osteoblastic differentiation and/or activation.

Effects of a static magnetic field were also studied on bone formation using an ischemic rat femur model³⁶. Metal rods were prepared from magnetized and unmagnetized samarium cobalt to have tapered structure, both with the same geometrical dimension, and were implanted transcortically into the middle diaphysis of 88 rat femurs. Both sides of

the rat femoral artery were ligated to create an ischemic bone model, followed by implantation of the tapered rod to the femur. The bone mineral density (BMD) and weight of the femurs were measured at 1st and 3rd week after implantation. The result at the 3rd week post-implantation revealed that the BMD and weight of the ischemic bone model rats were significantly reduced, compared with that of non-operated femur. It was also found that the magnetized group had significantly higher bone weights than the unmagnetized ($p < 0.05$). The BMD of the rats implanted with the magnetized rods were similar to those of the non-operated ($p > 0.05$). This enhancement of the femoral bone formation of the ischemic rat model by the static magnetic field seems to be due to the improved blood circulation of the femur.

Taking into account the actually scientific evidence it is possible to assert that the application of static magnetic fields for the therapy of the bone tissue promotes the differentiation and activation of osteoblasts generating an increase of bone mineral density.

3.2 Magnetic materials

Magnetism is known to all of us from childhood as the phenomenon by which some materials attract or repel other materials from a distance; examples of such materials include iron, lodestone and some steels. Broadly, magnetic forces are generated by moving charged particles, leading to magnetic fields³⁷.

Consider a material placed in an external magnetic field. The atoms in this material possess an atomic moment which responds to this external field. It is useful to think of magnetic dipoles existing in magnetic materials; these dipoles can be considered to be small bar magnets with north and south poles. The dipoles possess a magnetic dipole moment which can respond to the external magnetic field. Some field vectors are needed to understand this response: the external magnetic field strength is denoted by H (units A/m), the magnetic induction in the material is denoted by B (units tesla) and the magnetization by M (units A/m). B , H and M are related by

$$B = \mu_0 (H + M)$$

where μ_0 is the permeability of free space (its magnitude is 1.257×10^{-6} H/m) and M is

the magnetic moment m per unit volume of the material. The value of M depends on the type of material and the temperature and can be related to the field H through the volumetric magnetic susceptibility χ by the relation

$$M = \chi H$$

The magnetic response of bulk material results in materials being classified as either diamagnetic, paramagnetic or ferromagnetic.

Diamagnetism is very weak and not permanent; it persists only as long as the external field is present. It occurs due to a change in the orbital motion of electrons due to the external field, the direction of the induced magnetic moment is opposite to the field. In an inhomogeneous field, such materials are attracted towards regions where the field is weak. In **paramagnetism**, each atom has a permanent dipole moment because of incomplete cancellation of its electron magnetic moments. When a field is applied these atomic dipoles *individually* tend to align with the field, much as a compass needle aligns with the earth's magnetic field.

Diamagnetic and paramagnetic materials exhibit magnetization only in the presence of an external field; the low values of susceptibility χ imply that the magnetic induction in such materials is very weak.

Ferromagnetism is the most familiar type of magnetism. It occurs, for example, in body centred cubic (b.c.c.) iron, cobalt, nickel, and in many alloy compositions based on Fe, Co and Ni. Ferromagnetic materials, unlike dia- and para- magnetic materials, show permanent magnetic moments even in the absence of an external field. The susceptibility values are very high compared to those of para- and dia- magnetic materials, reaching up to 10^6 . The magnetic moments in such materials arise mainly from atomic spin magnetic moments. More importantly, interactions between atoms cause spin magnetic moments to align with one another in a *cooperative* fashion. Thus, large regions in a crystal can have atoms with their spins aligned with one another. When all the magnetic dipoles are aligned the magnetization reaches its saturation value (M_s).

As mentioned earlier, ferromagnetism results from a cooperative *parallel* alignment of spins. In other materials, e.g., MnO, the magnetic moment coupling between atoms (or ions) results in the spin moments of neighboring atoms being aligned in *opposite*

directions. Such materials are antiferromagnetic. In the case of MnO , the moments of adjacent Mn^{2+} ions are antiparallel, thus the material has no net magnetic moment.

Some materials include the magnetic biomaterial, magnetite (Fe_3O_4). Hexagonal ferrites and garnets are other ceramic materials that fall in this category. Cubic ferrites, such as magnetite, can be represented as MFe_2O_4 , where M is a metal. In the case of Fe_3O_4 , Fe ions exist in both the +2 and +3 valence states. The magnetic moments of the two types of Fe ions differs; in this case, there is a net magnetic moment because for the solid as a whole the spin moments are not completely cancelled; although the spin moments of the Fe^{3+} ions cancel one another, the magnetization arises from the parallel alignment of the moments of the Fe^{2+} ions (Fig. 1).

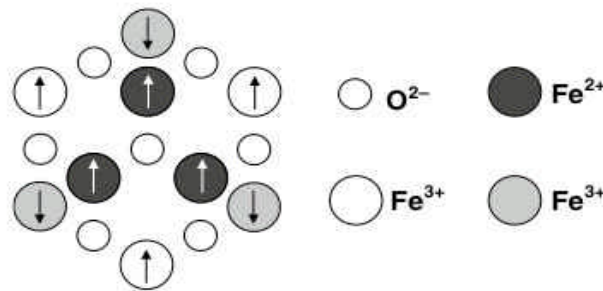


Fig. 1. Schematic depicting the spin magnetic moments for Fe^{3+} and Fe^{2+} in Fe_3O_4

3.2.1 The influence of Temperature

It can be expected that temperature will play an important role in determining magnetic properties, since entropy effects will be more dominant at high temperatures. The magnetic properties of both ferri- and ferro-magnets depend on the coupling forces between neighboring atoms; at higher temperatures, entropy effects favour a random arrangement of spins, resulting in a reduction in saturation magnetization. The saturation magnetization decreases with increasing temperature; at the Curie temperature T_c it becomes zero and the material becomes paramagnetic above this temperature. Thus a given material can change its magnetic behaviour depending on the temperature; its use as a magnetic biomaterial will consequently depend on the relative values of the service temperature and the Curie temperature. The ferromagnetic to paramagnetic phase transformation described above has been used to act as an on-off switch in hyperthermia

applications; the magnetic material is designed to have a Curie temperature equal to the temperature required for hyperthermia.

3.2.2 Factors affecting magnetic properties

Since size plays an important part in many magnetic biomaterials applications the effect of particle size on magnetic properties is discussed (Fig. 2)³⁸. In large particles (greater than about 1 μm) there are many magnetic domains; this leads to a narrow hysteresis loop. Such particles are useful in immunomagnetic separation of pathogenic microorganisms in microbiology. For smaller particle sizes (less than about 1 μm) it is energetically more favourable for only one domain to exist.

The response of such particles to a magnetic field is qualitatively different, resulting in a broader hysteresis loop.

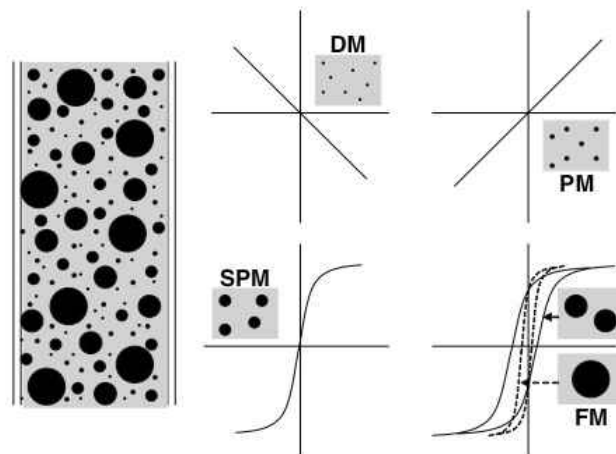


Fig. 2. Magnetic properties are affected by the particle size (DM = diamagnetic, PM = paramagnetic, SPM = superparamagnetic, FM = ferromagnetic)

If the particle size is reduced further to about 20 nm (the exact size depends on the composition of the material), the material becomes **superparamagnetic**, which means that the magnetic moment of the particle fluctuates because of the thermal energy (kT); at the atomic level the individual atomic moments continue to be ordered relative to each other. Importantly, the remanence is zero, the result is a B-H curve showing no hysteresis; this property is important for reducing the tendency of the particles to agglomerate. The

physical basis for the fluctuation of the magnetic moments can be understood as a battle between ΔE , the energy barrier to moment reversal and the thermal energy (kT). In the simplest approximation the energy barrier is the product of the anisotropy energy density K and the volume V . When the particle size is small (small V), the KV term is small and comparable to the thermal energy; this leads to flipping of the magnetic moment. The “blocking” temperature T_B can be regarded as the temperature above which the material becomes superparamagnetic.

3.2.3 Intelligent magnetic nanobiomaterial for Tissue Engineering

Development of functional engineered materials possessing intelligence has been one of the most challenging tasks in research over the past decade. The term “intelligent material” refers to materials that possess three main functions, including sensing changes in environmental condition, processing the sensed information and finally actuated by external stimuli.

The recent convergence of biomaterials and nanotechnology has enabled the development of intelligent nanobiomaterials, such as nanoparticle-encapsulating hydrogels for applications in tissue engineering and regenerative medicine³⁹⁻⁴¹. These nanobiomaterials provide unique properties to address challenges in biology, medicine, and materials science⁴¹⁻⁴³, e.g., modifiable mechanical and interfacial properties of a nanoscaffold to mimic native extracellular matrix (ECM)⁴⁴.

Among the magnetic materials usually used in the biomedical field, magnetic nanoparticles (MNPs) have drawn great interest owing to their unique magnetic properties, including the fact that they become superparamagnetic at diameters of < 20 nm³⁹. Coupled with their excellent biocompatibility, MNPs have been widely used in biomedical applications such as drug delivery, magnetic resonance imaging reagents, bioseparation, enzyme immobilization and magnetic hyperthermia⁴⁵⁻⁴⁸, but their application in tissue regeneration, especially in bone repair, has seldom been considered.

As mentioned, at a size of < 20 nm, the MNPs become nonmagnetic on a macroscopic scale and behave like common materials in the absence of an exterior magnetic field. However, each particle could be considered a single magnetic domain, providing a magnetic field at a nano-scale, which makes it possible for magnetic scaffolds to provide an intrinsic magnetic therapy. Meanwhile, once exposed under an exterior magnetic field,

MNPs will be rapidly magnetized to saturation and respond to the exterior magnetic field to provide enhanced magnetic therapy⁴⁹⁻⁵².

The greatest therapeutic potential in the use of MNPs is probably associated with applications involving ‘intelligent’ particles with a *magnetic core* (to direct the particles to the vicinity of the target and also for hyperthermia or for temperature-enhanced release of the drug), a *recognition layer* (to which suitable receptors are attached), and a *therapeutic load* (adsorbed inside the pores or hosted within internal cavities of the particles). The challenges are formidable, especially those related to the development of suitable recognition layers. Not only must useful recognition moieties be identified and attached to the particles, but they must be loaded to a high density while maintaining their desired characteristics. For example, MNPs can be coupled to bioactive molecules such as tissue grow factors (Gfs) and guided, under an external magnetic field, through a magnetic scaffold. Under an external magnetic field, the magnetic moment of the magnetic scaffolds can be continuously controlled. This allows reloading of the scaffold from an external supervising center so that the scaffolds will work like a fixed “station” providing the opportunity to regulate tissue formation to the personal needs of the patient⁵³.

The potential of drug delivery systems based on the use of nano- and microparticles stems from significant advantages such as: (i) the ability to target specific locations in the body; (ii) the reduction of the drug quantity needed to attain a particular concentration in the vicinity of the target; and (iii) the reduction of the concentration of the drug at non target sites minimizing severe side effects⁵⁴.

References

1. Chatterjee J, Haik Y, Ching-Jen Chen *J. Magn. Magn. Mater.* **2001**, 225, 21.
2. Popovic Z, Sjostrand J *Vision Res.* **2001**, 41, 1313.
3. Del Gratta C, Della Penna S, Battista P, Di Donato L, Vitullo P, Romani G L, Di Luzio S. *Phys. Med. Biol.* 1995, 40, 671.
4. Liberti PA, Rao CG, Terstappen LW. *J. Magn. Magn. Mater.* **2001**, 225, 301.
5. Andra W, Nowark H. *Magnetism in medicine (Hand book)*, Berlin:Wiley-VCH, 1998
6. Shinkai M, Yanase M, Suzuki M, Honda H, Wakabayashi T, Yoshida J, Kobayashi T *J. Magn. Magn. Mater.* **1999**, 194, 176.
7. Jordan A, Wust P, Scholz R, Tesche B, Fahling H, Mitrovics T, Vogl T, Cervos-Navarro J, Felix R *Int. J. Hyperthermia* **1996**, 12, 705.
8. Golui S, Datta D, Bahadur D *Proc. 8th Int. Conf. on ferrites (ICF 8)* Kyoto, Japan, **2000**, p 105.
9. Olsvik-O, Popovic T, Skjerve E, Cudjoe K S, Hornes E, Ugelstad J, Uhlen M *Clin. Microbiol. Rev.* **1994**, 7, 43.
10. Kuznetsov AA, Filippov VI, Kuznetsov OA et al. *J. Magn. Magn. Mater.* **1999**, 194, 22.
11. Lubbe AS, Bergemann C, Brock J, McClure DG. *J. Magn. Magn. Mater.* **1999** 194, 149.
12. Fricker J. *Drug Discovery Today* **2001**, 6, 387.
13. Widder KJ, Morris RM, Poore GA, Howards DP, Senyei AE *Eur. J. Cancer Clin. Oncol.* **1983**, 19, 135.
14. Gallo JM, Gupta PK, Hung CT, Perrier DG. *J. Pharm. Sci.* **1989**, 78, 190.
15. Pulfer SK, Gallo JM. 1997 In: *Scientific and clinical applications of magnetic carriers* (eds) U Hafeli, W Schutt, J Teller, M Zborowski (New York, London: Plenum) p. 445
16. Alexiou C, Arnold W, Hulin P, Klein R J, Renz H, Parak F G, Bergemann C, Lubbe AS *J. Magn. Magn. Mater.* **2001**, 225, 187.
17. Koenig SH *Acad. Radiol.* **1996**, 3, 597.
18. Overgaard K, Overgaard J. *Eur. J. Cancer.* **1972**, 8, 65.
19. Overgaard J. *Cancer.* **1977**, 39, 2637.

20. Field SB, Hand JW. *An introduction to the practical aspects of clinical hyperthermia*. 1990 (London: Taylor and Francis)
21. Gilchrist R K, Medal R, Shorey W D, Hanselman R C, Parott J C, Taylor C B 1957 *Ann. Surg.* 146: 596–606
22. Ohura K, Lkenaga M, Nakamura T, Yamamuro T, Ebisawa Y, Kokuko T, Kotoura Y, Oka M *Bioceramics (Proc. 3rd Int. Symp. Ceramics in Medicine)* **1990**, Terre Haute, Indiana, pp 225.
23. Chan DCF, Kirpotin DB, Bunn PA Jr. 1997 In: *Scientific and clinical applications of magnetic carriers* (eds) U Hafeli, W Schutt, J Teller, M Zborowski (New York, London: Plenum) p. 607
24. Streffer C, vanBeuningen D. 1987 In: *Hyperthermia and the therapy of malignant tumours* (ed.) J. Streffer (Berlin: Springer) p. 24.
25. Bassett CA, Schink-Ascani M, Lewis SM. *Clin. Orthop. Relat. Res.* **1989**, 246, 172.
26. Santini MT, Rainaldi G, Ferrante A, Indovina PL, Vecchia P, Donelli G. *Bioelectromagnetics.* **2003**, 24, 327.
27. McLeod KJ, Collazo L. *Radiat. Res.* **2000**, 153, 706.
28. Jansen JH, van der Jagt OP, Punt BJ, et al. *BMC Musculoskelet. Disord.* **2010**, 11, 188.
29. Fini M, Cadossi R, Canè V. *J. Orthop. Res.* **2002**, 20, 756.
30. Zhang XY, Xue Y, Zhang Y. *Bioelectromagnetics.* **2006**, 27, 1.
31. Chang K, Chang WH. *Bioelectromagnetics.* **2003**, 24, 189.
32. Taylor KF, Inoue N, Rafiee B, Tis JE, McHale KA, Chao EY. *J. Orthop. Res.* **2006**, 24, 2.
33. Singh P, YashRoy RC, Hoque M. *Biophysics and Electron Microscopy Section, Indian Veterinary Research Institute, Izatnagar-243122, UP, India.*
34. Kotani H, Kawaguchi H, Shimoaka T, Iwasaka M, Ueno S, Ozawa H, Nakamura K, Hoshi K, *J. Bone Miner. Res.* **2002**, 17, 814.
35. Yamamoto Y, Ohsaki Y, Goto T, Nakasima A, Iijima T. *J. Dent. Res.* **2003**, 82, 962.
36. Xu S, Tomita N, Ohata R, Yan Q, Ikada Y. *Biomed Mater Eng.* **2001**, 11, 257.
37. Callister WD. *Materials Science and Engineering*, Wiley: New York, 2003.

38. Pankhurst QA, Connolly J, Jones SK, Dobson J. *Phys. D. Appl. Phys.* **2003**, *36*, R167.
39. Hasirci V, Vrana E, Zorlutuna P, Ndreu A, Yilgor P, Basmanav FB, Aydin E. *J. Biomater. Sci. Polym. Ed.* **2006**, *17*, 1241.
40. Xu F, Wu CM, Rengarajan V, Finley TD, Keles HO, Sung Y, Gurkan UA, Demirci U. *Adv. Mater.* **2011**, *23*, 4254.
41. Geckil H, Xu F, Zhang X, Moon S, Demirci U. *Nanomedicine* **2010**, *5*, 469.
42. Hung HS, Chen HC, Tsai CH, Lin SZ. *Cell. Transplant.* **2011**, *20*, 63.
43. Miyahara Y, Kobayashi H, Chen G, Kikuchi M. *Sci. Technol. Adv. Mater.* **2010**, *11*, 010302.
44. Stevens MM, George JH. *Science* **2005**, *310*, 1135.
45. Jun S, Zeng H, Robinson DB, et al. *J. Am. Chem. Soc.* **2004**, *126*, 273.
46. Wang L, Yang Z, Gao J. *J. Am. Chem. Soc.* **2006**, *128*, 13358.
47. Kim J, Lee JE, Lee J. et al. *J Am Chem Soc.* **2005**, *128*, 688.
48. Jun YW, Huh YM, Choi JS et al. *J. Am. Chem. Soc.* **2005**, *127*, 5732.
49. Bretcanu O, Verné E, Cöisson M, Tiberto P, Allia P. *Magn. Mater.* **2006**, *305*, 529.
50. Jun YW, Seo JW, Cheon. *J. Acc. Chem. Res.* **2008**, *41*, 179.
51. Jeong U, Teng X, Wang Y, Yang H, Xia Y. *Adv. Mater.* **2007**, *19*, 33.
52. Gupta AK, Gupta M. *Biomaterials.* **2005**, *26*, 3995.
53. Panseri S, Russo A, Giavaresi G, Sartori M, Veronesi F, Fini M, Salter DM, Ortolani A, Strazzari A, Visani A, Dionigi C, Bock N, Sandri M, Tampieri A, Marcacci M. *J. Biomed. Mater. Res A.* **2012**, *100*, 2278.
54. Arruebo M, Fernandez-Pacheco R, Ibarra MR, Santamaria. *Nano Today* **2007**, *2*, 22.

CHAPTER 4

BIOMIMETIC MATERIALS

4.1 Calcium phosphates in biologic systems

The wide application in the last decades of calcium phosphates as biomaterials is mainly due to the biological properties of these materials, whose composition is very close to the one of bone mineral, which represents about 70% of the mass of dry bone tissue¹⁻³. The first study dates back to the 1920, reporting an accelerated bone healing in surgically created defects in rabbits⁴. Anyway, specific interest in calcium phosphates for biomedical applications, and specifically in apatites, raised up in the 1960s and initial studies principally involved the synthesis and analysis of hydroxyl apatites in an attempt to better understand the physico-chemical and biological behaviour of natural apatites, which constitute the mineral part of human bones and teeth^{3,5,6}. Following these studies, calcium phosphate-based bioceramics have been in use in medicine and dentistry for the last 40 years. Different phases of calcium phosphate ceramics are selected depending upon whether a resorbable or bioactive material is desired. These materials constituted a wide variety of biomaterials like coatings of metal orthopaedic (hip and knee joints) and dental implants, cements, injectable cements, composite materials, and drug carriers (antibiotics, anticancerous drugs, growth factors), three-dimensional dense and porous scaffolds for bone reconstruction or replacement, applied especially in small bones and middle ear bones, powder granulates for the repair of bone defect in maxillofacial surgery, alveolar ridge augmentation, otolaryngology. The stable phases of calcium phosphate ceramics depend considerably upon temperature and the presence of water, either during processing or in the use environment. At body temperature, only two calcium phosphates are stable in contact with aqueous media, such as body fluids: at pH < 4.2, the stable phase is $\text{CaHPO}_4 \cdot 2\text{H}_2\text{O}$ (dicalcium phosphate, brushite, DCPD), whereas, at pH > 4.2, the stable phase is $\text{Ca}_{10}(\text{PO}_4)_6(\text{OH})_2$ (Hydroxyapatite, HA). At higher

temperatures, other phases, such as $\text{Ca}_3(\text{PO}_4)_2$ (β -tricalcium phosphate, TCP), and $\text{Ca}_4(\text{PO}_4)_2\text{O}$ (tetracalcium phosphate, TeCP) are present. The unhydrated, high temperature calcium phosphate phases interact with water, or body fluids, at 37 °C to form HA. Thus, the solubility of TCP surface approaches the solubility of HA and decreases the pH of the solution, which further increases the solubility of TCP and enhances resorption.

Other calcium phosphates have been identified with or without association with apatite; they include: $\text{Ca}_8\text{H}_2(\text{PO}_4)_6 \cdot 5\text{H}_2\text{O}$ (octacalcium phosphate, OCP); $\text{Ca}_2\text{P}_2\text{O}_7$ (calcium pyrophosphate dehydrate in mono- and triclinic forms, CPP); amorphous calcium phosphate, ACP.

Apatites in normal calcified tissues of teeth and bone have been postulated to form either directly or indirectly by way of precursor calcium phosphates such as ACP, DCPD, OCP or TCP.

4.2 Tricalcium phosphate (TCP)

Tricalcium phosphate exists under two crystallographic forms: β and α -TCP. The α - form is unstable at low temperature and is obtained by quenching the β -form heated above 1125 °C (transition temperature). The β -form may however be stabilized by several ionic impurities, such as Mg^{2+} ions, frequently associated with Ca salts. α -tricalcium phosphate is more soluble and more reactive than β -TCP, and it can be rapidly hydrolyzed into apatite in aqueous media. Both varieties can be used in Ca-P cement preparations.

α -TCP is highly reactive in aqueous systems and can be easily hydrolyzed to a mixture of other calcium phosphates. α -TCP crystallizes in a monoclinic structure, space group P21/a and unit cell $a = 12.887(2) \text{ \AA}$, $b = 27.280(4) \text{ \AA}$, $c = 15.219(2) \text{ \AA}$ and $\beta = 126.20(1)^\circ$, with 24 formula units per unit cell⁷. There is an approximate subcell with a b -axis parameter of $b/3$ (9.09 Å) that contains 8 formula units, which corresponds to the unit cell reported⁸.

The structure of α -TCP is constituted of columns of Ca^{2+} and PO_4^{3-} ions which run parallel to the c -axis; the section of the structure of α -TCP corresponds to a unit cell of apatite. The correspondence can also be seen from a consideration of the dimensions of the unit cell of α -TCP with those of apatite: the α -TCP approximate subcell b -axis

parameter of 9.09 Å corresponds to the *a*-axis apatite parameter, whilst half the *c*-axis parameter of α -TCP (7.6 Å) corresponds to the *c*-axis parameter of apatite.

The β -form makes an excellent resorbable biomaterial. However, it is not found in biological systems and it cannot be obtained by precipitation. Biological TCP is always partially magnesium-substituted, giving rise to whitlockite $(\text{Ca,Mg})_9(\text{PO}_4,\text{HPO}_4)_6$. It is not detected as constituents of normal tissue calcifications but their presence in several pathological tissue calcifications, in abnormally calcified cartilage and in human dental carious lesions has been reported⁹⁻¹⁰. β -TCP is more soluble than apatite and can be hydrolyzed into apatitic phases; whitlockite on the contrary seems less soluble and has never been shown to convert into apatite¹¹⁻¹². The presence of Mg in β -TCP is thus an important parameter affecting its biological properties, especially its ability to be resorbed.

4.3 Bioactivity of calcium phosphate

Synthetic bioactive Ca-P materials are not in equilibrium with biological fluids. Thus, several reactions occur on the mineral surface. For apatites, very first reaction is the hydrolysis of the surface PO_4^{3-} groups into HPO_4^{2-} and the uptake of carbonate and sodium ions. Generally the hydrolysis of surface phosphate groups is associated with a decrease of the calcium concentration at the surface¹³. These reactions correspond simply to exchanges between the solution and the first atomic layers of the apatite surface. The extent of these reactions may vary according to the composition of the mineral and how it was produced. Inflammatory cells in close proximity to the material, may also create an acidic environment. Poorly crystalline apatites with many defects are particularly sensitive to these changes.

As biological fluids are generally supersaturated with respect to apatite, the Ca-P materials also serve as a template for the formation of carbonate-apatite crystals. This event has been shown to be the major factor behind the osteoconductivity of all biomaterials and has been evidenced in different classes of bioactive orthopaedic implants (polymers and bioactive glasses). The crystals formed are very much like bone mineral crystals. They are carbonated apatites and exhibit non-apatitic environments.

The precipitation of the neo-formed crystals can also be boosted by release of calcium, phosphate ions or rise in the pH that may locally increase the supersaturation ratio in the

vicinity of the implant surface. This phenomenon can be favoured by hydrolysis reactions of the material constituents. Enlarging the surface area is another way to increase the amount of reactive, neo-formed crystals.

The ability of a biomaterial to generate this layer has been considered as a measure of its biological activity, although such a relationship has not yet been established on a quantitative basis. Despite the analogy of the crystals formed with bone mineral crystals, the processes of formation and organization appear to be rather different. Bone mineral crystals are always formed in an organic collagen matrix with which they are closely associated. Although the layer formed on bioactive biomaterials frequently incorporates bone proteins, there is no organization like that of bone. It appears more like an uncontrolled mineralization.

The functions of the neo-formed layer have not yet been clearly established. This layer creates a very reactive surface with a high specific surface area, which is able to attach bone specific proteins, especially osteopontin and osteocalcin¹⁴. The neo-formed layer appears, as a support, and the adsorption of proteins to it is necessary to accommodate osteoblast cell attachment and favour their multiplication. Although such proteins might bind directly to the HA surface, the adsorption affinity could be quite different depending on the apatitic substrate. Thus, synthetic apatites rich in labile non-apatitic environments exhibit a high surface reactivity and have a higher affinity for some proteins than stoichiometric HA. Depending on the apatitic substrate and the rate of formation of the layer, the presence of labile non-apatitic environments and the reactivity of the neo-formed layer may vary.

4.4 Apatites

4.4.1 Hydroxyapatite: structure and chemistry

Apatites are an industrially important group of materials with applications in catalysis, environmental remediation, bone replacement and ceramic membranes amongst others, and constitute a large class of materials with general formula¹⁵ $[M(1)_2][M(2)_3](XO_4)_3Z$, where: M represents a bivalent cation; XO_4 represents a trivalent anion; Z represents a monovalent anion. Among all the apatites, calcium hydroxyapatite is the most relevant in biological systems, as it is the major component of bones and teeth; its formula is defined as: $Ca_5(PO_4)_3OH$ or, more often, $Ca_{10}(PO_4)_6(OH)_2$. M/X ratio commonly defines the

stoichiometry of an apatite, in case of HA it corresponds to $\text{Ca/P} = 1.667$. In ideal HA, calcium, phosphorus and hydroxyl ion are present in the following weight percentage: $\text{Ca}^{2+} = 39.84\%$; $\text{PO}_4^{3-} = 56.77\%$; $\text{OH}^- = 3.39\%$. The apatite prototype $\text{Ca}_5(\text{PO}_4)_3\text{F}$ structure was first determined by Naray-Szabo in 1930¹⁶ and was confirmed to adopt $\text{P6}_3/\text{m}$ symmetry (Fig. 1.).

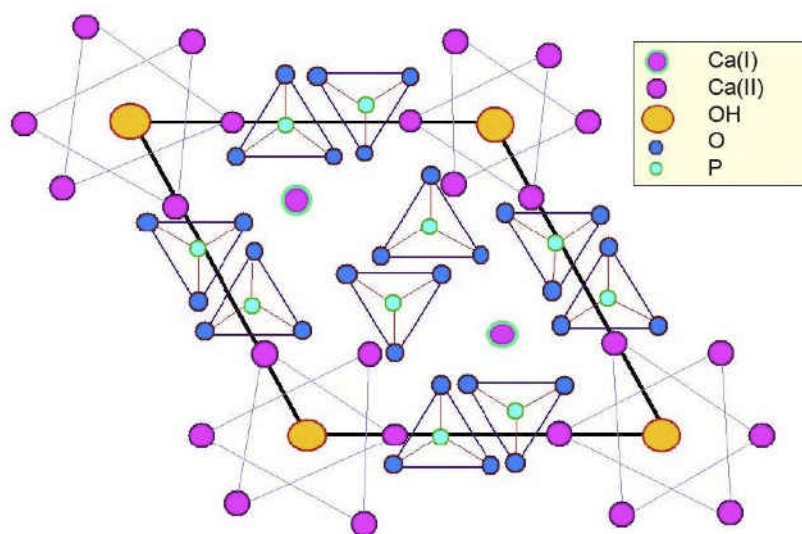


Fig. 1. Crystal structure of Hydroxyapatite.

The 10 Ca^{2+} ions occupy two crystallographically different symmetry sites, 4f and 6h. Four Ca^{2+} ions (4f) are located in columns along the three-fold axes at $1/3, 2/3, 0$ and $2/3, 1/3, 0$ separated by approximately one half of the c -axis. These are commonly referred to as Ca1 (or column Ca). Ca1 is coordinated to nine O atoms, with six shorter bonds that define an approximate trigonal prism and three longer bonds capping the prism faces. The Ca-O9 polyhedra share the trigonal faces to form chains parallel to the c -axis. The remaining six Ca^{2+} ions (6h sites, referred to as Ca2 or triangular Ca) form two triangular sets at $z = 1/4$ and $3/4$ on the mirror planes. The Ca2 ions are seven-coordinated, with six O atoms and one OH^- ion. The six XO_4 tetrahedra are PO_4^{3-} groups in a 6h site. OH^- anions occupy the special position 4e at $z/c=0.202$, that has multiplicity of 4. As in the hexagonal structure the presence of the mirror plane at $1/4$ and $3/4$ make hydroxyls ions in this position reflected too close to themselves, an occupation factor of 1 would result in

an incorrect stoichiometry. Thus, the occupation of the site must be 0.5, and in this case the orientation of the OH⁻ groups in the lattice cannot be known. A full description of OH⁻ sites in stoichiometric HA can be achieved by reducing the symmetry of the crystal to the subgroup P2₁/b¹⁷. As the cell contains twice the atoms of the hexagonal one, the correct stoichiometry is retained and the sticking of the hydroxyls is prevented; the resulting unit cell parameters are a = 9.421 Å, b = 18.843 Å, c = 6.881 Å, γ = 120.0°.

Thus, HA can be described in terms of two interpenetrating lattices: an overall P6₃/m structure, with a local P2₁/b in correspondence of the hydroxyls columns. For this reason and for sake of simplicity, we will always refer to the hexagonal description of HA, as the monoclinic description is required only for explaining the statistical occupation of OH⁻ ions and is not influent on the chemico-physical properties of HA related to the biologic behaviour.

4.4.2 Biological Apatites

Although the above-described structure of synthetic HA has been used as a model for the apatite present in the human hard tissues for many years, many differences in composition and in other properties make the biological apatites different from pure calcium hydroxyapatite and from each other and should be more appropriately referred to as calcium-deficient, multi-substituted hydroxyapatite. The apatite lattice is very tolerant of substitutions, vacancies and solid solutions, for example, X can be replaced by ½CO₃ or ½O; Ca by Sr, Ba, Pb, Na or vacancies¹⁸; and PO₄ by HPO₄, AsO₄, VO₄, SiO₄ or CO₃. Owing to this ability, biological apatites are capable of variable composition and therefore to be heterogeneous even within each category and even within each calcified tissue (enamel, dentine, bone). Non-stoichiometry (Ca/P of biological apatites ranges from 1.54 to 1.73 compared to 1.67 for pure HA), the presence structural or surface-bound of foreign ions and the co-existence or pre-existence of possible precursors such as DCPD, octacalcium phosphate (OCP), TCP, ACP make an accurate crystallochemical analysis and definition a difficult, if not an impossible undertaking.

Because of these difficulties, many studies on biological apatites have been made indirectly by studying apatites prepared from aqueous and non-aqueous systems. Notwithstanding, the chemico-physical behaviour of the synthetic apatites cannot always be directly extrapolated to biological apatites. The biological apatites are uniquely similar

in that they all contain carbonate in varying amounts as a substitute for phosphate in the apatite structure^{19,20}. They differ in crystallite sizes, shapes and other physico-chemical properties such as chemical (susceptibility to acid dissolution) and thermal stabilities^{21,22}. Based on observations from *in vitro* systems^{19,21,23-25}, some of these foreign ions affect the crystallinity (reflecting crystallite size and/or strain), morphology, lattice parameters of the biological apatites and as a consequence, impart stability or instability to the tissues involved. Some of these impurities are associated with the susceptibility or resistance of human tooth enamel to acid dissolution (caries) and of bone resorption processes^{26,27}. Biological apatite is not a stable material, as it is involved in the complex bone metabolism and thus subject to a continuous structural remodelling, due also to its very poor crystallinity degree. One important characteristics of biologic HA is for example, the increase of its crystallinity in the ageing and the increase of Ca/P ratio. This phenomenon reflects in a progressive decrease of the capacity of biologic HA to remodel itself, as the stability and solubility of HA strongly decreases when it approaches to the stoichiometry (Ca/P = 1.667).

4.4.3 Effect of Carbonate

The presence of carbonate ions in the biological apatites strongly contributes to the variation of Ca/P ratio. As higher its content as higher is the metabolic activity of the tissue: for example, enamel, which is a nearly inert tissue, contains very few carbonate, compared to bone and dentin, which are very active tissues. Carbonate ions are either adsorbed on the surface or incorporated into the HA structure, into two different crystallographic sites, hydroxyl (A-type carbonation) or phosphate (B-type carbonation). The B-type is the preferential carbonate substitution found in the human bone, in the range 2-8 wt%, depending on the age of individual²⁸, with the A/B type ratio in the range 0.7-0.9. A higher value of the A/B ratio was observed in old tissue, compared to young tissue²⁹. It has been observed by *in vivo* tests that the decrease of crystallinity in B-carbonated HA yields an increase of solubility³⁰. B-type carbonation is related to a higher affinity of apatite for osteoblast cells, compared to A-type carbonation, as it does not alter the surface polarity of HA. This reflects in a higher cellular adhesion and an increase production of collagen^{31,32}.

4.4.4 Effect of Magnesium

Among substituting cations, magnesium is widely studied due to its biological relevance. It has been verified that in calcified tissues, the amount of magnesium associated with the apatite phase is higher (about 5% at.) at the first stages of the bone remodelling process and decreases with increasing calcification and with the ageing of individual³³. The presence of magnesium increases the nucleation kinetic of HA contemporary retarding that of its crystallization; for this reason magnesium concentration is higher in the cartilage and in young bone and there is growing evidence that it may be an important factor in the qualitative changes of the bone matrix that determines bone fragility. Magnesium depletion adversely affects all stages of skeletal metabolism, causing cessation of bone growth, decrease of osteoblastic and osteoclastic activities and osteopenia.

4.4.5 Effect of Strontium

Among the bivalent cations that can replace calcium in CaHA, strontium has attracted a remarkable interest for its possible biological role.

Strontium is one of the alkaline earth metals. It never occurs free in nature, because metallic Sr oxidises easily forming strontium oxide, which has a yellowish colour. The elements of group 2 of the periodic system, to which Sr belongs along with Ca and Mg, form divalent cations in biological fluids, and have varying degrees of protein binding in biological fluids like serum or plasma.

Radioactive Sr isotopes are dealt with only when they are used for physiological or diagnostic purposes. Some of the Sr radioisotopes can be used in medicine. They have been used as excellent tools for kinetic studies, substituting for Ca in kinetic investigations because the two metals behave very much alike in the human body, both having strong bone-seeking properties.

However, biological differences between the two elements exist, explicable in part by the larger size of the Sr molecule.

Toxic symptoms due to overdosing of Sr have not been reported in man. However, intravenous administration of high doses of Sr induces hypocalcaemia due to increased renal excretion of Ca.

The only stable Sr-containing chemical that is considered to be harmful to humans in

small amounts is strontium chromate, the toxicity being caused by the chromium which is a genotoxic carcinogen.

The amount of Sr in the skeleton is only 0.035 of its Ca content. Radiostrontium is cleared from the blood almost immediately after injection³⁴.

It is present in the mineral phase of the bone, especially at the regions of high metabolic turn-over, and its beneficial effect in the treatment of osteoporosis is well known. In vitro, strontium increases the number of osteoblasts and decreases the number and the activity of osteoclasts, whereas strontium administration reduces bone resorption and stimulates bone formation. Strontium can replace calcium in the HA structure in the whole range of composition. The solid solutions, which have been obtained by hydrothermal methods or by treatment at high temperatures, display a linear variation in the lattice parameters with composition, whereas different data are reported on the preferential substitution site of Sr for Ca in CaHA. A better understanding of the interaction of Sr with hydroxyapatite structure could provide useful information also for clarifying the biological role of Sr in the process of biomineralization of bone and related pathologies³⁵ even though the role of strontium in human pathology had attracted less attention than the other two important divalent metals, calcium and magnesium. However, there has been an increasing awareness of the biological role of strontium since the development of the drug strontium ranelate, which has recently been shown to reduce incidence of fractures in osteoporotic patients. In fact, strontium is a trace element that is found in calcareous rocks and ocean water; it is also a natural component of food and beverages but there is growing evidence that strontium has a beneficial effect on bone because of its ability to enhance bone volume and prevent bone loss. In line with its chemical analogy to calcium, strontium is a one seeking element and 98% of the total body Sr content can be found in the skeleton. Sr has become increasingly popular in the prevention and treatment of osteoporosis as a ranelate compound. Sr has been associated with improving postmenopausal osteoporosis by reducing bone resorption and increasing bone formation with an eventual effect of decreasing the risk of fractures. The currently available data indicate that strontium administration at low dose reduces bone resorption and increases bone formation, resulting in increased bone mass in normal ovariectomized animals. In vitro studies revealed that strontium ranelate (SR) has an anabolic and antiresorptive activity which leads to an increase in both the collagen and non-collagen protein synthesis, an

enhancement in pre-osteoblast differentiation, an inhibition in osteoclast differentiation, and a reduction in osteoclast function^{36,37}.

4.5 Non-stoichiometric and substituted HA

As pH values decrease, a calcium deficient HA is more likely to be formed^{38,39}. During aqueous precipitation, other species may be substituted in the structure or adsorbed onto the surface. Non-stoichiometric apatites are quite easy to synthesize, as they can be obtained by any precipitation method over a wide range of pH, temperature and concentration. Their composition and crystal characteristics are however more difficult to control. The most interesting of these apatites are HPO_4^{2-} and CO_3^{2-} containing apatites which are close to bone mineral. Although bone mineral has a variable composition, diverse apatites mimicking the evolution of bone mineral in young and old animals can be prepared. These apatites also show similar crystal shape and dimensions and their composition can be represented by a chemical formula analogous to that of bone mineral. Addition of more than one substitute element group can lead to a combination of an expansion and contraction of the unit cell²⁴. For example, carbonate causes a decrease in the a -axis⁴⁰ that could be counteracted by an increase from an acid phosphate group⁴¹. This reaction sequence is complicated by the ability of carbonate to substitute phosphate or hydroxide, the former being the more common. The addition of many of these chemical groups decreases the growth rate at low concentrations. Full substitution of fluoride for the hydroxyl ion removes lattice distortion, produces a more stable apatite and, thus, is able to drive precipitation to completion more easily⁴². Carbonate replaces phosphate in reactions containing fluoride and at high pH⁴³. All ionic sites of the apatite structure accept substitutes. It is generally the size of the ionic substitute that determines its incorporation in a given lattice. For Ca-P apatites, the monovalent anionic site substitution of OH^- by F^- , Cl^- , Br^- are known but I^- is not. These sites may also be occupied by carbonate ions, as in enamel and bone. The trivalent anionic phosphate sites may be occupied by bivalent or tetravalent ions like carbonate, HPO_4^{2-} , or silicate SiO_4^{4-} and many other trivalent ions such as vanadate or arsenate. These sites cannot accept vacancies, probably because the trivalent anions are quite large and vacancies would destabilize the lattice. Cationic sites can also be occupied by other divalent cations like Pb^{2+} , Mg^{2+} , Zn^{2+} , Cu^{2+} , Mn^{2+} , and by monovalent ions such as Na^+ and K^+ or trivalent

ions like La^{3+} . The cationic site can also accept vacancies: up to maximum of 2 sites out of the 10 existing in stoichiometric apatites. This property of the apatite structure allows the adaptation of its physical and chemical properties to many different calcified tissues, such as enamel, bone, dentine, and fish scales. However, in the preparation of pure HA, this property is a drawback because many ions from the solution can be incorporated, including toxic ions, or mineral ions with a positive biological activity. Thus the preparation of pure apatite has to take these properties into account.

The pH is an important factor in the precipitation of apatites as it determines the HPO_4^{2-} content of the final product. Stoichiometric apatites are generally obtained at alkaline pH and in boiling solutions. Anyway, stoichiometric hydroxyapatite does not form spontaneously in solution; their formation in highly supersaturated solutions is preceded by the precipitation of an amorphous phase possessing a Ca/P ratio much lower than that of apatite. This first precipitate then transforms into an apatite phase whose Ca/P ratio tends progressively towards that of HA.

Surface properties also play a role in the preparation of apatites. Generally, precipitated apatites have a very high specific surface area (between 50 and 90 m^2/g) that may adsorb many ions or constituents. In fact, adsorbed ions may eventually be incorporated into the lattice during growth or maturation of the crystals. Surface constituents generally slow down the maturation process and the evolution towards stoichiometry. The surface CO_3^{2-} and HPO_4^{2-} ions play a special role as they may alter the global stoichiometry of the solid. Precipitation has been performed in various conditions. The preparation of HA seems to be better achieved in Ca-rich solutions than in phosphate-rich solutions.

Following, the effect of the most relevant ionic substitutes on the chemico-physical properties of synthetic HA are described in more detail.

Carbonate (CO_3^{2-})

A key target of biomaterials research is the preparation of a synthetic carbonate containing hydroxyapatite (CHA) bone-substitute ceramic, that mimics the chemical composition of the natural hard tissue. The carbonate group can substitute both the hydroxyl and the phosphate ions, giving rise to the A-type and B-type carbonation respectively, so that a CHA substituted in both sites can be described as $\text{Ca}_{10-x/2}[(\text{PO}_4)_{6-x}(\text{CO}_3)_x][(\text{OH})_{2-2y}(\text{CO}_3)_y]$. The charge unbalance occurring when $(\text{CO}_3)^{2-}$

ions replace $(\text{PO}_4)^{3-}$ (B-type CHA) groups is primarily compensated by vacancies in Ca1 sites⁴². The exact position of the carbonate ions in the lattice of the HA has been elucidated only recently^{42,44}. By using full Rietveld refinement of the crystal structure of the synthetic calcium-deficient carbonated apatite two orientations of CO_3 triangles, sharing one of their edges, were found. They occupy randomly the adjacent faces of a PO_4 tetrahedron that are parallel to the c axis.

Carbonate substitution in type B carbonate apatites causes the following effects: a) decrease in a axis and increase in c -axis dimensions compared to CO_3^- free apatites; b) decrease in crystal size as shown by the broadening of the diffraction peaks in the XRD patterns and in TEM; c) increase in crystal strain as shown by the loss of resolution of the PO_4 absorption bands in the IR spectra; d) change in crystal morphology; e) greater solubility. As carbonation in B site increases the biomimetism of the synthetic apatite, it is advisable to orient the synthesis techniques for the incorporation of suitable amounts of carbonate ions, substituting the phosphate.

Magnesium (Mg^{2+})

As Mg^{2+} is smaller than Ca^{2+} (0.86 Å vs. 1.14 Å), the incorporation of magnesium affects the crystal structure of HA and the substitution cannot occur over the full concentration range. Progressive increase of the amount of incorporated magnesium, in fact, slightly reduces the cell parameters of the crystal and the average crystal radius; above a concentration limit of $\sim 0.15 \text{ Mg}^{2+}/\text{Ca}^{2+}$ the apatite structure likely collapses and the formation of other phases (typically TCP or amorphous calcium magnesium phosphates), that act as segregating phases for this ion, is observed³. The incorporation of Mg in synthetic apatites is very limited (maximum of about 4 wt% Mg) unless carbonate or fluoride ions are simultaneously incorporated with Mg. The amount of Mg incorporated in the apatite is proportional to the Mg concentration in the solution. The incorporation of Mg increased by the simultaneous incorporation of F^- or CO_3^{2-} . The limited incorporation of Mg is also observed in apatites prepared at high temperatures (above 900 °C) by solid state reaction. The presence of Mg in the apatite causes the following effects on its properties: a) decrease in a -axis dimension; b) decrease in crystallinity as shown in XRD patterns and IR spectra; c) increase in HPO_4^{2-} incorporation as shown by the higher β -TCP/HA ratio in sintered Mg-containing HA and d) increase in extent of dissolution. As

for B-carbonation, the incorporation of magnesium in synthetic HA is of great interest for the design of biomimetic bone substitutes^{45,46}.

Strontium (Sr²⁺)

Sr (ionic radius 0.12 nm) can replace Ca (ionic radius 0.099 nm) in the structure of HA over the whole range of composition, causing a linear expansion of the lattice constants. A detailed structural and morphological investigation carried out on HAs precipitated from aqueous solutions at different Sr concentrations demonstrated that relatively low Sr replacement of Ca induces a decrease in the coherent length of the perfect crystalline domains and disturbs the shape of the crystals, whereas the crystallinity, as well as the mean dimensions of the crystals, significantly increase at relatively high Sr content⁴⁷. Moreover, the results of the structural refinements indicate that Sr exhibits a slight preference for the M(II) site, as expected on the basis of its greater ionic radius than that of Ca, for most of the composition range, but at very low content it displays a modest preference for the smaller M(I) site. Destabilization of crystal structure by the larger Sr atom has been invoked to justify the significant increase in solubility with Sr content.

Iron (Fe²⁺/Fe³⁺)

The concentration of iron within hard tissue is low, indicating that iron can be present within the body without disturbing the apatite structure and hence the function of bone. Exposure of teeth to externally applied solutions containing iron leads to easier incorporation of iron. Though iron is one of the most essential elements in the human metabolism, its effect on the properties of DCPD and HAP has not been reported in the literature so far. Ming Jung et al.⁴⁸ investigated the local geometry of Fe²⁺/Fe³⁺ in Fe-doped hydroxyapatite and they find that the Ca(2) site is energetically favoured over Ca(1) sites for Fe²⁺ substitution and that sixfold coordination is most stable. However for nonstoichiometric Fe³⁺ substitution, the fourfold case is most stable at the Ca(1) site.

4.6 Natural polymer

While many polymers have been studied for medical applications, they share certain properties that are fundamental to their use as biomaterials. Their application in tissue engineering requires them to be biocompatible, nontoxic, and noninflammatory, which is

particularly important when designing degradable polymers as the degradation products too must meet these criteria. David Williams proposed the following definition: “*The biocompatibility of a scaffold or matrix for a tissue engineering product refers to the ability to perform as a substrate that will support the appropriate cellular activity, including the facilitation of molecular and mechanical signalling systems, in order to optimise tissue regeneration, without eliciting any undesirable local or systemic responses in the eventual host*”⁴⁹.

The use of degradable polymers is desirable because the need for surgical removal is obviated; however, care must be taken to ensure the compatibility of both intermediate and final degradation products, the timing of the degradation process, and how each of these affects the regenerative process.

Naturally derived degradable polymers, such as collagen, alginate or gelatin, have also been explored clinically because they are biocompatible, easily modified, and easily processed into various structures⁵⁰.

Starting from the consideration that natural bone consisting of an organic and an inorganic phase interacting among themselves, natural polymer has been added to ceramic phase in order to improve the biomimetic properties of the materials.

4.6.1 Collagen

Collagen, the most abundant protein in animals, is the major component of connective tissue; represents the major protein of tendons, ligaments, and the cornea; and forms the matrix of bones and teeth⁵¹.

The collagen molecule consists of three polypeptide chains, in each of which one has the repeating unit tri-peptide Gly-XY, where X and Y positions are frequently occupied by proline and hydroxyproline, two amino acids that locally affect the configuration of the chain because of the rigidity of their structures (Primary Structure). Each single chain, wrapped in a helix-clockwise (Secondary Structure), consists of a series of amino acid residues linked together by means of peptide bonds (Fig. 2) originated from the reaction between the amine function of an amino acid and the carboxylic function of the next.

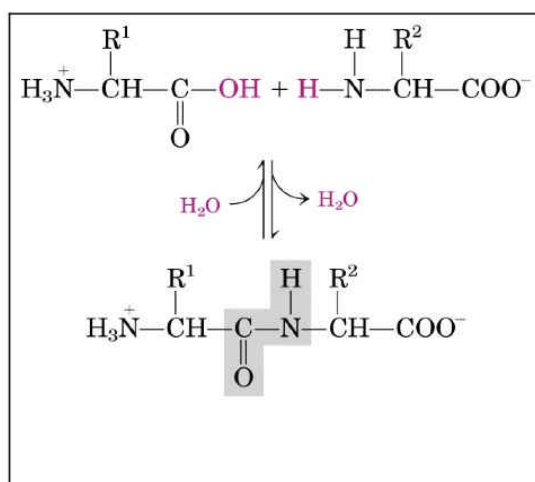


Fig. 2. Peptide bond

The partial double bond character of the peptide bond determines a limited freedom of rotation around it which, associated with the formation of interchain hydrogen bonds (a hydrogen bond every three amino acid residues, between the NH of glycine and the OR of the group C = O of the triplet close) and the complementary interactions between residues (R), make stable the structure of the α -helix typical of the collagen.

The three chains are wrapped in a right-handed super helix to form the characteristic coiled-coil structure (tropocollagen) (tertiary structure), stabilized by intra-and intermolecular interactions as well as the water of hydration; two molecules of water every three residues amino acid, arranged in a bridge to form H-bonds between the C=O of Gly-NH₂ and the residues X or Y.

In collagen type I, two of the three polypeptide chains, have identical amino acid composition, consisting of 1056 amino acid residues, while the third, has a different composition and comprises 1038 residues. The triple helix structure, involves 1014 residues for each of the three chains; the remaining residues, with a non-helical configuration, are called telopeptides.

The quaternary structure, characterized by the repetition of the structural unit in triple helix, packed to form a defined pattern representative of the basic element of the solid state, the microfibrilla (Fig. 3).

The collagen molecules are assembled into an almost-hexagonal geometry with a

interchain distance of about 1.3 nm which is considerably lower when the microfibrilla is dehydrated.

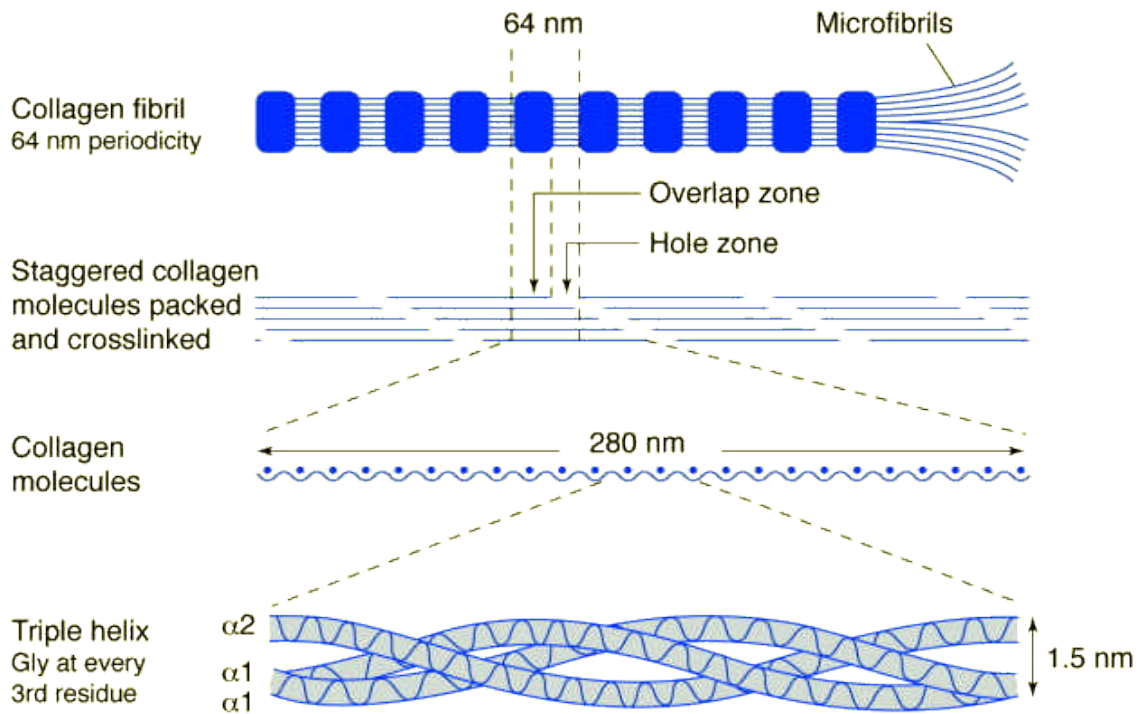


Fig. 3. Steps of collagen fibers assembling

The particular three-dimensional structure, makes the collagen a protein not soluble in water.

The amino acids present in the amino acid sequences of collagen contain amino ($-NH_2$), carboxyl ($-COOH$) and hydroxyl ($-OH$) groups which, together with the peptide bond of the main chain, represent the possible sites of chemical interaction of collagen molecule.

By the amino acid composition of the collagen protein depends its isoelectric point (pI) that is the value of pH where a particular molecule or surface carries no net electrical charge. For the collagen, this pH value is equal to 5.5⁵².

4.6.2 Alginate

Alginates is a natural polymer belonging to the family of carbohydrates that is extracted from brown algae (diatoms family). Alginate is a linear copolymer composed by the

repetition of two monomeric units that are (Fig. 4):

- D- mannuronic acid (M)
- L-guluronic acid (G)

linked by means of β -1.4 and 1.4 α -glycosidic bounds.

Alginates formed by binding with monovalent ions are generally water soluble, while salts with bivalent cations like Ca^{2+} form insoluble hydrogels, through an “egg box” model (Fig. 5); in the case of partial binding with bivalent ions, solubility in water is partially retained.

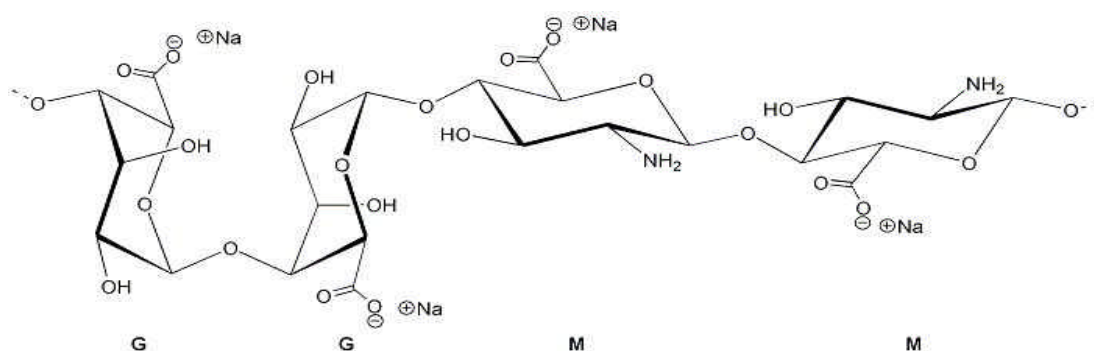


Fig. 4. Structural unit of Alginate

Calcium cross-linked alginate hydro-gels have been used in many biomedical applications, including cell transplantation and drug delivery⁵³.

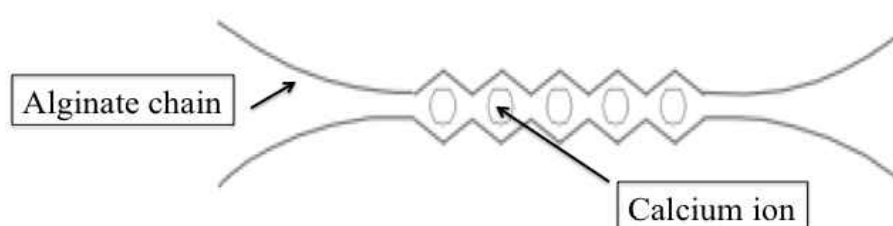


Fig. 5. “Egg box” model

There are various types of alginate that differ as a function of the ratio G/M and the length of the polymer chains.

Alginate used in this work for the production of composite materials described is characterized by G/M ratio equal to 65-70/35-30.

This ratio is important since alginate shows its ability to bind divalent ions, whereby it forms insoluble salts, in correspondence of the monomers of L-guluronic acid (G), according to the scheme of Fig. 6⁵⁴.

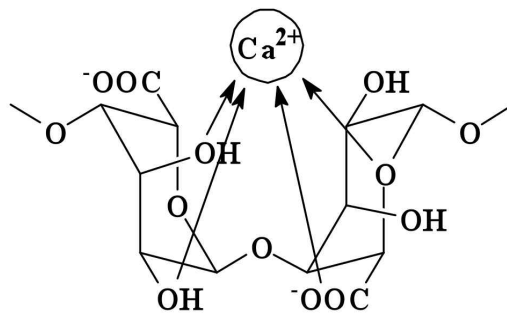


Fig. 6. Scheme of the bound between calcium ion and L-guluronic acid monomer

4.6.3 Gelatin

Gelatin is the product of thermal denaturation or disintegration of insoluble collagen with various molecular weights (MWs) and isoionic points (IEPs) depending on the source of collagen and the method of its manufacturing process of recovery from collagen⁵⁵. Gelatin is divided into two main types: Type A, which is derived from collagen of pig skin by acid pre-treatment with IEP of 7-9, and Type B, which is derived from collagen of beef hides or bones by liming (alkaline process) with IEP of 4.6-5.4. Type A gelatin (dry and ash free) contains 18.5 % nitrogen, but due to the loss of amide groups, Type B gelatin contains only about 18% nitrogen. Amino acid analysis of gelatin (Fig. 7) is variable, particularly for the minor constituents, depending on the raw material and process used, but proximate values by weight are: Gly 21%, Pro 12%, Hyp 12%, Glu 10 %, alanine (Ala) 9%, Arg 8%, Asp 6%, Lys 4%, serine (Ser) 4%, leucine (Leu) 3%, valine (Val) 2%, phenylalanine (Phe) 2%, threonine (Thr) 2%, isoleucine (Ile) 1%, hydroxylysine (Hyl) 1%, methionine (Met), His < 1% and Tyr < 0.5%.

References

1. Hench L. *J Am Ceram Soc.* **1998**, *81*, 1705.
2. Rey C. Calcium phosphates for medical applications. In (Amjad Z, ed): Calcium phosphates in biological and industrial systems. Kluwer Academic Publishers, Dordrecht, The Netherlands, 1998.
3. LeGeros R.Z, LeGeros JP. Phosphate minerals in human tissues. In (Nriagu JO, Moore PB, eds): Phosphate minerals. Springer-Verlag, New York, 1984.
4. Albee FH, Morrison HF. *Ann. Surg.* **1920**, *71*, 32.
5. McConnell D. *Arch. Oral. Biol.* **1965**, *10*, 421.
6. LeGeros RZ. *J. Dent. Res.* **1974**; *53*, 45.
7. Mathew M, Schroeder LW, Dickens B, Brown WE, *Acta Cryst.* **1997**, *B33*, 1325.
8. Mackay AL. *Acta Cryst.* **1953**, *6*, 743.
9. LeGeros RZ, Shannon IL. *J. Dent. Res.* **1979**, *58*, 2371.
10. LeGeros RZ, Miravite MA, Klein I. *J. Dent. Res.* **1974**, *53*, 117.
11. Nelson D. *J. Dent. Res.* **1981**; *60*, 1621.
12. LeGeros RZ. *Prog. Crystal Growth Charact.* **1981**, *4*, 1.
13. Rey C, Hina A, Amrah-Bouali S, Ranz X. Surface Reactions of Calcium-phosphate Bioceramics, Comparison with Bone Mineral Surface Chemistry. In (Ravaglioli A, ed): Fourth Euro-Ceramics. Symposium Bioceramics. Gruppo Editoriale Faenza Editrice SpA, Faenza, 1995.
14. Kawaguchi H, McKee MD, Okamoto H, Nanci A. *Cells and Materials* **1993**, *3*, 337.
15. Elliott JC, Wilson RM, Dowker SEP. Apatite Structures In: Advances in X-ray analysis. International Centre for Diffraction Data. 45, 2002, p 172.
16. Naray-Szabo S. *Kristallchem.* **1930**, *75*, 387.
17. Elliott JC, Mackie PE, Young RA. *Science* **1973**, *180*, 1055.
18. Elliot JC. Structure and Chemistry of the Apatites and Other Calcium Orthophosphates. Elsevier. Amsterdam, 1994.
19. LeGeros RZ, LeGeros JP, Trautz OR, Klein E. *Experienta* **1969**, *24*, 5.
20. McConnell D. Apatite. Its crystal chemistry, mineralogy, utilization and biologic occurrences. Springer, Vienna New York 1973, p. 68-80.
21. Eanes ED. *J. Dent. Res.* **1979**, *58*, 829.

22. Elliott JC. . *Clin. Orthop.* **1973**, *93*, 313.
23. LeGeros RZ, Bonel B, LeGeros R. *Calcif. Tiss Intl.* **1978**, *26*, 111.
24. LeGeros RZ, Miravite MA, Quiroigico GB, Curzon ME. *Calc. Tiss. Res.* **1977**, *22*, 362.
25. LeGeros RZ, Quiroigico G, LeGeros JP. *J. Dent. Res.* **1979**, *A58*, 168.
26. LeGeros RZ, Kerebel LM, Silverstone L. *J Dent. Res.* **1980**, *A59*, 523.
27. LeGeros RZ, Tung M. *J. Dent. Res.* **1982**, *61*, 232.
28. 73. Driessens FCM. *Bioceramics of Calcium Phosphates*. CRC Press, Boca Raton, FL, 1983, p. 1- 32.
29. Rey C, Renugopalakrishnan V, Collins B, Glimcher M. *Calcif. Tissue Intl.* **1991**, *49*, 251.
30. Le Geros RZ. Calcium phosphates in oral biology and medicine. In (Myers H, ed): *Monographs in oral science*, Basel: Karger AG Publishers, 1991, vol 15, p. 82-128.
31. Redey SA, Razzouk S, Rey C, Bernache-Assollant D, Leroy G, Nardin M, Cournot G. *J. Biomed. Mater. Res.* **1999**, *45*, 140.
32. Redey SA, Nardin M, Bernache-Assollant D, Rey C, Delannoy P, Sedel L, Marie PJ. *J. Biomed. Mater. Res.* **2000**, *50*, 353.
33. Bigi A, Foresti E, Gregoriani R, Ripamonti A, Roveri N, Shah JS. *Calcif. Tissue Intl.* **1992**, *50*, 439.
34. S.P. Nielsen. *Bone* **2004**, *35*, 583.
35. A. Bigi, E. Boanini, C. Capuccini, M. Gazzano. *Inorganica Chimica Acta.* **2007**, *360*, 009.
36. W. Xue, J.L. Moore, H.L. Hosick, S. Bose, A. Bandyopadhyay, W.W. Lu, K.M.C. Cheung, K.D.K. Luk, *Journal of Biomedical Materials Research Part A*, **2006**, *79*, 804.
37. Z.Y. Li, W.M. Lam, C. Yang, B. Xu, G.X. Ni, S.A. Abbah, K.M.C. Cheung, K.D.K. Luk, W.W. Lu. *Biomaterials* **2007**, *28*, 1452.
38. Silva VV, Lameiras FS, Domingues RZ. *Key Eng. Mater.* **2001**, *189,79*.
39. Raynaud S, Champion E, Bernache-Assollant D, Thomas P. *Biomaterials* **2002**, *23*, 1065.
40. LeGeros RZ. *Nature* **1965**, *206*, 403.

41. Young RA, Holcomb DW. *Calcif. Tiss. Intl.* **1984**, *26*, 60.
42. Ivanova TI, Frank-Kamenetskaya OV, Kol'tsov AB, Ugolkov VL. *J. Solid St. Chem.* **2001**, *160*, 340.
43. Shimoda S, Aoba T, Moreno EC, Miake Y. *J. Dent. Res.* **1990**, *69*, 1731.
44. Feki HE, Savariault JM, Salah AB, Jemal M. *Solid St. Sci.* **2000**, *2*, 577.
45. Percival M. *Appl. Nutr. Sci. Rep.* **1999**, *5*, 1.
46. Kim SR, Lee JH, Kim YT, Riu DH, Jung SJ, Lee YJ, Chung SC, Kim YH. *Biomaterials* **2003**, *24*, 1389.
47. E. Boanini et al. *Acta Biomaterialia* **2010**, *6*, 1882.
48. Jung M, Terra J, Rossi MA, Morales MA, Saitovitch EMB, Ellis DE. *Phys. Rev. B: Condens. Mater. Phys.* **2002**, *66*, 224107.
49. Williams, D. F. *Biomaterials* **2008**, *29*, 2941.
50. Molly S. Shoichet, *Macromolecules* **2010**, *43*, 581.
51. Maria G. Patino et al., *Journal of Oral Implantology*, **2002**, Vol. XXVIII/No. Five
52. B.D. Ratner, A. S. Hoffman, F. J. Schoen “An introduction to materials in medicine”.
53. A. Tampieri, M. Sandri, E. Landi, G. Celotti, N. Roveri, M. Mattioli-Belmonte, L. Virgili, F. Gabbanelli, G. Biagini, *Acta Biomaterialia* **2005**, *1*, 343.
54. G.T. Grant, E.R. Morris, D.A. Rees, P.J.C. Smith, D. Thom. *FEBS Letters* **1973**, *32*, 195,
55. Gomez-Guillen, MC, Perez-Mateos, M, Gomez-Estaca, J, Lopez-Caballero, E., Gimenez, B., & Montero, P. *Trends in Food Science & Technology*, **2009**, *20*, 3.
56. Mohanty, B., & Bohidar, H.B. *International Journal of Biological Macromolecules* **2005**, *36*, 39.
57. Selestina Gorgieva1 and Vanja Kokol. *Biomaterials: Applications for Nanomedicine*, ISBN 978-953-307-661-4.

PART II:
EXPERIMENTAL

CHAPTER 5

ANALYTICAL TECHNIQUE

5.1 X-Ray Diffraction (XRD)

X-ray diffraction is a non-destructive analytical technique which reveals information about the crystallographic structure, crystallite size, and preferred orientation in polycrystalline or powdered solid samples. This technique is based on observing the scattered intensity of an x-ray beam hitting a sample as a function of incident and scattered angle, polarization, and wavelength or energy.

Powder diffraction is commonly used to identify unknown substances, by comparing diffraction data against a database of Powder Diffraction Files (PDF) maintained by the International Centre for Diffraction Data (ICDD). It may also be used to characterize heterogeneous solid mixtures to determine relative abundance of crystalline compounds and, when coupled with lattice refinement techniques, such as Rietveld refinement, can provide structural information on unknown materials. Powder diffraction is also a common method for determining strains in crystalline materials.

The great advantages of the technique are:

- ▲ simplicity of sample preparation
- ▲ rapidity of measurement
- ▲ the ability to analyze mixed phases

When X-rays hit an atom, they make the electronic cloud move as does any electromagnetic wave. The movement of these charges reradiates waves with the same frequency (blurred slightly due to a variety of effects); this phenomenon is known as the Rayleigh scattering (or elastic scattering). The scattered waves can themselves be scattered but this secondary scattering is assumed to be negligible. A similar process occurs upon scattering neutron waves from the nuclei or by a coherent spin interaction

with an unpaired electron. These re-emitted wave fields interfere with each other either constructively or destructively (overlapping waves either add together to produce stronger peaks or subtract from each other to some degree), producing a diffraction pattern on a detector or film (Fig. 1).

The resulting wave interference pattern is the basis of diffraction analysis. X-ray wavelength is comparable with interatomic distances (~ 150 pm) and thus is an excellent probe for this length scale.

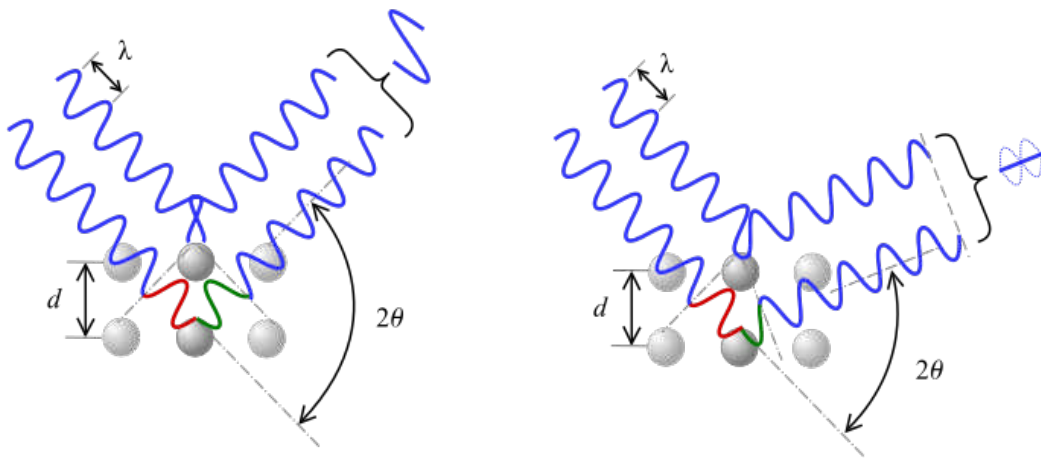


Fig. 1. Constructive and destructive interference in Rayleigh scattering of X rays

The interference is constructive when the phase shift is a multiple to $2d$; this condition can be expressed by Bragg's law:

$$n\lambda = 2d \cdot \sin \theta$$

where:

- n is an integer determined by the order of diffraction,
- λ is the wavelength of x-rays,
- d is the spacing between the planes in the atomic lattice,
- θ is the angle between the incident ray and the scattering planes.

Powder diffraction data are usually presented as a *diffractogram* in which the diffracted intensity I is shown as function either of the scattering angle 2θ .

The most widespread use of powder diffraction is in the identification and

characterisation of crystalline solids, each of which produces a distinctive diffraction pattern. Both the positions (corresponding to lattice spacings) and the relative intensity of the lines are indicative of a particular phase and material, providing a "fingerprint" for comparison. A multi-phase mixture will show more than one pattern superposed, allowing for determination of relative concentration.

Crystal structure

The crystal structure of a material or the arrangement of atoms in a crystal can be described in terms of its unit cell. The unit cell is a tiny box containing the spatial arrangement of atoms. The unit cells stacked in three-dimensional space describe the bulk arrangement of atoms of the crystal. The unit cell is given by its lattice parameters, the length of the cell edges and the angles between them, while the positions of the atoms inside the unit cell are described by the set of atomic positions (x_i, y_i, z_i) measured from a lattice point. The symmetry properties of the crystal are embodied in its space group. Crystal structure and symmetry play a role in determining many of its properties, such as cleavage, electronic band structure, and optical properties.

Although there are an infinite number of ways to specify a unit cell, for each crystal structure there is a conventional unit cell, which is chosen to display the full symmetry of the crystal. However, the conventional unit cell is not always the smallest possible choice. A **primitive unit cell** of a particular crystal structure is the smallest possible volume one can construct with the arrangement of atoms in the crystal such that, when stacked, completely fills the space. This primitive unit cell does not always display all the symmetries inherent in the crystal. In a unit cell each atom has an identical environment when stacked in 3 dimensional space. In a primitive cell, each atom may not have the same environment. The crystal structure consists of the same group of atoms, the basis, positioned around each and every lattice point. This group of atoms therefore repeats indefinitely in three dimensions according to the arrangement of one of the 14 Bravais lattices (Table 1).

The possible lattice centring are:

- ✓ P: Primitive centring, lattice points on the cell corners only;
- ✓ I: Body centred, one additional lattice point at the center of the cell;
- ✓ F: Face centred, one additional lattice point at centre of each of the faces of the

cell;

- ✓ A, C: Centred on a single face, one additional lattice point at the centre of one of the cell faces

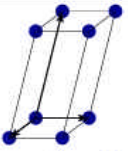
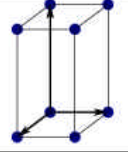
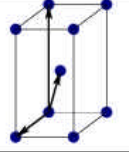
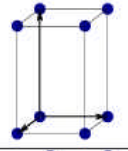
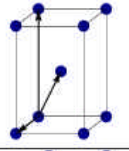
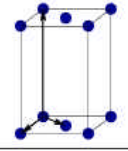
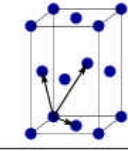
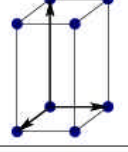
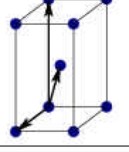
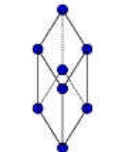
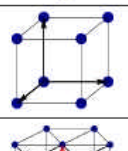
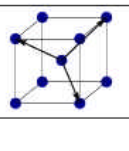
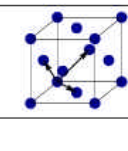
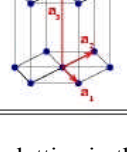
Bravais lattice	Parameters	Simple (P)	Volume centered (I)	Base centered (C)	Face centered (F)
Triclinic	$a_1 \neq a_2 \neq a_3$ $\alpha_{12} \neq \alpha_{23} \neq \alpha_{31}$				
Monoclinic	$a_1 \neq a_2 \neq a_3$ $\alpha_{23} = \alpha_{31} = 90^\circ$ $\alpha_{12} \neq 90^\circ$				
Orthorhombic	$a_1 \neq a_2 \neq a_3$ $\alpha_{12} = \alpha_{23} = \alpha_{31} = 90^\circ$				
Tetragonal	$a_1 = a_2 \neq a_3$ $\alpha_{12} = \alpha_{23} = \alpha_{31} = 90^\circ$				
Trigonal	$a_1 = a_2 = a_3$ $\alpha_{12} = \alpha_{23} = \alpha_{31} < 120^\circ$				
Cubic	$a_1 = a_2 = a_3$ $\alpha_{12} = \alpha_{23} = \alpha_{31} = 90^\circ$				
Hexagonal	$a_1 = a_2 \neq a_3$ $\alpha_{12} = 120^\circ$ $\alpha_{23} = \alpha_{31} = 90^\circ$				

Table 1. Bravais lattice in three-dimension

There are only seven possible crystal systems that atoms can pack together to produce an infinite 3D space lattice in such a way that each lattice point has an identical environment to that around every other lattice point. The simplest and most symmetric, the cubic (or isometric) system, has the symmetry of a cube. The other six systems, in order of decreasing symmetry, are hexagonal, tetragonal, rhombohedral (also known as trigonal), orthorhombic, monoclinic and triclinic.

When the crystal systems are combined with the various possible lattice centring, we arrive at the Bravais lattices. They describe the geometric arrangement of the lattice points, and thereby the translational symmetry of the crystal. In three dimensions, there are 14 unique Bravais lattices which are distinct from one another in the translational symmetry they contain.

Miller indices

Miller indices are an useful tool to describe the lattice plans, specifying their orientation with respect to the three axis of the unit cell. To calculate the Miller indices of a plane one has to determine the reciprocal of its intersections with the three axes in terms of fractions or multiples of the unit cells edges; these numbers are indicated in brackets, e.g. (hkl), which indicates an infinite number of equidistant parallel planes, so that the following expression is satisfied:

$$h(x/a) + k(y/b) + l(z/c) = n$$

where n indicates the plane position with respect to the origin.

In Fig. 2 some examples of the use of Miller indices are illustrated.

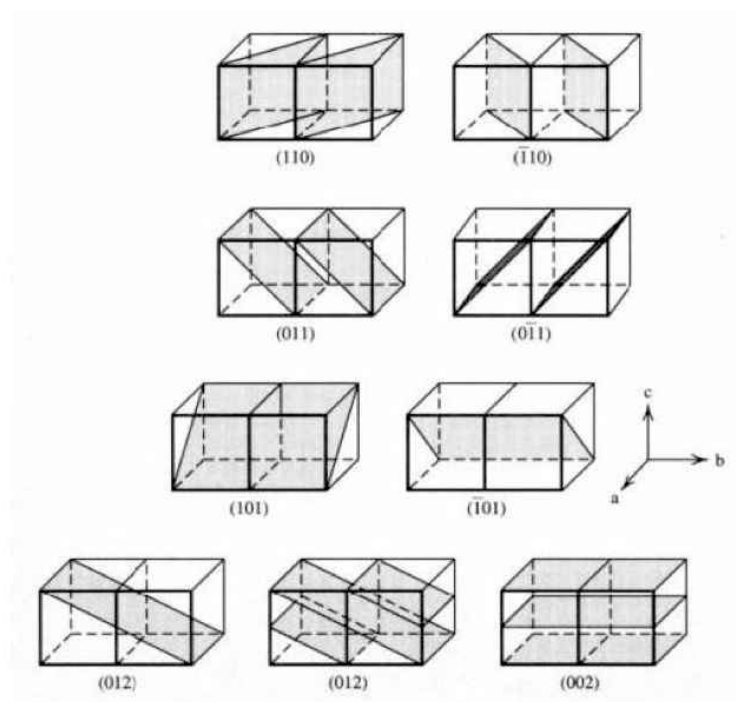


Fig. 2. Some examples of Miller planes

Crystallinity

In contrast to a crystalline pattern consisting of a series of sharp peaks, amorphous materials (liquids, glasses etc.) produce a broad background signal. Many polymers, organic molecules or inorganic glasses usually exhibit this kind of pattern, but often also inorganic nanostructured crystalline phases can contain also an amorphous fraction. XRD can be used to determine the degree of crystallinity by comparing the integrated intensity of the background pattern to that of the sharp peaks.

Size and Strain Broadening

There are many factors that determine the width B of a diffraction peak. These include:

1. instrumental factors
2. the presence of defects to the perfect lattice
3. differences in strain in different grains
4. the size of the crystallites

In powder samples, the strain can often be neglected, so that a simple formula can be applied to obtain the average size of the diffracting coherent domains, the Scherrer formula:

$$D = \frac{K\lambda}{B \cos \theta}$$

where:

D is the crystallite average size;

K is a form factor, usually taken as 0.9;

λ is the wavelength of the incident radiation;

B is the peak width corrected for the instrumental broadening;

θ is the diffraction angle.

5.1.1 Quantitative phase analysis: Reference Intensity Ratio (RIR) Method

The Reference Intensity Ratio (RIR) is a method used for quantitative analysis by powder diffraction. The reference intensity ratio (***RIR***) for a phase i is defined as:

$$RIR_i = \frac{I_i}{I_s}$$

where I_i is the intensity of the 100% peak of phase i , and I_s is the intensity of the 100% peak of a reference phase s , taken by convention to be α -Al₂O₃, corundum, in a 50:50 mixture by weight. Even without the addition of a known amount of an internal standard to a sample it is possible to compute the ratio of the weight fractions of any two phases in a mixture, provided their RIRs are known and assuming that the sum of all phases is 100 wt%.

5.1.2 Rietveld Method

The Rietveld method for structural refinement of powder diffraction data has been developed over the last four decades and has proved indispensable in solving crystal structures. The process involves minimising the difference between a crystallographic model and experimental data, via a least squares refinement; such intricate modelling of the height, width and position of Bragg reflections in an X-ray diffraction pattern can yield a lot of information about the crystal structure of a material.

5.2 Fourier-Transform Infrared Spectroscopy (FTIR)

Infrared spectroscopy (IR spectroscopy) is the subset of spectroscopy that deals with the infrared region of the electromagnetic spectrum. The infrared portion of the electromagnetic spectrum is divided into three regions; the near-, mid- and far- infrared, named for their relation to the visible spectrum.

The far- infrared, approximately 400-10 cm⁻¹ (1000-30 μ m), lying adjacent to the microwave region, has low energy and may be used for rotational spectroscopy. The mid-infrared, approximately 4000-400 cm⁻¹ (30-1.4 μ m) may be used to study the fundamental vibrations and associated rotational-vibrational structure. The higher energy near-IR, approximately 14000-4000 cm⁻¹ (1.4-0.8 μ m) can excite overtone or harmonic vibrations. Infrared spectroscopy exploits the fact that molecules have specific frequencies at which they rotate or vibrate corresponding to discrete energy levels (Fig. 3). These resonant frequencies are determined by the shape of the molecular potential energy surfaces the masses of the atoms and, by the coupling of vibrational and electronic interactions in the

molecule. Thus, the resonant frequencies can be in a first approach related to the strength of the bond, and the mass of the atoms at either end of it. Thus, the frequency of the vibrations can be associated with a particular bond type and can be used for the characterization of very complex mixtures.

The infrared spectra of a sample is collected by passing a beam of infrared light through the sample. Examination of the transmitted light reveals how much energy was absorbed at each wavelength. This can be done with a monochromatic beam, which changes in wavelength over time, or by using a Fourier transform instrument to measure all wavelengths at once. From this, a transmittance or absorbance spectrum can be produced, showing at which IR wavelengths the sample absorbs. Analysis of these absorption characteristics reveals details about the molecular structure of the sample.

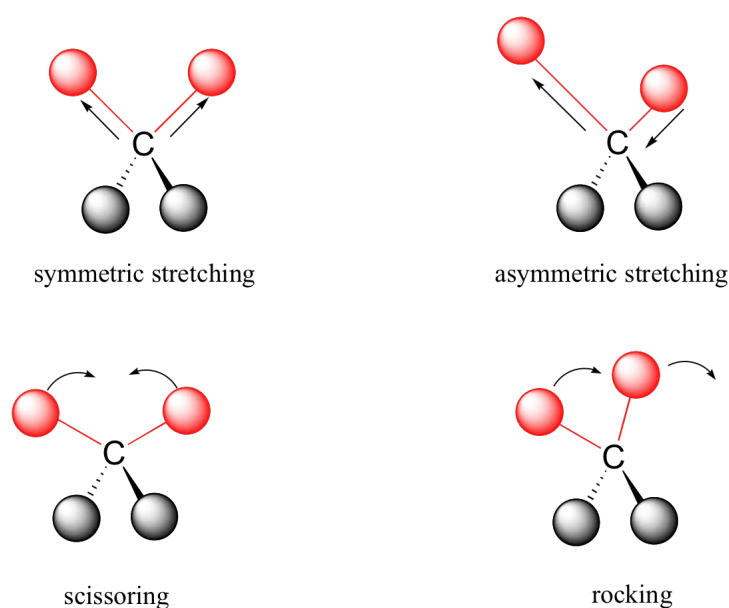


Fig. 3. Possible vibrations detected by infrared spectroscopy

The method employed for sample preparation is to grind a quantity of the sample with potassium bromide finely (to remove scattering effects from large crystals), which is used also as a reference. This powder mixture is then crushed in a mechanical die press to form a translucent pellet through which the beam of the spectrometer can pass. A reference is used for two reasons:

1. This prevents fluctuations in the output of the source affecting the data;

2. This allows the effects of the solvent to be cancelled out (the reference is usually pure solvent)

The equipment employed in the present work was a Thermo Nicolet-Avatar 320 FT-IR

5.3 Inductively Coupled Plasma Atomic Emission Spectroscopy (ICP- AES)

ICP-AES, also referred to as Inductively Coupled Plasma Optical Emission Spectrometry (ICP-OES), is a type of emission spectroscopy that uses a plasma (e.g. inductively coupled plasma) to produce excited atoms that emit electromagnetic radiation at a wavelength characteristic of a particular element. The intensity of the radiation is proportional to the concentration of the element, which is obtained through a previous calibration obtained with opportune standard solutions. An inductively coupled plasma (ICP) for spectrometry is sustained in a torch that consists of three concentric tubes, usually made of quartz. The end of this torch is placed inside an induction coil supplied with a radio-frequency electric current. A flow of argon gas is introduced between the two outermost tubes of the torch and an electrical spark is applied for a short time to introduce free electrons into the gas stream. These electrons interact with the radio-frequency magnetic field of the induction coil and are accelerated first in one direction, then the other, as the field changes at high frequency. The accelerated electrons collide with argon atoms, and sometimes a collision causes an argon atom to part with one of its electrons. The released electron is in turn accelerated by the rapidly- changing magnetic field. The process continues until the rate of release of new electrons in collisions is balanced by the rate of recombination of electrons with argon ions (atoms that have lost an electron). This produces a ‘fireball’ that consists mostly of argon atoms with a rather small fraction of free electrons and argon ions. The samples to be analyzed are firstly solubilized and then introduced into the hot region through an atomizer. The temperature of the plasma is very high, of the order of 10.000 K, so that the atomization of the sample is nearly complete, improving the accuracy of the analysis. Moreover, the carrier gas is inert (usually argon), so preventing the formation of oxides. As a droplet of atomized sample enters the central channel of the ICP, it evaporates and any solids that were dissolved in the liquid vaporize and then break down into atoms. At the temperatures prevailing in the plasma a significant proportion of the atoms of many chemical elements are ionized, each atom

losing its most loosely-bound electron to form a singly charged ion.

The equipment employed in the present work was a Liberty 200, Varian, Clayton South, Australia.

5.4 Scanning Electron Microscopy (SEM)

The scanning electron microscope (SEM) is a type of electron microscope that creates various images by focusing a high energy beam of electrons onto the surface of a sample and detecting signals from the interaction of the incident electrons with the sample's surface. The types of signals gathered in a SEM vary and can include secondary electrons, characteristic x-rays, and back scattered electrons (Fig. 4). In a SEM, these signals come not only from the primary beam impinging upon the sample, but from other interactions within the sample near the surface.

The SEM is capable of producing high-resolution images of a sample surface in its primary use mode, secondary electron imaging. Due to the manner in which this image is created, SEM images have great depth of field yielding a characteristic three-dimensional appearance useful for understanding the surface structure of a sample. This great depth of field and the wide range of magnifications are the most familiar imaging mode for specimens in the SEM.

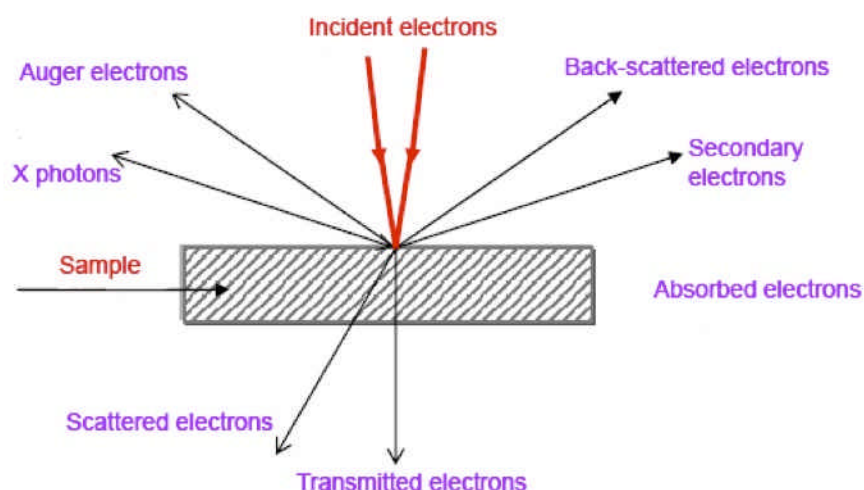


Fig. 4. Signals produced by the interaction of the electron beam with the sample.

Characteristic X-rays are emitted when the primary beam causes the ejection of inner shell electrons from the sample and are used to tell the elemental composition of the sample. The back-scattered electrons emitted from the sample may be used alone to form an image or in conjunction with the characteristic X-rays as atomic number contrast clues to the elemental composition of the sample.

In a typical SEM, thermo-ionic electrons are emitted from a tungsten cathode and are accelerated towards an anode (Fig. 5).

Tungsten is used because it has the highest melting point and lowest vapour pressure of all metals, thereby allowing it to be heated for electron emission. The electron beam, which typically has an energy ranging from a few hundred eV to 100 keV, is focused by one or two condenser lenses into a beam with a very fine focal spot sized 0.4 nm to 5 nm. The beam passes through pairs of scanning coils or pairs of deflector plates in the electron optical column, typically in the objective lens, which deflect the beam horizontally and vertically so that it scans in a raster fashion over a rectangular area of the sample surface. When the primary electron beam interacts with the sample, the electrons lose energy by repeated scattering and absorption within a teardrop-shaped volume of the specimen known as the interaction volume, which extends from less than 100 nm to around 5 μm into the surface. The size of the interaction volume depends on the electrons's landing energy, the atomic number of the specimen and the specimen's density. The energy exchange between the electron beam and the sample results in the emission of electrons and electromagnetic radiation, which can be detected to produce an image, as described below.

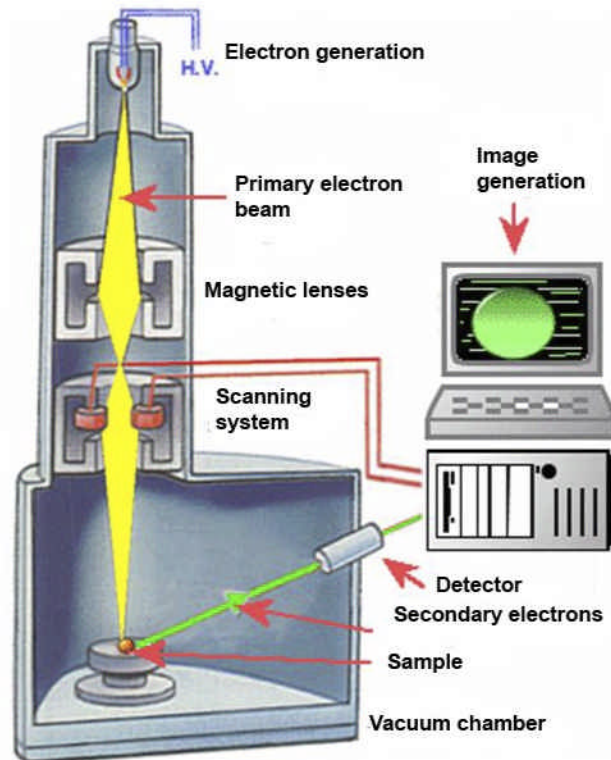


Fig. 5. Scheme of a Scanning Electron Microscope.

Detection of secondary electrons

The most common imaging mode monitors low energy (< 50 eV) secondary electrons. Due to their low energy, these electrons originate within a few nanometers from the surface. The electrons are detected by a scintillator-photomultiplier device and the resulting signal is rendered into a two-dimensional intensity distribution that can be viewed and saved as a digital image. This process relies on a raster-scanned primary beam. The brightness of the signal depends on the number of secondary electrons reaching the detector. If the beam enters the sample perpendicular to the surface, then the activated region is uniform about the axis of the beam and a certain number of electrons "escape" from within the sample. As the angle of incidence increases, the "escape" distance of one side of the beam will decrease, and more secondary electrons will be emitted. Thus steep surfaces and edges tend to be brighter than flat surfaces, which results in images with a well-defined, three-dimensional appearance. Using this technique, resolutions less than 100 nm are possible.

Resolution of the SEM

The spatial resolution of the SEM depends on the size of the electron spot, which in turn depends on both the wavelength of the electrons and the magnetic electron-optical system which produces the scanning beam. The resolution is also limited by the size of the interaction volume, or the extent to which the material interacts with the electron beam. The spot size and the interaction volume both might be large compared to the distances between atoms, so the resolution of the SEM is not high enough to image individual atoms, as is possible in the shorter wavelength (i.e. higher energy) transmission electron microscope (TEM). The SEM has compensating advantages, though, including the ability to image a comparatively large area of the specimen; the ability to image bulk materials (not just thin films or foils); and the variety of analytical modes available for measuring the composition and nature of the specimen.

The equipment employed in the present work was a Stereoscan 360, Leica, Cambridge, UK.

Energy dispersive X-ray spectroscopy (EDS)

EDS (or EDX) is an analytical technique, coupled with the SEM equipment, used predominantly for the elemental analysis or chemical characterization of a specimen. Being a type of spectroscopy, it relies on the investigation of a sample through interactions between electromagnetic radiation and matter, analyzing X-rays emitted by the matter in this particular case. Its characterization capabilities are due in large part to the fundamental principle that each element of the periodic table has a unique atomic structure allowing X-rays that are characteristic of an element's atomic structure to be uniquely distinguished from each other. To stimulate the emission of characteristic X-rays from a specimen, an high energy beam of charged particles such as electrons or protons, or a beam of X-rays, is focused into the sample to be characterized. At rest, an atom within the sample contains ground state (or unexcited) electrons situated in discrete energy levels or electron shells bound to the nucleus. The incident beam may excite an electron in an inner shell, prompting its ejection and resulting in the formation of an electron hole within the atom's electronic structure. An electron from an outer, higher-energy shell then fills the hole, and the difference in energy between the higher-energy shell and the lower energy shell is released in the form of an X-ray. The X-ray released by

the electron is then detected and analyzed by the energy dispersive spectrometer. These X-rays are characteristic of the difference in energy between the two shells, and of the atomic structure of the elements from which they were emitted.

A detector is used to convert X-ray energy into voltage signals; this information is sent to a pulse processor, which measures the signals and passes them onto an analyzer for data display and analysis. The equipment employed in the present work was an INCA 300, Oxford Instruments, UK.

5.5 Thermogravimetric and Thermoanalytical analyses (TG-DTA)

Thermogravimetric Analysis or TGA is a type of testing that is performed on samples to determine changes in weight in relation to change in temperature. Such analysis relies on a high degree of precision in three measurements: weight, temperature, and temperature change. As many weight loss curves look similar, the weight loss curve may require transformation before results may be interpreted. A derivative weight loss curve can be used to tell the point at which weight loss is most apparent. The analyzer usually consists of a high-precision balance with a pan loaded with the sample. The sample is placed in a small electrically heated oven with a thermocouple to accurately measure the temperature. The atmosphere may be purged with an inert gas to prevent oxidation or other undesired reactions. A computer is used to control the instrument. Analysis is carried out by raising the temperature gradually and plotting weight against temperature. After the data is obtained, curve smoothing and other operations may be done such as to find the exact points of inflection.

Differential thermal analysis (or **DTA**) is a thermoanalytic technique. In DTA, the material under study and an inert reference (Al_2O_3 in our case) are heated (or cooled) under identical conditions, while recording any temperature difference between sample and reference. This differential temperature is then plotted against time, or against temperature (DTA curve or thermogram). Changes in the sample, either exothermic or endothermic, can be detected relative to the inert reference. Thus, a DTA curve provides data on the transformations that have occurred, such as phase transitions, glass transitions, crystallization, melting and sublimation. The area under a DTA peak can be to the enthalpy change and it is not affected by the heat capacity of the sample. A DTA

apparatus consists of a sample holder comprising thermocouples, sample containers and a ceramic or metallic block; a furnace; a temperature programmer; and a recording system. The key feature is the existence of two thermocouples connected to a voltmeter. One thermocouple is placed in the inert reference material, while the other is placed in a sample of the material under study. As the temperature is increased, there will be a brief deflection of the voltmeter if the sample is undergoing a phase transition. This occurs because the input of heat will raise the temperature of the inert substance, but be incorporated as latent heat in the material changing phase.

The equipment employed in the present work was a Netzsch Gerätebau Jupiter STA (Simultaneous Thermal Analysis) 449C, Selb, Germany.

5.6 Powder Analysis

5.6.1 Specific surface area

Specific surface area is a material property of solids which measures the total surface area per unit of mass, solid or bulk volume, or cross-sectional area. It is a derived scientific value that can be used to determine the type and properties of a material (e.g. soil). It is defined either by surface area divided by mass (with units of m^2/kg), or surface area divided by the volume (units of m^2/m^3 or m^{-1}). The SSA can be measured by adsorption using the BET isotherm. This has the advantage of measuring the surface of fine structures and deep texture on the particles. BET theory is a well-known rule for the physical adsorption of gas molecules on a solid surface, that is basis for an important analysis technique for the measurement of the specific surface area of a material. In 1938, Stephen Brunauer, Paul Hugh Emmett, and Edward Teller published an article about the BET theory in a journal for the first time; “BET” consists of the first initials of their family names. The concept of the theory is an extension of the Langmuir theory, which is a theory for monolayer molecular adsorption, to multilayer adsorption with the following hypotheses: (a) gas molecules physically adsorb on a solid in layers infinitely; (b) there is no interaction between each adsorption layer; and (c) the Langmuir theory can be applied to each layer. The resulting BET equation is expressed by (1):

$$\frac{1}{\lambda[(P_0 - P) - 1]} = \frac{c - 1}{v_m c} \left(\frac{P}{P_0} \right) + \frac{1}{v_m c}$$

P and P_0 are the equilibrium and the saturation pressure of adsorbates at the temperature of adsorption, v is the adsorbed gas quantity (for example, in volume units), and v_m is the monolayer adsorbed gas quantity. c is the BET constant, which is expressed by (2):

$$c = \exp\left(\frac{E_1 - E_L}{RT}\right)$$

E_1 is the heat of adsorption for the first layer, and E_L is that for the second and higher layers and is equal to the heat of liquefaction. Equation (1) is an adsorption isotherm and can be plotted as a straight line with $1 / v[(P_0 / P) - 1]$ on the y-axis and $\phi = P / P_0$ on the x-axis according to experimental results. This plot is called a **BET plot**. The linear relationship of this equation is maintained only in the range of $0.05 < P/P_0 < 0.35$. The value of the slope A and the y-intercept I of the line are used to calculate the monolayer adsorbed gas quantity v_m and the BET constant c .

The following equations can be used:

$$v_m = \frac{1}{A + I}$$

$$c = 1 + \frac{A}{I}$$

The BET method is widely used in surface science for the calculation of surface areas of solids by physical adsorption of gas molecules.

A total surface area S_{total} and a specific surface area S are evaluated by the following equations:

$$S_{BET, total} = \frac{v_m N s}{V}$$

$$S_{BET} = \frac{S_{total}}{a}$$

where N is Avogadro's number, s is the adsorption cross section, V is the molar volume of adsorbent gas and a is the molar weight of adsorbed species. The equipment adopted in the present work was a Sorpty 1750, Carlo Erba, Milano, Italy.

5.6.2 Granulometric Analysis

The behaviour of particles which, subjected to gravity force, drop and sediment when immersed in a liquid medium (generally water), is a very common method to determine particles dimensions. It is a versatile method because it is efficient for a huge range of materials and because it permits to analyze dimensions lower than microns.

The most simple case occurs when spherical particles sediment with laminar motion with a constant speed.

The relationship between drop speed and particles dimensions is defined by the **Stoke's law**:

$$D^2 = 18 \nu \eta / (\rho - \rho_0) g$$

Where:

D = diameter of spherical particles (cm)

ν = drop speed (cm/sec)

η = viscosity of the fluid ($\text{g cm}^{-1} \text{sec}^{-1}$)

ρ = density of the sedimenting material (g/cm^3)

ρ_0 = density of the fluid (g/cm^3)

g = acceleration of gravity ($= 981 \text{ cm/sec}^2$)

The analysis is based on the Stoke's law with the hypotheses that the particles are spherical and that the drop speed is in function only of their dimensions. The suspension

is stirred by a magnetic stirrer and poured in the cell of analysis through a peristaltic pump, providing for a continuous refill of the cell with the suspension. The refill stops when the sedimentation begins. The apparatus uses an X-ray beam to test the transparency of the suspension.

So, as soon as the analysis begins, the beam measures the transparency in the lowest part of the cell, and then the cell is moved upward, in order to reduce the sedimentation speed of the finest particles (slow sedimentation). This kind of analysis is easy for the instrument employed, but the suspension need to be very carefully prepared, because the powder needs to be disaggregated and the suspension stable. The equipment adopted is a Sedigraph 5100, Micromeritics, Norcross, GA.

5.7 Mechanical properties

Compressive strength is the capacity of a material or structure to withstand axially directed pushing forces. It provides data (or a plot) of force vs deformation for the conditions of the test method. When the limit of compressive strength is reached, brittle materials are crushed. By definition, the compressive strength of a material is that value of uniaxial compressive stretch reached when the material fails completely.

The easier-to-handle transverse test is used to determine the compressive strength of ceramics materials. The specimen is loaded up to failure.

For ceramic specimens the test is performed on cylindrical porous specimens, 12 mm x 18 mm (diameter x height), with a crosshead speed of 2 mm/min. To avoid stress concentration, a thin paper foil was inserted between each end of the specimen and the loading plates of the machine.

The compressive strength was calculated from the maximum load registered during the test (P_{\max}) divided by the original area (A).

$$\sigma_c = P_{\max} / A$$

The maximum stress at fracture is commonly referred to as fracture strength. Five specimens were tested for each batch.

Apparatus for ceramics specimens: Zwick/Roell Z050 machine (ULM, Germany).

Young's Modulus

Young's Modulus of Elasticity is defined as the ratio of stress (force per unit area) to corresponding strain (deformation) in a material under tension or compression.

Elastic modulus is sometimes called Young's modulus after Thomas Young who published the concept back in 1807. An elastic modulus (E) can be determined for any solid material and represents a constant ratio of stress and strain (a stiffness):

$$E = \sigma/\varepsilon$$

where σ = stress and ε = strain.

A material is elastic if it is able to return to its original shape or size immediately after being stretched or squeezed. Almost all materials are elastic to some degree as long as the applied load does not cause it to deform permanently. Thus, the "flexibility" of any object or structure depends on its elastic modulus and geometric shape. A static method to test Young's modulus of a material basically consists in measuring the slope of its stress-strain plot within the elastic range (as shown in Fig. 6).

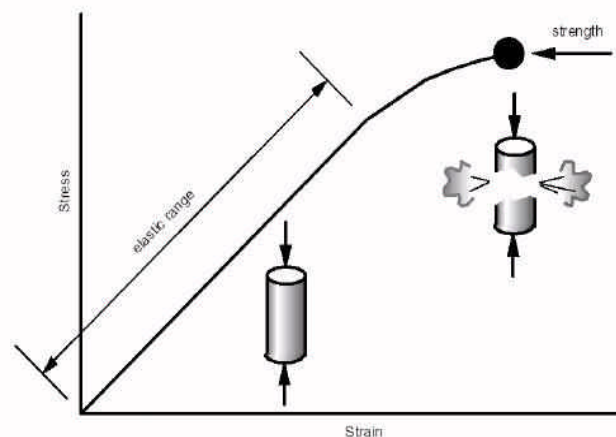


Fig. 6. Stress-Strain Plot Showing the Elastic Range

The initial straight-line portion of the curve is the elastic range. If the material is loaded to any value of stress in this part of the curve, it will return to its original shape. Thus, the

modulus of elasticity is the slope of this part of the curve. It is important to remember that a measure of a material's modulus of elasticity is not a measure of strength.

Strength is the stress needed to break or rupture a material (as illustrated in Fig. 6), whereas elasticity is a measure of how well a material returns to its original shape and size.

5.8 Magnetic measurement

5.8.1 Magnetic Susceptibility

Based on their magnetic properties, all substances can be classified into one of three groups, those attracted by a strong magnetic field, known as *paramagnetic*, those repelled, designated *diamagnetic*, and, finally, the most recognised class, *ferromagnetic*, unique in their ability to retain their own magnetic field. Ferromagnets are able to retain a permanent magnetic field since their free electrons are in close proximity and remain aligned even after the external magnetic field is removed. Unlike the ferromagnets, the magnetic properties of the diamagnetic or paramagnetic materials could only be observed and measured when these samples are held within a magnetic field applied externally.

In electromagnetism the magnetic susceptibility χ is defined as the ratio of the intensity of magnetism induced in a substance to the magnetising force or intensity of field to which it is subject.

The volume susceptibility χ_v is defined by:

$$\chi_v = I/H$$

Where:

I = Intensity of magnetism produced in a substance

H= Intensity of magnetic field applied externally

The Mass Susceptibility (χ_g) is defined by:

$$\chi_g = \chi_v / d$$

Where:

d = Density of substances

The nature of the electrons within a sample determines the magnetic properties. The

magnetic forces that are generated are more less neutralised when two electrons become paired. Free unpaired electrons give rise to magnetic forces which are attracted to a strong magnetic field, and the strength of these attractive forces are in direct proportion to the number of free electrons. The presence of free electrons results in materials being classified as paramagnetic and the lack of them results in a compounds being diamagnetic. Crystallinity, chemical reactions, oxidation states, and virtually anything that can alter the electronic configuration of a compound, may also change the magnetic properties. Analogous to spectral measurements, magnetic susceptibility measurements are both qualitative and quantitative in nature.

Magnetic Susceptibility values of the powders at low field was measured at $34 \times 10^{-4} \text{ N A}^{-1} \text{ m}^{-1}$ via a YSZ 01C/02C Susceptometer (Sartorius Mechatronics, Italy)

In this procedure, the interaction between a permanent magnet and the weight being tested is determined as a weight using a high-resolution mass comparator. Taking into account the known properties of the test magnet, the distance of the weight from the test magnet and the weight geometry, the desired magnetic quantities of the weight can be calculated. At the core of the susceptometer is a Sartorius mass comparator with a resolution of $10\mu\text{g}$ or $1\mu\text{g}$. This is securely mounted on a stable base plate and surrounded by a housing that is resistant to air and temperature changes and holds the loading platform onto which samples are placed.

Susceptometer is used to determine both the magnetic susceptibility and the permanent magnetization of weakly-magnetized weights through measurement of the force exerted on a mass standard in the magnetic field gradient of a strong permanent magnet. The direction that magnetic field moves indicates whether the sample is paramagnetic or diamagnetic which is shown by a plus or minus indication on the display balance.

CHAPTER 6

MAGNETIC Fe²⁺/Fe³⁺ DOPED HYDROXYAPATITE (FeHA)

The first step in the development of a bone-like biomaterial concerns the synthesis of a powder having chemical and physical properties as much as possible corresponding to the ones of the inorganic component of bone tissue. Thus, the above-mentioned powder should be biomimetic and suitable for the production of devices able to integrate with living tissues and, simultaneously, stimulate new bone growth.

A synthesis of a magnetic biomimetic apatitic powder has been optimized in order to introduce iron ions into the cell structure, rising higher bioactivity and bioreabsorbibility in comparison to stoichiometric hydroxyapatite.

Numerous stoichiometric HA synthesis techniques have been developed¹. The most commonly used are the wet method in aqueous solution by precipitation^{2,3}, or the technique of hydrolysis of acid calcium phosphate salts^{4,5}. The former is a wet neutralization reaction that allows to precipitate pure apatites with controlled crystallinity degree in function of nucleation temperature and ripening.

To prepare a stoichiometric hydroxyapatite calcium hydroxide and phosphoric acid was used as reagents in suitable stoichiometric ratio according to the following reaction:



The synthesis process above described was also used to develop magnetic FeHA powder. For this purpose both iron species (Fe²⁺ and Fe³⁺) were introduced in form of soluble iron salts in the synthesis process; in this way the substitution of specific Ca crystallographic sites with a specific coordination⁶ by iron ions generates in the apatitic lattice two different sublattices whose interaction induce superparamagnetic behaviour⁷.

With this aim a synthetic procedure to obtain a magnetic (Fe²⁺/Fe³⁺)-lattice substituted HA has been developed and optimized, minimizing the formation of magnetite as secondary phase.

6.1 Synthesis of FeHA powder

The synthesis of magnetic FeHA powders was carried out by employing calcium hydroxide (Ca(OH)₂, 95wt% pure) and phosphoric acid (H₃PO₄, 85wt% pure), with the addition of iron(III) chloride hexahydrate (FeCl₃·6H₂O, 97wt% pure) and iron(II) chloride tetrahydrate (FeCl₂·4H₂O, ≥ 99wt% pure), as sources of Fe³⁺ and Fe²⁺ ions respectively, in aqueous solution; all reactants were provided by Sigma-Aldrich (S. Louis, MO, USA). The amount of reactants was set up in order to keep the calcium/phosphorus ratio equal to 1.667, so that a competition between Ca²⁺, PO₄³⁻ and the substituting ions (Fe³⁺ and Fe²⁺) could be established. The total amounts of Fe ions with respect to Ca ions were adjusted so as to obtain Fe/Ca=20 mol%.

In details a phosphoric acid (44.40 g in 300 ml H₂O) solution was added dropwise into a basic suspension of calcium hydroxide (50 g in 400 ml H₂O) containing Fe ions, over a period of 2 h, under constant heating and stirring. To study the relationship between the synthesis parameters and physicochemical properties of the powders, the process was carried out in the temperature range 25-60 °C and pH decreased from 12 to 5 during neutralization.

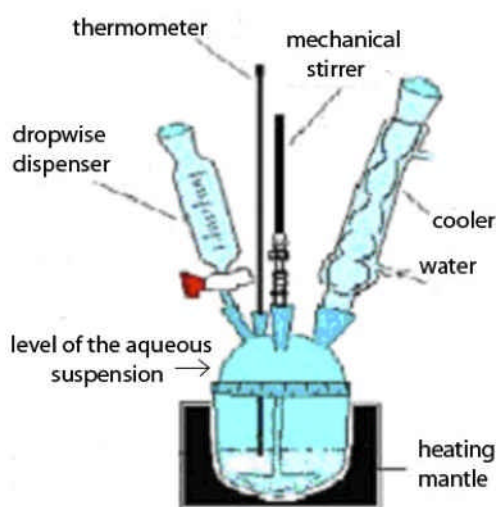


Fig. 1. Equipment for the synthesis of FeHA powder

During synthesis, a brownish precipitate formed; after the dripping of the phosphate solution was completed, the precipitate was left to ripen and decant in the mother liquor for 24 hours (Fig. 1), then the supernatant was eliminated and the cake-like product was washed three times in 1 litre of distilled water and centrifuged. The product was freeze-dried and sieved under 150 μm .

To obtain a magnetic iron doped hydroxyapatite, three synthesis methods based on the Fe source added to calcium hydroxide suspension have been developed and investigated starting by the synthesis method above described.

Method 1: reductive process

$\text{FeCl}_3 \cdot 6\text{H}_2\text{O}$ (35.72 g in 150 ml H_2O) was used as a source of Fe^{3+} ions to substitute Ca^{2+} during the nucleation of HA, carried out at 40 $^\circ\text{C}$. A reductive process was subsequently applied on the freeze-dried and sieved material to convert some of the Fe^{3+} into Fe^{2+} ions and to maintain both species in the HA lattice. The process was performed at 300 $^\circ\text{C}$ in a closed autoclave (Parr, Alloy C276) for 1 h under continuous stirring. A gas mixture Ar/H_2 (96:4) was used as a reductive atmosphere at different pressures: 0.1 Mpa (sample A), 1.9 MPa (sample B) and 2.8 MPa (sample C). The features of the obtained samples are reported in Table I (p. 104)

Method 2: oxidative process

$\text{FeCl}_2 \cdot 4\text{H}_2\text{O}$ (25.48 g in 150 ml H_2O) was used as a source of Fe^{2+} ions and HA was synthesized, exploiting the spontaneous oxidation of Fe^{2+} ions, due to the reaction environment. Different synthesis temperatures were tested: 25, 40 and 60 $^\circ\text{C}$; the respective products were coded D, E and F (see Table II p.104).

Method 3: simultaneous addition

$\text{FeCl}_2 \cdot 4\text{H}_2\text{O}$ (12.74 g in 75 ml H_2O) and $\text{FeCl}_3 \cdot 6\text{H}_2\text{O}$ (17.86 g in 75 ml H_2O) were added together to calcium hydroxide suspension as sources of Fe^{2+} and Fe^{3+} ions during the neutralization process. Different synthesis temperatures were investigated (25, 40 and 60 $^\circ\text{C}$) and the synthesis products identified as samples G, H (Fig. 2) and K, respectively (Table III p.104).

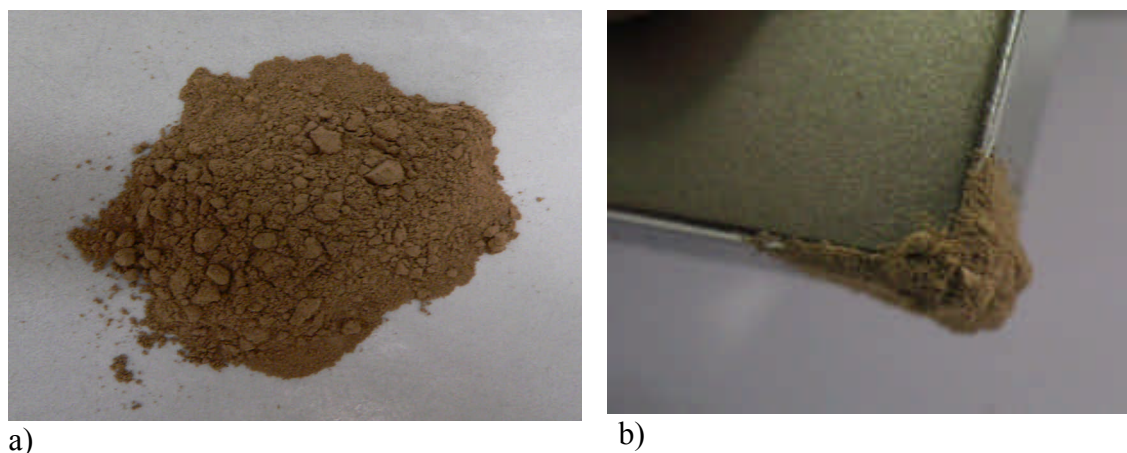


Fig. 2. a) FeHA powder (sample H) obtained by synthesis method 3 at T= 40°C; b) FeHA powder (sample H) attracted by a magnet.

6.2 Chemical, structural and magnetic characterizations of FeHA powder

The as-prepared FeHA powders were characterized by several analytical techniques (see also Chapter 5).

The phase composition was determined by X-ray powder diffraction (XRD), performed by a D8 Advance Diffractometer (Bruker, Karlsruhe, Germany) using CuK α radiation at 40kV and 40mA. XRD spectra were recorded in the 2 θ range 10-60° or 15-120°, with a step size of 0.02 and a counting time of 1 second (corresponding to 185 seconds using a conventional detector). Quantitative evaluation of phase compositions and cell parameters was performed by full- profile Rietveld analysis of the XRD spectrum (TOPAS v. 4.2, Bruker AXS, Karlsruhe, Germany). Computer simulation of XRD patterns of FeHA powders based on structural models was carried out by the aid of the software Powder cell 2.4 (W. Krause and G. Nolze, 2000).

Quantitative inductively coupled plasma-atomic emission spectrometry (ICP-OES) analysis, using an (ICP-OES: Liberty 200, Varian, Clayton South, Australia), was applied to determine the overall content of Ca, P and Fe. The samples for ICP analysis were prepared dissolving 20 mg of powder in 2 ml of HNO₃ (Aldrich, 65 wt.% pure) and the solution volume was increased up to 100 ml with deionized water. A reference solution was prepared by mixing standard solutions containing the investigated atoms at the expected concentrations. An equally diluted solution of nitric acid was also analysed and the corresponding spectrum subtracted by the experimental one.

The amount of Fe^{2+} present in the HA lattice was measured by a colorimetric method⁸ based on the use of orthophenantroline (Merck 1,10-phenantroline, P99% pure): ferrous ions in the presence of orthophenantroline form a stable red-orange complex $[(\text{C}_{12}\text{H}_8\text{N}_2)_3\text{Fe}]^{2+}$ in the pH range 4-5; this complex is detectable at 510 nm by UV-Visible spectrophotometry (Lambda 35 UV/VIS Spectrometer; Perkin Elmer Instrument, USA). The samples for UV/VIS analysis were prepared dissolving 20 mg of powder in 0.8 ml of H_2SO_4 (Aldrich, 96 wt.% pure) after having verified that sulfuric acid did not affect the concentration of the Fe^{2+} -complexed compound, at least in the time required to make the analysis. 10 ml of sodium citrate (0.5 M) were added to the solution containing sulfuric acid to set the pH around 4-5, then orthophenantroline (0.1 M) was added to the solution to set the molar ratio Fe^{2+} /orthophenantroline at 1/3. The volume of the final solution was increased up to 50 ml using deionized water.

An estimation of the amount of Fe^{3+} was performed calculating the difference between the total amount of Fe (determined by ICP) and the total amount of Fe^{2+} (determined by UV-VIS). The concentration of Fe^{2+} and Fe^{3+} associated to HA was derived by subtracting the contribution of Fe^{2+} and Fe^{3+} forming magnetite (detected by XRD and quantified by Rietveld refinement) from the total amount of Fe^{2+} and Fe^{3+} determined by ICP and UV analysis.

To gain information about the local chemical environment of Fe, X-ray absorption spectroscopy (XAS) at the Fe K-edge has been performed at the SUL-X beamline of the synchrotron radiation source ANKA (Karlsruhe Institute of Technology; Karlsruhe, Germany). SUL-X is a beamline with a wiggler as radiation source. A Si (111) crystal pair with a fixed beam exit was used as a monochromator. Higher harmonics have been suppressed by a silicon mirror behind the double-crystal monochromator. The beam was focused on the sample position by Kirkpatrick-Baez mirrors to about 100 x 100 μm . Fe K-edge XAS data were acquired in transmission (with ionization chambers as detectors) and fluorescence modes. The Fe concentration of the FeHA samples was sufficient to use the transmission data for evaluation. Energy was calibrated using a 3 μm thick Fe foil mounted between the second and third ionization chambers to the first inflection point of the Fe K-edge at 7112 eV. A typical scan ranges from 150 to 50 eV with a 5 eV energy step width and from 50 to 20 eV with a 2 eV step width prior to the edge. In the edge region between 7092 and 7142 eV the step width has been decreased to 0.3 eV and above

the edge, in the EX- AFS region, up to $k = 16$, a k step width of 0.5 has been chosen. The measurement time per scan was 1 s, increasing with $k = 0.5$ above the edge. Two scans have been performed on two different sample positions for FeHA-F and at one sample position for FeHA-H. Spectra were pre-edge and post-edge background corrected, and normalized to an edge jump of 1 using the Athena programme of the IFFEFIT package⁹. Reference spectra of magnetite (Fe₃O₄) and maghemite (c-Fe₂O₃) have been taken from the SUL-X reference database and these were obtained with similar parameters.

The analysis of powder morphology was carried out by scanning electron microscopy (SEM; Stereoscan 360, Leica, Cambridge, UK).

High-resolution transmission electron microscopy (HRTEM) analyses was performed by a JEOL JEM 3010-UHR, operating at 300 kV. As apatite samples might evolve under the electron beam, potentially leading to further crystallization and/or to a loss of constitutive water¹⁰, observations were carried out under feeble illumination conditions (significantly lower than that indicated in the literature) to avoid any modifications of the materials during the analysis.

Magnetization (M) of FeHA powders at low field was measured at $34 \times 10^{-4} \text{ N A}^{-1} \text{ m}^{-1}$ via a YSZ 01C/02C Susceptometer (Sartorius Mechatronics, Italy). Magnetic measurements were also performed at higher field in a superconducting quantum interference device (SQUID) magnetometer from Quantum Design (San Diego, CA, USA), capable of operating from 1.8 to 350 K under a maximum applied magnetic field of $H = 5 \text{ N A}^{-1} \text{ m}^{-1}$. In this case, about 20 mg of powder were measured from 5 to 300 K at an applied magnetic field of $H = 0.01 \text{ N A}^{-1} \text{ m}^{-1}$ in order to obtain the magnetization vs. temperature (M vs. T) curves, while the magnetization vs. magnetic field (M vs. H) curves were measured in a magnetic field cycle from 2 to -2 $\text{N A}^{-1} \text{ m}^{-1}$ at $T = 300 \text{ K}$. Measurements of magnetically induced heating were performed by placing each sample in the center of a coil of a homemade device generating an alternating magnetic field of $0.03 \text{ N A}^{-1} \text{ m}^{-1}$ at a frequency $m = 293 \text{ kHz}$.

6.2.1 Phase analysis by XRD

XRD spectra reveal a low-crystalline apatite (ICDD card no. 09-0432) with a crystallinity extent much lower than the non-substituted HA prepared at the same temperature (see Figs. 3-5), while the presence and amount of secondary phases can be related to the

synthesis methods and parameters.

XRD structural analysis confirms the substitution of Fe ions into the HA lattice. Computer simulations clearly indicate that the Fe ions found in the HA lattice are not situated at cell interstitial positions but at Ca-substituting positions (with small differences between the 4f and 6h positions). In fact, the substitution of one Ca^{2+} ion by Fe^{2+} or Fe^{3+} , both in 4f and 6h positions, has little effect on the intensity of the diffracted X-ray lines. On the other hand, the introduction of one Fe^{2+} or Fe^{3+} ion into one of the possible interstitial positions (2b, 2c, 2d, 4a and 6g) heavily modifies the line intensities, always making the calculated pattern rather different from the observed one and significantly increasing the discrepancy factor. It can be observed that even if the Fe substitution into the HA lattice does not remarkably twist the structure, the presence of Fe and/or Fe–O species during HA nucleation hampers the crystallite organization.

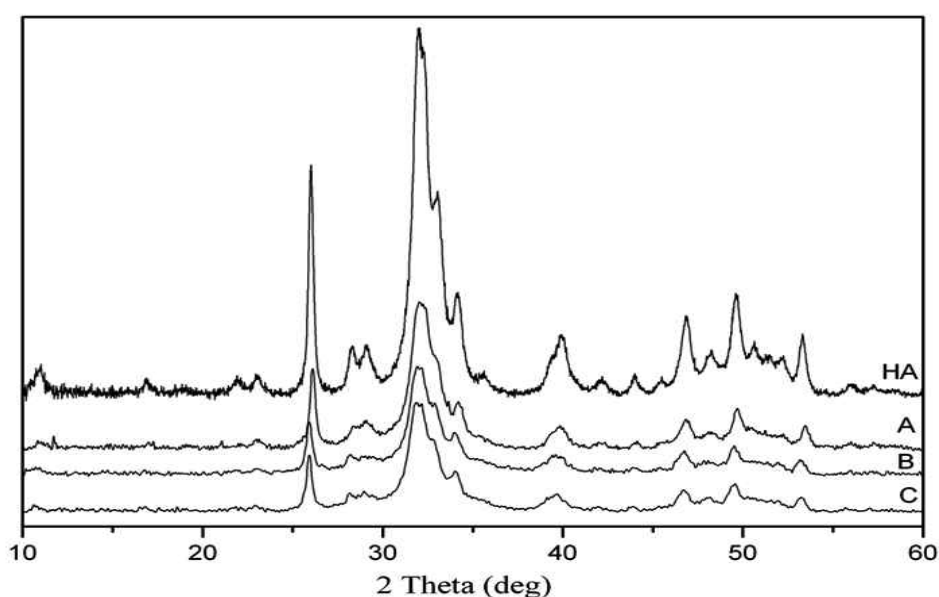


Fig. 3. XRD profiles of the HA synthesized at $T=40\text{ }^{\circ}\text{C}$ and samples obtained by a reductive process at different pressures applied to a FeHA powder synthesized by method 1 at $T=40\text{ }^{\circ}\text{C}$.

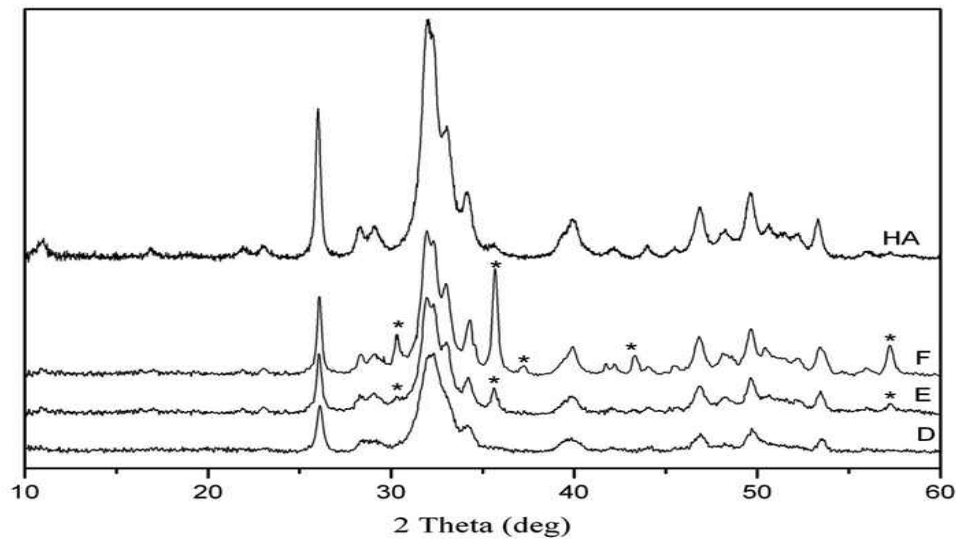


Fig. 4. XRD profiles of the HA synthesized at T= 40 °C and FeHA synthesized by method 2 at different temperatures (D=25°C; E=40°C; F=60°C). The peaks identified by * correspond to magnetite

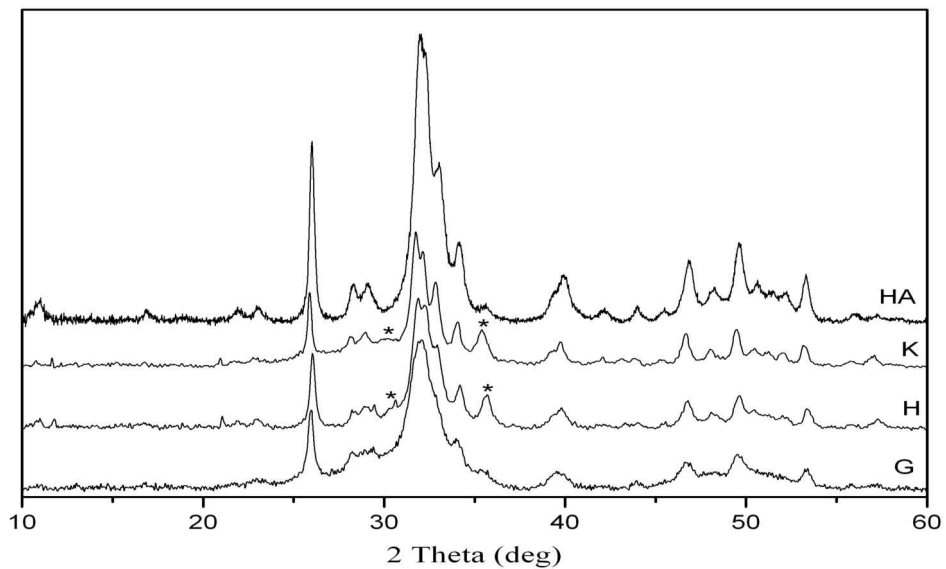


Fig. 5. XRD profiles of the HA synthesized at T= 40 °C and FeHA synthesized by method 3 at different temperatures (G = 25 °C; H = 40 °C; K = 60 °C). The peaks identified by * correspond to magnetite.

The XRD analysis (Fig. 3) of the powders prepared following method 1 reveals no secondary phases apart from HA whose crystallinity increases with synthesis temperature: the degree of crystallinity is ~8% at 40°C and ~30% at 60°C¹⁰.

The powders prepared following synthesis method 2 have characteristics strictly dependent on the synthesis temperature: the formation of magnetite starts at $T = 40$ °C as also reported in a previous work¹¹. It follows that magnetite is absent in sample D and the HA crystallinity is very low (see XRD profiles in Fig. 4)¹².

Increasing the temperature causes the kinetics of both magnetite formation and apatite crystallization to increase: XRD patterns of samples E and F (Fig. 4) show the peak of magnetite at $2\theta \approx 36^\circ$ which strengthens when the synthesis temperature is increased.

The simultaneous addition of both Fe species makes both Fe^{2+} and Fe^{3+} available simultaneously during the first stage of the HA nucleation (synthesis method 3). In sample G (Fig. 4) magnetite is absent as expected for a synthesis temperature of 25 °C¹¹; the crystallization extent of HA is very low and the lack of organization of the HA lattice reflects also the poor coordination level of the Fe ions substituting calcium. At $T = 40$ °C (sample H) the formation of magnetite is minimized when compared with method 2 since both ions preferentially enter the newly formed HA (Fig. 5).

A further increase of the synthesis temperature up to 60°C (sample K) results detrimental: the doping efficiency lowers and the formation of magnetite slightly increases (Fig. 5).

6.2.2 Chemical analysis by ICP

Table I-II-III shows the results of the chemical analysis of the iron-substituted HA powders examined in this work. The chemical analysis performed on FeHA confirms the presence of Fe in the powders at a level of 90% with respect to the one nominally introduced as reagent. For all the prepared FeHA samples, the molar ratio $(\text{Fe} + \text{Ca})/\text{P}$ ranges between 1.61 and 1.73, while Ca/P ratio is lower than the theoretical one: $1.31 < \text{Ca}/\text{P} < 1.51$, confirming the replacement of Ca with Fe.

The highest effectiveness of Fe^{2+} and Fe^{3+} substitution into the HA lattice is reached in sample H where it approaches a nominal doping of 20 mol.%. The $(\text{Fe} + \text{Ca})/\text{P}$ ratio is 1.68 which corresponds to the theoretical Ca/P ratio for HA, and the content of magnetite is only 1.6 vol.% (Table III).

Sample code	Fe _{tot} wt%	FeHA						M Am ² Kg ⁻¹
		Fe ³⁺ wt %	Fe ²⁺ wt %	Fe ³⁺ /Fe ²⁺ wt %	Fe/Ca % mol.	Ca/P mol.	(Fe+Ca)/P mol.	
A	10.42	6.28	4.14	1.52	27.92	1.31	1.68	0.00
B	10.42	3.10	7.32	0.42	27.92	1.31	1.68	0.00
C	10.42	0.83	9.59	0.09	27.92	1.31	1.68	0.00

Table 1. Characteristics of powders prepared by method 1 + reductive process

Sample code	Fe _{tot} wt.%	Magnetite			FeHA						M Am ² Kg ⁻¹
		vol.%	wt.%	Fe _{tot} wt.%	Fe ³⁺ wt.%	Fe ²⁺ wt.%	Fe ³⁺ /Fe ²⁺ wt.%	Fe/Ca %mol.	Ca/P mol.	(Fe+Ca)/P mol.	
D T=25°C	8.71	0.0	0.0	0.0	7.41	1.30	5.70	22.78	1.41	1.73	0.00
E T=40°C	8.80	3.0	4.8	3.5	4.26	1.04	4.10	13.51	1.51	1.72	0.34
F T=60°C	9.09	5.5	8.7	6.7	0.32	2.47	0.13	6.97	1.49	1.61	0.56

Table 2. Characteristics of powders prepared by method 2

Sample code	Fe _{tot} wt.%	Magnetite			FeHA						M Am ² Kg ⁻¹
		vol.%	wt.%	Fe _{tot} wt.%	Fe ³⁺ wt.%	Fe ²⁺ wt.%	Fe ³⁺ /Fe ²⁺ wt.%	Fe/Ca %mol.	Ca/P mol.	(Fe+Ca)/P mol.	
G T=25°C	9.26	0.0	0.0	0.0	8.39	0.87	9.64	26.63	1.31	1.66	0.15
H T=40°C	9.93	1.6	2.6	1.9	6.03	2.00	3.01	19.89	1.41	1.68	0.95
K T=60°C	9.61	2.0	3.2	2.3	5.26	2.05	2.56	17.99	1.44	1.69	1.20

Table 3. Characteristics of powders prepared by method 3

6.2.3 Magnetic and microstructural investigation

In the synthesis method 1 iron is present into HA only in its higher oxidation state and the powder does not show any magnetisation signal. After application of the reductive process no magnetite-like phase forms as detected by XRD (Fig. 3) and magnetisation signal results zero for samples A, B and C (Table I). It can be supposed that the reduction of Fe^{3+} trapped into HA lattice, which occurs at the heterogeneous gas-solid interface, is not homogeneous throughout the whole bulk and cannot assure a balanced distribution of Fe^{2+} and Fe^{3+} inside the structure¹³.

Detailed magnetic and microstructural characterizations were performed on samples E and H: zero-field-cooled (ZFC) and field-cooled (FC) magnetization curves as function of temperature were acquired under a high magnetic field (Fig. 6). Each sample shows behavior typical of a system of interacting magnetic particles¹⁴. The average blocking temperature, T_B , is found to be around 170 K for sample H, while for sample E it is beyond the measured temperature (300 K). T_B is closely related to the particle size and dipolar interparticle interactions and gets higher as the dipolar interactions increase. As a consequence of the formation of aggregates, the local concentration of nanoparticles and hence the strength of dipolar interparticle interactions increases, changing the energy barrier for magnetization relaxation and determining the collective magnetic behavior of the sample¹⁵. The significantly higher value of T_B for sample E suggests the presence of larger magnetic aggregates (ascribable to magnetite as secondary phase) in respect to sample H. This is in agreement with the XRD analysis which reports a higher concentration of magnetite in sample E vs. sample H.

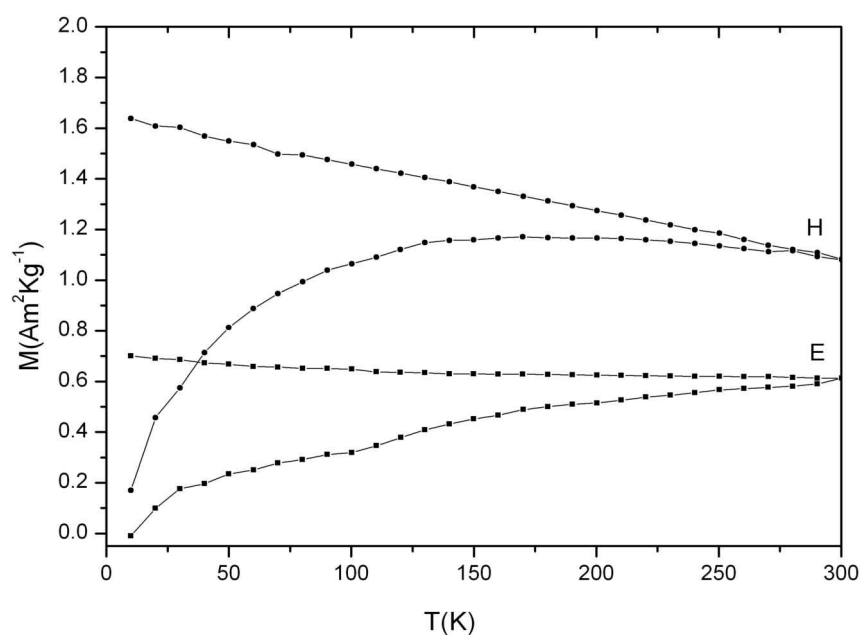
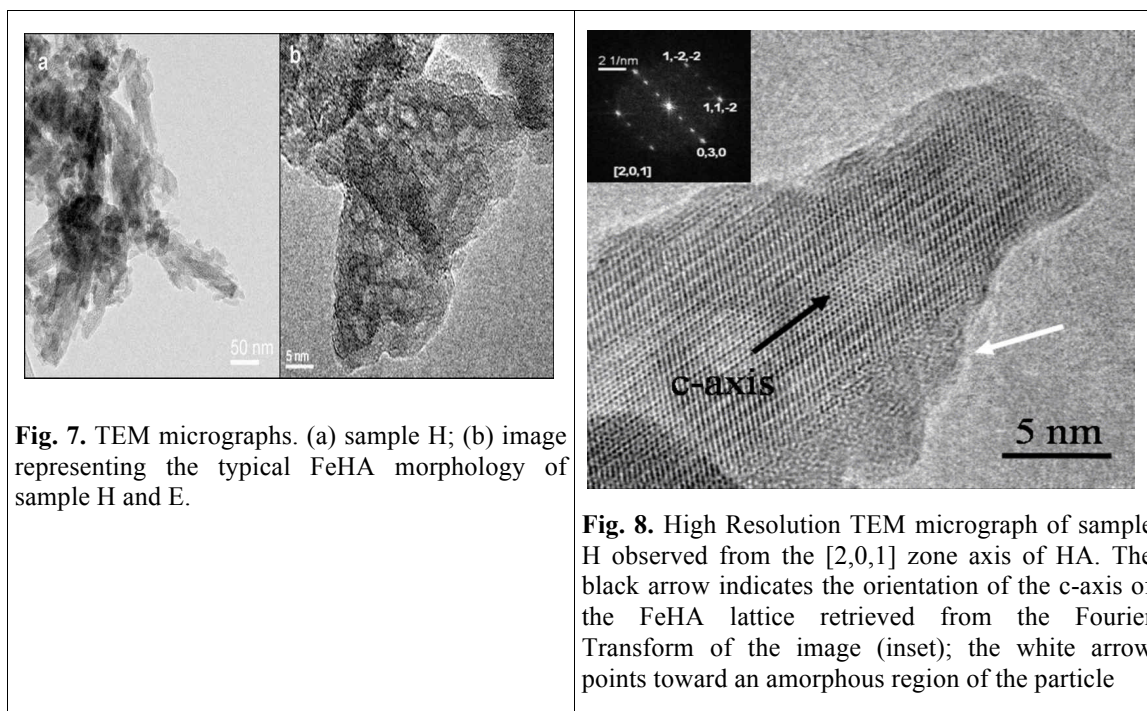


Fig. 6. Magnetization curves at zero-field-cooled (ZFC) and field-cooled (FC) in function of temperature. ZFC-FC magnetic curves for sample E (square symbol) and H (circle symbol) at an applied magnetic field of 100 Oe.

In agreement with magnetization measurements, TEM analysis of sample H shows very low concentration of dark spots (5-10 nm in size) corresponding to inclusions of iron rich phases (Fig. 7a). For samples E and H the micrograph in Fig. 7b shows calcium phosphate particles with needle-like morphology, rather heterogeneous in size, 5-20 nm in width and up to 50-80 nm in length.

The magnetization curves as function of the applied magnetic field for samples E and H (Fig. 9) show the typical superparamagnetic (SPM) behaviour of single-domain magnetic nanoparticles. Contrary to what expected on the basis of the amount and aggregate size of magnetite, the magnetization of saturation (M_s) of sample H (4.0 - 4.2 emu/g) is higher than sample E (1.8 - 2.0 emu/g). The 1.6 vol% of magnetite as secondary phase in sample H is not sufficient to justify such a magnetization value, therefore a contribute of another magnetic phase must be claimed.



As a support for this assumption, HRTEM analysis on sample H reveals that the material is made up of both amorphous and crystalline HA domains elongated in the direction of the c-axis, that can even coexist in the same particle (Fig. 8 and relative inset). By EDS analysis (carefully choosing the apatitic matrix and avoiding the few iron oxides clusters) no evidence of iron-rich phases is found by a series of punctual analyses on sample H. Iron appears homogeneously dispersed in the materials likely in form of single ions substituting Ca^{2+} into the HA lattice. The total Fe content as well as the Ca/P ratios of the calcium phosphate phase for both powders E and H has been measured by EDS (carefully choosing those regions where no iron oxides particles were detected) and the results are nicely consistent with those obtained by ICP and XRD analyses reported in Tables II and III.

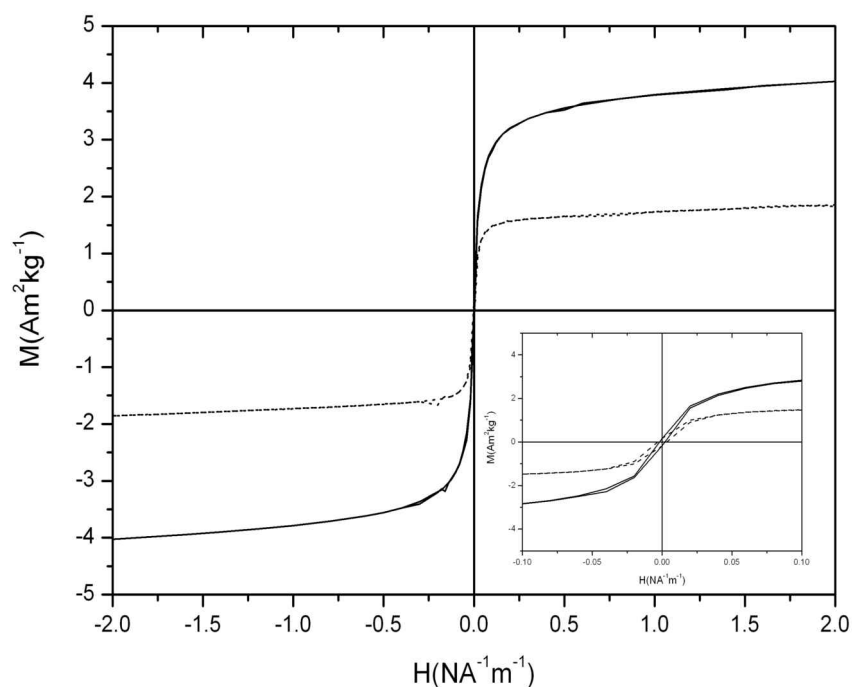


Fig. 9. Magnetic curves in function of the applied magnetic field up to 2 Tesla for the sample H (continue line) and E (dotted line) at $T = 300$ K.

Fig. 10A contains the XANES spectra of FeHA powders (i.e. samples E and H), in comparison with magnetite and maghemite, selected as reference materials. In this respect, FeHAs gave XANES spectra that differ from those of magnetite and maghemite, particularly concerning the different features at energies in the range 7126-7155 eV. Because of the magnetite content in the samples E and H, X-ray absorption spectra are a superposition of Fe in FeHA and Fe in magnetite, so that the shape of the pure Fe K-edge spectra of FeHA cannot be extracted easily. Nevertheless, the differences in shape indicate that part of the Fe does not belong to magnetite or maghemite and hence can be assigned to FeHA. A shift in the absorption edge (flank and white line) from magnetite (containing both Fe ions) to maghemite (containing only Fe³⁺) can be observed and it can be related to different Fe³⁺/Fe²⁺ ratios. Looking at the curves in the range between 0.5 and 1 of the edge jump, it is possible to notice that the flank and the maximum position of the white line shift from magnetite (Fe³⁺/Fe²⁺ ratio=2) to sample H (Fe³⁺/Fe²⁺ ratio=3), sample E (Fe³⁺/Fe²⁺ ratio=4) and last to maghemite (Fe³⁺/Fe²⁺ ratio = ∞).

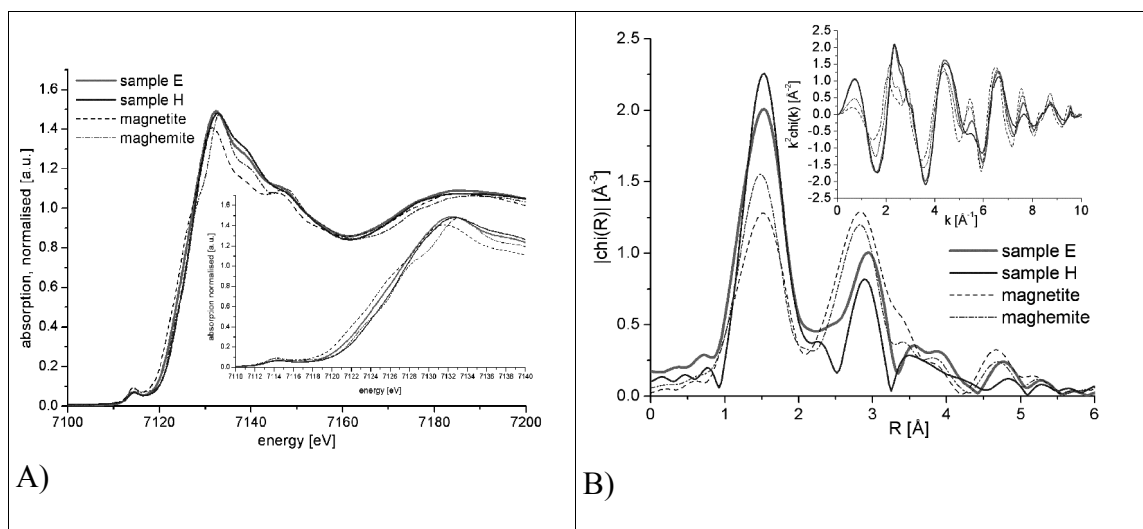


Fig. 10. Fe K-edge X-ray absorption near edge (XANES) spectra with edge region in the inset (A) and Fourier Transform of the EXAFS function (B), both k^2 weighted for samples E and H and the magnetite and maghemite reference substances.

In Fig. 10B the Fourier Transform for $3.5 < k < 9$ of the EXAFS function (inset) for samples E and H, magnetite and maghemite standards are reported. Samples E and H show a higher intensity of the peak related to the first coordination shell and a shift of the bond length to higher values for both the first and the second shell when compared to maghemite and magnetite. This is in agreement with the bond length contraction from 2.43\AA to 2.04\AA reported by Jiang et al.⁶ for substitution of Ca(1) with Fe^{3+} and also reinforces the conclusion that part of the iron is entering in the hydroxyapatite lattice.

6.2.4 Hyperthermia effect of FeHA powder

The evolution of heat versus time of exposure to magnetic field (hyperthermia) is reported in Fig. 11. Sample H exhibits an increase of temperature of about 40°C in 60s; the hyperthermia curves B and C are relative to magnetite mixed with stoichiometric HA, in the amount of 5/95 wt% and 10/90 wt% respectively. Fig. 11 gives evidence to a much higher hyperthermia effect for the magnetic FeHA powder in comparison with the magnetite/HA mixtures which exhibit lower increases of temperature in longer time. Since the two magnetite/HA mixtures contain higher amounts of magnetite (5 and 10 wt%) compared to sample H (magnetite = 1.6 vol%, i.e. ≈ 2.6 wt%), the intense

hyperthermia is not justifiable by the sole presence of magnetite in sample H and a bulk effect due to the existence of a new magnetic HA phase must be called into question.

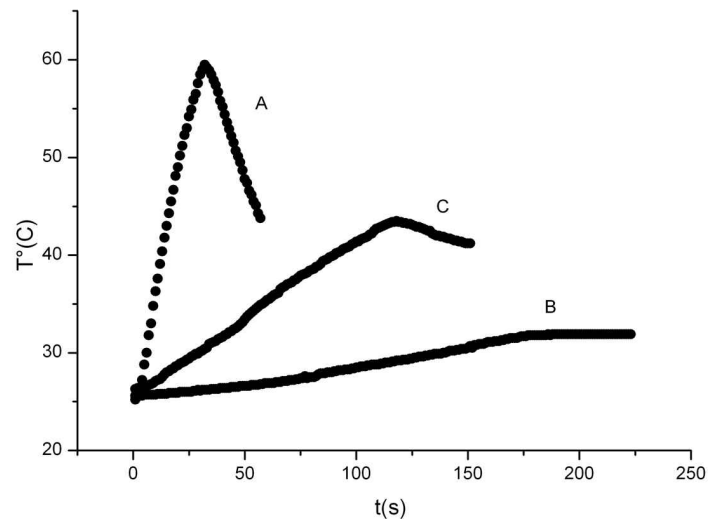


Fig. 11. Hyperthermia curves: (A) sample H, (B) mixture of magnetite/HA (95/5wt%) and (C) mixture of magnetite/HA 10/90wt%.

6.3 Development of FeHA granulate

FeHA powder was processed in order to obtain a more stable granulate (400-600 μm) (Fig. 12). In detail, the powder was hydrated with distilled water and agglomerated. Agglomerates were dried at 40°C for 48 h and sieved in the range 400-600 μm .

For the *in vitro* and *in vivo* tests glass vials containing 0.5 g of granulates were prepared and sterilized with 25 kGy γ -ray.

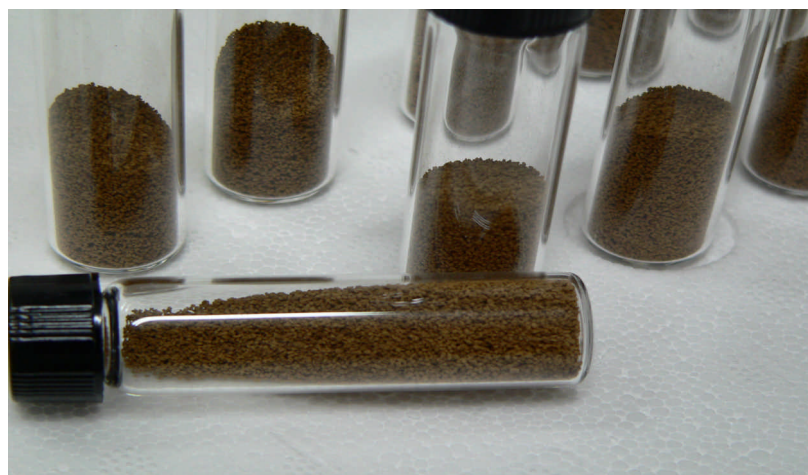


Fig. 12. FeHA granulates

6.4 Biocompatibility tests

6.4.1 *In vitro* evaluation of biocompatibility and cell morphology

In vitro tests were performed on FeHA powder to verify any toxic effects induced by the magnetic material compared to the HA, keeping in mind its future *in vivo* applications. At this purpose the *in vitro* evaluation of the effects of the FeHA powder on osteoblast-like cell culture was conducted. In detail, 24 hours after Saos-2 cells were plated, 4 different concentrations of FeHA and HA, in a range from 200 µg/ml up to 2000 µg/ml, were added to the culture medium.

The cell culture was analysed for 7 days for cell viability, with the Live/Dead assay showing for both FeHA and HA groups a very high ratio of viable cells at each experimental time point with no significant differences among the two groups, with a range respectively between $98.0 \pm 0.5\%$ and 100% at day 1, $96.7 \pm 0.4\%$ and $99.1 \pm 0.5\%$ at day 3, $97.3 \pm 0.5\%$ and $99.7 \pm 0.2\%$ at day 7 (Fig.13).

Furthermore, the presence of FeHA powder in the cell culture media positively influences cell proliferation compared to HA powder. In fact, analysing the DNA content, significant differences are observed at day 3 and day 7 for FeHA and HA groups (Fig.14). While at day 1 there are no statistically significant differences among the superparamagnetic and the control nanoparticles, there is a trend showing a higher number of cells in FeHA groups compared to the HA groups. These data are in agreement with several studies where different types of magnetic particles were used and they influence cell proliferation¹⁶⁻¹⁸.

The obtained results demonstrate the good biocompatibility of the FeHA powder. In fact not only they do not reduce the cell viability, they also enhance cell proliferation compared to respective HA groups.

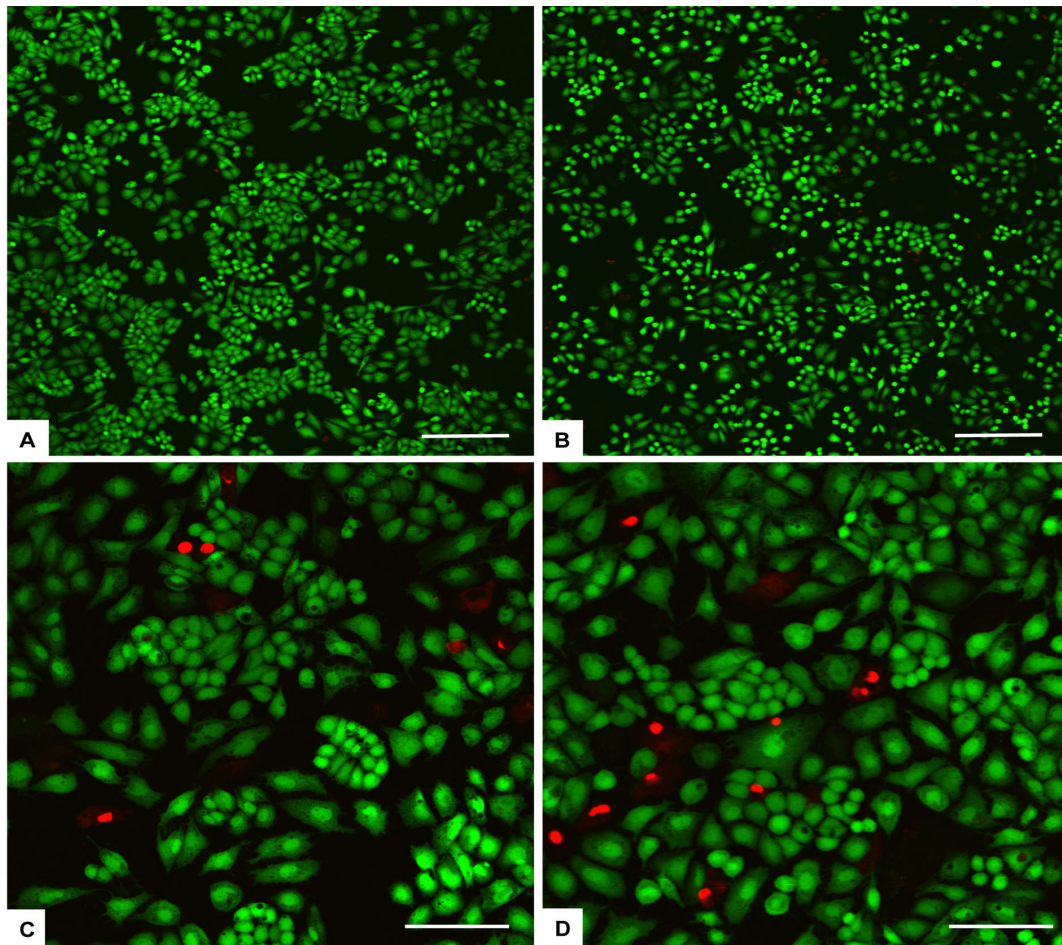


Fig. 13. Analysis of cell viability. Cell viability was analysed by the Live/Dead assay (n = 2). Calcein AM stains for live cells in green, EthD-1 stains for dead cells in red. A) HA 1000 µg/ml at day 3. B) FeHA 1000 µg/ml at day 3. C) HA 200 µg/ml at day 7. D) FeHA 200 µg/ml at day 7. Scale bars: A,B) 200 µm. C,D) 100 µm.

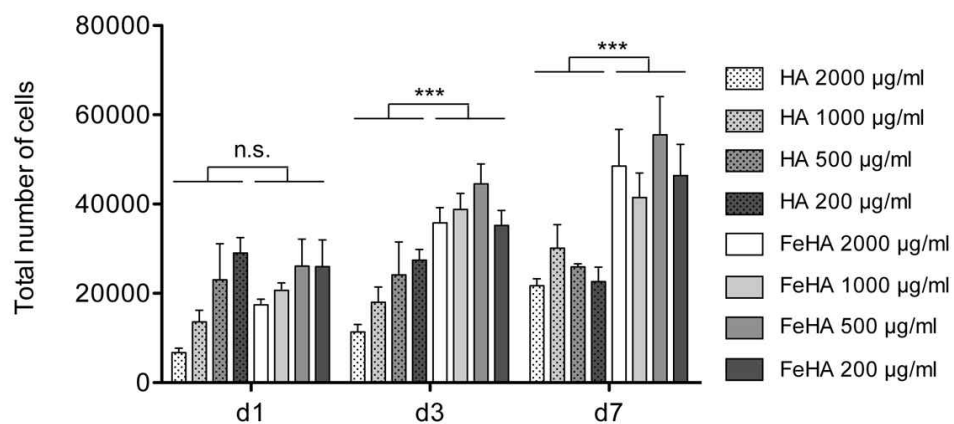


Fig. 14. Cell proliferation assay. The Picogreen DNA content assay was performed on cultures of osteoblast-like cells seeded with 4 different concentrations of HA and FeHA nanoparticles at 1, 3 and 7 days of culture (n = 5). n.s. = not significant; *** p ≤ 0.001

Looking in detail at the cell morphology, FeHA nanoparticles seems to be accumulated in the cytoplasm (Fig. 15A,B) and even when the cells show high MNP accumulation they remain firmly attached to the well surface. This fact suggests that the novel intrinsically magnetic FeHA powder is well tolerated by the cells in a similar way as the HA groups, where HA serves as the main component of several bone substitutes already used in clinical applications, and have also been shown to induce cell proliferation.

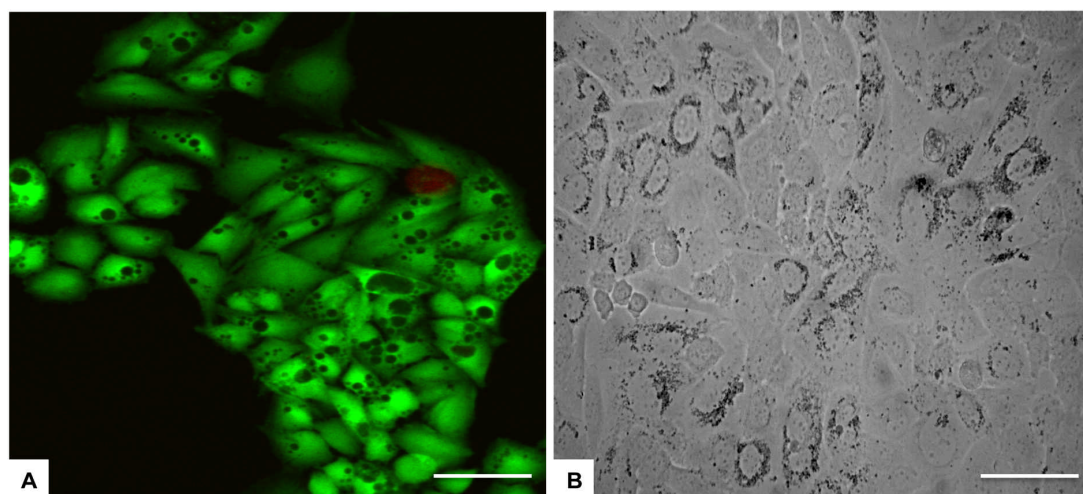


Fig. 15. Analysis of cell morphology. Cells are spread with good morphology and firmly attach to the surface. Black spots are the MNPs that have been internalized by cells. A) FeHA 500 $\mu\text{g}/\text{ml}$ at day 3, cells stained with Calcein AM in green and EthD-1 in red. B) FeHA 200 $\mu\text{g}/\text{ml}$ at day 7, bright field image. Scale bars: 50 μm .

6.4.2 Effect of the *in vitro* application of a static magnetic field

After demonstrating the similar biocompatibility of FeHA and HA particles, the presence of an externally applied static magnetic field (SMF) was investigated in order to study how it could modulate the cell proliferative effects and bone regenerative capacity induced by this FeHA material. All the experiments were conducted with or without applying a 320 mT SMF on cells seeded with the 4 different concentrations of FeHA particles.

In the literature, there have been far fewer studies on the cellular effects of static magnetic field at the cellular level, compared to those of extremely low frequency electromagnetic fields. While several studies showed that exposure to static magnetic fields alone has no or extremely small effects on cell growth and genetic toxicity regardless of the magnetic density, in combination with other external factors such as ionizing radiation and some chemicals, there is evidence to strongly suggest that a SMF modifies their effects¹⁹. The

results obtained are strongly in agreement with these data. In fact, after confirming that SMF on cells in culture by itself does not affect cell behaviour (data not shown), data with FeHA MNPs confirm a statistically significant increase in cell proliferation from day 1 to day 7 between FeHA groups with SMF application compared to groups without magnetic field application (Fig. 16). In detail, the 200 µg/ml FeHA powder concentration induce a higher cell proliferation compared to the 2000 µg/ml FeHA powder only with exposure to the SMF, suggesting that the lowest concentration of FeHA particles acts synergy with the magnetic field to stimulate cell proliferation (Fig. 16).

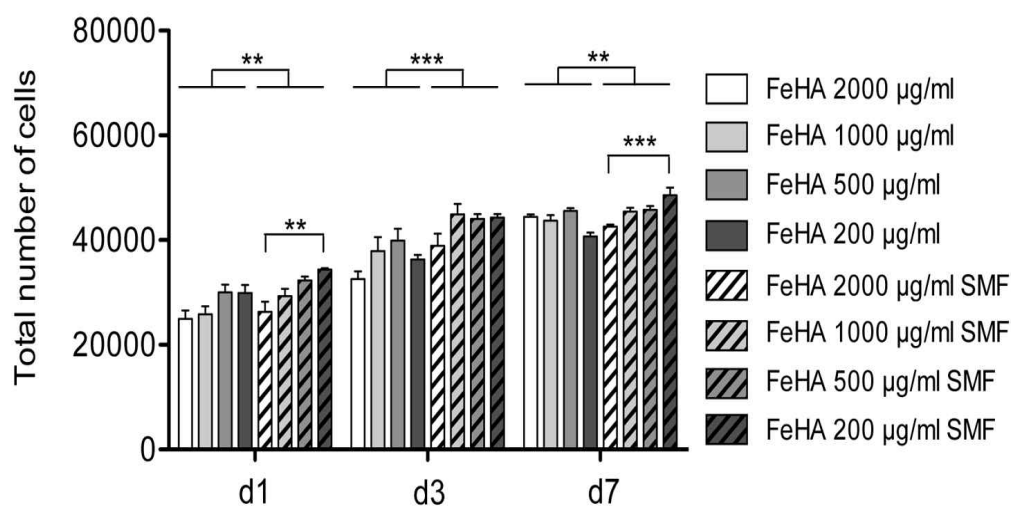


Fig. 16. Cell proliferation assay in the presence of a static magnetic field. The Picogreen DNA content assay was performed on cultures of osteoblast-like cells seeded with 4 different concentrations of FeHA MNPs at 1, 3 and 7 days of culture, either in the presence or absence of a static magnetic field (SMF) (n = 5). ** $p \leq 0.01$; *** $p \leq 0.001$.

Furthermore, with respect to osteoblast activity on each condition, AP activity seems to be influenced by the synergic effect of FeHA and SMF, with a significant effect at day 3, indicating that there might be also a positive effect on osteoblast activity given by the presence of SMF (Fig. 17).

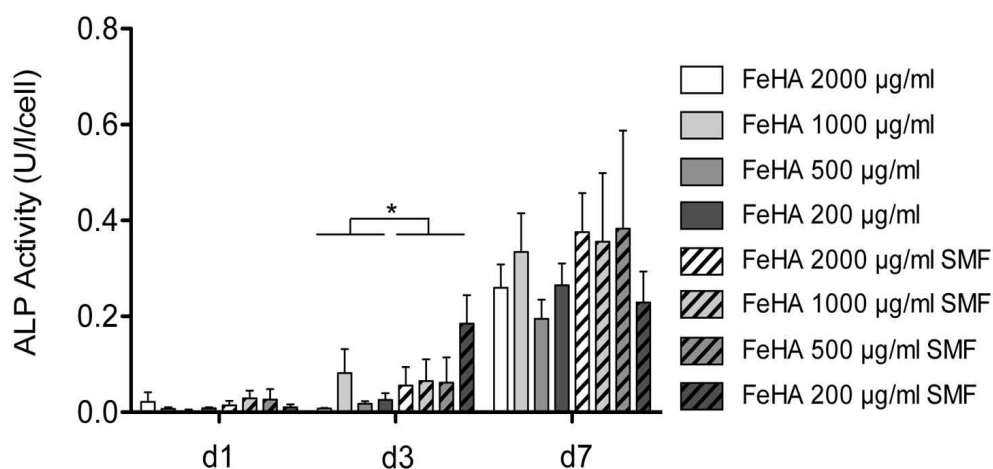


Fig. 17. Alkaline phosphatase activity assay in the presence of a static magnetic field. AP activity was measured with different concentrations of FeHA seeded with human osteoblast-like cells at 1, 3 and 7 days, either in the presence or absence of a static magnetic field (SMF) ($n = 5$). * $p \leq 0.05$.

6.4.3 In vivo pilot experimental and histological analysis

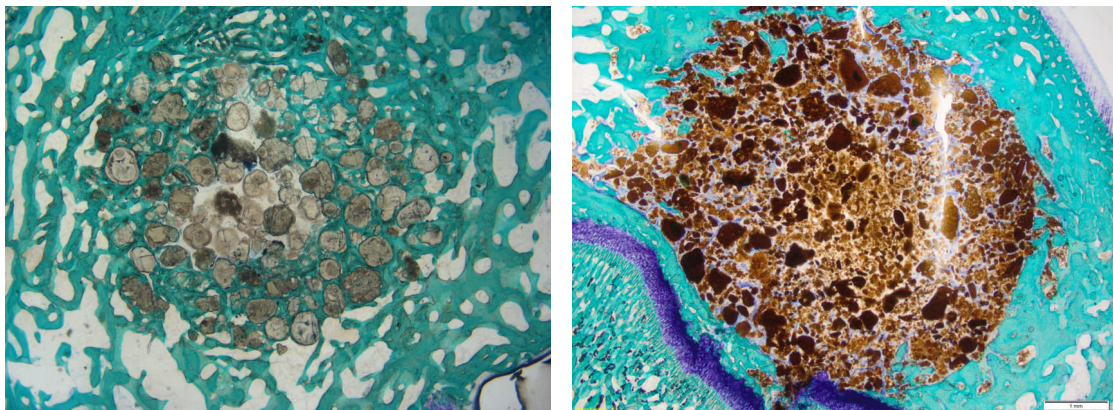
In order to assess how well in vitro observations translate in vivo, the biocompatibility of FeHA materials in a pilot animal study of bone repair (a rabbit critical bone defect model) has been tested. For this purpose FeHA powder was processed in order to obtain a granulate (400-600 μm) more easily handled and similar to bone fillers already used in clinical applications (see paragraph 6.3). The FeHA granules were not stabilized with the same thermal treatment applied to the reference material to avoid chemico-physical modification of the nanostructure.

The control group consist of a bone filler made of HA granulate of identical size (400-600 μm), already commercially available, and stabilized for one hour at 300°C (FinGranule, Finceramica Faenza Spa, Italy).

The study was performed in accordance with EC guide-lines (EC Council Directive 86/609, 1986) and the Italian legislation on animal experimentation (Decreto L.vo 116/92). The research protocol on animals has been approved by the Ethical Committee of Rizzoli Orthopaedic Institute and by the responsible public authorities.

Six male rabbits (*Oryctolagus cuniculus*, Charles River, Lecco, Italy), 2.4 ± 0.2 kg body weight, were housed at a controlled temperature of $22 \pm 1^\circ\text{C}$ and relative humidity of $55 \pm 5\%$ in single boxes and fed a standard diet (Mucedola, Milano, Italy) with filtered tap water *ad libitum*. After quarantine of at least 10 days, the animals were fasted for 24

hours before surgery. The animals were subjected to surgery to implant the tested biomaterials at the distal femoral epiphysis under general anaesthesia and in aseptic conditions. After having shaved and disinfected the posterior legs, the animals underwent a lateral longitudinal incision of lateral femoral condyle. Femoral lateral condyle trabecular bone was cross-sectionally drilled at low speed and a profuse irrigation with cold sterile 0.9% NaCl solution was maintained throughout the process to prevent the risk of bone necrosis. A critical bone defect of 6.00 mm in diameter and 8.00 mm in depth was made in each lateral femoral condyle. Defects were filled with FeHA granules and with the HA granules in the contralateral condyle as a control group. For each defect, approximately 0.5 g granules, sterilized by 25 kGy γ -ray radiation, were used. Finally, the skin was sutured. General anaesthesia was induced by an intramuscular injection of 44 mg/kg ketamine (Imalgene 1000, Merial Italia S.p.A, Milan, Italy) and 3 mg/kg xylazine (Rompun, Bayer SpA, Milano).



A)

B)

Fig. 18. Histological evaluation of the in vivo implanted HA and FeHA granules. Toluidine Blue, Acid Fucsin and Fast Green staining shows similar histocompatibility for both biomaterials 4 weeks after implantation (n = 6). A) HA control group, B) FeHA group. Scale bars: 1 mm.

At 4 weeks post-implantation, macroscopic evaluation shows that the HA and FeHA biomaterials are in the proper position and there is no evidence of haematoma, edema, infection or tissue necrosis in either bone and peri-implant soft tissue associated with control or magnetic implants. Bone tissue is well visible around the biomaterials in both groups demonstrating a good bone integration of FeHA granules (Fig. 18). In detail, between the granules, the magnetic FeHA group shows more immature bone not yet

completely mineralized stained with Toluidine Blue respect to HA granulate control group (Fig. 18).

This is probably due to the lower physical stability of the FeHA granules in comparison with the reference material, which has been subjected to the thermal treatment. This would result in a less compact material with a higher specific surface available for bone integration, possibly making FeHA more bioactive than control. In the long term these characteristics might positively influence tissue regeneration and stability and reduce biomaterial resorbability.

6.5 Conclusion

A neutralization method has been employed to synthesize HA nanopowders in which Ca is partially substituted by Fe^{2+} and Fe^{3+} . The simultaneous addition of both Fe species under controlled synthesis conditions leads to FeHA with a $(\text{Fe} + \text{Ca})/\text{P}$ ratio very close to the theoretical one ($\text{Ca}/\text{P} = 1.67$) and a very small content of magnetite as secondary phase. XRD, ICP and TEM analysis confirm that both Fe^{2+} and Fe^{3+} ions enter the HA lattice. The new FeHA exhibits very low crystallinity and a structural coherence at the nanometer length scale together with very low thermal stability. Likewise, XANES and EXAFS spectra reveal additional contribution from the Fe K-edge, besides Fe in magnetite, assignable to Fe in apatite. Powder H shows the superparamagnetic-like behaviour typical of single-domain magnetic nanoparticles: the signal largely exceeds the one expected for such a low content of magnetite. A relevant hyperthermia effect indicates a bulk phenomenon that even more clearly confirms the intrinsic magnetic behaviour of this FeHA phase.

The occupation of the Ca(1) and Ca(2) crystallographic positions of the HA lattice by the two Fe species and their specific spatial distribution (which implies a specific $\text{Fe}^{3+}/\text{Fe}^{2+}$ ratio) raises the hypothesis of two distinct interacting structural domains or sublattices, whose nature deserves further investigation, as does as the mechanism underlying the superparamagnetic effect.

Overall, the *in vitro* results show that the novel superparamagnetic FeHA powder not only does not reduce cell viability, but it enhances cell proliferation compared to HA particles controls already used in clinical application. Moreover, the positive effect of these nanoparticles is significantly increased when a SMF is applied.

The magnetic property of the FeHA phase together with its biocompatibility open the door of the regenerative medicine to a conceptually new family of biomimetic scaffolds able to be biologically manipulated or activated in situ by means of an external magnetic field. Additionally, the high hyperthermia of FeHA offers a true advantage with respect to the present solutions in anti-cancer therapies: the benefits foreseen are not only the more intense and rapid local effect, but most of all its biocompatibility/degradability, which overcome the side effects of long-term cytotoxicity. Injected MNPs can also increase the resolution, up to the cellular scale, of diagnostic techniques such as resonance. Hence, such FeHA nanoparticles could be effectively used in cancer prevention, allowing further development of the resonance technique that can be improved towards the early detection of even small tumoral cell aggregates. In conclusion, regenerative medicine and the wider field of theranostics may benefit from solutions represented by these completely biocompatible and biodegradable magnetic nanocarriers.

References

1. N.Y. Mostafa, *Mat. Chem. Phys.* **2005**, *94*, 333.
2. Y. Luia, W. Wanga, Y. Zhana, et al., *Mater. Lett.* **2002**, *56*, 496.
3. R.E. Riman, W.L. Suchanek, et al., *Solid State Ionic* **2002**, *151*, 393.
4. K.S. TenHuisen, P.W. Brown, *Biomaterials* **1998**, *19*, 2209.
5. R. Martin, P.W. Brown, *J. Biomed. Mater. Res.* **1997**, *35*, 299.
6. Jiang M, Terra J, Rossi MA, Morales MA, Saitovitch EMB, Ellis DE, *Phys. Rev. B: Condens. Mater. Phys.* **2002**, *66*, 224107.
7. A. Tampieri et al. *Acta Biomaterialia* **2012**, *8*, 843.
8. Potts PJ. A handbook of silicate rock analysis. Blackie: Glasgow; 1987.
9. Ravel B, Newville M. *J. Synchr. Rad.* **2005**, *12*, 537.
10. Celotti G, Tampieri A, Sprio S, Landi E, Bertinetti L, Martra G, et al. *Mater. Sci. Mater. M.* **2006**, *17*, 1079.
11. Perez OP, Umetsu Y, Sasaki H. P. *Hydrometallurgy.* **1998**, *50*, 223.
12. Liu C, Huang Y, Shen W, Cui J. *Biomaterials* **2001**, *22*, 301.
13. Koksharov Y.A. Magnetism of nanoparticles: effect of size, shape and interaction. In: Gubin P, editor. *Magnetic Nanoparticles*. Weinheim: VCH; 2009. p. 197–246.
14. Hoppe C.E., Rivadulla F., Vidal-Vidal J., Lopez-Quintela M.A., Rivas J. J. *Nanosci. Nanotechnol.* **2008**, *8*, 2883.
15. Klabunde K.J, Mulukutla R.S. Nanoscale materials in chemistry. In: Klabunde KJ, editor. *New York: Wiley-Interscience*; 2001. p. 223–61
16. Pareta R.A., Taylor E., Webster T.J. *Nanotechnology* **2008**, *19*, 265101.
17. Wu H.C., Wang T.W., Sun J.S., Wang W.H., Lin F.H. *Nanotechnology* **2007**, *18*, 1.
18. Wu Y, Jiang W, Wen X, He B, Zeng X, Wang G, Gu Z. *Biomed. Mater.* **2010**, *5*, 15001.
19. Miyakoshi J. *Prog. Biophys. Mol. Biol.* **2005**, *87*, 213.

CHAPTER 7

DEVELOPMENT OF MAGNETIC BIOHYBRID FeHA/COLL SCAFFOLDS

Magnetic biohybrid scaffolds (FeHA/Coll) was developed following the bio-inspired mineralization process^{1,2}: the reproduction of biomimetic conditions of bone synthesis allowed to obtain hybrid constructs where the mineral phase is nucleated upon guidance of the chemical features and physical confinement imposed by the polymeric matrix, so that the mineral phase has physical, chemical and ultra-structural similarity with the mineral bone^{3,4}. In this way, the chemico-physical properties of the biohybrid scaffolds are highly affected not only by the chemical interactions between FeHA crystals and proteinic matrix but also by the structural organization of the matrix itself⁵. Taking into account the biomineralization concept², not only the mineral phase was nucleated on the collagen fibres, creating a tissue conductive system that resembled the complex hierarchic structure of bone¹, but also during the stage of mineral phase nucleation, both iron species (Fe^{2+} and Fe^{3+}) were introduced into the apatitic lattice in different Ca crystallographic sites with a specific coordination⁶ generating *in situ* a magnetic mineral phase (FeHA) endowed with intrinsic superparamagnetism⁷.

The nucleation method is based on the same acid-base reaction already discussed for the synthesis of the mineral phase (FeHA powder) (§ 6.1) but differs in the presence of collagen added during the process.

7.1 Synthesis process of HA/Coll composite

The synthesis of the non-magnetic composites HA/Coll was performed following the biologically inspired synthesis previously described⁸. In order to obtain scaffold that resembling the chemical composition of the bone tissue, the weight ratio percent between the mineral and organic phase was fixed to 70/30 wt%.

The organic component, working as matrix mediating the mineralization process, was Collagen (Coll) Type I extracted from equine tendon, telopeptides free and supplied as buffered acetic gel (an aqueous acetic buffer solution with pH=3.5 containing 1 wt% of pure type-I collagen) (Opocrin S.p.A., Italy).

In detail, 250 ml of H₃PO₄ solution (0.083M, Sigma Aldrich 85 wt%), mixed with 150 g of 1 wt% collagen gel, were dropped in a basic suspension, containing 2.71 g of Ca(OH)₂ (Sigma Aldrich 95 wt% pure) in 500 ml of distilled water to yield a composite material HA/Coll in the ratio 70/30 wt%. The drop-wise addition procedure was performed under manual stirring, assuring a slow decrease of pH up to neutrality. During the nucleation of HA the synthesis temperature was kept at 25°C.

7.2 Synthesis process of magnetic FeHA/Coll composite

The nucleation of FeHA on the self assembling collagen fibres requires the preservation of both iron species so that they can enter the HA structure in two different coordination position and induce the superparamagnetism⁷: actually the oxidation condition of the acidic (by acetic acid) suspension of collagen would have oxidize Fe²⁺, therefore the procedure previously set up to prepare HA/Coll hybrid composite⁸ could not be applied.

In particular, to avoid the oxidation of Fe²⁺ to Fe³⁺ due to the acetic acid present in the collagen gel suspension, 150 g of 1 wt% of collagen gel were precipitated with NaOH (0.1M) solution added up to pH 5.5 and washed three times with distilled water. Then, the precipitated collagen gel was mixed with 250 ml of H₃PO₄ (0.083 M) solution that was dropped in a basic calcium hydroxide suspension (g 2.71 of Ca(OH)₂ in 500 ml of distilled water) previously enriched with FeCl₂ × 4H₂O (Aldrich, ≥ 99 wt% pure, 0.689 g in 25 ml of distilled water) and FeCl₃ × 6H₂O (Aldrich, ≥ 98 wt% pure, 0.956 g in 25ml of distilled water) to yield a composite FeHA/Coll material in the ratio 70/30 wt%. The total amount of iron chloride salts was calculated to obtain a molar ratio (Fe/Ca) = 0.20 mol in the mineral phase. The pH of the basic suspension after the addition of iron ions was unchanged (pH=12) and at the end of the synthesis the pH value of the aqueous medium was 8.

For the realization of magnetic biohybrid FeHA/Coll scaffolds three different synthesis temperatures (25, 40 and 50 °C) were investigated and the respective synthesis products were coded FeHA/Coll25; FeHA/Coll40 and FeHA/Coll50.

After the synthesis, HA/Coll and FeHA/Coll materials were filtered and poured into plastic moulds.

To obtain dried and porous samples, a freeze-drying process with a controlled freezing and heating ramp was performed from 25 °C to -25°C and from - 25°C to 25°C for 50 min under vacuum conditions ($P = 0.20$ mbar).

The samples after the freeze-drying process were treated with the cross-linking agent 1,4-butanediol diglycidyl ether (BDDGE) through immersion for 24 h at 25°C in a BDDGE aqueous solution (2.5 mM), setting up a BDDGE/Collagen ratio equal to 1 wt%. After this cross-linking treatment, each sample was washed from the un-reacted BDDGE residual and freeze-dried again.

7.3 Chemico-physical and magnetic characterization of FeHA/Coll magnetic composite

Following the biomineralization process, ($\text{Fe}^{2+}/\text{Fe}^{3+}$) substituted bone-like hydroxyapatite nano-crystals were nucleated on self-assembling collagen fibres, exploiting the ability of the negatively charged carboxylate groups of collagen to bind the calcium ions of HA.

7.3.1 X-ray diffraction analysis (XRD)

The scaffold phase composition was determined by X-ray sample diffraction (XRD) performed by a D8 Advanced Diffractometer (Bruker, Karlsruhe, Germany) using $\text{Cu K}\alpha$ radiation at 40 kV and 40 mA. XRD spectra were recorded in the 2θ range 10° - 60° , step width 0.02° and counting time 1 second. The samples were ground using a cryo-milling apparatus to obtain a relatively uniform particle size material.

For FeHA/Coll composites XRD profiles (Fig. 1) displays patterns typical of a very low crystalline apatite indicating that the nucleation happens according to the natural process of bio-mineralization: the nano-size dimension of HA crystallites is responsible for the large broadening of reflections in the pattern, they are growing inside collagen fibres with their c-axis preferentially oriented parallel to the direction of orientation of the collagen fibres⁸.

The resolution of the spectra are quite low, however it can be stated that no secondary phase is appreciated except for FeHA/Coll25 sample where Calcium Carbonate has been detected in traces (Fig. 1) as also confirmed by Tg-DTA analysis in Fig. 3 showing a peak

in the DTA curve at 400°C corresponding to the decomposition of calcium carbonate.

In the Fig. 1 the peak at $2\theta \approx 36^\circ$ relative to sample FeHA/Coll50 can be attributed to growing amount of magnetite as expected since the formation of magnetite is favoured at temperature above 40°C⁷.

During the FeHA nucleation process, the morphology of FeHA crystallites is influenced by the synthesis temperature, as confirmed by XRD analysis: for samples synthesized at higher temperatures (FeHA/Coll40 and FeHA/Coll50) a more crystalline FeHA phase is detected (Fig. 1) compared to the FeHA/Coll25 composite.

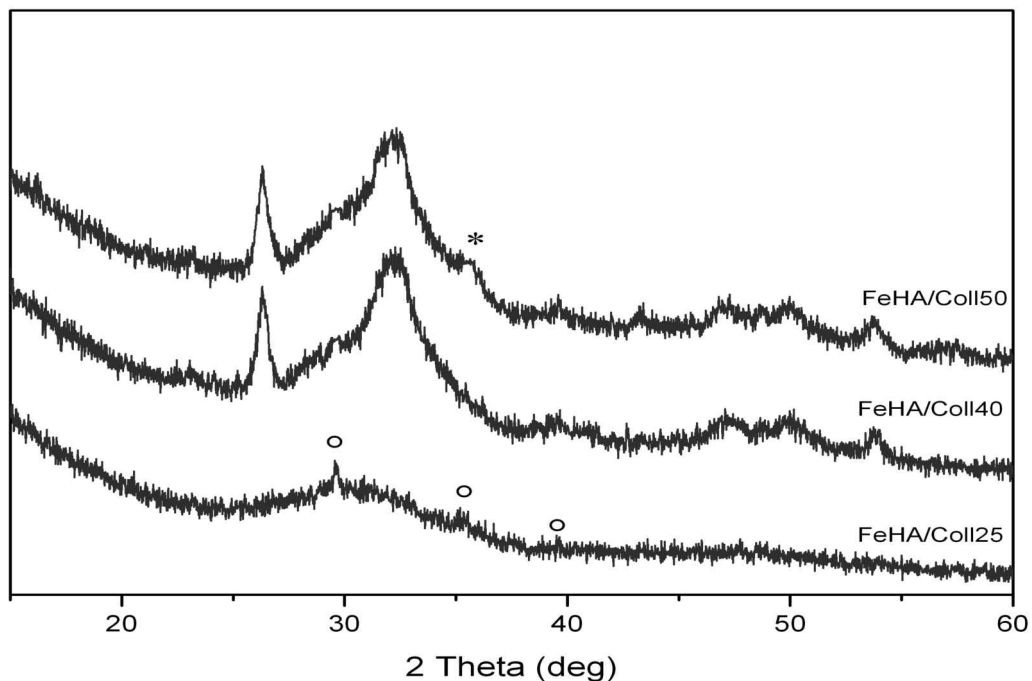


Fig. 1. XRD spectrum of FeHA/Coll25, FeHA/Coll40 and FeHA/Coll50. The peak identified by * corresponds to magnetite while peaks identified by ° correspond to calcium carbonate.

7.3.2 Thermogravimetric analysis (TG-DTG)

Thermogravimetric investigations (STA 449 Jupiter Netzsch Gerätebau, Selb, Germany) were carried out on dried samples using an alumina crucible in air and a heating ramp rate of 10 °C/min, from 20 to 1200 °C to estimate the amount of mineral phase bound to collagen phase.

The thermal decomposition profile of collagen used as starting material in the production of composite materials (Fig. 2) shows three distinct weight losses, attributable to three processes activated by the temperature increase during the analysis, according to the

thermal cycle ramp performed from 20 °C to 800 °C. The first weight loss was observed in the range temperature 50-150 °C and it was due to the loss of water, the second weight loss occurred between 200 and 450 °C and it was attributed to depolymerization and decomposition of collagen molecules into gelatin fragments, followed by a third final loss of weight in the range 500-650 °C due to the combustion of the organic residue composite⁹.

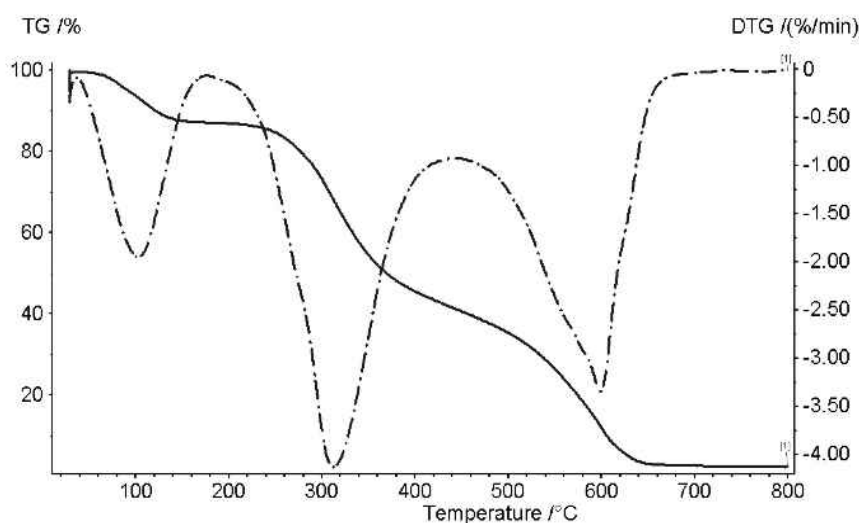


Fig. 2. Thermal decomposition profile (TG-DTG) of freeze-dried pure collagen

The TG-DTG curves relative to the composite FeHA/Col prepared at three different temperatures using the weight ratio 70:30 are shown in Fig. 3: the plot appear modified if compared with those of pure freeze-dried collagen, demonstrating the interaction of inorganic phase with collagen fibers.

The overall loss of weight undergone by the samples (Fig. 3), derived from the sum of the effects of processes of dehydration and thermal decomposition of collagen over that of dehydration and decarbonation of hydroxyapatite. From consideration of the overall losses suffered, the reaction yield of FeHA synthesis, turns out to be rather high.

In the case of the profile of thermal decomposition of the composite FeHA/Coll (70/30), there are still three distinct weight losses in three temperature ranges. In the range of 50-100 °C, there is a reduction in weight by about 10%, due to the loss of water adsorbed on the surface of the particles of HA and that of hydration of the collagen molecules. At about 200 °C starts the subsequent weight loss, as a result of a first

degradation and decomposition of collagen. The processes of thermal decomposition are completed in the neighborhood of 550 °C, about 100 °C before compared to pure collagen, with an overall decrease of about 40% of the total weight.

Thermal analysis (Fig. 3) performed on FeHA/Coll25, FeHA/Coll40 and FeHA/Coll50 composites showed the same extent of mineralization for all the composites: a loss of collagen of about 40 wt% with respect to the total mass of the sample was detected, so that the final weight ratio was fixed to 60/40 wt/wt instead of 70/30 wt/wt of the one nominally set up.

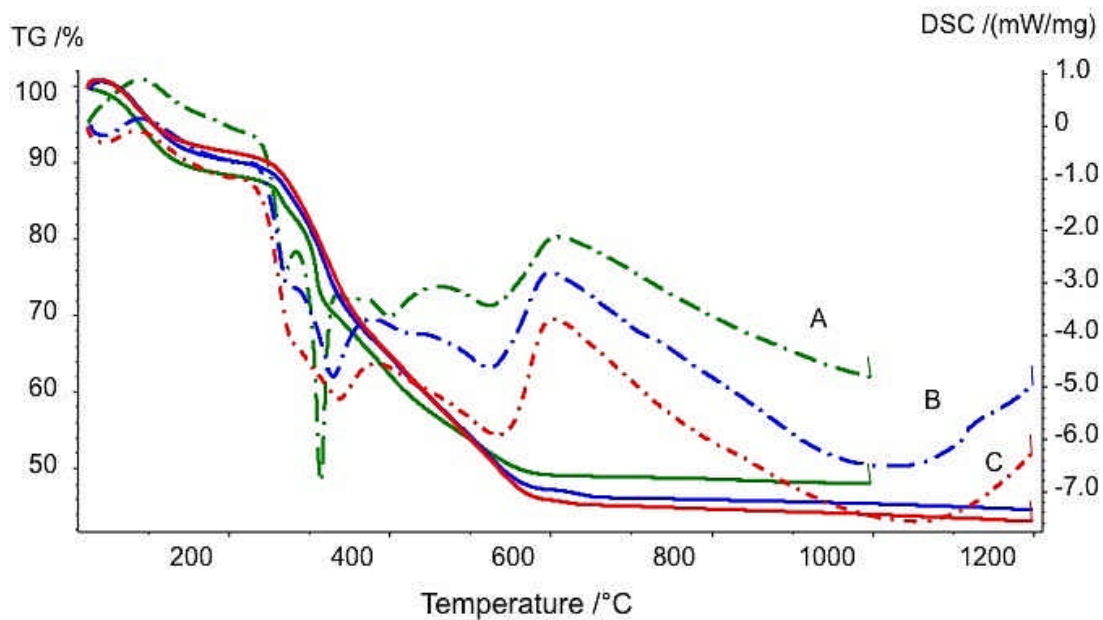


Fig. 3. TG–DTG curves of freeze-dried (A) FeHA/Coll25; (B) FeHA/Coll40 and (C) FeHA/Coll50

7.3.3 Infrared spectroscopy analysis (FTIR)

Infrared spectroscopy analysis (FTIR) were performed by using a Thermo Nicolet Avatar 320 FT-IR Spectrometer on pellets (13 mm Ø) prepared by mixing 2 mg of ground sample with 100 mg of KBr in a mortar and pressing. The analysis was used to determine the typical bands relative to functional groups present in apatite and collagen and also to study the probable interaction between organic and inorganic phases in the composites.

Fig. 4 compares FeHA spectrum with spectra relative to FeHA/Collmix composite obtained by simply mixing of FeHA nanopowder and collagen and FeHA/Collnucl composite obtained by nucleation of FeHA on collagen fibres.

In table 1 are reported wave number signals characteristic of collagen and hydroxyapatite.

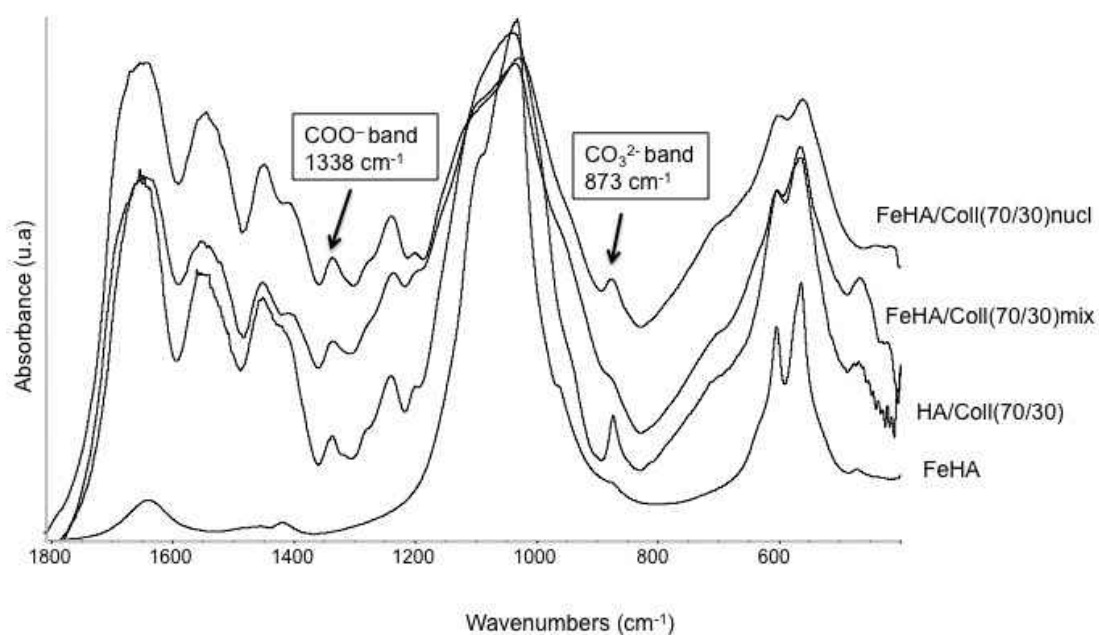


Fig. 4. FTIR analysis of FeHA/Coll 70/30 composite compared with FeHA, HA/Coll and the composite (FeHA/Coll(70/30)mix) obtained by mixing of the mineral phase with the collagen.

Functional group	Wave number (cm ⁻¹)	Vibrational motion
Carboxylic Acid -COOH	1000-1300 1340 1600-1700 3000	bending C-O Asymmetric stretching (COO) stretching (C=O) (O-H)
Secondary amide -CONHR	1550 1680 3300	bending (C-N) stretching (C=O) stretching (N-H)
-CO ₃	850-880 1410-1545 2350	bending stretching stretching
-PO ₄	560-600 1630 980-1100	bending (O-P-O) stretching (HPO ₄) stretching (P-O)
-OH	600 1640 3000-3600	bending (O-H) stretching

Table 1. Intervals of wave numbers (cm⁻¹) characteristic of collagen and hydroxyapatite

A proof of the chemical interaction between FeHA and collagen fibres comes from the study of the FTIR spectra (Fig. 4), in which a shift from 1340 to 1338 cm^{-1} of the band corresponding to the stretching of $-\text{COO}$ group of collagen was observed. This shift is absent in the composite material obtained by simply mixing of FeHA nanopowder and collagen (FeHA/Coll (70/30) mix) (Fig. 4). The band at 873 cm^{-1} is stronger for the nucleated FeHA/Coll scaffolds with respect to the pure FeHA, indicating that the nucleation of FeHA into collagen implies carbonation of the inorganic phase. Moreover the carbonation can be assigned only to the B position as confirmed by the absence of the band at 880 cm^{-1} .

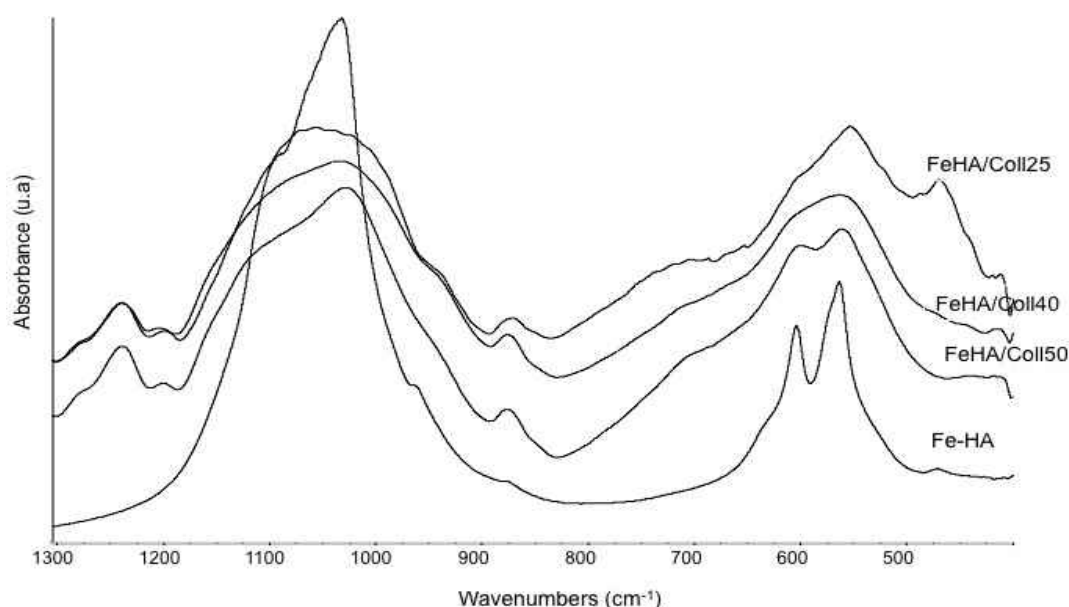


Fig. 5. FTIR analysis of FeHA and FeHA/Coll composites synthesized at 25; 40 and 50°C.

In Fig. 5 a comparison between spectra of FeHA/Coll composites synthesized at different temperatures is reported: normally the low site symmetry of the PO_4^{3-} tetrahedron of crystalline HA splits the ν_4 PO_4^{3-} contour into three components which fall near 630, 600, and 550 cm^{-1} .^{10,11} The triplets, according to the synthesis temperature, tend to merge in two and one broad band, respectively for the composite FeHA/Coll50, FeHA/Coll40 and FeHA/Coll25. All these features indicate that the mineral phase nucleated on collagen fibres is non-stoichiometric and that decreasing the synthesis temperature results in an increase in the amorphous character of the apatite resembling that of newly formed bone.

7.3.4 Morphological analysis by scanning electron microscope (SEM) and by transmission electron microscope (TEM)

Scaffolds morphology determination was carried out by scanning electron microscopy (SEM; Stereoscan 360, Leica, Cambridge, UK). SEM analysis shows, for all the composites, assembled collagen fibres completely covered by the mineral phase (Fig. 6F, I, L). The morphology of the sample FeHA/Coll25 (Fig. 6F) appears very similar to that of natural bone: nano-globular apatite crystals cover completely the collagen fibres giving to the material a porous architecture with a network of micro-macro porosity (Fig. 6D) to allow cell adhesion and proliferation.

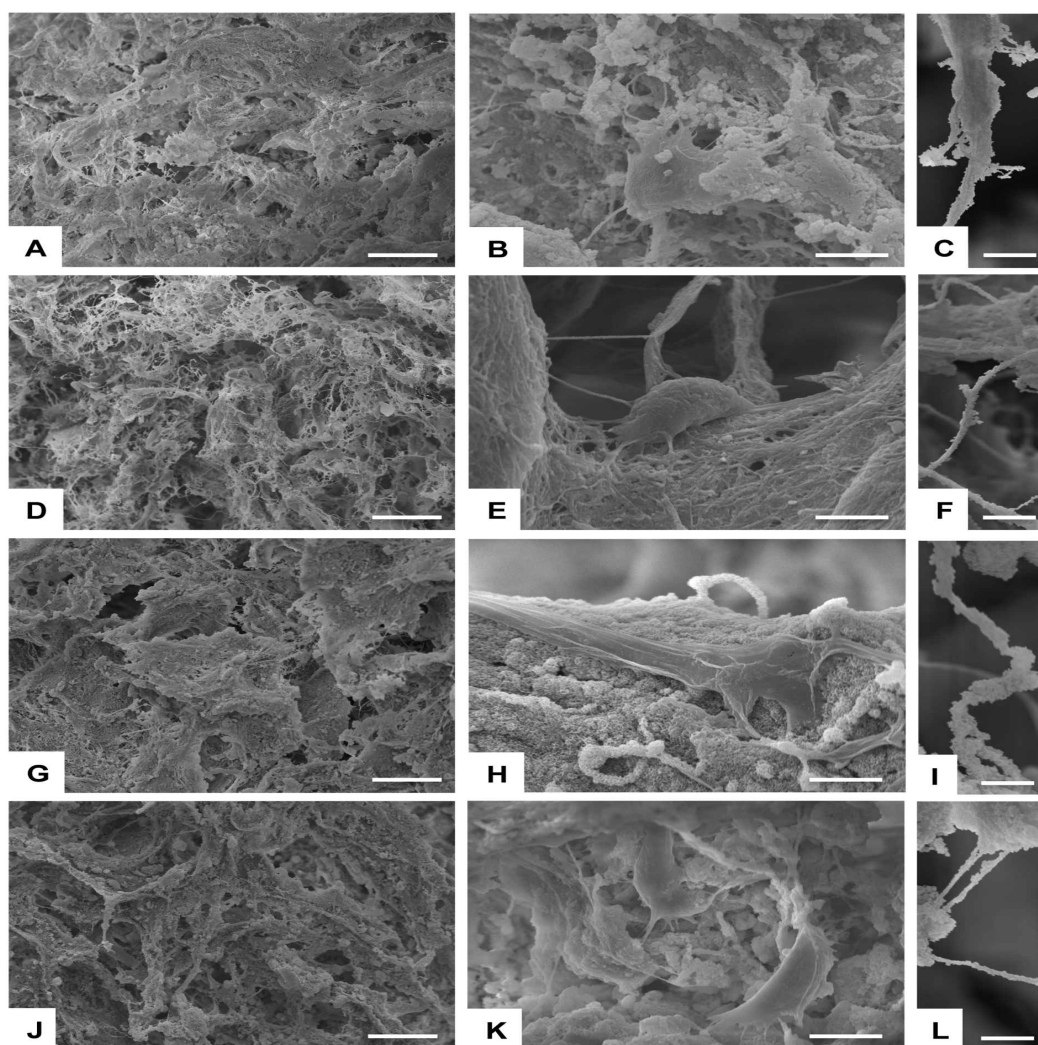


Fig. 6. A,D,G,J) Detailed analysis of morphology of bio hybrid scaffolds B,E,H,K) Detailed analysis of cell morphology of cell-seeded scaffolds at day 1. C,F,I,L) Details of morphological features of the mineral phase. A,B,C) HA/Coll. D,E,F) FeHA/Coll25. G,H,I) FeHA/Coll40. J,K,L) FeHA/Coll50. Scale bars: A,D,G,J) 100 μ m. B,E,H,K) 10 μ m. C,F,I,L) 5 μ m.

For samples FeHA/Coll40 (Fig. 6I) and FeHA/Coll50 (Fig. 6L) composites, the higher synthesis temperature causes the growing of bigger apatitic crystals with a plate-like morphology that, thickening the collagen fibres, reduce the porosity of the samples (Fig. 6 G,J).

Morphological investigations on the apatitic nuclei and on their interaction with the collagen fibres are augmented by TEM observations of samples FeHA/Coll40 and FeHA/Coll50. Low magnification images provide evidence of the close assembly of the apatitic nuclei on the surface of collagen fibres (Fig. 7, left). In several cases, overlayers are observed, anyway resulting from the stacking of FeHA nano-particles on a “primary layer” in close contact with the surface of the collagen matrix (Fig. 7, inset).

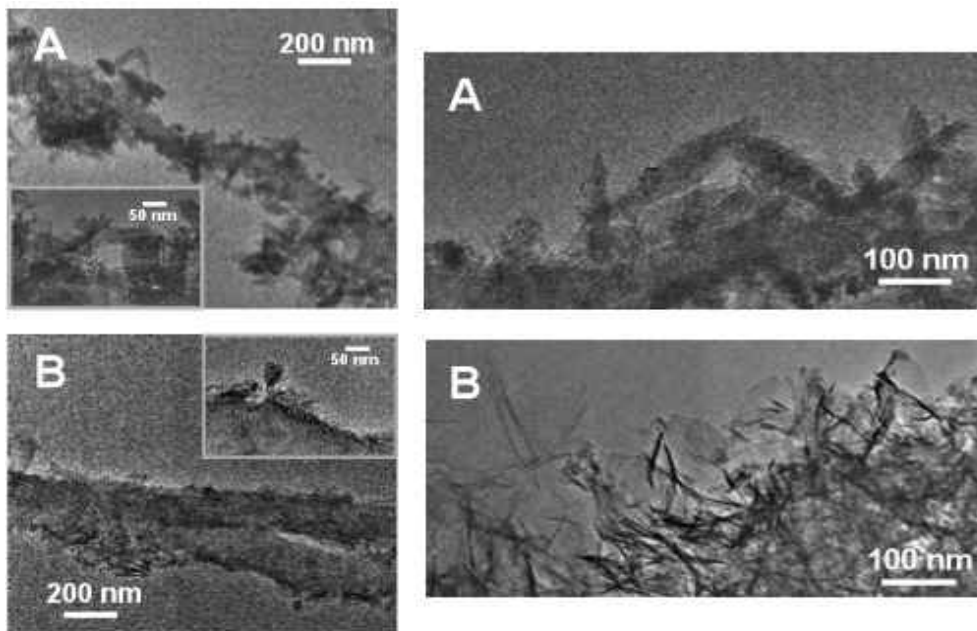


Fig. 7. (Left) TEM images of the external border of the assemblies of apatite particles around collagen fibres. Panel A: FeHA/Coll40; Panel B: FeHA/Coll50. Insets: view, at higher magnification, of the interface between collagen and the mineral phase.

(Right) TEM images representative of the assembly of apatite particles around collagen fibres. Panel A: FeHA/Coll40; Panel B: FeHA/Coll50.

Noticeably, the morphology of the apatitic nano-particles appears different in dependence on the synthesis temperature. As better observed in the images at higher magnification of the external border of FeHA assemblies on the collagen fibres, many of the particles of FeHA/Coll40 projected on the image plane a rectangular shape, 150-200 nm long and 25-50 nm width (Fig. 7A, right). Differently, the particles of FeHA/Coll50 produce two

different projections on the image plane, one resulting in tabular shapes ca. 100-150 nm (length) x 75-100 nm (width) in size, characterized by a weak contrast, and the other in needle-like shapes ca. 100-150 nm (length) x 5-10 nm (width), appearing significantly darker. On the base of the mass-thickness contrast mechanism¹² they might then correspond to “side view” of the particles with tabular morphology. It is worth to notice that for both materials no particles with significant different morphology, likely due to separated iron oxide phases have been observed.

7.3.5 Chemical analysis by ICP

ICP-OES quantitative analysis, using an inductively-coupled plasma-atomic emission spectrometer, (ICP-OES: Liberty 200, Varian, Claython South, Australia), was applied to determine the content of the chemical elements (Fe, Ca and P) constituting the mineral phase of biohybrid materials.

	(Ca+Fe)P (mol)	Ca/P (mol)	Fe/Ca (mol)	Fe (wt%)
HA/Coll	-	1.544	-	-
FeHA/Coll25	1.940	1.708	0.136	2.968
FeHA/Coll40	1.691	1.426	0.186	3.833
FeHA/Coll50	1.699	1.380	0.231	4.432

Table 2. ICP features of HA/Coll and FeHA/Coll composites synthesized at 25, 40 and 50°C.

For FeHA/Coll40 and FeHA/Coll50 composites the Ca/P molar ratio is lower with respect to the HA/Coll reference while the (Ca+Fe)/P molar ratio is very close to the theoretical one (1.68), confirming the effective replacement of Ca ions with Fe ions (Table 2). Moreover, for these two samples the highest substitution of iron ions in the HA lattice is reached since the amount of iron ions detected by ICP resembled the nominal one fixed

for the synthesis with an experimental mistake of about 15%, indicating that the higher temperature favours the replacement of Fe ions instead of Ca in agreement with the results previously published for the synthesis of the pure FeHA⁷.

In the case of FeHA/Coll25 sample, the Ca/P molar ratio and (Ca+Fe)/P molar ratio are higher than the ones of the reference (HA/Coll) (Table 2) due to the presence of Calcium Carbonate; at the same time the formation of Calcium Carbonate during the synthesis causes a depletion of Calcium ions available for the formation of the apatitic phase, so that the amount of iron ions entered in the HA lattice results lower ($\text{Fe/Ca} = 0.136 \text{ mol}$) than the nominal one fixed for the synthesis of FeHA ($\text{Fe/Ca} = 0.20 \text{ mol}$).

7.3.6 Magnetic properties of FeHA/Coll composite

The magnetic properties (Fig. 8) of the FeHA/Coll samples are affected by the substitution of iron ion in the HA lattice and hence by the synthesis temperature, as reported in a previously work⁷. The magnetic curves measured (black curves) can be decomposed into two components: one background component (blue curves) that increases linearly with field, typical for paramagnetism far away from saturation, probably assigned to collagen, and one following a Brillouin function (red curves) that is due to the superparamagnetism of FeHA. The paramagnetic background is of comparable magnitude for all the samples investigated here, with a trend towards stronger background for those samples that were synthesized at higher temperatures. For the sample FeHA/Coll25 (Fig. 8A), the low crystallization and the scarce organization of the HA lattice cause a poor coordination level of the iron ions inside the crystalline structure, reflecting in a low magnetization in the sample (0.091 emu/g at 7T). Higher magnetization values are measured for samples synthesized at higher temperatures, indicating that temperature influences the substitution and the coordination of the iron ions in the HA lattice, as confirmed also by ICP analysis. FeHA/Coll40 has a value of magnetization (0.182 emu/g at 7T; Fig. 8B) quite low for the disturbing effect of collagen on the measure and much lower than the one of FeHA/Coll50 (1.103 emu/g at 7T; Fig. 8C) in agreement with the presence of magnetite in sample prepared at the highest temperature, that even if in very low concentration (as can be argued by the presence of a feeble peak in XRD patten in spite of the high scattering power of magnetite) contribute consistently to the increase of magnetization.

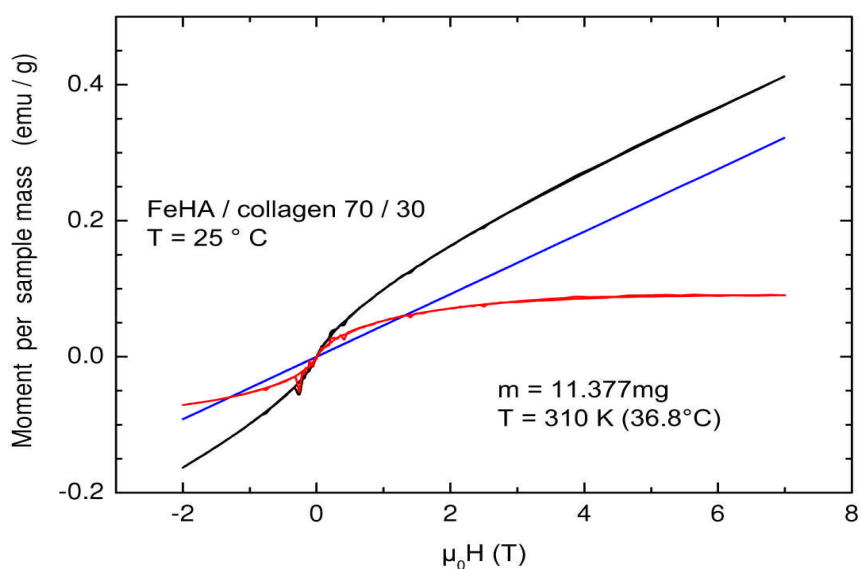


Fig. 8A. Magnetic measurements of FeHA/Coll25. Black: measured curves. Blue and red: non-saturating and saturating paramagnetic contributions, respectively. Non-saturating contributions are roughly equal for all three samples.

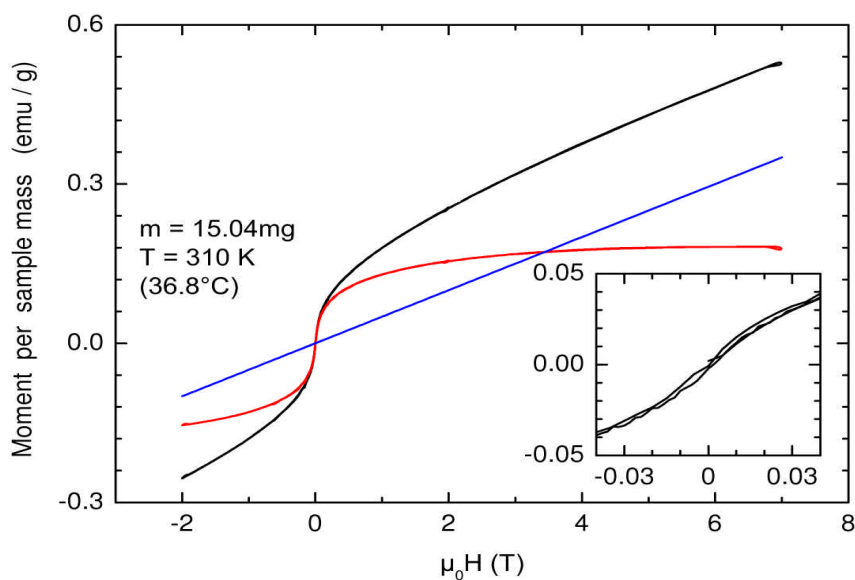


Fig. 8B. Magnetic measurements of FeHA/Coll40. Black: measured curves. Blue and red: non-saturating and saturating paramagnetic contributions, respectively. *Insets:* small hysteresis indicates the superparamagnetic nature of the samples.

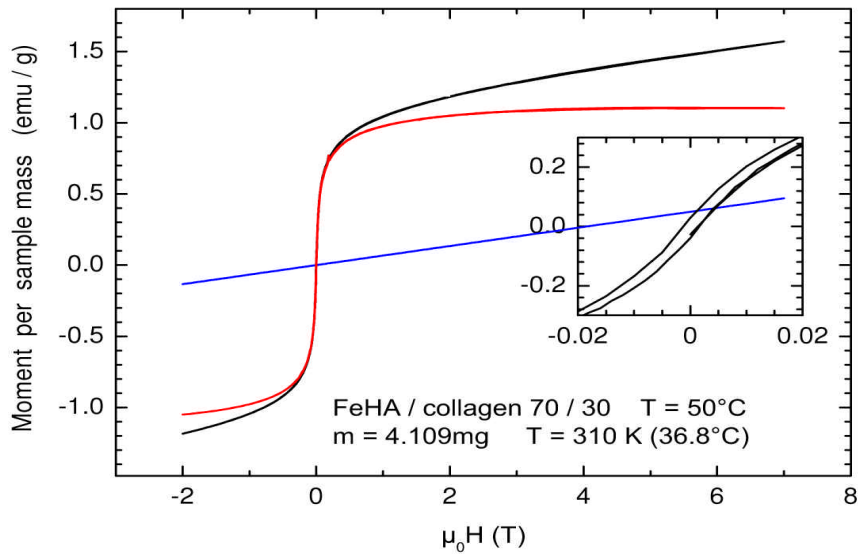


Fig. 8C. Magnetic measurements of FeHA/Coll50. Black: measured curves. Blue and red: non-saturating and saturating paramagnetic contributions, respectively. *Insets:* small hysteresis indicates the superparamagnetic nature of the samples

7.4 *In vitro* evaluation of FeHA/Coll scaffolds

MG-63 human osteoblast-like cells were cultured within the biohybrid FeHA/Coll scaffolds for 1, 3 and 7 days. Non magnetic HA/Coll, already tested in several *in vitro* and *in vivo* studies was used as control¹³.

Live/Dead assay was performed for each time point without magnetic field application in order to evaluate the cell viability of the novel magnetic FeHA/Coll scaffolds. All groups demonstrate high cell viability representing good biocompatibility, with FeHA/Coll25 presenting a better performance than FeHA/Coll40 and FeHA/Coll50 (Fig. 9A-C). Moreover the cell morphology, visualized with Live/Dead Calcein staining, shows that cells seeded on FeHA/Coll25 have more widespread morphology, respect to the other groups (Fig. 9A-C).

This could also be seen with immunofluorescence staining against actin, where already at day 3 FeHA/Coll25 group shows better cell adhesion and distribution, exhibiting more characteristic osteoblast morphology throughout the scaffold (Fig. 9D).

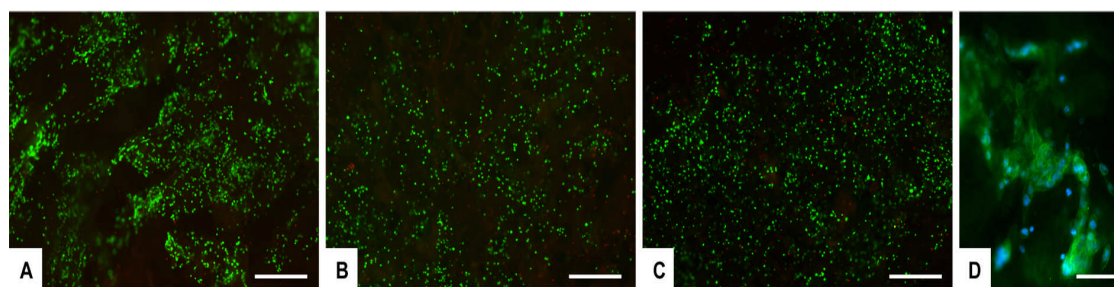


Fig. 9. Analysis of cell viability and morphology. Cell viability was analysed by the Live/Dead assay (Calcein acetoxymethyl stains live cells in green, Ethidium homodimer-1 stains dead cells in red). A,B,C) FeHA/Coll25, FeHA/Coll40, FeHA/Coll50 respectively at day 3. D) FeHA/Coll25 at day 7, cell morphology was analysed by actin staining (actin is shown in green, DAPI in blue). Scale bars: A-C) 500 μm , D) 100 μm

For a detailed analysis of cell morphology within these composite scaffolds, SEM characterization has been performed and it reveals very high cell integration within the nanostructure of the scaffold for all groups. The complex HA/collagen fibre mesh and how cells exploit such a matrix can be observed, illustrating high biocompatibility and osteoinductivity performances of such scaffolds (Fig. 6B, E, H, K).

From the above viability and morphological characterization, it results that the cell behavior on FeHA/Coll40 and FeHA/Coll50 scaffolds is very similar. Considering the higher magnetization of FeHA/Coll50 sample, a detailed cell proliferation assay was done comparing FeHA/Coll25 and FeHA/Coll50 to the control scaffold.

Cell proliferation was quantified by the MTT assay and results were plotted on graph (Fig. 10). As it is possible to observe in Fig. 10A, the magnetic material groups present a high rate of cell proliferation, equal or even higher than control group without static magnetic field application (SMF). FeHA/Coll25 presents better performance than FeHA/Coll50 scaffold, with a statistically significant difference seen at day 3 ($p \leq 0.001$). FeHA/Coll25 scaffold has therefore the potential to strongly enhance cell proliferation at an early stage, and focusing on tissue regeneration application this fact could be extremely important to shorten the regeneration timing. Even though, at day 7 no significant difference was seen between the magnetic scaffold groups and the control group, already used in clinic application.

Overall, both novel magnetic FeHA/Coll composites show high biocompatibility. The *in vitro* performance of the magnetic biohybrid composites seems to be affected more by their chemical and morphological features than by their magnetic properties. In fact, the

best *in vitro* performance of FeHA/Coll25 can be assigned, as previously described, to its more open porosity that resembles that of the natural bone, respect to FeHA/Coll50 composite, which allow increased cell adhesion and proliferation.

In order to address magnetic properties contribution to *in vitro* performance, the MTT experiment was performed also with the application of a 320 mT static magnetic field (SMF). An overall increase in cell proliferation due to the SMF application is observed. In particular, a statistical significant difference is seen at day 3 ($p \leq 0.01$) and at day 7 ($p \leq 0.05$) (Fig. 10B). Looking in detail to the behavior of cells seeded into scaffolds under SMF application it possible to observe that, again, FeHA/Coll25 shows the best performance, with a trend comparable to the results obtained without SMF application (Fig. 10C).

FeHA/Coll25 shows a significantly higher cell proliferation compared to the control group for every time point (day 1 $p \leq 0.05$, day 3 and day 7 $p \leq 0.001$), demonstrating that the SMF enhances cell proliferation, in fact this difference between FeHA/Coll25 does not seen at day 7 without SMF application (Fig. 10A). Also the FeHA/Coll50 scaffold shows a significant increase in cell proliferation at day 7 compared to the control group ($p \leq 0.01$). These results underline how the superparamagnetic properties of the novel scaffolds which are emphasized by the application of an external static magnetic field enhancing cell proliferation.

Gene expression analysis shows an increase in Collagen type I, alpha 1 (Col1A1) and Runt-related transcription factor 2 (RUNX2) in cells cultured in the magnetic scaffolds respect to control (1.53-fold and 1.13-fold, respectively). Moreover, the application of SMF increases this difference even further (2.91-fold Col1A1, and 2.12-fold RUNX2).

The above results show that not only the novel magnetic scaffolds are biocompatible, but moreover if they are subjected to a SMF application, their performance in cell proliferation is even improved respect to the control scaffold already used in clinic.

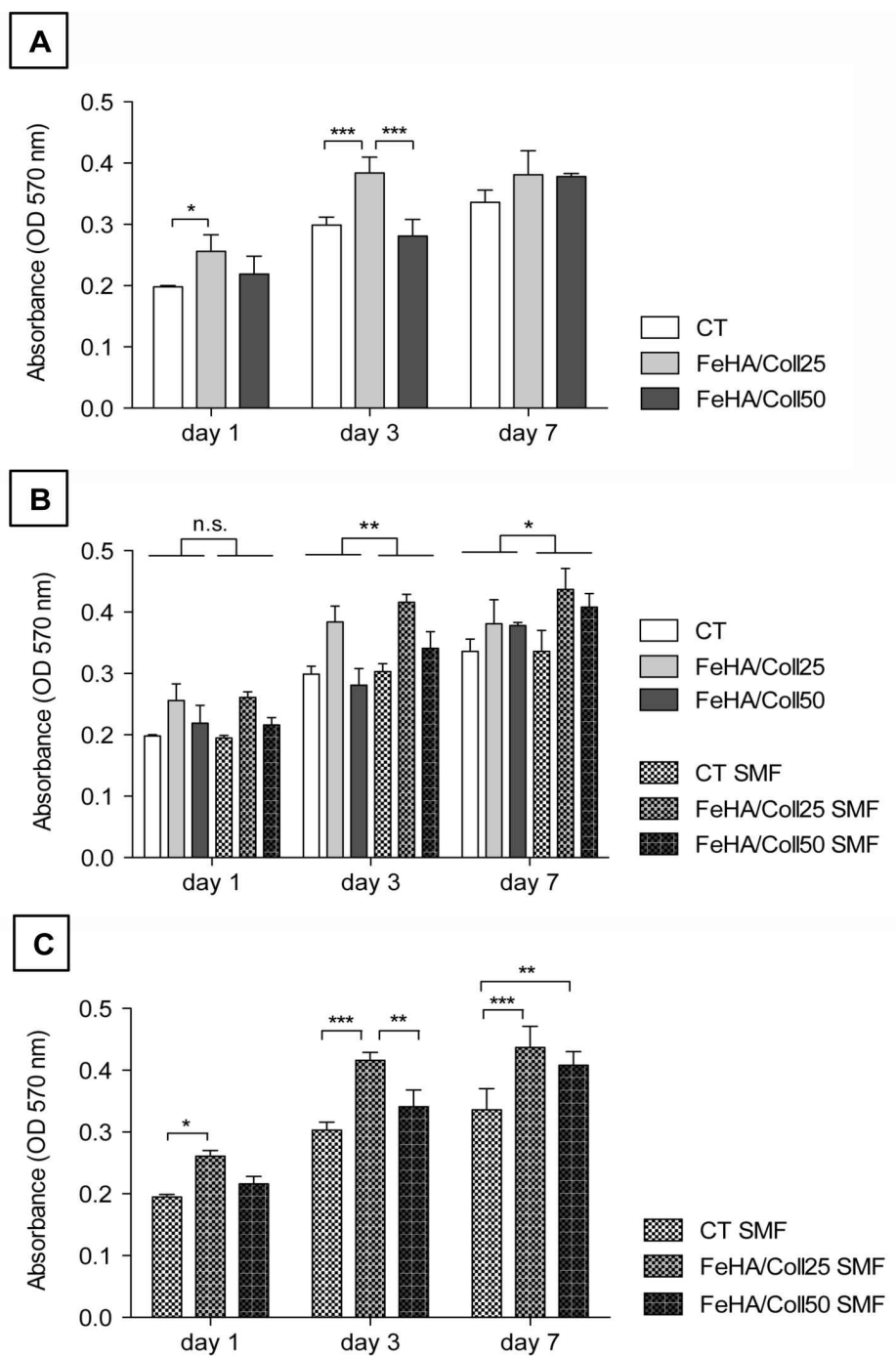


Fig.10. Cell proliferation assay. MTT assay was performed 1, 3 and 7 days after MG63 human osteoblast-like cells seeding (n=3), either without (A,B) or with (B,C) the application of a static magnetic field. A) Cell proliferation is higher for FeHA/Coll25 composite at day 1 and day 3, B) Application of a static magnetic field (SMF) results in an overall increase in cell proliferation, C) Magnetic scaffold have the best performance under the application of a SMF. * $p \leq 0.05$, ** $p \leq 0.01$, *** $p \leq 0.001$.

7.5 Development of a three-layer magnetic scaffold

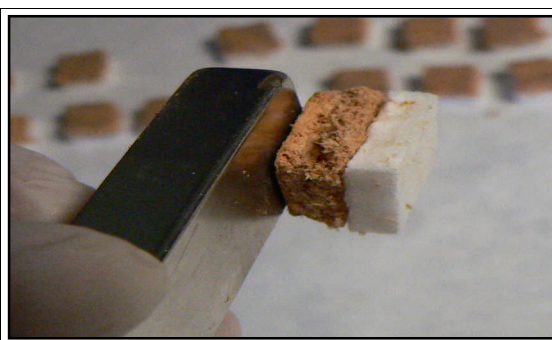
Taking into consideration the good results coming from the pre-clinical and clinical application of Maioregen® as one of the most effective scaffold^{14,15} in the current innovative orthopaedic practise, a three-layered structure resembling the sub-chondral bone, the tide-mark and the cartilagineous layer as been designed and developed following the same paradigm⁸ but nucleating FeHA instead HA as the mineral component of the composite.

To realize the scaffold with different grade of mineralization, mimicking the complexity of the osteochondral region and having an associated magnetization gradient (Fig. 10a), three different layers were prepared following the nucleation method described (§ 7.2) and assembled: (a) the upper one, mimicking the cartilagineous layer, and composed of pure collagen; (b) the intermediate one, mimicking the tidemark, and composed of FeHA/Coll (40/60 wt%) composite; (c) the lower one, mimicking the sub-chondral bone, and composed of FeHA/Coll (70/30 wt%) composite.



a)

Fig. 10a. Picture of tree-layer scaffold: the upper layer was constituted of FeHA/Coll (70/30wt%), the intermediate of FeHA/Coll (60/40 wt%) and the lower one of pure collagen.



b)

Fig. 10b. Picture of tree-layer scaffold attracted by a magnet

The nucleation of the superparamagnetic phase in different concentration from 0% (in the layer charged for cartilage regeneration) up to 70% (in the layer charged for sub-condral bone regeneration) generated also a magnetic gradient, as schematically described in Fig. 11.

This design has been conceived to exploit the simple activation that the magnetized

scaffold can exert on osteoblast cells, as previously demonstrated^{16,17} and in addition to attract growth factors or other important biomolecules linked to magnetic nanoparticles. In fact FeHA in form of nanoparticles could be injected as magnetic carriers, and, exploiting the magnetic guiding process, recalled from the physiological environment towards the three-layered scaffold up to the scaffold/sub-chondral bone interface. Tuning the intensity of the external static magnetic field it can be also envisage to direct the carriers specifically into one of the scaffold layer on demand following a particular regenerative need. A simple horizontal assemblage of two plastic tubes, having the scaffold in the middle, was realized and by means of XRD and ICP analysis was proved that FeHA nano-carriers contained in a suspension inside one of the plastic tube can be recalled towards the highly mineralized and magnetized layer of the scaffold (in contact with the second plastic tube) under the action of an external static magnetic field of 320 mT.

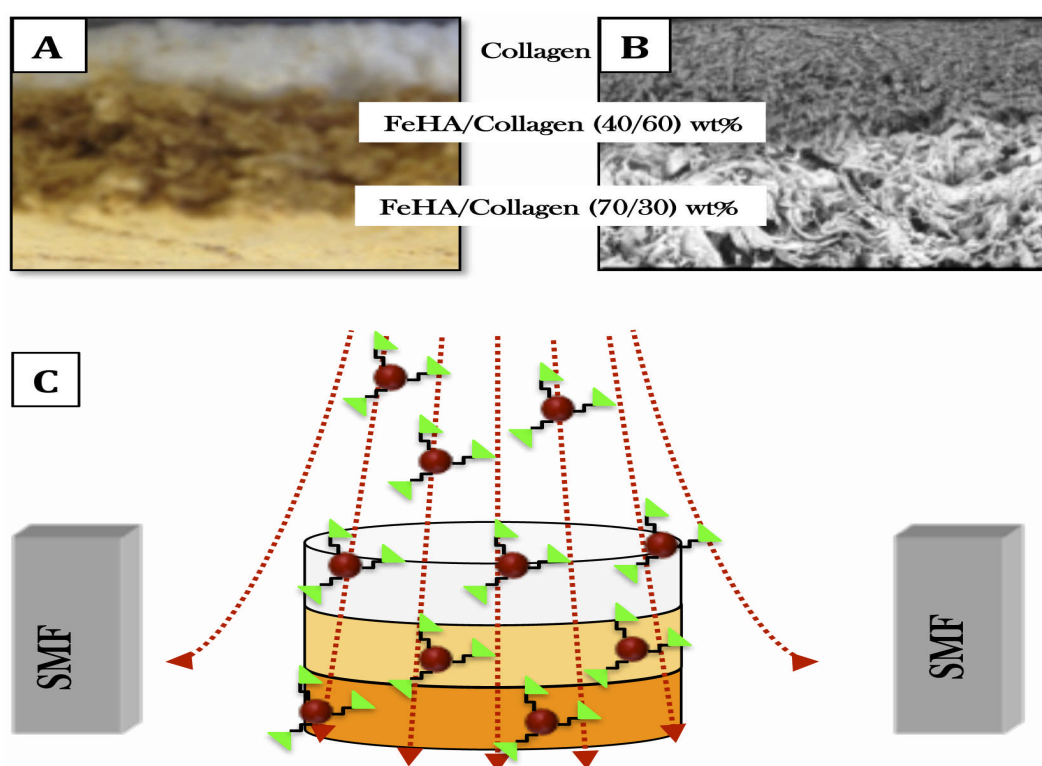


Fig. 11. Development of a 3-layer magnetic scaffold. A) Photo of the three-layer magnetic scaffold. B) ESEM micrograph of scaffold morphology: three different layers are distinguishable due to the different content of mineral phase that increases moving from the upper (cartilagineous: collagenic only) to the intermediate (tidemark: FeHA/Coll 40/60 wt% composite), and to the lower layer (bone layer: FeHA/Coll 70/30 wt% composite). C) Scheme of the activation that the magnetized scaffold can exert on osteoblast cells or to recall growth factors.

Additionally the magnetically graded scaffold allows the positional/mechanical stabilization of the scaffold into the osteochondral defect thanks to the merging of a small magnet into the sub-chondral bone¹⁸. Such a tool prevents the occurring of micro-movements at the regenerative interface and opens a completely new area of investigation related to a morphological control in the newly formed tissue. In fact the strength lines of the magnetic field induce a specific anisotropic imprinting, favouring the growth of a lamellar mechanically competent new bone tissue as recently demonstrated.

7.6 Conclusion

FeHA/Coll magnetic biohybrid composites were prepared through a biologically inspired mineralization process. The introduction of the iron ions into the apatitic lattice during the stage of HA nucleation induces in the final composite (FeHA/Coll) those chemico-physical, structural and morphological features typical of newly formed bone along with superparamagnetic properties. The synthesis temperatures influence the chemico-physical features of the magnetic biohybrid scaffolds and hence their performance biological performance.

In vitro investigations indicate firstly the biocompatibility of these novel magnetic biohybrid scaffolds showing good ability to support cell adhesion and proliferation. Moreover, the superparamagnetic properties of the novel scaffolds are emphasized by the application of an external static magnetic field improving their performance in cell proliferation respect to the control scaffold already used in clinic.

These first positive results constitute the necessary prerequisites for further investigations into the potential application of the magnetic scaffolds to control and direct osteogenesis and/or simultaneous chondrogenesis.

References

1. A. Tampieri, G. Celotti, E. Landi. *Anal. Bioanal. Chem.* **2005**, 381, 568.
2. S. Mann. *Bio-mineralization: Principles and Concepts in Bioinorganic Materials Chemistry*, Oxford University Press, **2001**
3. J. Matthew, X. C. Olszta, J. Sang Soo, K. Rajendra, K. Yi-Yeoun, M.J. Kaufman, E. P. Douglas, B. L. Gow. *Mat. Sci. Eng.* **2007**, 58, 77.
4. A. Tampieri, S. Sprio, M. Sandri, F. Valentini. *Trends in Biotechnol.* **2011**, 29, 10.
5. A. Tampieri, G. Celotti, E. Landi, M. Sandri, N. Roveri, G. Falini. *J. Biomed. Mater. Res. A.* **2003**, 67, 618.
6. M.T.J. Jiang, M.A. Rossi, M.A. Morales, E.M.B Saitovitch, D.E. Ellis. *Phys. Rev. B: Condens. Mater. Phys.* **2002**, 66, 224107.
7. A. Tampieri, T. D'Alessandro, M. Sandri, S. Sprio, E. Landi, L. Bertinetti, S. Panseri, G. Pepponi, J. Goettlicher, M. Banobre-Lopez, J. Rivas. *Acta Biomater.* **2012**, 8, 843.
8. A. Tampieri, M. Sandri, E. Landi, D. Pressato, S. Francioli, R. Quarto, I. Martin. *Biomaterials.* **2008**, 29, 3539.
9. A. Bigi, A. Ripamonti, G. Cojazzi, G. Pizzuto, N. Roveri, M. H. J. Kock. *Int J Biol Macromol.* **1991**, 13, 110.
10. L. M. Miller, V. Vairavamurthy, M. R. Chance, R. Mendelsohn, E. P. Paschalis, F. Betts, et al. *Biochim Biophys Acta.* **2001**, 1527, 11.
11. C. Rey, M. Shimizu, B. Collins, M.J. Glimcher. *Calcif. Tissue. Int.* **1990**, 46, 384.
12. D. B. Williams, C. Barry Carter. *Materials Science.* **2009**, 1, 717.
13. S. Scaglione, P. Giannoni, P. Bianchini, M. Sandri, R. Marotta, G. Firpo, U. Valbusa, A. Tampieri, A. Diaspro, P. Bianco, Quarto *Sci. Rep.* **2012**, 2, 274.
14. E. Kon, M. Delcogliano, G. Filardo, M. Busacca, A. Di Martino, M. Marcacci. *Am. J. Sports Med.* **2011**, 39, 1180.
15. E. Kon, F. Vannini, R. Buda, G. Filardo, M. Cavallo, A. Ruffilli, M. Nanni, A. Di Martino, M. Marcacci, S. Giannini. *J. Bone Joint Surg. Am.* **2012**, 94, 8.
16. S. Panseri, C. Cunha, T. D'Alessandro, M. Sandri, G. Giavaresi, M. Marcacci, J. C. T. Hung, A. Tampieri. *Nanobiotechnol.* **2012**; 10, 32.
17. S. Panseri, C. Cunha, T. D'Alessandro, M. Sandri, A. Russo, G. Giavaresi, M. Marcacci, C.T. Hung, A. Tampieri. *PLoS One.* **2012**, 7, 38710.

18. A. Russo, T. Shelyakova, D. Casino, N. Lopomo, A. Strazzari, A. Ortolani, A. Visani, V. Dediu, M. Marcacci. *Med Eng. Phys.* **2012**.

CHAPTER 8

BIOACTIVE CALCIUM PHOSPHATE BONE CEMENTS: BASIC CONCEPTS

Calcium phosphate cements (CPCs) are increasingly used as bone substitute materials to repair bone defects resulting from trauma or disease¹.

A ceramic bone cement consists in a powder mixture which upon mixing with a liquid phase results in a paste which spontaneously sets at body temperature. Upon mixing, dissolution of the calcium phosphate powders and precipitation of a new calcium phosphate occurs in the mixing liquid. When the new formed crystals become entangled, hardening occurs. Despite the large range of possible CPC starting compositions, it is generally agreed that only two end-products are formed: (i) brushite, also called dicalcium phosphate dihydrate ($\text{CaHPO}_4 \cdot 2\text{H}_2\text{O}$) or (ii) an apatite with a composition close to that of hydroxyapatite ($\text{Ca}_5(\text{PO}_4)_3\text{OH}$).

In recent years, there has been increasing interest in the use of CPCs for the reinforcement of osteoporotic bone, either to fix osteo-synthesis plates² or for vertebroplasty in which a cement is injected into osteoporotic vertebral bodies^{3,4}.

8.1 Features of injectable bone cement

To be suitable for use in vertebral fracture surgery, the main parameters to consider in the development of bone cements are⁵:

- ✓ **Setting time:** the time required to attain a specified degree of rigidity with particular reference to initial and final setting time. For clinical use a good paste will have a setting time in the range 10-30 minutes. The setting time of a cement can be modified¹:
 - by changing of the powder size: more the size of the powder is small shorter is the setting time;
 - by changing of the powder/liquid ratio: smaller is the amount of liquid added

- to the powder shorter is the setting time;
- adding rapidly available calcium and/or phosphate ions (either pre-dissolved in the mixing liquid or as freely soluble salt): higher salts concentrations shorter is the setting time;
 - by adding crystal nuclei (e.g. apatite nanocrystals for apatite cements): more are nuclei added shorter is setting time,
 - by adding crystal growth inhibitors: more are inhibitors added longer is setting time.
- ✓ **Low setting temperature:** reducing potential thermal injury to surrounding bone or neural elements.
 - ✓ **Injectability:** ability of the cement paste to be extruded through a small and long needle without de-mixing. Demixing occurs when the mixing liquid is too fluid compared with the particle size of the cement powder, resulting in filter pressing: the liquid comes out without the CaP particles.
 - ✓ **Cohesion:** ability to set in a fluid without disintegrating. Good cohesiveness properties could be achieved maintaining a high viscosity for CaP pastes. An increase of the cement viscosity with the addition of a gel forming polymer into the mixing solution increases the cement cohesion⁶.
 - ✓ **Bioactivity:** ability of CaP phase to release ions and drugs active in osteogenesis;
 - ✓ **Bioresorbability:** ability of CaP phase to be progressively resorbed during bone remodelling;
 - ✓ **Osteoconductivity:** creation of an open and interconnected porosity to allow cell adhesion and colonization using selected bio-erodible polymer;
 - ✓ **Mechanical properties:** ability of paste to withstand biomechanical loads after injection in diseased vertebrae. During the setting reaction of the cement, CaP crystals grow and became partially interlocked, hence making the cement mechanically rigid. As CaP are brittle, the compressive strength of a CPC is always much greater than its tensile strength. Most CPC have a tensile strength of 1-10 Mpa, whereas the compression strength ranges between 10-100MPa⁷.
 - ✓ **Radioopacity:** addition of radio-opacifiers into CPC might provide a better visualization during injection, particularly for vertebroplasty. For example, iodide-based organic contrasting agents can be incorporated in a powder or liquid form,

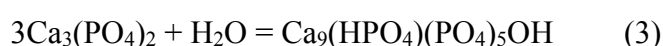
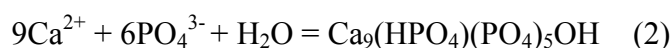
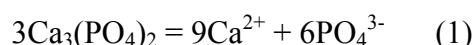
but their slow release from the cement and the occurrence of deadly allergic reactions strongly impairs their use. The use of strontium carbonate appears to be the most suitable choice because the powder has solubility close to that of calcium carbonate, so the powder should be resorbable. Moreover, strontium ions have a good biocompatibility¹.

8.2 Hardening mechanism

The present study aims at looking at these aspects using an apatite cement consisting of α -tricalcium phosphate (α -TCP; $\text{Ca}_3(\text{PO}_4)_2$) powder and an aqueous phase.

During the setting reaction of α -TCP-based hydraulic CPC, two main reactions occur:

[1] the exothermic dissolution of α -TCP and [2] the endothermic precipitation of calcium deficient hydroxy-apatite (CDHA; $\text{Ca}_9(\text{HPO}_4)(\text{PO}_4)_5\text{OH}$) leading to [3] an exothermic global reaction (for α -TCP, this value is close to -133 kJ/mole^8):



During dissolution, the raw powders release calcium and phosphate ions, generating a supersaturation in the solution. Once the ionic concentration reaches a critical value, the nucleation of the new phase occurs, generally surrounding the powder particles. Afterwards, the new phase keeps growing as the dissolution of the reagents goes on. During the first hours the setting process is controlled by the dissolution kinetics of the raw materials, but once the new phase surrounds the reactants, the process is controlled by diffusion across the new phase⁹.

8.3 Cement microstructure and porosity

CPCs are highly porous materials due to free spaces between precipitated crystals, with pore size in the nano/micrometric range. While porosity can be a limitation for the use of these materials in high load-bearing applications, it is crucial for other applications¹⁰.

Thus, porosity is sought to enhance the material's resorbability and the extent of bioactivity by increasing the surface area available for reaction. In the same way, their inherent porosity makes these materials good carriers for controlled drug delivery systems. Not only the total interconnected porosity is relevant for the loading and delivery of drugs, but also the pore dimensions and pore size distribution within the cement, as well as its specific surface area. These parameters vary with the processing conditions of the cements, such as the liquid to powder (L/P) ratio and the particle size of the starting powder. Thus, the total porosity increases when the L/P ratio is increased, and otherwise the particle size of the starting powder conditions the shape and size of the precipitated crystals. In this way, it has been shown that HA needle-like crystals with high specific surface area are obtained when fine α -TCP powder is used, whereas plate-like crystals with lower specific surface area are obtained using coarser powder¹¹.

8.4 Bioactivity and resorption of calcium phosphate cements

One of the most important properties of CPCs is bioactivity. When referring to bone substitutes, a bioactive material is one that is able to bind directly with the surrounding bone without the formation of fibrous tissue^{12,13}. Bioactivity, together with the perfect adaptability of the cement paste during implantation, leads to a stable connection between defect and implant, speeding up bone healing process. Once implanted, CPCs can be resorbed by two different mechanisms. Active resorption regulated by living cells like macrophages or osteoclasts, and/or passive resorption via chemical dissolution or hydrolysis in the body fluids. Since brushite is soluble in body fluids, brushite cements are mainly resorbed by passive mechanism^{14,15} while apatites being less soluble, cause apatite cements to be mostly resorbed by the active mechanism^{16,17}, i.e. macrophages and osteoclasts locally drop down the pH at values at which apatite becomes soluble. The incorporation of ionic substitutions is a method to control the degradation of CPCs. For example, incorporation of carbonates increases apatite lattice disorder favouring crystal dissolution^{18,19}. Further factors that modulate CPC resorption are porosity and crystallinity among others. Besides, external factors like patient age, sex, metabolism, health, social habits, site of implantation, blood supply or mechanical loads, can affect resorption. Ideally, when CPC is resorbed, it is progressively replaced by new bone in vivo. The replacement arises with the resorption of the cement surface in parallel with

bone growth, thus avoiding gaps between implant and tissue, and guiding bone formation (osteoconduction)²⁰.

References

1. M. Bohner, U. Gbureck, J. E. Barrale. *Biomaterials*, **2005**, *26*, 6423.
2. M. Bohner, J. Lemaitre, J. Cordey, S. Gogolewski, T. A. Ring, S. M. Perren, *Orthop. Trans*, **1992**, *16*, 401.
3. B. Bai, L. M. Jazrawi, F. J. Kummer, J. M. Spivak. *Spine*, **1999**, *24*, 1521.
4. P. Galibert, H. Deramond, P. Rosat, D. Le Gars, *Neurochir*, **1987**, *33*, 166.
5. Y. W. Li, J. C. Y. Leong, W. W. Lu, K. D. K. Luk, K. M. C. Cheung, K. Y. Chiu, S. P. Chow, A novel injectable bioactive bone cement for spinal surgery: a developmental and preclinical study, **2000**]
6. K. Ishikawa, Y. Miyamoto, M. Kon, M. Nagayama, K. Asaok. *Biomaterials* **1995**, *16*, 527.
7. B. Bai, L. M. Jazrawi, F. J. Kummer, J. M. Spivak. *Spine*. **1999**, *24*, 1521.
8. R. I. Martin, K. S. TenHuisen, P. Leamy, P. W. Brown. *J Phys Chem B*. **1997**, *101*, 9375.
9. M.P. Ginebra, E. Fernandez, F.C.M. Driessens, J.A. Planell. *J. Am. Ceram. Soc*, **1999**, *82*, 2808.
10. M. Espanol, R.A. Perez, E.B. Montufar, C. Marichal, A. Sacco, M.P. Ginebra. *Acta Biomater*. **2009**, *5*, 2752.
11. M.P. Ginebra, F. Driessens, J.A. Planell. *Biomaterials*, **2004**, *25*, 3453.
12. L.L. Hench, R. Splinter, W. Allen, T. Greenlee. *J. Biomed. Mater. Res*. **1971**, *5*, 117.
13. W. Cao, L.L. Hench. *Ceram. Int*. **1996**, *22*, 493.
14. L. Grover, J. Knowles, G. Fleming, J. Barralet. *Biomaterials*, **2003**, *24*, 4133.
15. F. Theiss, D. Apelt, B. Brand, A. Kutter, K. Zlinszky, M. Bohner, et al. *Biomaterials*, **2005**, *26*, 4383.
16. E.P. Frankenburg, S.A. Goldstein, T.W. Bauer, S.A. Harris, R.D. Poser. *J. Bone Joint Surg*, **1998**, *80*, 1112.
17. S. Wenisch, J.P. Stahl, U. Horas, C. Heiss, O. Kilian, K. Trinkaus, et al. *J. Biomed. Mater. Res. A*, **2003**, *67*, 713.
18. I. Khairoun, M. Boltong, F. Driessens, J. Planell. *J. Biomed. Mater. Res*, **1997**, *38*, 356.
19. E. Fernandez, J.A. Planell, S. Best, *J. Biomed. Mater. Res*. **1999**, *47*, 466.

20. F. Driessens, J.A. Planell, M.G. Boltong, I. Khairoun, M.P. Ginebra. *Proc. Inst. Mech. Eng.* **1998**, *H 212*, 427.

CHAPTER 9

DEVELOPMENT OF BIOMIMETIC CALCIUM PHOSPHATE BONE CEMENT

A new injectable Calcium phosphate bone cement paste with appropriate biomimetic and biomechanical characteristics able to regenerate the spinal region weakened by osteoporosis has been developed according the following step:

- 1) Synthesis of metastable CaP phases which transform in ion-substituted HA (Sr, CO₃) upon setting;
- 2) Addition of organic phases (natural or bio-erodible polymers) to the ceramic paste to create an open and interconnected porosity;
- 3) Incorporation of bio-active reinforcing phases and cross-linking of polymers to improve the mechanical properties of the bone cements

At this purpose the ability of α -TCP to set in situ and to form, in contact with a liquid solution, a paste that resulting, upon hydrolysis in water, into calcium deficient hydroxyapatite whose composition is very close to the mineral composition of bone has been investigated. Ions like Strontium and Carbonate were introduced in the cement paste formulation to improve the biomimetic aspect of the material. The incorporation of selected bio-erodible natural polymer (alginate and gelatin) was studied to create an interconnected macroporosity in the hardened construct. Setting time, viscosity and injectability of the cements pastes were investigated as function of the reagents milling and the liquid-powder ratio. The mechanical features of harden materials was improved using bioactive inorganic phases (titania) as reinforcing agents and by cross-link of polymeric phase so to have a final material similar in the structure to that of the bone.

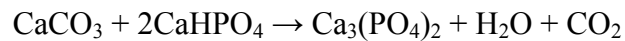
9.1 Synthesis of metastable CaP phase

9.1.1 Synthesis of α -TCP

Alfa tricalcium phosphate (α -TCP) is one of the three polymorphs of TCP, which is stable above $\approx 1125^\circ\text{C}$ ¹. It is known that the relative stability of the α - and β -polymorphs is highly affected by the presence of some impurities².

The synthesis of α -TCP requires high temperature thermal treatments and in many cases fast cooling or quenching to avoid reversion of the reconstructive $\alpha \rightarrow \beta$ transformation.

Alfa-tricalcium phosphate (α -TCP) was obtained by solid state reaction of a mixture of calcium carbonate and calcium hydrogen phosphate in the molar ratio 1:2 according to the following reaction:



After 30 minutes mixing, the solid powder blend was fired in a Platinum crucible in an open atmosphere furnace at 1400°C for 1h. At the end of the soaking period, the product was air quenched to room temperature to insure the formation of α form. After it was ground with a mechanical milling machine and sieved at $150\mu\text{m}$.

XRD diffractogram of pure α -TCP phase is showed in fig. 1.

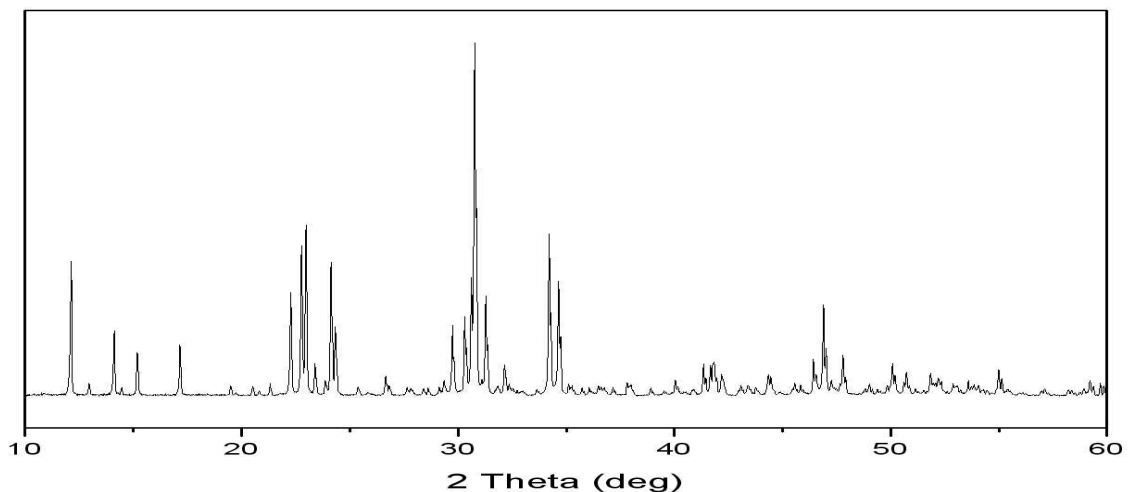
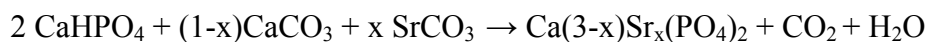


Fig.1. XRD profile of α -TCP

9.1.2 Synthesis of Sr α -TCP

Sr- α TCP ($\text{Ca}_{(3-x)}\text{Sr}_x(\text{PO}_4)_2$) was obtained by solid state reaction of a mixture of calcium carbonate, calcium hydrogen phosphate and strontium carbonate according the following

reaction:



In order to clarify the influence of Sr^{2+} ions on the reactivity of α -TCP stoichiometric amount of CaHPO_4 , CaCO_3 and SrCO_3 were used to reach the respective compositions 2, 5, 7, 10 and 20 mol% of Sr^{2+} replacing Ca^{2+} in Sr- α TCP.

Starting by a fixed amount of CaCO_3 (MW = 100,01 g/mol) equal to 20g and following the stoichiometric reaction above reported, the amount of CaHPO_4 (MW = 136,06 g/mol) and SrCO_3 (MW = 147,63 g/mol) was calculated (Tab. 1).

	CaCO₃ (g)	CaHPO₄ (g)	SrCO₃ (g)
α-TCP	20	54.40	-
Sr2% α-TCP	20	57.77	1.84
Sr5% α-TCP	20	63.44	4.92
Sr7% α-TCP	20	67.65	7.20
Sr10% α-TCP	20	70.77	11.06
Sr20% α-TCP	20	108.75	29.50

Table 1. Amount of reactive used to prepare Sr- α TCP samples with different amount of Sr

After 30 minutes reactive mixing, the solid powder blend was fired in a Platinum crucible in an open atmosphere furnace for 1h at 1400°C. At the end of the soaking period, the product was air quenched to room temperature to insure the formation of α form, and further analyzed by means of X-ray powder diffraction.

After thermal treatment powder was ground with a mechanical milling machine and sieved at 150 μm .

The X-ray diffraction analysis was carried out to evaluate the purity and the crystallinity

degree of the synthesised powders. The XRD spectra were acquired in the 2θ range 10-60, counting 1 second. XRD diffractogram of pure Sr- α TCP phase is showed in fig. 2.

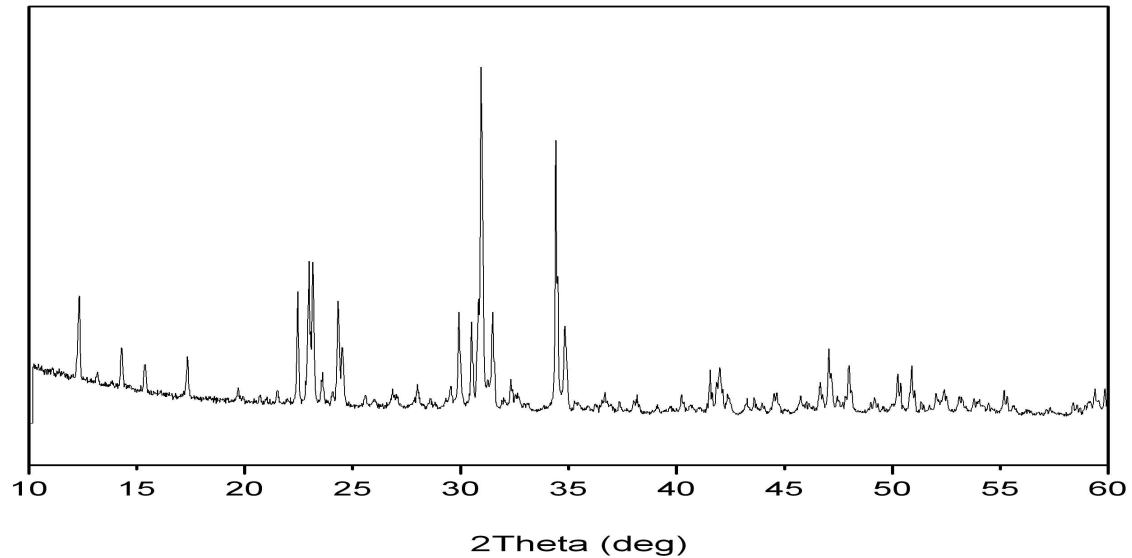


Fig. 2. XRD profile of Sr- α TCP

The examination of the X-ray diffraction patterns of the TCP powders prepared with various Sr amounts reveals the presence of α -form with traces of β -form formed during the quenching. For each sample the amounts of α -TCP and β -TCP obtained after the thermal treatment and quantified by XRD analysis (RIR method) are reported in table 2. High amount of Sr favours the formation of β -TCP.

Amount of Sr introduced	α -TCP (wt%)	β -TCP (wt%)
Sr2% α -TCP	100	0
Sr5% α -TCP	93	7
Sr7% α -TCP	90	9
Sr10% α -TCP	83	17
Sr20% α -TCP	80	20

Table 2. Amount of α -TCP and β -TCP quantified by XRD analysis (RIR method) performed on Sr- α TCP powders characterized by increasing Sr content.

The diffraction patterns of the TCP powders are slightly and continuously shifted to lower diffraction angles as increasing Sr amount introduced. This is characteristics of an increase of the lattice volume and indicates that strontium is incorporated in the structure (ionic radii: $\text{Sr}^{2+} = 1.13\text{\AA}$, $\text{Ca}^{2+} = 1.00\text{\AA}$)³.

Rietveld refinement analyses performed on the powder data reveal an almost linear evolution of lattice parameters as showed in Fig. 3.

Rietveld analysis was performed by TOPAS 4.2 software (Bruker AXS, Karlsruhe, Germany).

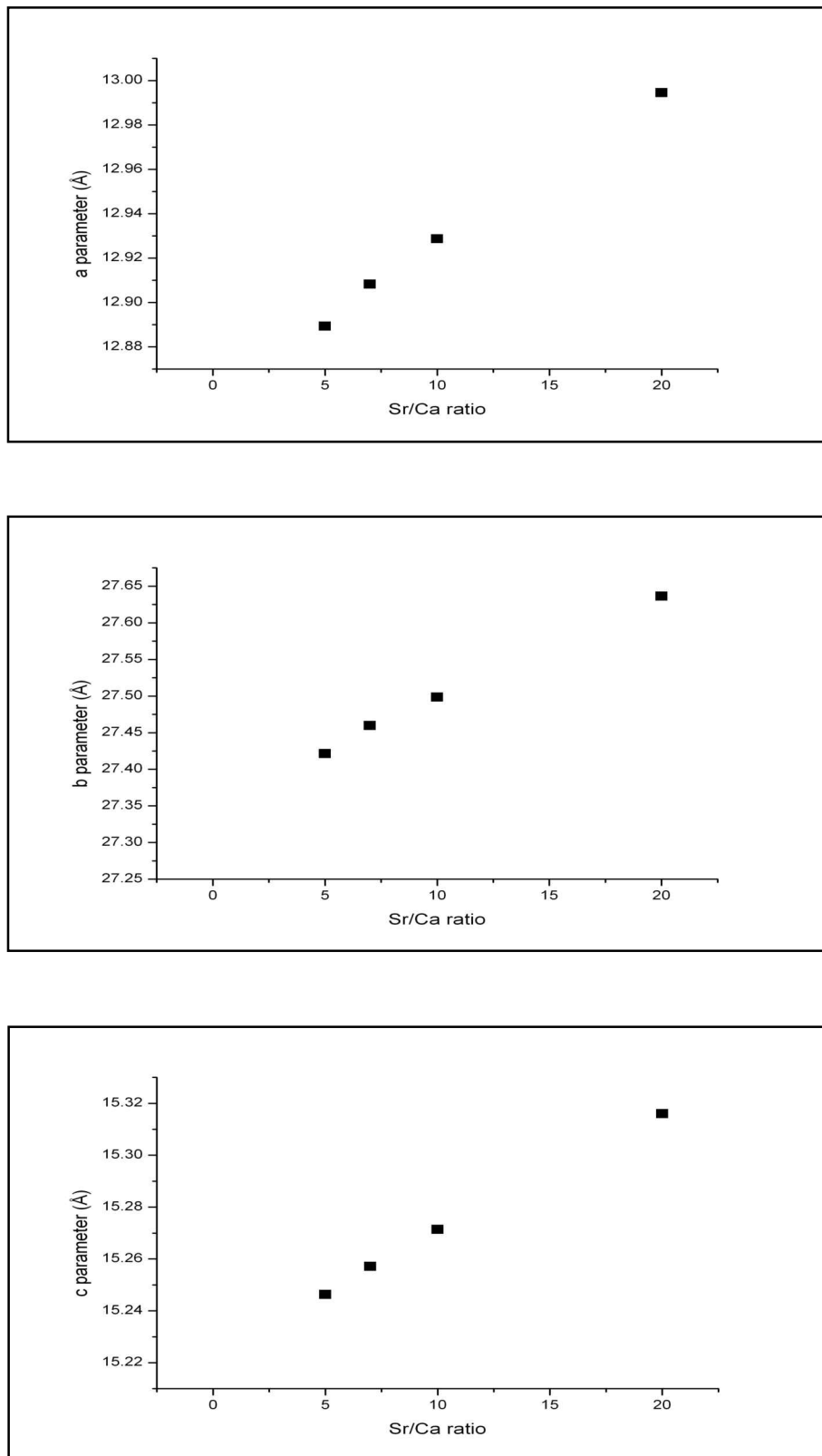


Fig. 3. Variation of the lattice dimension of Sr- α TCP with increasing Sr content

9.2 Development of biomimetic hydroxyapatite based bone cement

The rate of the setting reaction of α -TCP-based CPCs can be modulated by the physical properties of the phosphate (such as particle size), powder to liquid ratio, and addition of small amounts of organic and polymeric additives, as well as inorganic salts⁴⁻⁷. It follows that the information acquired through the study of the hydrolysis reaction of α -TCP in the presence of additives, such as bioactive ions and molecules, can be usefully applied to the design and optimization of CPCs⁸.

In this work the effect of ions substitution (Sr^{2+} and CO_3^{2-}) and that of biopolymers on the hydrolysis reaction of α -TCP was studied.

9.2.1 Hydrolysis of α -TCP powder: synthesis of HA cement

Since the rate of setting of α -TCP is influenced by particle size of the powder, the α -TCP powder was ground using a mechanical milling machine (Pulverisette, Germany) to provide a fine powder (particle size $< 10\mu\text{m}$).

The grinding reduces the particle size and increases the specific surface of the powder increasing its surface reactivity. In the graph (Fig. 4) relative to granulometric analysis performed on α -TCP powder ground at different milling time, it is possible to observe that the size of the particles decrease significantly by grinding the powder: the effects of this phenomenon decrease with increasing grinding time. In particular it can be noted that for grinding times greater than 50 minutes, the decrease of the particle size of the powder is less sensitive: $d_{50} = 2.8\ \mu\text{m}$ for powder ground for 50 minutes and $d_{50} = 2.2\ \mu\text{m}$ for the same powder ground for 90 minutes. For this reasons the milling time of α -TCP powder was fixed at 50 minutes.

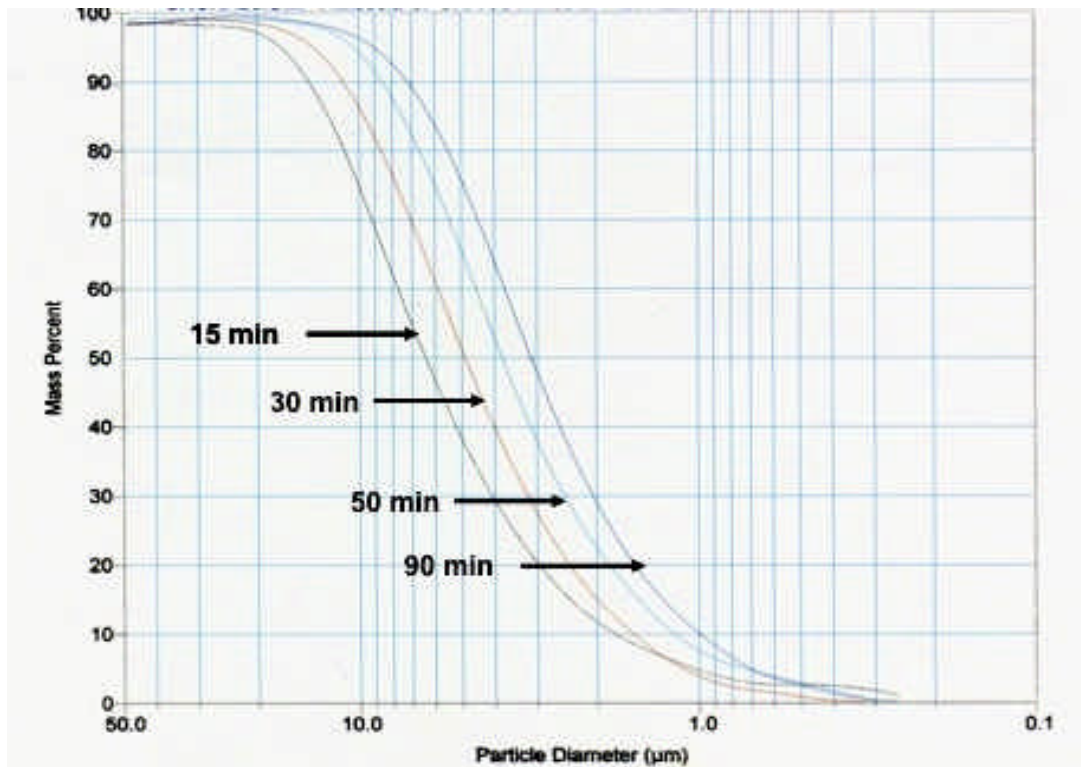


Fig. 4. Granulometric analysis performed on α -TCP powder ground at different milling time

After the milling process, α -TCP powder was hydrolyzed using a 2.5 wt% $\text{Na}_2\text{HPO}_4 \cdot 2\text{H}_2\text{O}$ accelerating setting solution at a liquid to powder ratio $L/P = 0.8 \text{ ml/g}$.

The obtained pastes were injected in silicon cylindrical moulds immersed in a thermostated bath at 37°C (Fig. 5a).

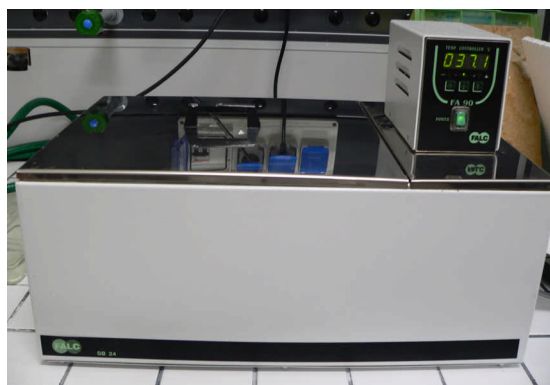


Fig. 5a. Thermostated bath

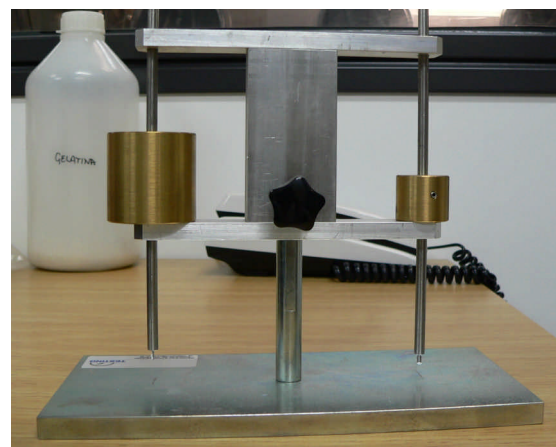


Fig. 5b. Gillmore Needle

Gillmore Needles, an American Standard Test Method (ASTM C266-89) (ASTM 1993b), was used for the determination of the setting times for cement pastes.

The Gillmore Needles instrument (Fig. 5b) consists of two different needles: one with a weight of 113 ± 0.5 g and a tip diameter of 2.12 ± 0.05 mm giving a static pressure of 0.3 MPa used for the initial setting time and the other one with a weight of 453.6 ± 0.5 g and a tip diameter of 1.06 ± 0.05 mm giving a static pressure of 5 MPa used for the final setting time. The initial setting time (I_{st}) is the time required for the test specimen to bear the initial Gillmore needle without leaving any mark on the surface, while the time required for the test specimen to bear the final Gillmore needle without leaving any mark is the final setting time (F_{st}).

The setting time was measured by injecting the paste into cylindrical forms with a diameter of 12 mm and a height of 20 mm (Fig. 6).

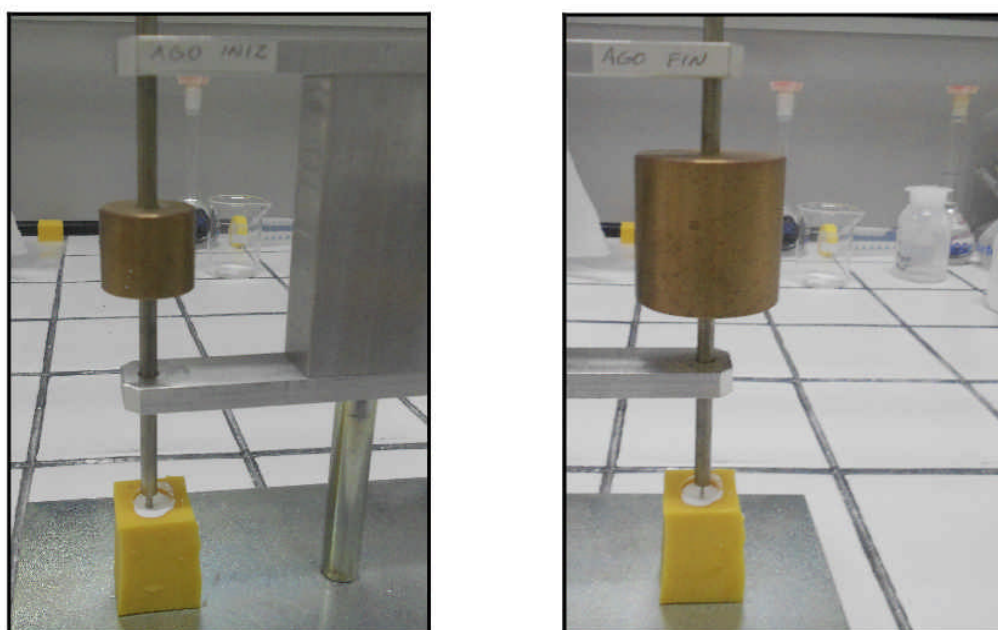


Fig. 6. Gillmore needle used to measure I_{st} (left) and F_{st} (right)

The Kinetic of phase transformation of α -TCP paste into HA was studied as function of time (Fig. 7), using X-ray diffraction to identify the amount (%vol) of HA phase formed. XRD analysis (Fig. 8) performed on cement paste during α -TCP hydrolysis reaction indicates that the transformation of α -TCP in HA is fulfilled after 13h by the initial setting time.

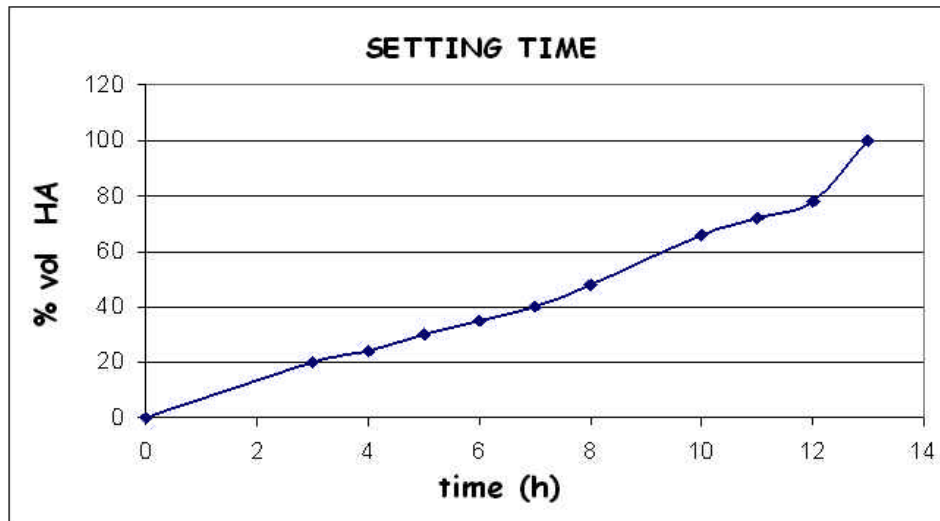


Fig. 7. % vol of HA formed by α -TCP hydrolysis in function of time

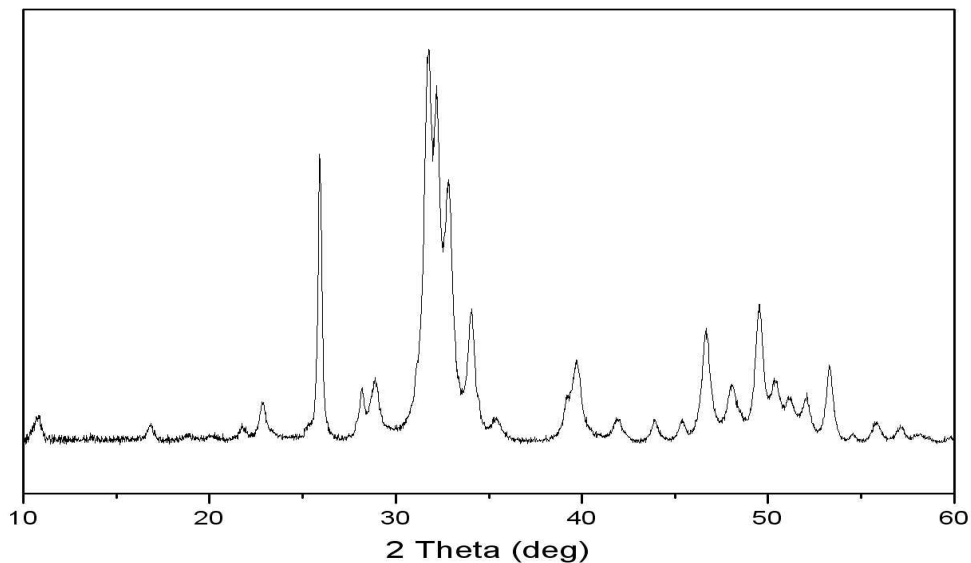
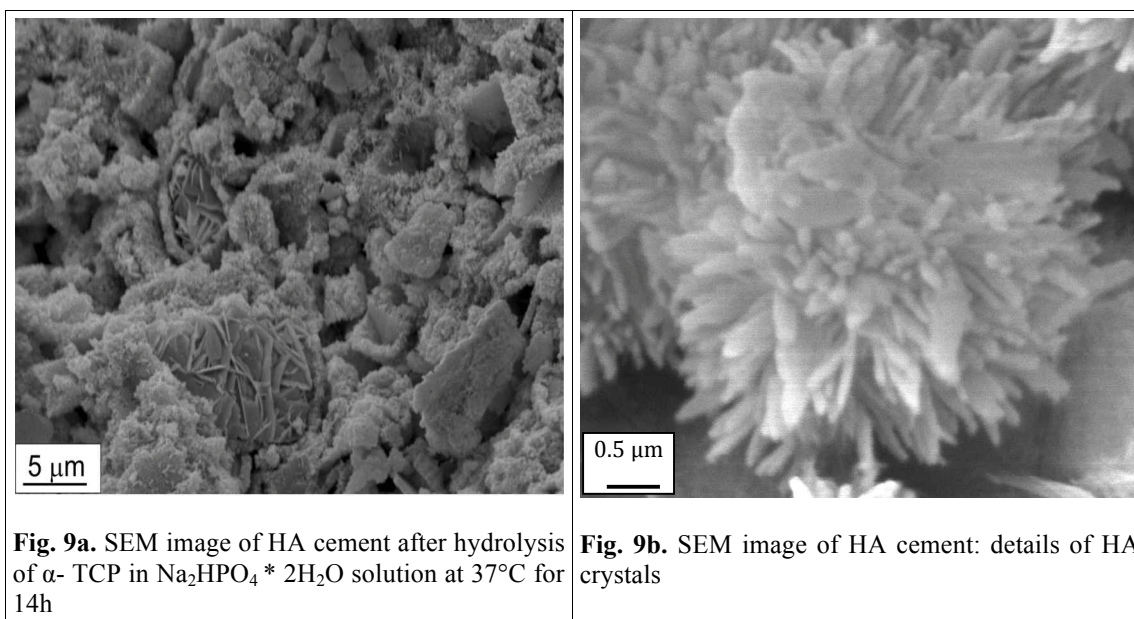


Fig. 8. XRD patterns of HA

Morphological evaluation of the materials was performed by scanning electron microscopy (SEM; Stereoscan 360, Leica, Cambridge, UK) on samples coated with gold. After 14h soaking at 37°C, it can be noted the needle-like morphology of the crystals of HA originating from the dissolution of grains of α -TCP; such grains tend to dissolve gradually leaving characteristics cavity empty (Fig. 9a). These needles of HA tend to coalesce in lamellar structures (platelet-like) (Fig. 9b).



9.2.2 Hydrolysis of Sr- α TCP powder: synthesis of SrHA cement

Sr- α TCP powders containing different amount of Sr were milling and hydrolyzed in the same conditions used for α -TCP.

From the perspective of the clinical uses, the setting time of a CPC cement paste is of paramount importance since it should not harden too fast to allow moulding or injection and should not harden too slowly to allow the surgeon to close the defect shortly after placement of the cement. Therefore, the CPC must have an optimal setting time in order to lead to an acceptable mechanical strength after hardening and to prevent migration of cement to undesirable sites. At this purpose, the setting time and the kinetic transformation of Sr- α TCP in SrHA was investigated. The hydrolysis reaction of Sr- α TCP occurred at 37°C using a 2.5 wt% $\text{Na}_2\text{HPO}_4 \cdot 2\text{H}_2\text{O}$ accelerating solution at a liquid to powder ratio $L/P = 0.8 \text{ ml/g}$.

The hydrolysis of Sr- α TCP was influenced by Sr amount present in the powder; increasing the amount of Sr present in the starting Sr- α TCP speed of hydrolysis reaction decreased with a consequent increase in the cement setting time (Table 3). These results are consistent with the higher solubility of Sr-substituted hydroxyapatite⁹. The increase in solubility with strontium content in Sr-substituted hydroxyapatite can be interpreted as a destabilization of the crystal structure by the larger Sr^{2+} ion¹⁰, which could justify the observed inhibition of crystallization.

Sample	I_{st} (min)	F_{st} (min)	Transformation in SrHA (h)
CPC	30	40	14
Sr2%CPC	30	40	24
Sr5%CPC	40	60	96
Sr7%CPC	60	100	120
Sr10%CPC	120	240	168
Sr20%CPC	240	1440	240

Table 3. Setting time and kinetic transformation of Sr- α TCP in SrHA

The hydrated products are well crystallized and present diffraction patterns characteristics of apatitic phase with small amount of unreacted β -TCP remaining from the cement powders containing high amount of Sr.

Rietveld refinement analyses (Fig. 10a, 10b) performed on the starting powders and on the hardened cements confirm the considerable increase in the lattice parameters of SrHA in both the a and c axis directions (Fig. 10)^{11,12}.

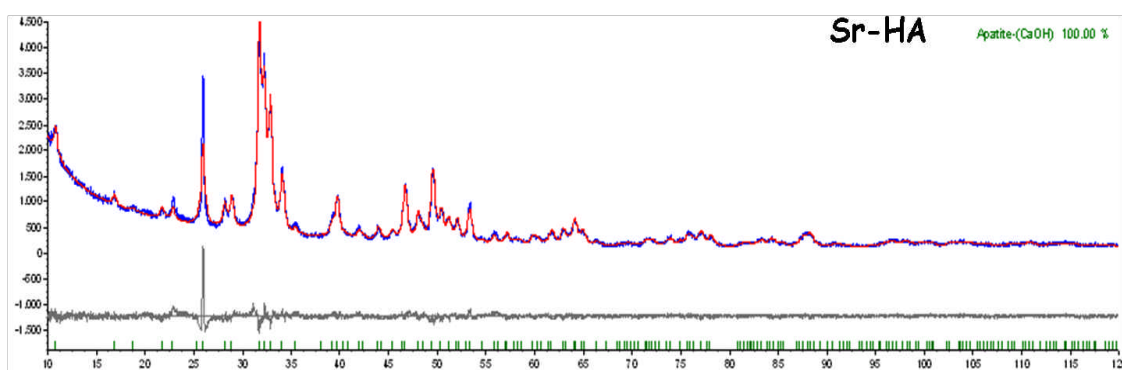
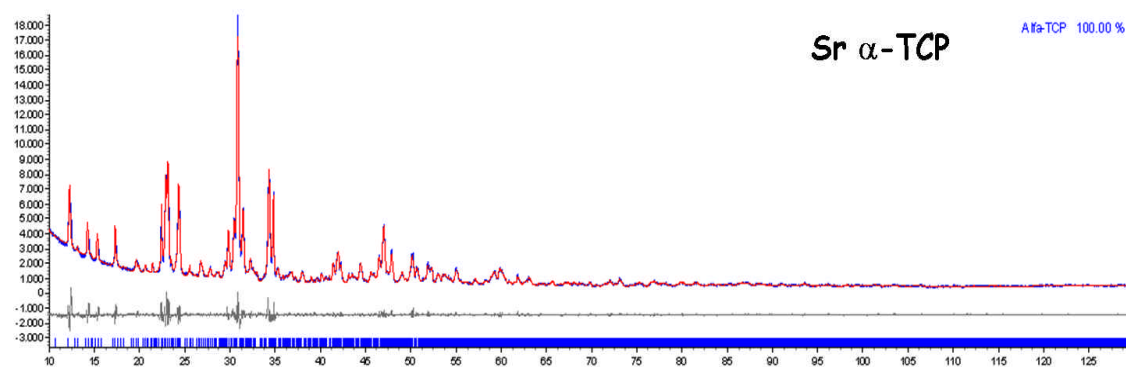


Fig. 10a. XRD pattern profiles of Sr- α TCP (Sr/Ca = 2% mol) powder before and after setting

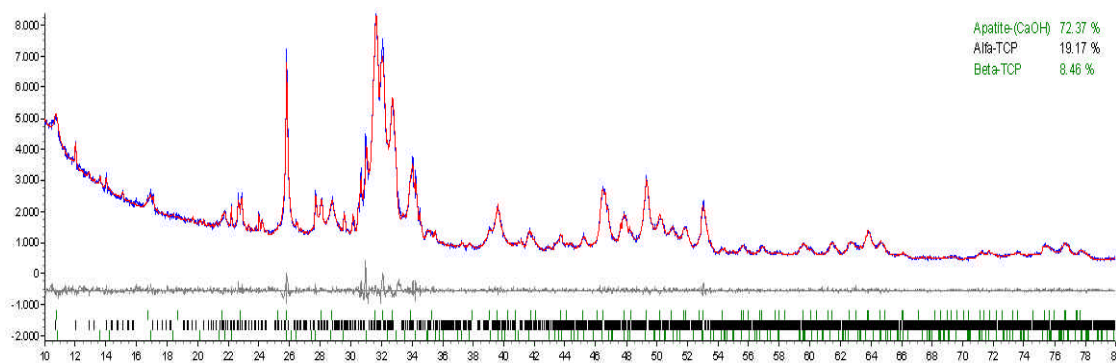
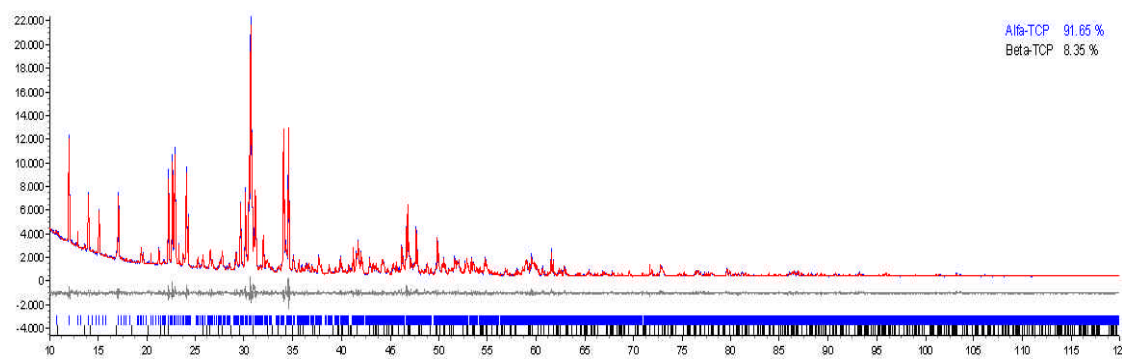


Fig. 10b. XRD pattern profiles of Sr- α TCP (Sr/Ca = 7% mol) powder before and after setting

The synthesis of Sr- α TCP containing small amount of Sr (Sr/Ca = 2%mol) occurred without the formation of β -TCP phase; accordingly the hydrated powder formed by Sr- α TCP hydrolysis was a pure strontium substituted hydroxyapatite (SrHA) (Fig. 10a). Increasing the amount of Sr introduced during the synthesis of Sr- α TCP (Sr/Ca = 7% mol) increases the amount of β -TCP formed as secondary phase (Fig. 10b). β -TCP phase does not take part in the reaction of Sr- α TCP hydrolysis and hence is present as secondary together with SrHA.

As with the TCP phase, a slight shift to lower 2θ angles of the diffraction peaks of apatite phase can be observed indicating the incorporation of Sr in the crystals. The refinement results are presented in Fig. 11 and reveal an almost linear evolution of the lattice parameters of HA cell as increasing Sr amount introduced.

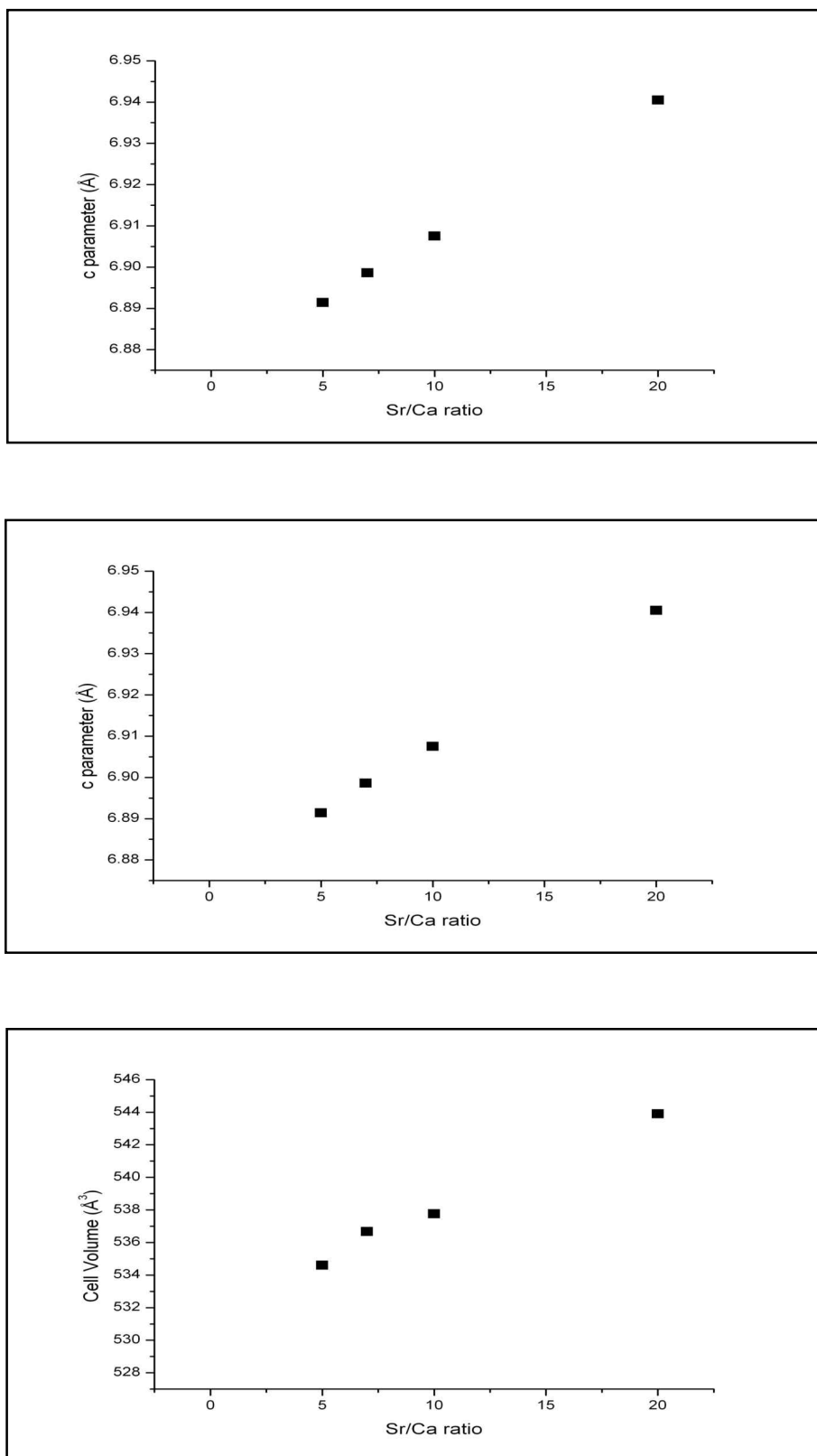


Fig. 11. Variation of the lattice dimension and cell volume of SrHA with increasing Sr content

The substitution of Sr instead of Ca site in the HA cell is also confirmed by quantitative evaluation (ICP-analysis) performed on the hydrated paste after the setting: the Ca/P molar ratio is 1.51 and the amount of Sr detected is the same nominally introduced in the starting Sr- α TCP, indicating that all amount of Sr introduced takes place to the hydrolysis reactions of Sr- α TCP. Values obtained by ICP-analysis are reported in Table 4.

Sr- α TCP	HA		
	Sr/Ca (mol %)	Ca/P (mol)	(Sr + Ca)/P (mol)
2	1.44	1.46	1.8
5	1.40	1.46	4.9
7	1.35	1.45	6.8
10	1.33	1.46	9.5
20	1.21	1.44	19.0

Table 4. Chemical composition (ICP) performed on SrHA cement after the setting

9.2.3 Introduction of carbonate ions during Sr- α TCP hydrolysis: synthesis of SrCHA cement

The incorporation of carbonate ion during the hydrolysis reaction of Sr- α TCP was studied with the purpose to obtain a multi-doped HA for osteogenesis stimulation.

Strontium carbonate hydroxyapatite (SrCHA) cement paste was obtained by the mixture of a solid phase made of Sr- α TCP (2%mol), calcium carbonate (CaCO_3) and calcium dihydrogenphosphate monohydrate ($\text{Ca}(\text{H}_2\text{PO}_4)_2 \cdot \text{H}_2\text{O}$) previously milling with a 2.5 wt% $\text{Na}_2\text{HPO}_4 \cdot 2\text{H}_2\text{O}$ accelerating setting solution according the following reaction:



fixing the following parameters:

$$(\text{Ca} + \text{Sr})/\text{P} = (3n + x + a)/(2n + 2a)$$

$$1.5 \leq (3n + x + a)/(2n + 2a) \leq 1.67$$

The liquid powder molar ratio was fixed so to have $L/P = 0.8 \text{ ml/g}$.

The setting of the pastes was performed during their aging in a silicon moulds thermostated at 37°C in a closed bath and measured with Gillmore Needles.

The presence of Carbonate ions reduces the speed of Sr- α TCP hydrolysis; in fact initial and final setting time is 60 and 120 min respectively, higher if compared with that of sample without carbonate (Sr2%CPC) (Table 3). Time required to have a completely transformation of Sr- α TCP in SrCHA is equal to 72h, as expected by the presence of carbonate ions together with strontium ions that inhibit the precipitation of SrCHA.

X-ray diffraction spectra (Fig. 12) performed on the hardening cement samples detects a monophasic SrCHA phase.

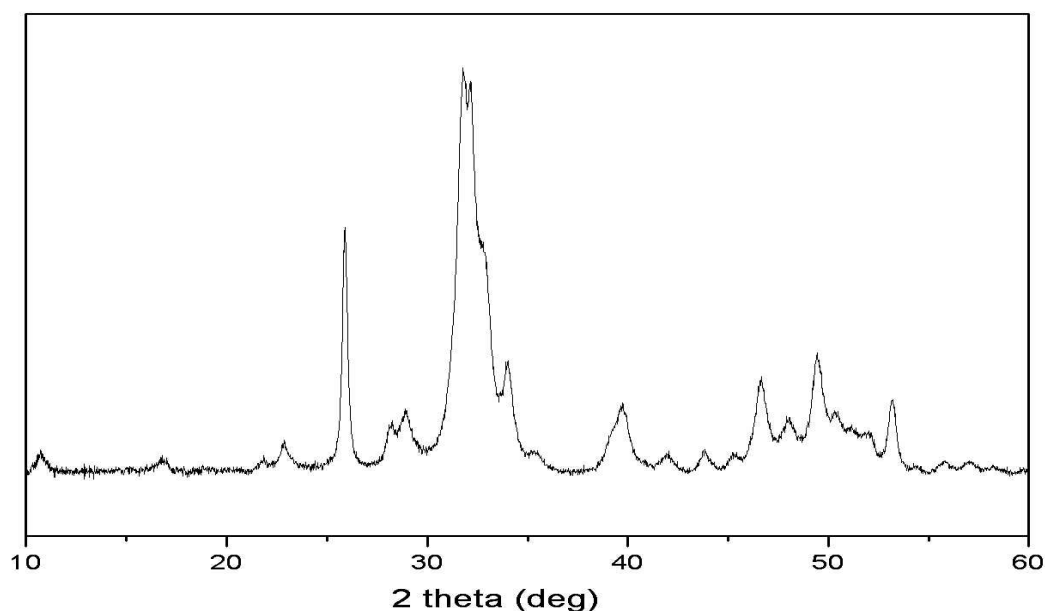


Fig. 12. XRD profile of SrCHA cement

Both the Sr^{2+} and CO_3^{2-} substituting ions influence the detection of SrCHA cell parameters (c and a) variations, from stoichiometric HA cell parameters¹³. CO_3^{2-} substituting PO_4^{2-} (B-type substitution) provokes a contraction of the a axis and an increase of c/a ratio while Sr^{2+} substitution provokes an increase of both axis, so that is not easy to establish by XRD analysis what kind of substitutions (A-type and B-type) occurs in the HA cell during the formation of SrCHA cement paste¹³.

Fourier Transform Infrared Spectroscopy (FT-IR Thermo Nicolet-Avatar 320) was used to check the occurrence of the typical functional groups present in calcium phosphate phases (phosphate, hydroxyl, water (adsorbed and structural), carbonate); in particular FTIR spectroscopy (Fig.13) allowed to assess whether carbonation occurs in phosphate (B) and/or hydroxyl (A) position in the HA paste.

Sample was prepared by carefully mixing 1 mg of hardening cement paste powder with 100 mg of potassium bromide by pestle and mortar; the obtained pellet was put in a ventilated oven at 130 °C for 2 hours prior the spectrum acquisition, in order to eliminate the water adsorbed on the powder surface¹⁴; prior analysis, anyway, the pellet was briefly exposed to air atmosphere. Following this procedure, the water detected by FTIR analysis is more strictly related to the structural water characterizing the specific HA powder, as the contribution of the water adsorbed by potassium bromide is completely eliminated and the H_2O adsorbed by the HA surface is strongly reduced. FTIR spectra performed on SrCHA cement (Fig.13) was obtained by averaging 32 scans collected in the wavelength range 400-4000 cm^{-1} , with a spectral resolution of 4 cm^{-1} .

As shown in Fig. 13, bands at 980-1050 cm^{-1} , and 570-600 cm^{-1} confirm the presence of PO_4^{3-} groups, typical of apatites. The large band at about 3400 cm^{-1} and the band at 1644 cm^{-1} detect absorbed water and occluded water into the powder.

Furthermore B-type carbonation is confirmed by the detection of strong typical peaks^{15,16}: the stretching peaks at $\approx 1430 \text{ cm}^{-1}$ and 1460 cm^{-1} and the bending peak at $\approx 873 \text{ cm}^{-1}$.

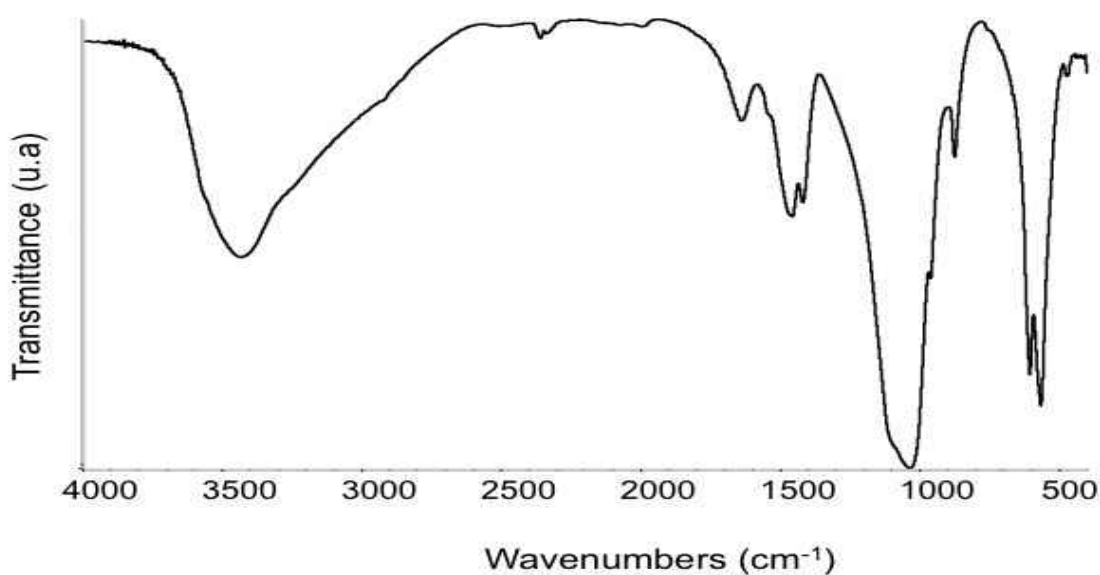


Fig. 13. FTIR spectrum of SrCHA cement

The incorporation of carbonate ions in the apatite lattice was also confirmed by Thermal analysis that was used to explore the thermal transformation process and the thermal stability of the powder and to estimate the carbonate content of the apatite. The analysis was performed on a specimen of about 20 mg using a heating rate of $10\text{ }^{\circ}\text{C min}^{-1}$ up to $1000\text{ }^{\circ}\text{C}$. The extent of the powders carbonation was evaluated by the weight loss in the range $500\text{-}1000\text{ }^{\circ}\text{C}$, due to the decomposition of carbonate groups with evaporation of carbon dioxide, and the corresponding stoichiometric coefficient of CO_3 anion was estimated considering that the highest possible degree of substitution of carbonate ions in the phosphate site (B- carbonation) is $\sim 50\text{ mol}\%$, corresponding to $\sim 21\text{ wt}\%$ CO_3 loss¹⁷. Thermal profile (Fig. 14) shows a weight loss occurring from about 50°C up to 500°C imputable to dehydration of the absorbed and occluded water and to the removal of absorbed species (such as CO_2)¹⁸. At higher temperatures (in particular from 500 to 1000°C), carbonate ions decompose causing a weight loss of about $2\text{ wt}\%$ due to CO_2 elimination, allowing to estimate as about $3\text{ wt}\%$ the starting carbonation of the powder.

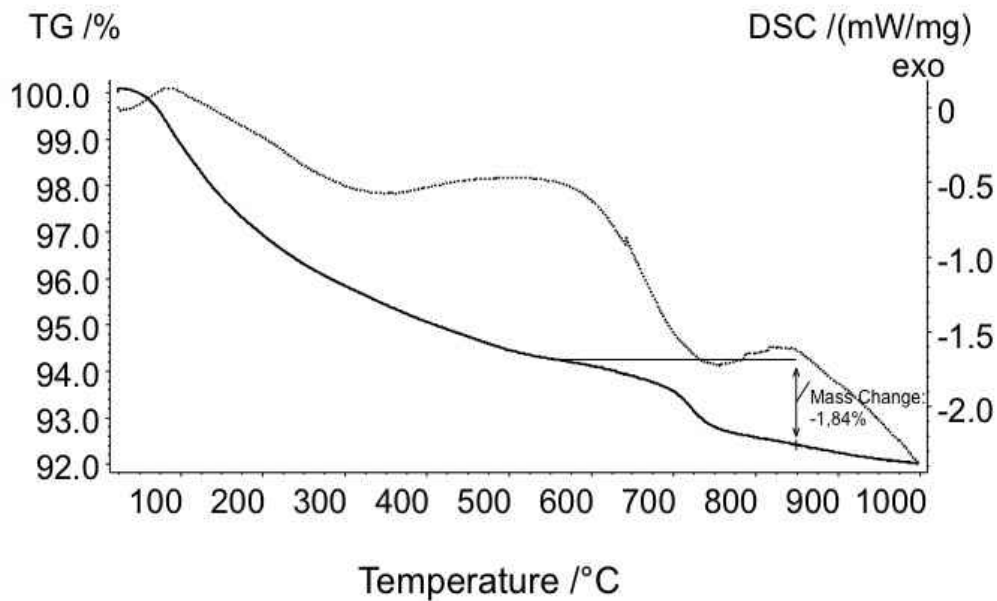


Fig. 14. Thermal analysis profile performed on SrCHA cement

9.3 Introduction of polymeric phase into calcium phosphate cement

CPCs are composed of a powder phase and a liquid phase. Therefore, polymers can be added to CPC, either dissolved in the liquid phase or in a solid state as an additive to the powder phase. Obviously, only water-soluble polymers can be added to the CPC liquid phase. In this case, the polymer will be present as a continuous phase throughout the entire CPC and, what is more important, the solubilized polymer will be able to interact with the cement setting reaction, namely the dissolution of the original phase and the precipitation of the final product. Depending on the final CPC properties desired, the liquid phase properties may be altered by changing several features of the polymer, such as concentration, molecular weight, and polymer chain length. Conversely, when the polymers are added in solid form, they will act as a second and discontinuous phase in the cement inorganic matrix. Although the extent of chemical interaction with the setting reaction is expected to be lower, the morphology, size, and percentage of this second phase will have significant effects on the handling properties and on the final performance of the material.

Therefore, the incorporation of polymers into CPC formulation appears to be an excellent

option to enhance CPC performance and improve not only some properties relevant for the clinical use of these materials, such as injectability, cohesion, or setting time, but also their final performance in terms of resorption rate and cell/tissue response¹⁹. In this view Gelatine and Sodium-Alginate were chosen as bio-soluble organic phase adding to ceramic paste to design CPC with an open and interconnected macroporosity. In fact the gradual formation of pores upon degradation of the polymer phase opens a route for cell colonization thus favouring bone in-growth and, later, bone remodelling.

9.3.1 Calcium phosphate/gelatine bone cement

One of the main reasons to incorporate gelatin into CPC is to enhance cell adhesion. Some studies have shown a positive effect of incorporating gelatin on initial cell adhesion and proliferation²⁰ although other studies have reported only a small effect on cell proliferation^{21,22}.

Three methods were investigated to incorporate gelatine into ceramic paste:

- 1) **Dry method:** consisting in a dry mixture between gelatine and milling Sr2%- α TCP. The resulting powder was mixed with setting liquid solution $\text{Na}_2\text{HPO}_4 \cdot 2\text{H}_2\text{O}$ (2.5 %wt) and injected.
- 2) **Foaming method:** consisting in the melting of gelatine in the liquid setting solution $\text{Na}_2\text{HPO}_4 \cdot 2\text{H}_2\text{O}$ (2.5 %wt) at 50-60 °C followed by the foaming of gelatine solution with an electrical mixer. To this mixture the inorganic phase (Sr2%- α TCP) was added and gently mixed with the created foam. Thereafter, the cement foam was placed into a syringe and extruded in silicon moulds thermostated at 37°C.
- 3) **Addition of foaming agents:** in order to improve the foaming ability of gelatine solutions, a synthetic surfactant, Tween 20, was added to gelatine suspension during the foaming process. To this foamed suspension the inorganic phase (Sr2%- α TCP) was added and gently mixed with the created foam. Thereafter, the cement foam was placed into a syringe and extruded in silicon moulds thermostated at 37°C.

In table 5.1; 5.2 and 5.3 are reported respectively the experimental condition used to prepare SrHA/gelatine cement pastes according dry mixing (method 1); foaming of gelatine (method 2) and addition of foaming agents (method 3). In the tables setting time are also reported.

Sample code	Gelatine/ Na ₂ HPO ₄ * 2H ₂ O (wt %)	Gelatine/ powder (wt%)	Setting time	
			I _{st}	F _{st}
CPMG5	5	5	30 min	3 h

Table 5.1. Experimental details of SrHA/Gelatine cement prepared according method 1

Sample code	Gelatine/ Na ₂ HPO ₄ * 2H ₂ O (wt%)	Gelatine/powder (wt%)	Setting time	
			I _{st}	F _{st}
CPFG12	15	12	1h	5h
CPFG22	15	22	2h	6h
CPFG27	15	27	6 h	1 day
CPFG30	15	30	1day	2day

Table 5.2. Experimental details of SrHA/Gelatine cement prepared according method 2

Sample code	Gelatine/ Na ₂ HPO ₄ * 2H ₂ O (wt%)	Gelatine/ powder (wt%)	Tween20/ gelatine (wt%)	Setting time	
				I _{st}	F _{st}
CPTG	15	12	0.05	1 day	2 day

Table 5.3. Experimental details of SrHA/Gelatine cement prepared according method 3

Foaming process (method 2 and 3) increases setting time of the paste respect to dry mixing because of the presence of bubble in the foamed solution.

SEM images (Fig.15) show the features of composites cements (SrHA/gelatine) obtained by the three synthesis methods tested. It is possible to observe that samples present a good porosity with a dimension of pores ranges between 300-150 mm for sample derived by

method 1 (Fig. 15a); between 500-300 mm for sample derived by method 3 (Fig. 15b) and between 250-100 mm for samples derived by method 2 (Fig. 15c).

Sample in Fig. 15a presents a superficial macro-porosity: probably the no-homogeneous dispersion of gelatine in the inorganic phase hampered the growth of HA crystals creating large pore that are not interconnected. The distribution of pores in sample 15b and 15c is more uniform and pores present a good interconnection.

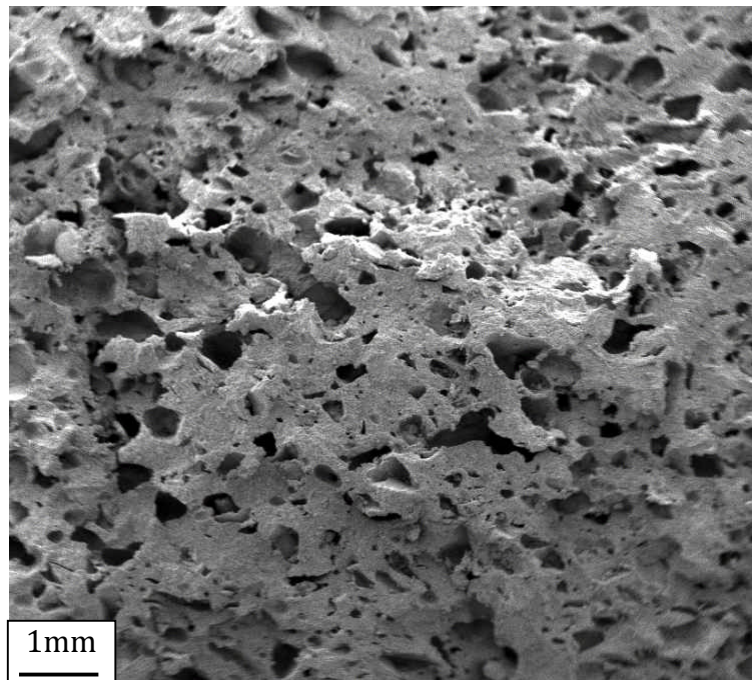


Fig. 15a. SEM image of SrHA/Gelatine cement obtained by method 1

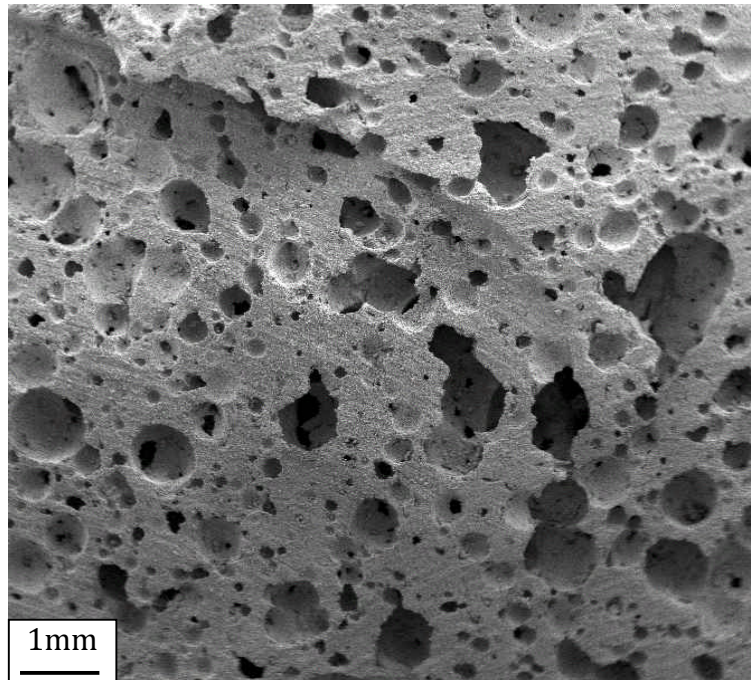


Fig. 15b. SEM image of SrHA/Gelatine cement obtained by method 2

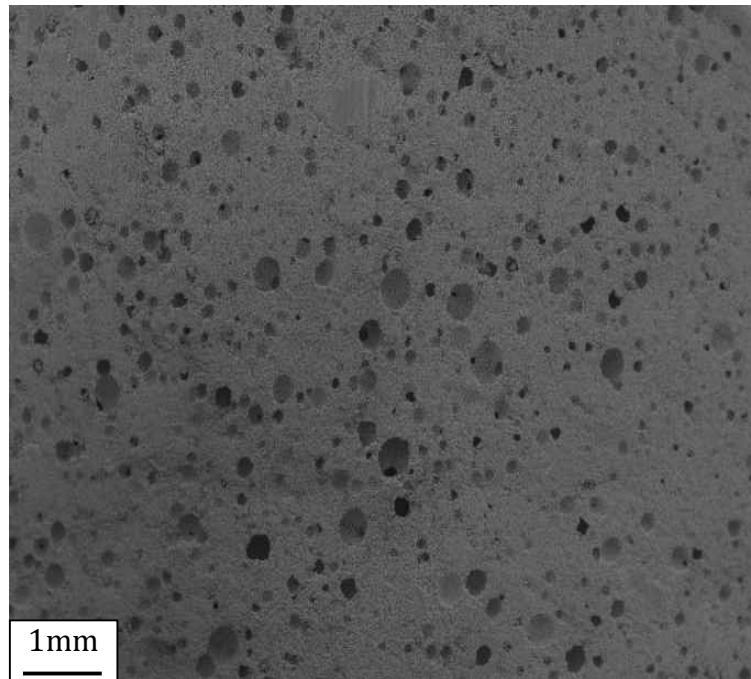


Fig. 15c. SEM image of SrHA/Gelatine cement obtained by method 3

9.3.2 Calcium phosphate/Sodium alginate bone cement

Another polymer tested to create porosity into ceramic paste was Sodium Alginate. Two methods were investigated to incorporate Sodium Alginate into ceramic paste:

1) Addition of HA/Alg (60/40 wt%) beads synthesized with different size. HA/Alg 60/40 wt% beads were prepared mixing a solution of Sodium Alginate (1 wt%) with a biomimetic MS-CHA (magnesium-strontium-carbonate hydroxyapatite). The suspension was sprayed into a solution of CaCl_2 (0.07 M): Ca^{2+} ions cross-link hydroxyls group of alginate according an egg-boxes model. Beads obtained were milling and sieved at different size range (400-600; 400-250; < 250 μm). Pastes with different HA/Alg size were obtained by simply mixing of HA/Alg beads with Sr2%- α TCP and Na_2HPO_4 (2.5 wt%) solution. Pastes obtained were injected in silicon moulds thermostated at 37°C. In table 6.1 are reported the main experimental details used to prepare pastes containing HA/Alg beads.

2) Addition of Sodium Alginate solution: consisting in the mixing of Sr2%- α TCP with a suspension of Sodium Alginate dissolved in $\text{Na}_2\text{HPO}_4 \cdot 2\text{H}_2\text{O}$ (2.5 wt%) solution. Pastes obtained were injected in silicon moulds thermostated at 37°C. In table 6.2 are reported the main experimental conditions used to prepare SrHA/Alginate cements.

Sample code	Beads Size (μm)	HA-Alg/powder (wt%)	Alg/powder (wt%)	Setting time	
				I _{st}	F _{st}
CPA<250	<250	10	4	20 min	60 min
CPA250-400	250-400	10	4	15 min	80 min
CPA400-600	400-600	10	4	15 min	60 min

Tab. 6.1. Experimental details of SrHA/Alg cements prepared with different HA/Alg beads sizes

Sample code	Alginate/ $\text{Na}_2\text{HPO}_4 \cdot 2\text{H}_2\text{O}$ (wt %)	Alginate/powder (wt%)	Setting time	
			I_{st}	F_{st}
CPMA2	2	2	10 min	30 min

Tab. 6.2 Experimental details of cement SrHA/Alginate prepared according method 2

The addition of Sodium Alginate seems not affect setting time of CPC. In fact when it is added as polymeric solution to Sr2%- α TCP the setting time of the paste was faster than Sr2%CPC without polymeric phase (see Table 3), indicating that Sodium Alginate does not inhibit Calcium phosphate precipitation and crystallization. When Sodium Alginate was added as solid phase (HA/Alg beads) in CPC, setting time of pastes increase by increasing the size of HA/Alg beads indicating that they act as a discontinuous phase that hampered the growth of HA crystals.

The addition of HA/Alg beads in solid state, as a second phase in the CPCs, is aimed at achieving two main objectives. On one side, to act as a reinforcing phase that enhances the mechanical properties of the CPC and on the other side to create macroporosity in the CPC after dissolving the polymer, which promotes tissue colonization and eventually enhances CPC resorption. Figures 16a; 16b and 16c show the morphology (SEM images) of samples obtained by the mixer of the inorganic phase (Sr2%- α TCP) with HA/Alg beads prepared at different sizes. Sample reported in Fig. 16b shows a good and uniform distribution of HA/Alg beads in the inorganic matrices (pores range 250-500 μm). Sample reported in Fig. 16c shows a not uniform distribution of pores due to the presence of bigger HA/Alg beads (pores range 400-800 μm). On the contrary, by method 2, cement with a good uniform porosity (pore range 150-300 μm) has been obtained (Fig. 16d).

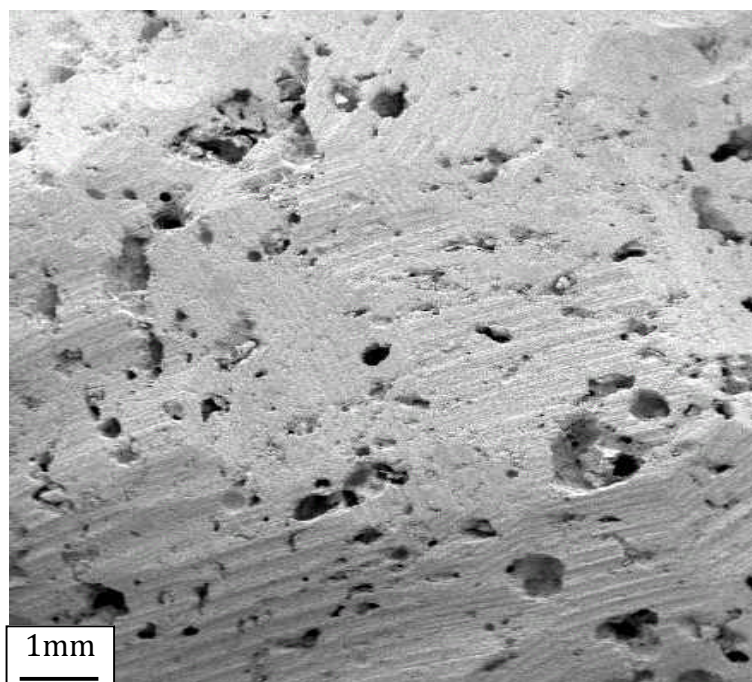


Fig. 16a. SEM image of SrHA cement mixed with HA/Alg beads size $< 250 \mu\text{m}$

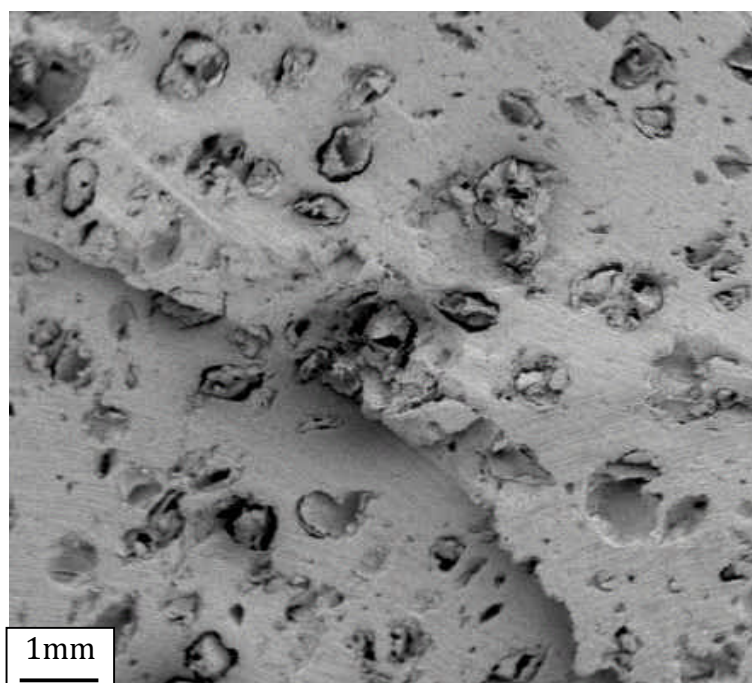


Fig. 16b. SEM image of SrHA cement mixed with HA/Alg beads size $250\text{-}400 \mu\text{m}$

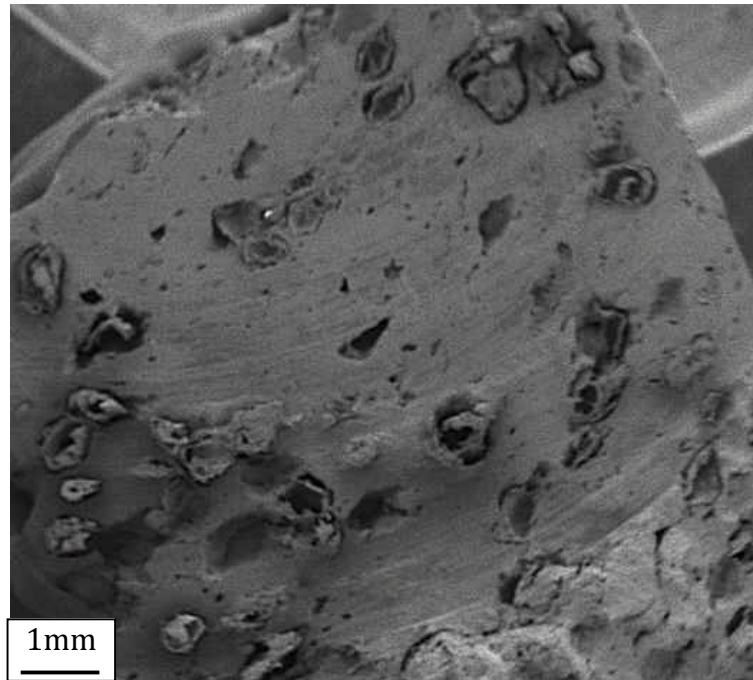


Fig. 16c. SEM image of SrHA cement mixed with HA/Alg beads size 400-600 μm

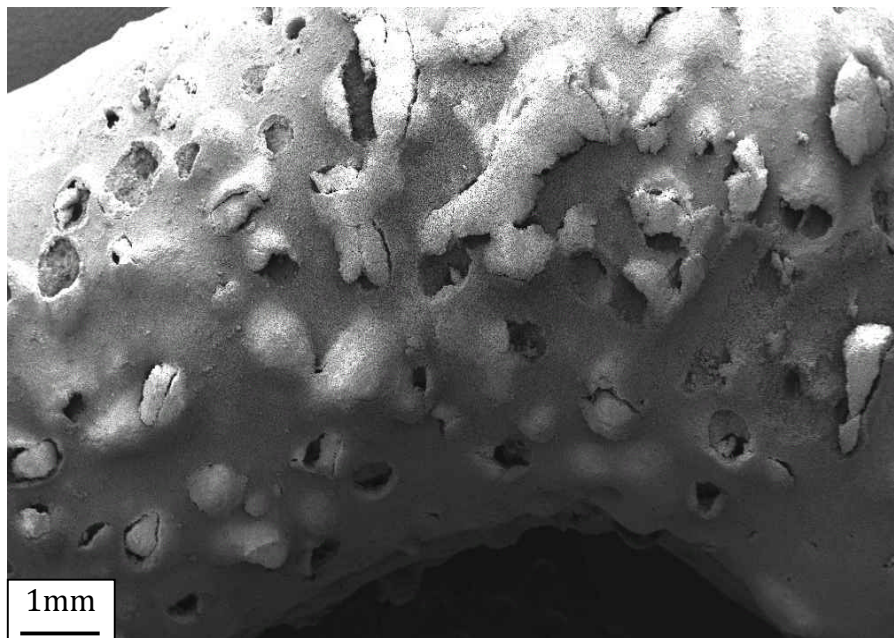


Fig. 16d. SEM image of SrHA/Alginate cement obtained by method 2

Thermal analysis (Fig. 17) applied to the sample mixer with HA/Alg beads size 250-400

μm shows that the amount of alginate present in the sample was 4 wt%, in agreement with the nominally value introduced in the synthesis and reported in Table 6.1, indicating that the mineral phase (Sr2%- α TCP) and HA/Alg beads are homogeneous mixer.

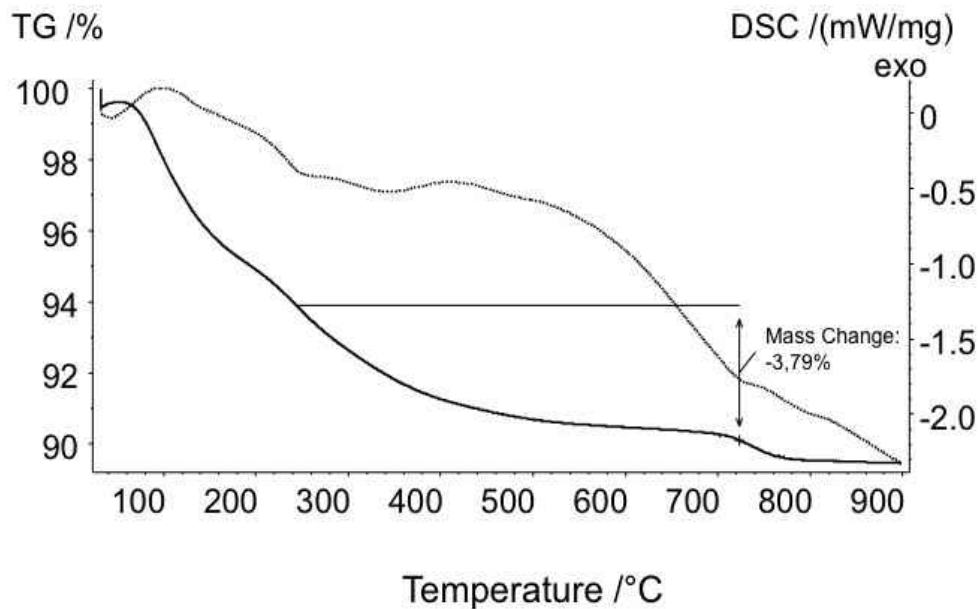


Fig. 17. Thermal analysis profile performed on SrHA cement mixed with HA/Alg beads size 250-400 μm

9.4 Porosity measurement

After drying in a thermal oven at 37 °C for 24 h, the total porosity of the specimens CPCs was measured according to the equation:

$$p_{\text{total}} = 1 - \rho / \rho_{\text{HA}}$$

where ρ_{HA} is the density of fully dense HA (3.16 g cm^{-3}) and ρ is the apparent density of the specimen measured by dividing its weight by its volume. The volume of the parallelepiped specimens was calculated from its dimensions measured with a micrometer. Five specimens were measured to calculate the mean porosity and its standard deviation.

The introduction of polymeric phase in CPC formulation influences the porosity of

materials (Table 7): sample with the highest value of porosity is that obtained by gelatin foaming method indicating that this method is more suitable than the simple mix method to generate materials with a good porosity as also previously confirmed by SEM image (Fig.15b).

Sample	P _{total}
Sr2%CPC	0.62 ± 0.01
CPA < 250	0.67 ± 0.03
CPA250-400	0.68 ± 0.02
CPA400-600	0.68 ± 0.01
CPMA2	0.63 ± 0.01
CPMG5	0.67 ± 0.02
CPFG12	0.78 ± 0.01

Table 7. Porosity values of SrHA cement

The presence of HA/Alg beads with different size in CPC not influence the porosity of materials that remains constant, otherwise when Alginate is added to CPC in form of liquid phase porosity decreases.

9.5 Mechanical properties

Mechanical properties of materials usually decrease with porosity, which is also the case for CaP materials²³⁻²⁵. Therefore, within a general context of material performance improvement and optimisation, it is important to measure the mechanical behaviour of such material.

9.5.1 Compression strength

The compressive strength values of SrCPC are in the range of 1-24 MPa for the compressive strengths reported in the literature for brushite-forming cements²⁶.

The results (Fig. 18) show that Sr2%CPC specimen exhibits higher compressive strength respect the same materials containing a polymeric phase. This is in agreement with porosity value obtained (Table 7): the mechanical properties decrease as porosity increases.

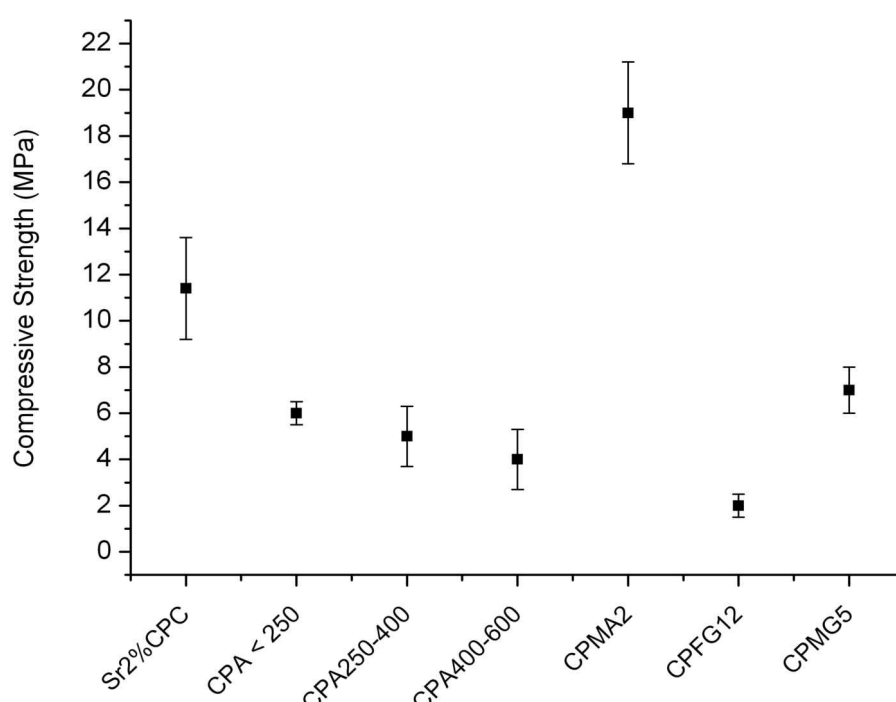


Fig. 18. Compressive Strength of SrHA cement

The presence of HA/Alg beads into CPC formulation influences negatively the mechanical properties of materials since microbeads helped the formation of macro-channels in the CPC, which stimulate vascularization in vivo and help bio-degradation of material²⁷. Moreover, the presence of macro-channels in the CPCs caused an increase of the setting time of materials resulting in a decrease of CPC mechanical properties. It is reasonable that the mechanical strength compression decreases by increasing the dimension of HA/Alg beads introduced into CPC formulation.

The addition of Alginate in form of liquid phase seems to help the hardening reaction of

CPC. In fact the alginate added should come into contact with the calcium ions, which are abundant in the CPC, consequently being cross-linked through the ionic exchange of sodium by calcium. The cross-link assures a fast setting time of the material resulting in an hardened cement with the highest mechanical properties (Fig. 18).

Gelatin also affects CPC mechanical properties, although in different ways depending on the amount of gelatin incorporated. In literature²⁸ is reported that Gelatin increases the compressive strength of an α -TCP cement fourfold, which is related to a decrease in sample porosity. Compressive strength increases linearly as a function of gelatin concentration²⁹. Nevertheless, the general trend is that the highest strengths are obtained with low gelatin concentrations rather than with high gelatin concentrations.

When gelatin is added in form of solid phase (CPMG5) mechanical properties are slower than values reported in literature²⁸ for the same amount of gelatine incorporated into CPC in form of liquid phase. In fact, when gelatine is incorporated as solid phase, acts as a second and discontinuous phase in the cement inorganic matrix causing a decrease of mechanical properties. Gelatin is also used as foaming agent in CPC. Self-setting Sr(2%)- α TCP/gelatin foams are obtained by mixing Sr2%- α TCP with a foamed gelatin solution, which after setting results in a HA solid foam, with high macro-porosity that influences negatively the mechanical features of bone cements that collapse at values of 1-2 MPa.

9.5.2 Young's Modulus

An adequate value of the elasticity modulus is a requirement of fundamental importance in the development of ceramic materials to use in the realization of bone substitutes. It is indeed necessary that the mechanical properties of the system are as similar as possible to those of human bone; high value of the Young's modulus corresponds to a high rigidity and thus to a high fragility of the material. Moreover, Young's modulus values of CPC have not to be high to avoid a fracture of adjacent vertebrae when cement is injected in a vertebral site. In fact, excessive cement rigidity reduces the endplate bulge of the augmented vertebra, thereby reducing the local spinal joint flexibility. As a consequence of the reduced joint flexibility there is an increase in the pressure on the intervertebral disc leading to an abnormal mechanical load transfer on the adjacent vertebral body with increased risk of fracture. It is also generally believed that the relatively hard bone cement leaks out from the vertebral body into the intervertebral disc resulting in new fractures as

a consequence of the excessive stimulation of the adjacent endplate.

The incorporation of polymer in SrCPC formulation increases ductility and plasticity of the materials, allowing for a higher deformation before breaking. In fact Young's modulus (Fig. 19) calculated for SrCPC/polymer cements result slower than cement without polymeric phase (Sr2%CPC). However, all SrCPC formulations present good Young's modulus values that are less than 1GPa.

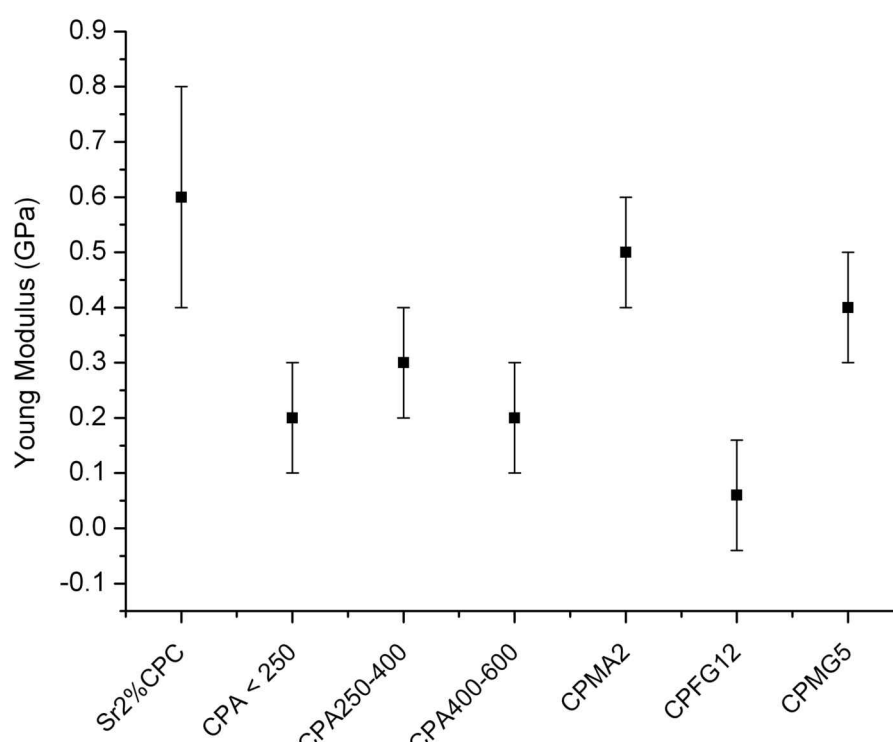


Fig. 19: Young's Modulus values of SrHA cement

9.6 Route to enhance the mechanical properties of CaP bone cement

As already discussed in paragraph 8.2, a critical problem that limits wider clinical application of Calcium phosphate ceramic cements is their mechanical properties, as they are brittle and have low impact resistance and relatively low tensile strength (6 to 10 MPa). After the injection in the vertebral body in fact, cement should harden quickly to achieve a compressive strength at least of 30 Mpa so that the individual can be stand up. In order to improve the mechanical strength of CPC two routes have been experimented:

- 1) Incorporation of bio-active reinforcing phase (TiO_2)³⁰ into Sr2%- α TCP paste.
- 2) Cross-link of Sodium Alginate suspension.

9.6.1 Incorporation of TiO_2 as bio-active reinforcing phase

TiO_2 (Degussa) was mixed with Sr2%- α TCP through a ball milling in Ethanol for two hours. Wet mixture was dried and mixed with a solution of $\text{Na}_2\text{HPO}_4 \cdot 2\text{H}_2\text{O}$ (2.5 wt%) to form a paste that was injected in silicon moulds thermostated at 37°C. In table 8 are reported the main experimental details used to prepare SrHA/ TiO_2 pastes.

Sample code	TiO_2 (wt %)	Sr2%- α TCP (wt %)	L/P ml/g	Setting time	
				I _{st}	F _{st}
CPTi95/5	5	95	0.6	5 min	15 min
CPTi90/10	10	90	0.6	5 min	15 min

Table 8. Experimental details of SrHA/ TiO_2 cement

Sr2%- α TCP/ TiO_2 cement pastes show a faster setting time indicating that TiO_2 does not influence the setting process of the paste.

In table 9 are reported the mechanical features and porosity values obtained for cement paste containing different amount of Titania. Porosity values of both cement paste containing Titania are equal to that obtained for Sr2% α CPC cement, indicating that Titania does not affect the porosity of materials. Moreover, Titania does not influence the compressive strengths of the cements but only their stiffness; in fact Young's modulus values are higher if compared to that of Sr2% α CPC.

Sample code	P_{total}	σ_{comp} (MPa)	E (GPa)
CPTi95/5	0.63 ± 0.01	12 ± 2	0.9 ± 0.03
CPTi90/10	0.63 ± 0.01	10 ± 2	0.9 ± 0.03

Table 9. Porosity values and mechanical features of SrHA/TiO₂ cement

9.6.2 Sodium Alginate cross-linking

As previously discussed, the addition of Sodium Alginate enhanced the hardening reaction of CPCs showing shorter setting time.

In order to improve the mechanical strength of Sr2%CPC, the addition of a cross-linked Sodium Alginate suspension to Sr2%- α TCP phase was investigated. Sodium Alginate in fact is soluble in aqueous media and become cross-linked with divalent cations including Ca²⁺ through the ionic interaction between the ions and glucuronate groups. Moreover the addition of a cross-linked Sodium Alginate suspension could also improve the injectability and the cohesiveness of Sr2%CPC when immersed in a simulated body fluid (SBF) at 37°C.

In details, Sr2%- α TCP powder was mixed with a suspension made of 2 w% of Sodium Alginate dissolved in Na₂HPO₄ * 2H₂O (2.5 wt%); this last used as accelerating setting. Soon after, the obtained paste was cross-linked with a solution of CaCl₂ (5 wt%) and injected in cylindrical teflon mould immersed in SBF solution stored at 37°C. The mixing ratio of power-to-liquid was 0.8 ml/g.

In fig. 20 is reported the synthesis scheme for the development of Sr2%CPC/Alg cement.

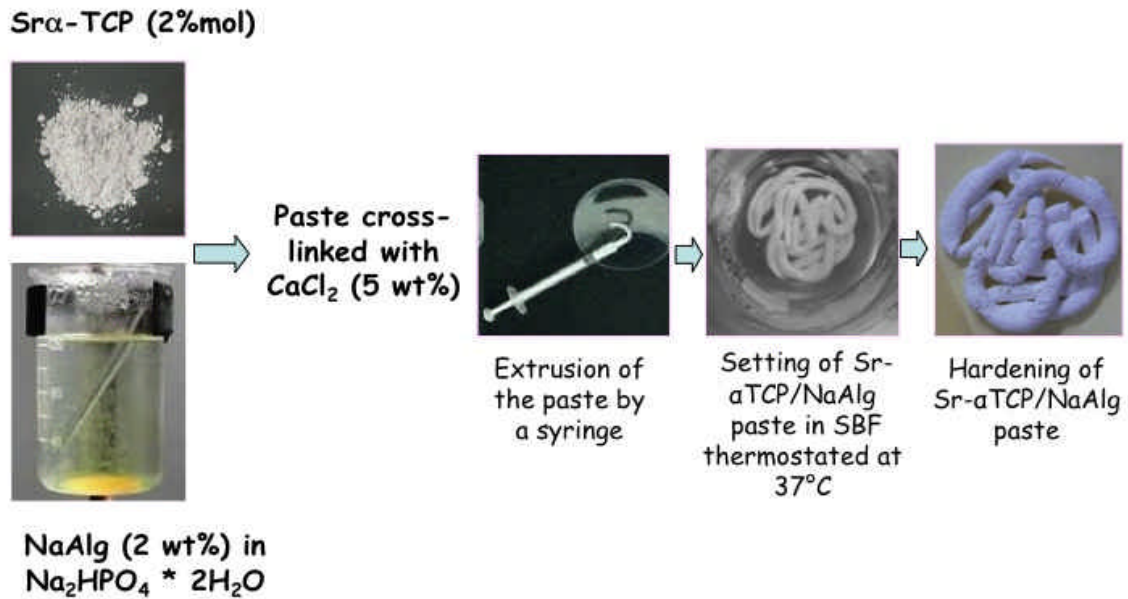


Fig. 20. Synthesis scheme of Sr2% α TCP/Alg cement

The effect of the addition of Alginate on the setting time of Sr2%- α TCP was observed by the Gillmore Needle test. The initial setting time was 15 minutes while the final setting time was 30 minutes. After the hardening, Sr2% α TCP/Alg cement was removed by cylindrical teflon mould and soaked in SBF solution stored at 37°C for 3 days. The surface morphology of Sr2% α TCP/Alg cement after the incubation period in SBF was observed by SEM (Fig. 21a).

The hardened cement showed a completely phase transformation of the initial Sr(2%)- α TCP into a nano-crystallite HA in a simulated biological fluid, as deduced by SEM morphology (Fig. 21b) that showed HA crystallite with a plate-like morphology.

The properties of crystalline HA formed during the incubation in a fluid, such as the degree of crystallization and the crystal morphology should play important roles in the mechanical properties of the cement. The HA nano-crystallites form an interconnected network within the porous structure of the CPCs, leading to an improvement in strength. Therefore, the increase in strength is highly associated with the HA nano-crystalline formation.

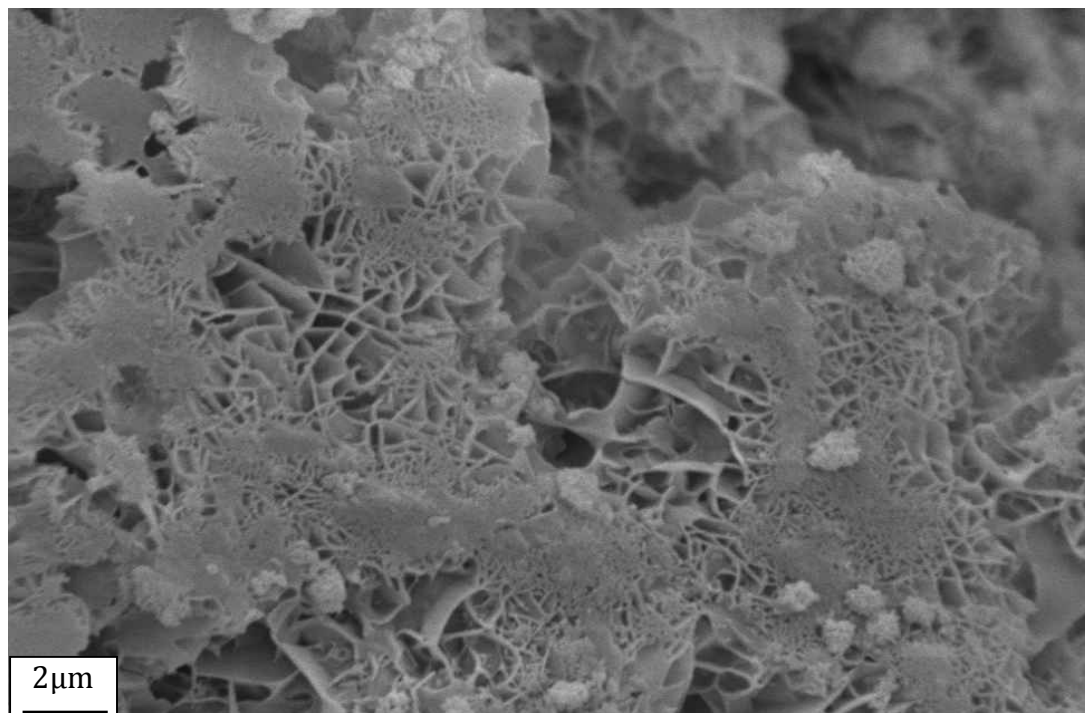


Fig. 21a. SEM surface morphology of Sr2%CPC/Alg cement after the hardening.

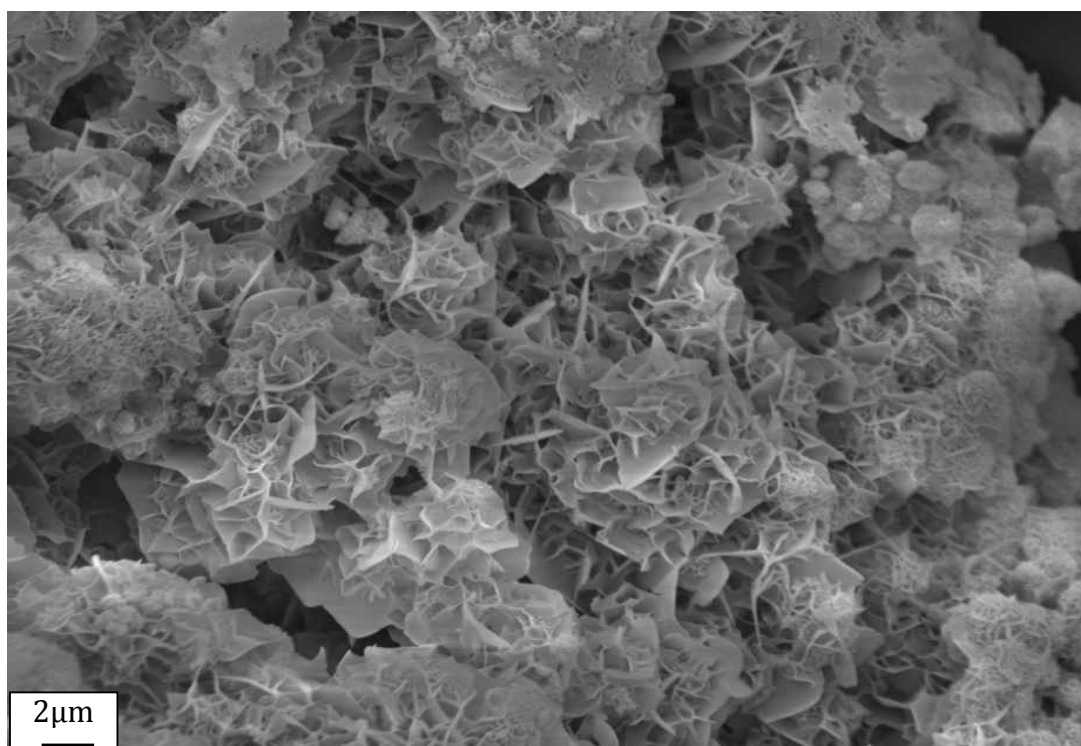


Fig. 21b. Details of Apatitic crystallite of Sr2%CPC/Alg cement: after the incubation in SBF, apatitic crystallites were well developed and showed a plate-like morphology.

The mechanical properties of cross-linked Sr2%CPC/Alg cement samples after 3 day of incubation time in SBF were investigated based on compressive strength. The compressive strengths of Sr2%CPC/Alg cements are in the range 30-35 Mpa while their elastic modulus are close to 1 Gpa. In Fig. 22 are showed three stress-strain curves typical of Sr2%CPC/Alg hardened cement.

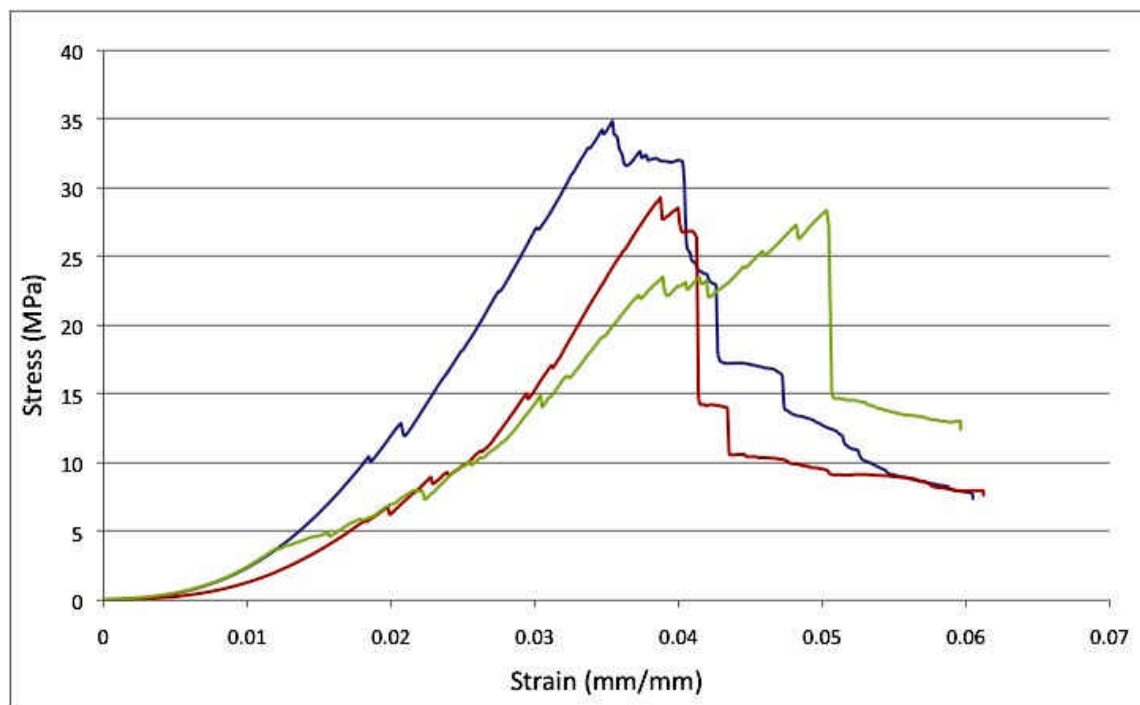


Fig. 22. Stress-strain curves of Sr2%CPC/Alg cement.

Injectability and cohesiveness

Injectability is the ability of a paste to be extruded through a needle without demixing. Water-soluble polymers, such as Sodium-Alginate was used also to enhance CPC injectability and to increase cohesion time.

Cohesion is the ability of a paste to set in a fluid without disintegrating. Nevertheless, disintegration of the cement paste, in addition to preventing the cement from setting, can provoke an inflammatory response and cell apoptosis³¹. For this reason, the cohesion time should be lower than the initial setting time to guarantee the structural integrity of the cement paste when injected in liquid solution³². In general, adding soluble polymers during the liquid phase tends to enhance CPC cohesion. The mechanism underlying this

phenomenon is the increased viscosity of the CPC paste, which prevents penetration of the surrounding fluid.

The cross-link of Sr2%CPC/Alg paste with CaCl_2 solution, before the injection in SBF solution, increases the cohesiveness of the paste since Sodium-Alginate forms with Ca^{2+} ions an insoluble hydrogel, calcium alginate, that inhibits the decay of cements paste in liquid solution (Fig. 23a). In fact after the hardening in SBF at 37°C , the paste does not disintegrate in liquid phase keeping its original shape (Fig. 23b). Moreover the presence of Sodium-Alginate in CPC formulation improves the injectability of the cement paste that was easily injected through a needle having a cannula with a diameter of 0.8 mm without demixing.



Fig. 23a. Morphology of Sr2%CPC/Alg paste after the injection in SBF solution at 37°C (before setting)



Fig. 23b. Morphology of Sr2%CPC/Alg cement after the hardening in SBF solution at 37°C (after setting)

9.7 Conclusion

Inorganic and hybrid CaP cements were successfully synthesized through the controlled setting of Sr- α TCP phases into SrHA. Sr²⁺ ion exerts an active role in the hydrolysis of α -TCP: in the presence of increasing amounts of Sr²⁺ in solution, the speed of the conversion reaction of α -TCP into SrHA is highly reduced and the formation of β -TCP as secondary phase is favoured. Moreover, increasing strontium substitution for calcium in the HA structure provokes a linear variation of the cell parameters in agreement with the increasing mean dimensions of the cation. Carbonate ion was also introduced into SrHA cement formulation to obtain cement with enhanced biomimetic property.

The combination of polymers with CPC, either solubilized in the liquid phase or as a second solid phase, has proven to be an interesting strategy for the development of bone substitutes with improved performance. The addition of gelatin and sodium alginate into Sr- α TCP phases enhances the porosity of material that is necessary to allow cell colonization and hence to improve cement resorption and bone remodelling. Gelatin

cements exhibit high setting time, high porosity and low mechanical properties. Instead, the addition of alginate enhances the hardening reaction of CPCs showing shorter setting times. When immersed in a body simulating fluid the Alginate/CPC fully induces a formation of an apatite crystalline phase. The compressive and tensile strengths of the Alginate/CPCs greatly improve after the cross-link of the paste with a calcium chloride solution. Moreover, alginate improves the injectability of the paste and its cohesiveness in liquid solution so that the paste hardens without disintegrates.

In order to assess the effect of Strontium amount on cell response and the osteogenic aspect of the development cement an *in vitro* cell cytotoxicity test must be carried out.

Moreover, the regenerative properties of developed cements in terms of biomaterial resorption rate and the quality of newly formed bone have to be evaluated by *in vivo* test.

References

1. Elliott JC. *Structure and chemistry of the apatites and other calcium orthophosphates*. Amsterdam: Elsevier; **1994**.
2. Ando J. *B. Chem. Soc. Jpn.* **1958**, *31*, 196.
3. Saint-Jean SJ, Camiré CL, Nevsten P, Hansen S, Ginebra MP. *J. Mater. Sci. Mater. Med.* **2005**, *16*, 993.
4. Durucan C, Brown PW. *J. Mater. Sci.* **2002**, *37*, 96.
5. Camiré CL, Gbureck U, Hirsiger W, Bohner M. *Biomaterials* **2005**, *26*, 2787.
6. Bohner M, Malsy AK, Camiré CL, Gbureck U. *Acta Biomater.* **2006**, *2*, 343.
7. Brunner TJ, Grass RN, Bohner M, Stark WJ. *J. Mater. Chem.* **2007**, *17*, 4072.
8. Iogo Y, Ito A, Kamo M, Sakurai T, Onuma K, Ichinose N, et al. *Mater. Sci. Eng. C* **2004**, *24*, 709.
9. Pan H, Li Z, Lam WM, Wong JC, Darvell BW, Luk KDK, et al. *Acta Biomater.* **2009**, *5*, 1678.
10. Bigi A, Panzavolta S, Rubini K. *Chem. Mater.* **2004**, *16*, 3740.
11. Shannon RD, Prewitt CT. *Acta Crystallogr. Struct. Crystallogr. Cryst. Chem.* **1969**, *25*, 925.
12. Kim HW, Koh YH, Kong YM, Kang JG, Kim HE. *J. Mater. Sci. Mater. Med.* **2004**, *15*, 1129.
13. Landi E, Sprio S, Sandri M, Celotti G, Tampieri A. *Acta Biomaterialia* **2008**, *4*, 656.
14. Bertinetti L. Nanomateriali per applicazioni biomediche: sintesi e caratterizzazione delle funzionalità di superficie. PhD thesis, University of Torino.
15. Gibson IR, Bonfield W. *J Mat Sci: Mat Med.* **2002**, *13*, 685.
16. Gibson IR, Bonfield W. *J Biomed Mater Res.* **2002**, *59*, 697.
17. LeGeros RZ. In: Myers KH, editor. Calcium phosphates in oral biology and medicine, Monographs in oral science. Vol. 15. Basel, Switzerland: AG Publishers, **1991**, 82-107.
18. E. Landi, A. Tampieri, G. Celotti, L. Vichi, M. Sandri. *Biomaterials*, **2004**, *25*, 1763.
19. RA Perez, HW Kim, MP Ginebra, *J. Tissue Eng.* **2012** DOI:10.1177/2041731412439555

-
20. Perez RA, Del Valle S, Altankov. *J. Biomed. Mater. Res. B* **2011**, 97, 156.
 21. Chiang TY, Ho CC, Chen DC. *Mater. Chem. Phys.* **2010**, 120, 282.
 22. Bigi A, Panzavolta S, Sturba L. *J. Biomed. Mater. Res. A* **2006**, 78, 739.
 23. M. Bouler, M. Trécant, J. Delécrin, J. Royer, N. Passuti, G. Daculsi, *Journal of Biomedical Materials Research* **1996**, 32, 603.
 24. K. De Groot, *Annals of the New York Academy of Sciences* **1988**, 523, 227.
 25. Xu HHK, Quinn JB, Takagi S, Chow LC, Eichmiller FC, *Journal of Biomedical Materials Research* **2001**, 57, 457.
 26. Bohner M. *Injury Int. J. Care Injured* **2000**, 31, 37.
 27. Lian Q, Li DC, He JK. *Proc. Inst. Mech. Eng. H.* **2008**, 222, 347.
 28. Bigi A, Bracci B and Panzavolta S. *Biomaterials* **2004**, 25, 2893.
 29. Bigi A, Centelli I, Panzavolta S. *J. Appl. Biomater. Biomech.* **2004**, 2, 81.
 30. Dapporto M. Progettazione e caratterizzazione di compositi biomimetici rinforzati a base apatitica per la realizzazione di impianti per sostituti ossei, Tesi di Laurea, 2009, Università di Bologna.
 31. Pioletti DP, Takei H, Lin T, et al. *Biomaterials* **2000**, 21, 1103.
 32. Driessens FC, Planell JA, Boltong MG, et al. *Proc. Inst. Mech. Eng. H.* **1998**, 212, 42

Conclusion and Future Perspective

The aim of this work was to design and produce newly conceived biomimetic nano-structured biomaterials as scaffolds for bone and osteochondral regeneration as new solutions towards the local treatment of hard tissues affected by degenerative diseases such as Osteoarthritis (OA) and Osteoporosis (OP). Since bone and cartilage are highly organised over multiple length scales, approaches such as self-assembly and biomimetic mineralisation have been used to control scaffold nanostructure and mechanics; in this way materials endowed with the ability to guide and enhance bone regeneration have been developed.

Following the biomineralization approach, magnetic biohybrid composites (FeHA/Coll) have been realized nucleating a nano sized iron doped hydroxyapatite (FeHA), with an intrinsic superparamagnetic property, directly on collagen fibres. At this purpose, a synthetic procedure to obtain a magnetic ($\text{Fe}^{2+}/\text{Fe}^{3+}$)-lattice substituted HA, minimizing the formation of magnetite as secondary phase, have been developed and optimized showing that it possible to introduce both iron species into the HA lattice at different Ca sites with a specific coordination generating two different sublattices whose interaction could induce superparamagnetic behavior.

The introduction of the iron ions into the apatitic lattice during the stage of HA nucleation induces in the final composite (FeHA/Coll) those chemico-physical, structural and morphological features typical of newly formed bone along with superparamagnetic properties. The synthesis temperatures influence the chemico-physical features of the magnetic biohybrid scaffolds and hence their biological performance.

In vitro investigations performed on these novel biomimetic magnetic scaffolds indicate firstly their biocompatibility showing their good ability to support cell adhesion and proliferation. Moreover, *in vitro* results show that not only the novel magnetic scaffolds are biocompatible, but moreover if they are subjected to a static magnetic field (SMF) application, their performance in cell proliferation is even improved respect to the control scaffold already used in clinic. These results underline how the superparamagnetic

properties of the novel scaffolds which are emphasized by the application of an external static magnetic field enhancing cell proliferation.

Taking into consideration the good results coming from the pre-clinical and clinical application of Maioregen® as one of the most effective scaffold used in the current innovative orthopaedic practise, a three-layered structure resembling the sub-chondral bone, the tide-mark and the cartilaginous layer has been designed and developed nucleating FeHA instead HA as the mineral component of the composite. Soon, this three-layered scaffold will be implanted in the sheep femoral condyle and its regenerative properties under the application of an external magnetic field will be evaluated.

Therefore, magnetic biohybrid scaffolds developed in this work are promising candidates for the regeneration of osteochondral region and hence for regeneration of tissues damaged by OA since they have not only the potential to provide a tissue-conductive system that mimics the three-dimensional environment of the extracellular matrix (ECM), but also, thanks to their magnetic properties, they give the osteoinductive stimuli necessary for a faster and significant bone regeneration directly and specifically in the target site.

Moreover, the magnetic property of the FeHA phase together with its biocompatibility open the door of the regenerative medicine to a conceptually new family of biomimetic scaffolds able to be biologically manipulated or activated in situ by means of an external magnetic field. Additionally, the high hyperthermia value obtained for FeHA powder offers a true advantage with respect to the present solutions in anti-cancer therapies: the benefits foreseen are not only the more intense and rapid local effect, but most of all its biocompatibility/degradability, which overcome the side effects of long-term cytotoxicity. Bioactive and bioresorbable calcium phosphate bone cements have been also investigated as biomaterials to use in regenerative vertebroplasty to treat tissue damaged by OP.

In this work the ability of Sr- α TCP to set in situ and to form, in contact with a liquid solution, a paste that resulting, upon hydrolysis in water, into strontium calcium deficient hydroxyapatite has been investigated.

Sr²⁺ ion exerts an active role in the hydrolysis of α -TCP: in the presence of increasing amounts of Sr²⁺ in solution, the speed of the conversion reaction of α -TCP into HA is highly reduced. Moreover, increasing strontium substitution for calcium in the HA structure provokes a linear variation of the cell parameters in agreement with the

increasing mean dimensions of the cation. However, the resulting apatitic phase contains significant amounts of Sr^{2+} suggesting that the addition of Sr^{2+} to CPC formulation could be successfully exploited for its local delivery in bone defects.

Carbonate ion was also introduced into SrHA cement formulation to obtain cement with enhanced biomimetic property. The combination of polymers with CPC, either solubilized in the liquid phase or as a second solid phase, has proven to be an interesting strategy for the development of bone substitutes with improved performance. The results obtained indicated that the addition of gelatin and sodium alginate into Sr- α TCP phases enhances the porosity of material that is necessary to allow cell colonization and hence to improve cement resorption and bone remodelling. Fast setting time (15-30 minutes), high mechanical performance (compressive strength 30-35MPa), good cohesiveness and injectability have been achieved adding to CPC formulation an alginate suspension cross-linked with calcium chloride solution.

Despite the numerous scientific articles on CPCs, there is still a lot to be done to reach a better understanding of the physical, chemical and biological properties of CPC. Additionally, the gap between CPC research and clinical use should be decreased, for example by studying and defining the needs of specific applications (e.g. vertebroplasty: injectability, radio-opacity, viscosity, absence of clotting) in terms of cement properties and by finding adequate solutions. Recent and future developments will enable the commercialisation of better and more differentiated products that should improve the clinical outcome and hence the patient life quality. Further, CPCs await a major role as model cold setting systems for the study of inorganic/organic molecule interactions as interest in hard tissue mimetics grows in materials science. Main trends are in the field of drug delivery (e.g. bone morphogenetic proteins), synthesis of granules and blocks with improved biological properties, more resorbable cements (e.g. via macropores or using brushite CPC), better handling (e.g. mixing, injection) and novel organic-inorganic hybrid materials with properties yet to be evaluated.

